Max-Planck-Institut
für Polymerforschung
Max Planck Institute
for Polymer Research

Max Planck Graduate Center
mit der Johannes Gutenberg-Universität Mainz

Biodegradable Protein Nanocarriers for Drug Delivery

Dissertation

zur Erlangung des akademischen Grades

„Doktor der Naturwissenschaften“

im Promotionsfach Chemie

am Fachbereich Chemie, Pharmazie und Geowissenschaften

der Johannes Gutenberg-Universität Mainz

vorgelegt von

Keti Piradashvili

Mainz 2016

Für meine Eltern

Declaration

I hereby declare that I wrote the dissertation submitted without any unauthorized external assistance and used only sources acknowledged in the work. All textual passages which are appropriated verbatim or paraphrased from published and unpublished texts as well as all information obtained from oral sources are duly indicated and listed in accordance with bibliographical rules. In carrying out this research, I complied with the rules of standard scientific practice as formulated in the statutes of Johannes Gutenberg-University Mainz to insure standard scientific practice.

Mainz, 2016 Keti Piradashvili

Amtierender Dekan:
Erster Gutachter:
Zweiter Gutachter:
Tag der mündlichen Prüfung:

CONTENT

Abstract

The application of synthetic polymers for drug delivery often requires tremendous efforts to ensure biocompatibility and -degradation. To use body's own substances, e.g. proteins, can help to overcome these problems. This thesis covers the synthesis of hollow nanocarriers entirely composed of proteins. The versatility in terms of protein choice as well as cross-linking chemistry highlights the potential impact of these systems on the field of nanoparticular drug delivery.

The thesis is structured as follows. In the first chapter, a general overview of interfacial reactions is given. The advantages of a confinement of two reactants at the liquid-liquid interface to form a new product are emphasized regarding the improved reaction kinetics, higher yields and selectivity. It is shown that the use of immiscible systems, e.g., (mini)emulsions, offers an attractive strategy for the production of nano- and microcarriers for various applications. Furthermore, a brief introduction into (bio)orthogonal chemistries with focus on their application for nanocarrier formation is given.

In the second chapter, the results obtained in the course of this thesis are reviewed and critically discussed. The chapter is divided into four sections, beginning with hollow ovalbumin and bovine serum albumin nanocarriers synthesized via interfacial polyaddition reaction with 2,4-toluene diisocyanate. In this section, it is shown that protein nanocarriers provide a platform for the production of biocompatible drug delivery vehicles. These nanocarriers with core-shell morphology are capable to both encapsulate model hydrophilic compounds as well as therapeutic substances, and release them upon enzymatic cleavage. Furthermore, they accumulate preferentially in the liver and are well taken up by dendritic cells. For this reason, protein nanocarriers represent a promising approach for treatment of liver-associated diseases such as hepatitis C.

In the following section, these findings are pursued in more detail. Protein nanocarriers synthesized out of the non-structural hepatitis C protein NS5A are used in a mouse model for the efficient targeting of liver-resident antigen presenting cells to induce intrahepatic immunity against HCV infection.

The idea to avoid additional carrier substances in drug delivery design in general for every drug and to produce instead nanocarriers with both shell and cargo consisting of

the same material is described in the third section. The drug dexamethasone used for this purpose is responsible for severe side effects when administered in the soluble form. Therefore, a delivery of this drug exclusively to the targeted organs by nanovehicles is desirable. The possibilities but moreover the limitations of this full-drug nanocarrier approach are discussed in this section.

In the last section, an alternative, bio(orthogonal) method for protein nanocarrier preparation is discussed using the Huisgen 1,3 dipolar tetrazole-ene cycloaddition. Protein nanocarriers obtained via this method are characterized according to both their colloidal properties as well as their impact on biological systems such as dendritic cells and human blood plasma. The bioorthogonality of the route of preparation is verified by the encapsulation of an immunostimulant, which maintains its effectiveness upon release.

In the third chapter, the experimental details for each section of the second chapter are listed. The fourth chapter gives a brief summary of the topics covered in this thesis and draws an outlook for future directions.

Zusammenfassung

Die Verwendung synthetischer Polymere für den Wirkstofftransport bedeutet häufig erheblichen Aufwand, um Biokompatibilität und –abbaubarkeit zu gewährleisten. Um diese Probleme zu überwinden, können körpereigene Substanzen, z.B. Proteine, nützlich sein. Diese Doktorarbeit behandelt die Herstellung und Verwendung von Nanocarriern, die vollständig aus Proteinen aufgebaut sind. Diese Nanocarrier wurden durch Grenzflächenreaktionen in Miniemulsion hergestellt. Um die Proteine zu Nanocarriern zu vernetzen, wurden sowohl die Proteinstrukturen modifiziert, als auch unterschiedliche chemische Reaktionen an der Grenzfläche verwendet. Die Vielseitigkeit bezüglich der Wahl an Proteinen als auch der Vernetzungschemie hebt hervor, welchen potentiellen Einfluss diese Systeme auf das Gebiet des nanopartikulären Wirkstofftransports haben können.

Die Arbeit ist wie folgt strukturiert. Im ersten Kapitel wird ein allgemeiner Überblick über Grenzflächenreaktionen gegeben. Eine chemische Reaktion an einer flüssig-flüssig Grenzfläche ist im Vergleich zur gleichen Reaktion in Lösung oder Substanz von Vorteil: Sie zeichnet sich durch eine verbesserte Reaktionskinetik, höhere Ausbeuten und größere Selektivität aus. Durch Grenzflächenreaktionen können auch nicht-mischbare Reagenzien miteinander zur Reaktion gebracht werden. Die (Mini)emulsion ist hierbei eine attraktive Strategie, da stabile Nano- und Mikrotröpfchen generiert werden, an deren Grenzfläche Reaktionen ablaufen können, wie z.B. die Vernetzung von Proteinen für Nanocarrier. Weiterhin gibt dieser Abschnitt der Arbeit einen kurzen Überblick über die (bio)orthogonale Chemie, insbesondere um damit Nanocarrier herzustellen und gleichzeitig zu beladen.

Das zweite Kapitel präsentiert die experimentalen Ergebnisse dieser Doktorarbeit. Das Kapitel ist in vier Abschnitte unterteilt, beginnend mit Nanocarriern aus Ovalbumin und bovinem Serumalbumin, die mittels einer Polyadditionsreaktion mit 2,4-Toluoldiisocyanat an der Grenzfläche von Nanotröpfchen hergestellt wurden. In diesem Abschnitt wird gezeigt, dass Protein-Nanocarrier eine Plattform dafür bieten, biokompatible Wirkstofftransportsysteme herzustellen. Diese Nanocarrier mit einer Kern-Schale-Morphologie ermöglichen es, sowohl hydrophile Modellsubstanzen als auch Therapeutika einzukapseln und durch enzymatische Spaltung wieder freizugeben. Des

Weiteren akkumulieren sie bevorzugt in der Leber und werden gut von dendritischen Zellen aufgenommen. Aus diesem Grund stellen Protein-Nanocarrier eine vielversprechende Herangehensweise für die Behandlung leberbezogener Krankheiten wie Hepatitis C, dar.

Im nächsten Abschnitt werden Protein-Nanocarrier, die aus dem nicht-strukturellen Hepatitis C-Protein NS5A hergestellt sind, im Mausmodell für ein effizientes Targeting von in der Leber befindlichen, antigen-präsentierenden Zellen verwendet. Ziel ist es, eine intrahepatische Immunität gegen die HCV-Infektion zu induzieren.

Die Idee, bei jeglichen Wirkstoffen auf zusätzliche Materialien für die Herstellung von Transportsystemen zu verzichten und stattdessen Nanocarrier aus dem Wirkstoff zu produzieren, wird im dritten Abschnitt beschrieben. Der Wirkstoff Dexamethason, der hierfür verwendet wird, verursacht schwere Nebenwirkungen wenn er in löslicher Form angewendet wird. Aus diesem Grund ist ein Transport dieses Wirkstoffes ausschließlich zu den Zielorganen durch Nanovehikel erstrebenswert. Die Möglichkeiten und die Grenzen der Synthese von vollständig aus Wirkstoff bestehenden Nanocarriern werden in diesem Abschnitt diskutiert.

Im letzten Abschnitt wird eine neue, (bio)orthogonale Methode zur Herstellung von Protein-Nanocarriern diskutiert. Zum ersten Mal wird hierfür die Huisgen-1,3-dipolare Cycloaddition verwendet. Protein-Nanocarrier, die durch dieser Methode erhalten wurden, werden hinsichtlich ihrer kolloidalen Eigenschaften als auch ihres Einflusses auf biologische Systeme, wie dendritische Zellen und humanes Blutplasma, untersucht. Die Bioorthogonalität dieser Herstellungsweise wird durch das Einkapseln eines Immunostimulans gezeigt, welches seine Effektivität nach der Freisetzung beibehält.

Im dritten Kapitel sind die experimentellen Details für jeden Abschnitt aus dem zweiten Kapitel gelistet. Das vierte Kapitel fasst die jeweiligen Themen, die in dieser Doktorarbeit behandelt wurden, zusammen und gibt einen Ausblick auf die zukünftige Ausrichtung.

Motivation

The human body reacts to the intrusion of foreign matter with resistance. Our immune system recognizes every intruder, be it a threat or a lifesaving drug, as a deviation from the normal state and takes measures against it according to the severity of invasion.[1] Due to this efficient host defense and clearance system of our body, targeted medication of a pathological site is a challenge.[2] A high overall dosage is usually required for reaching sufficient concentrations in the organ of interest for the drug to make an impact. This can result in severe adverse effects and damage of healthy organs or tissue.[3]

Nanomedicine, i.e. the application of nanotechnology in the medical field, is a promising approach to change the course of diagnostics and treatment towards a more tailored and personalized medication.[4-5] Efficient methods are searched for to construct vehicles on nanoscale able to deliver pharmaceuticals to the target site in the body, at a therapeutic concentration, and for the required period. The 2016's Nobel prize in chemistry reflects both the fascination with nanoscopic transport devices and their significance for the future.

Protein nanocarriers presented in this work can have a high potential to act as the versatile drug delivery agent being searched for.[6-7] Proteins, e.g. albumins, are natural polymers, and since they are an essential constituent of our body, we are acquainted with processing them. Albumin, chosen for this purpose, is especially known for its high drug binding capacity, since it is inherently a transport protein for various endogenous and exogenous compounds.[8-9] Albumin is easily available, robust and allows further modifications with various ligands for site-specific targeting.[10] It is non-toxic, metabolizing into innocuous degradation products.[11] The design of albumin nanocarriers offers the possibility to combine the advantages of a hollow carrier (encapsulation and protection of the cargo) with the benefits provided by the nature of the protein (biocompatibility and, very importantly, biodegradability to release the cargo).

The versatility of protein nanocarriers further expresses itself in the almost free selection of the protein as the carrier material. Since albumin-based nanocarriers show a preferential uptake in the liver,[12-14] their application in rational liver-targeted drug delivery systems is promising. However, the use of functional proteins such as proteins from

hepatitis B and C viruses enables us to synthesize nanocarriers that constitute the drug themselves and co-deliver additional therapeutics, stimulants or imaging agents.

The choice of chemistry used for nanocarrier synthesis is sometimes limited by the requirements set by certain cargos. Avoiding a reaction with the sensitive compound, which might otherwise lose its properties, is possible with bioorthogonal chemistries, which are inert against the native functionalities of the drug.[15-16] A further motivation of this work is therefore the transformation of a bioorthogonal technique, usually used for protein labeling, to hone the preparation of hollow protein nanocarriers towards the transport of sensitive compounds.

1. Theoretical background

This chapter covers reactions and polymerizations at the interface of two immiscible liquids. Special emphasis is given to the orthogonal chemistry for nanocarrier preparation. Parts of this chapter have been published in collaboration with E. M. Alexandrino, F. R. Wurm and K. Landfester in the review "Reactions and Polymerizations at the Liquid–Liquid Interface." by Piradashvili *et al.*, *Chemical Reviews,* **2016**, *116,* 2141-2169 and have been altered for this thesis with permission from reference [17]. Copyright 2016 American Chemical Society.

1.1 Interfacial reactions

130 years after Schotten and Baumann, reactions at the liquid-liquid interface still hold a great potential for synthetic chemistry. Reactions “on water”, “at the interface”, or by “phase-transfer” are important platforms for modern chemistry, notably as in most cases water can be used as the second phase. Immiscible reaction partners react at the interface of two liquids, which is especially a convenient and versatile route for the preparation of (nano)materials, which are not accessible by any other technique.

The interface between hydrophilic and hydrophobic liquids can be used to combine immiscible reaction partners or to protect sensitive reactants, from hydrolysis for example. There are many types of reactions that can be either conducted at the interface of two immiscible liquids in a static environment or mechanically stirred. The surface can be adjusted by the choice of an emulsification technique. The use of different environments for selectively solubilizing the partners of a reaction is a convenient and efficient pathway, which is widely used, e.g., for the formation of esters and amides by the reaction of electrophilic acid chlorides (carboxylic acid, phosphoric acid, etc.) dissolved in an organic phase with nucleophiles, dissolved in an aqueous environment. Catalysis at the interface is also an interesting approach with the catalyst in one phase, the product in the other. The adjustment of the reactivity of each compound in the mixture is important to guarantee high yield reactions, i.e., the competition between the hydrolysis of the acid chloride vs. the amidation, in the case of an amide formation. This was taken to the industrial level already in the 1930s with the first interfacial polycondensation of Nylon, which was presented to the public at the New York World’s Fair in 1939.[18-20]

Besides the vast applications of interfacial reactions (from macro to nano) for the formation of low molecular weight compounds, one should also note their potential as a tool for modern polymer chemistry.[21-28] At the droplet interface, monomers provided from either phase meet and react to generate a polymer, which can be soluble or insoluble in one or both phases. If an insoluble polymer is generated it can – on the macroscale – be removed from the interface. If the droplet size is reduced to micro and nanometers, a shell surrounding a liquid core, i.e., a hollow capsule is generated. This platform allows the generation of smart nanocarriers for various applications.

The reaction at the interface can be regarded as a molecular "screw clamp" forcing two or more molecules to undergo a reaction. This allows performing reactions that cannot be performed in homogeneous solutions. For example, alkyne-azide click reactions normally need copper catalysts, which are not necessary in heterogeneous conditions, as the interface, i.e., the close proximity of the two components, promotes the reaction.[29] This technique allows the encapsulation of various compounds (bioactive or sensitive molecules, as enzymes, vitamins, DNA, or proteins, monomers) (cf. section 1.2). If water-soluble compounds are encapsulated, the polymeric shell protects them from the organic solvent at the outside. After the reaction, the carriers can be transferred into an aqueous phase and used in the field of materials science or for biomedical applications.

This section is structured as follows: In the first part, a brief overview is given about emulsification strategies which are used to generate high interfacial areas. In the second part, organic reactions both at the macro- and nanoscopic liquid-liquid interfaces are summarized. The last part deals with polymerizations at the interface either to control polymer microstructure and reaction kinetics or to prepare nanocarriers.

1.1.1 Emulsification techniques

A reaction at the interface of two immiscible liquids can be performed with macroscopic phase separation, i.e., typically under static conditions, without stirring and only relying on the diffusion of the reactants to the interface, where the reaction takes place. In most examples of interfacial reactions, however, heavy stirring is used in order to increase the interfacial area and thus to optimize the reaction. Various emulsification techniques have been developed to produce droplets from micrometer to nanometer scale, which can be used to conduct the interfacial reaction. Control over the size, shape, and dispersity of the formed droplet additionally to the rate of droplet formation are the major

criteria for preferring one technique to the other. Figure 1 presents the techniques for the formation of droplets with average diameter in the micrometer or nanometer range. The relevant techniques for reactions at droplet interfaces will be presented in the following.

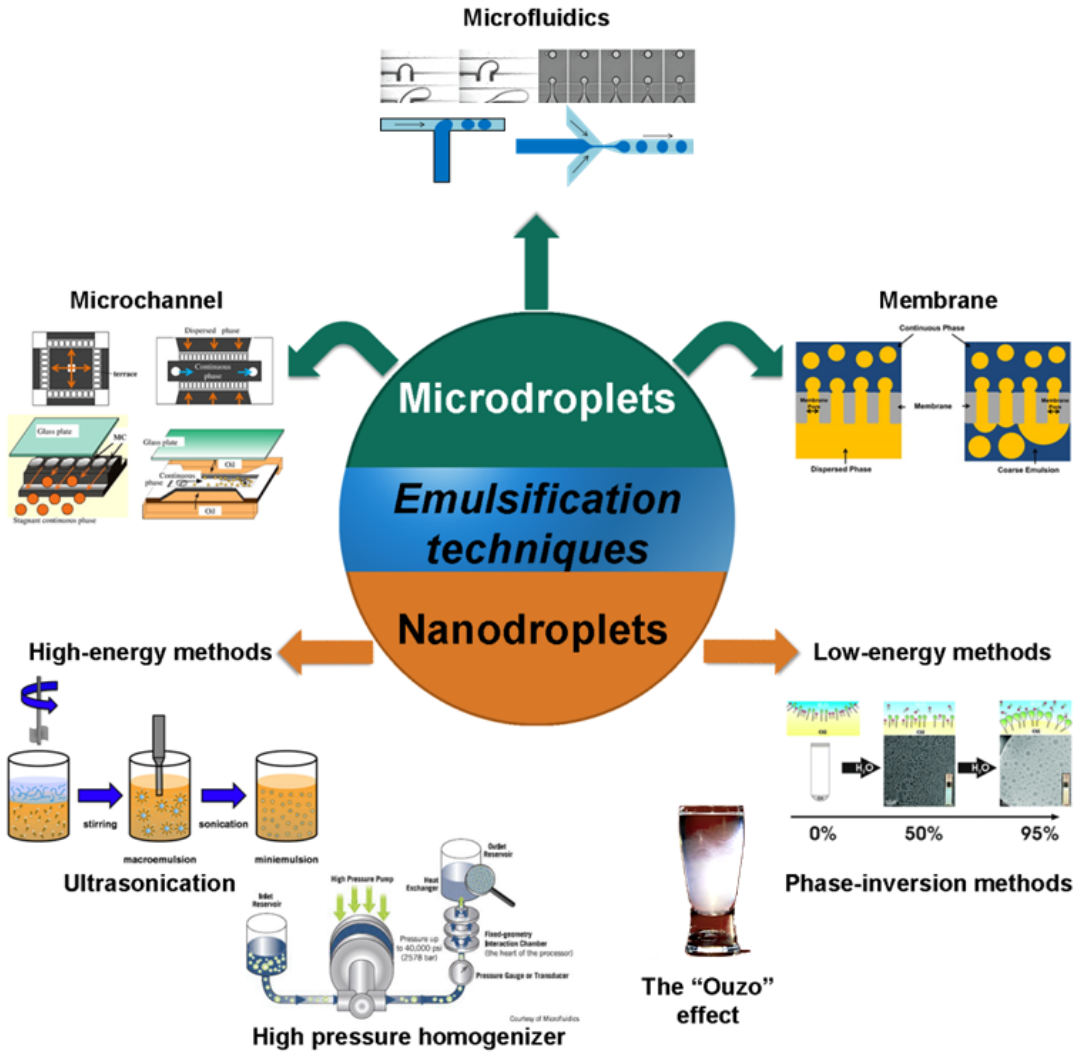

Figure 1: Schematic representation of the emulsification techniques used in the production of droplets in the micrometer region, as microchannel, microfluidics or membrane emulsification, or in the nanometer range. The production of nanodroplets is divided in high-energy methods, as ultrasonication or high pressure homogenization, or low-energy methods as for example phase inversion methods (pH, temperature, composition) and spontaneous emulsification ("Ouzo" effect). Images reprinted with permission from references [30-34]. Copyright 2014 Elsevier B.V. Copyright 2013 Elsevier B.V. Copyright 2011 Royal Society of Chemistry. Copyright 2008 Microfluidics International Corp. Copyright 2003 AIP Publishing LCC. Copyright 2010 Elsevier.

For the formation of droplets at the micrometer scale, membrane, microchannel, and microfluidic devices are widely used.[35] In all these techniques, microengineered devices control the droplet size by their geometry.[36] For the formation of nanodroplets, mechanical (ultrasonication;[37] high pressure homogenization[22, 38]) and spontaneous (Ouzo effect[39] and phase inversion phenomenon[38, 40]) formation can be applied. For all methods,

the composition of the emulsion, hydrodynamic conditions and wetting effects and the nature of the surfactants also have an influence on the system.[41-43]

1.1.1.1 Microfluidics

For the production of emulsions with narrow droplet size distributions and droplet diameters as small as 5 µm,[44] droplet-based microfluidics can be used. The precise control over single droplets,[45] a high throughput at kHz rates[42, 46] with lab-on-chip devices[47-48] and the generation of almost monodisperse droplets[49-50] (with coefficients of variation as low as 1.3%[51]) represent the main advantages of droplet-based microfluidics. Furthermore, the versatility of structures that can be obtained, the generation of double[45, 52] or multiple emulsions,[53-55] the synthesis of irregular particles,[56-59] core-shell structures,[60-63] Janus particles,[64-65] and liposomes[66-67] or polymersomes[68-69] have contributed to the popularization of microfluidic devices.

The simplest microfluidic device for droplet generation consists of a T-junction (see top image in Figure 1).[70] The continuous phase and the disperse phase are introduced in two perpendicular channels and form an interface at the junction. Due to the shear force exerted by the continuous phase, the disperse phase is dragged into the channel of the continuous phase and breaks into discrete droplets.[71] Another commonly used geometry is the flow-focusing device developed by Anna *et al.* where the disperse phase flows in the middle channel and the continuous phase in two outer channels (see top image in Figure 1).[30] A small orifice is located downstream of the channels and the two phases are forced to pass through it. Through pressure and shear stress applied from the continuous phase the inner fluid forms a narrow thread and breaks eventually into droplets.

For a stable droplet generation, it is crucial that the disperse phase does not wet the channel walls, whereas the wettability by the continuous phase and the chemical stability of the channel material towards the fluids should be guaranteed.

1.1.1.2 Microchannel emulsification

Microchannel emulsification allows the production of droplets from approximately 4 to 100 µm[72-74] with a coefficient of variation below 5%.[75] The microchannel device consists of a comb-like channel array on a silicon chip fabricated via photolithography. The microchannel modules can be designed either as dead-end or cross-flow devices (Figure 1, top left image).

In the dead-end module, microchannels are arranged on a terrace at all four sides of a silicon chip.[76] The disperse phase is placed in the center of the terrace and pushed through the channels. At the end of the terrace the droplet detaches and flows into the continuous phase.[77] No external shear stress is required for the droplet production as the formation is governed by the interfacial tension force.[78] The droplet is pushed through the microchannels and inflates on the terrace in a disc-like shape.[79] This shape has a higher interfacial area per volume than a spherical shape and is thus hydrodynamically unstable. This instability is the driving force for the droplet detachment as the preferred spherical shape is regained.[80]

To summarize, via this method uniform droplets are formed spontaneously at mild conditions as a high energy input and turbulent mixing with high shear forces are not required.[81-82] Thus, it is especially attractive for sensitive compounds in the food and pharmaceutical industry.[83-85] Furthermore, a direct microscopic observation of the emulsion formation process is possible.[86] However, this method still suffers from a low emulsion formation rate compared to standard emulsification methods[76] making large scale productions challenging.

1.1.1.3 Membrane emulsification

In membrane emulsification, the fluid representing the disperse phase is injected through a microporous membrane with uniform pore size into the continuous phase. Alternatively, a premix is passed through the membrane resulting in the homogenization of the mixture (Figure 1, top right image).[87-88] Through membrane emulsification minimal droplet sizes of 0.1 µm[34] can be obtained. With this method much higher throughputs compared to microfluidic and microchannel devices can be achieved making membrane emulsification suitable for a scale-up to large-scale productions. However, due to the relatively broad size distribution (with a coefficient of variation of around 10%[51]), fouling of the membrane material,[34] and the sensitivity to the viscosity of the disperse phase, this method is of limited use for particle preparation but can be used to generate reactors for the interfacial reaction.[89] In comparison to conventional turbulence-based methods, less energy is needed to achieve emulsification, avoiding a raise in temperature, and less stress is applied.[90] Thereby, this method is applicable for temperature and shear-sensitive substances, such as proteins or enzymes.[91-92]

1.1.1.4 High energy emulsion preparation: mini- or nanoemulsions by ultrasonication and high-pressure homogenization

According to the IUPAC recommendation, miniemulsion (or nanoemulsions) are defined as emulsions, i.e., systems formed by one disperse and one continuous phase, with the disperse phase having diameters between 50 nm and 1 μm.[93] Other emulsions characterized by nanoscale dimension are the so-called microemulsions. Both systems are classified according to the composition as direct (oil-in-water) or inverse (water-in-oil) emulsions.[22] While miniemulsions are kinetically stable systems, stabilized against coalescence and against diffusion degradation (Ostwald ripening),[22, 93-94] microemulsions are defined as thermodynamically stable systems, containing a high amount of surfactant and possibly a co-surfactant in their formulation. Microemulsions are formed spontaneously, while miniemulsions need external force to be generated (e.g., ultrasound).[95]

The mechanical emulsification process for the formation of a miniemulsion starts with a pre-emulsification step, with the initial two phases and additives being mixed, generating droplets with a large size distribution which are stabilized by surfactants,[22] typically in the range of 1 to 20 μm.[96] Diverse methods can be used subsequently for the formation of the miniemulsion. The provision of an energy higher than the surface tension multiplied by the amount of surface is necessary to break the droplets from the micrometer scale into nanometer droplets.[22] Today, for bench scale experiments, the main source of energy for the formation of stable and well-defined miniemulsions are ultrasonication and high-pressure homogenization (HPH).[22, 97]

The final size and size distribution of the obtained miniemulsion are controlled by a Fokker-Planck type dynamic rate equilibrium of droplet fusion and fission processes and can be controlled by the applied conditions like surfactant load, volume fraction, temperature, salinity, etc., so that the resulting nanodroplets are at the critical borderline between stability and instability. Additionally, the size and size distribution also depend on the shear rate and emulsion rheology, which will vary depending on the ultrasonication conditions, process parameters and the system physicochemical properties.[96]

After the formation of the droplets, Ostwald ripening can still affect the stability of the miniemulsion. Ostwald ripening describes the growth of larger objects at the expense of smaller ones, when monomodal distribution is not given.[98] Ostwald ripening is a

consequence of the higher surface energy, and hence high Gibbs free energy of smaller droplets in comparison to larger ones. Ostwald ripening can be counterbalanced by the use of highly hydrophobic or lipophobic molecules (for direct or indirect emulsion, respectively) inside the dispersed droplets. Typically, a low content of hydro-/lipophobe is added, which can hardly diffuse through the continuous phase, i.e., exchange between the droplets. Thereby, they generate an osmotic pressure, counteracting the Ostwald ripening and resulting in a final state of equal pressure inside the droplets. Thus, a final steady-state miniemulsion is obtained.[22]

1.1.2 Reactions at the (droplet) interface

Processes taking place at the interface of two immiscible liquids have been investigated intensively as they differ from those in bulk and often occur only due to the unique features of this region. One of the most famous examples of a chemical reaction at the interface is, as previously mentioned, the synthesis of Nylon discovered by Wallace Hume Carothers at DuPont in 1935.[19, 99] Nevertheless, the historical background of the use of the interface as a shortcut to enable or improve chemical reactions starts much earlier, with the early works of Schotten[100] and Baumann[101] at the end of the 19th century. Since then, systematical improvement of the setups has been investigated, e.g., stabilization of the interface between two immiscible liquids and increase thereof through droplet formation. Starting from an introduction of reactions at a macroscopic liquid/liquid interface, examples of reactions in emulsified systems/at droplet interfaces are given in the following.

1.1.2.1 Reactions at macroscopic interfaces

As previously mentioned, the works from Schotten and Baumann were the starting point of the exploration of the liquid-liquid interface for organic chemistry. The so-called “Schotten-Baumann reaction conditions” involve the synthesis of amides from amines and acid chlorides in a biphasic reaction mixture. Even though this is one of the classic examples of organic synthesis in a biphasic system, in this case both product and reactants are present in the organic phase. The use of the interface is crucial to force the equilibrium towards the formation of the products. An alkaline aqueous solution is added to the reaction mixture and reacts at the interface with the protons of the amine-acid chloride reaction, preventing the amine to be protonated. This classic example is for sure not the only case where the presence of water is primordial to perform organic synthesis. Even though water is not a conventional solvent applied in organic reactions, a series of

examples can be found in the literature, where the use of biphasic aqueous/organic systems provide unique conditions. One of the most popular examples nowadays is the use of the so-called "on water" organic synthesis protocol. "On water" synthesis is related to a series of different chemical reactions that happen or are catalyzed by the interface in biphasic systems (where one of the phases is always water). One of the first to demonstrate the catalytic effect of such systems, Breslow has studied how Diels-Alder reactions could be accelerated in the presence of water.[102] He attributed this effect to be a "hydrophobic effect", which forces organic molecules in water to aggregate resulting in increased reaction kinetics. The term "on water" reactions was coined almost 15 years later in the work of Sharpless and collaborators.[103] The authors presented a series of examples where insoluble reactants were stirred in an aqueous suspension (Figure 2). Many of the studied systems presented a certain level of acceleration when performed in "on water" conditions, but even where negligible acceleration was observed, the authors claimed many other advantages of these systems, such as ease of product isolation and safety.

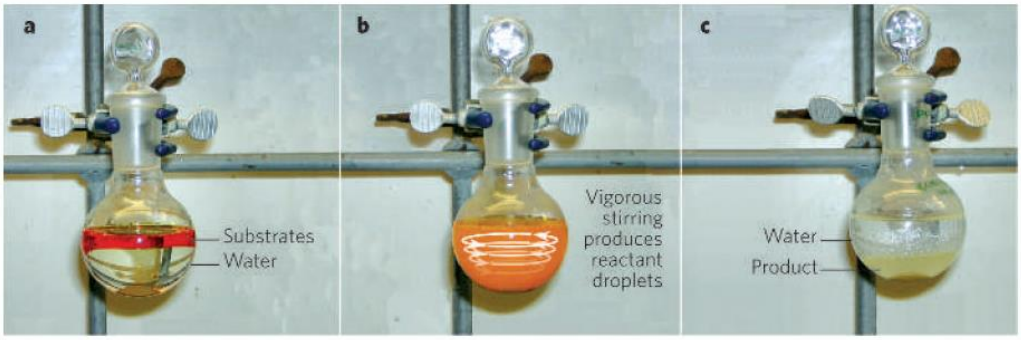

Figure 2: "On water" approach developed by Sharpless *et al.*: (a) the initial macroscopic biphasic system containing the substrates and the aqueous phase is submitted to (b) vigorous stirring, transforming the system in a suspension and thus increasing the surface area between the water phase and the substrates. (c) After the end of the stirring process, the product can be easily separated either by precipitation or by forming a film between both phases. Reprinted with permission from reference [104]. Copyright 2005 Nature Publishing Group.

Since the work of Sharpless, a high level of interest in the investigation of the mechanism of action and on the possibilities of such "on water" systems has arisen in the scientific community. Manna and Kumar more recently performed an exhaustive analysis in order to understand how the interface influences the mechanism of "on water" organic reactions.[105] The authors studied the reaction between cyclopentadiene and alkyl acrylates, demonstrating that the increase of the interfacial area between organic and aqueous phase leads to an increase of the kinetics for this system (Figure 3). The authors considered the nature of the interface and the ease of hydrogen bonding between water and the reactants

in the disperse phase (or the transition state) as vital factors together with the hydrophobicity and cohesive energy density at the interfacial region.

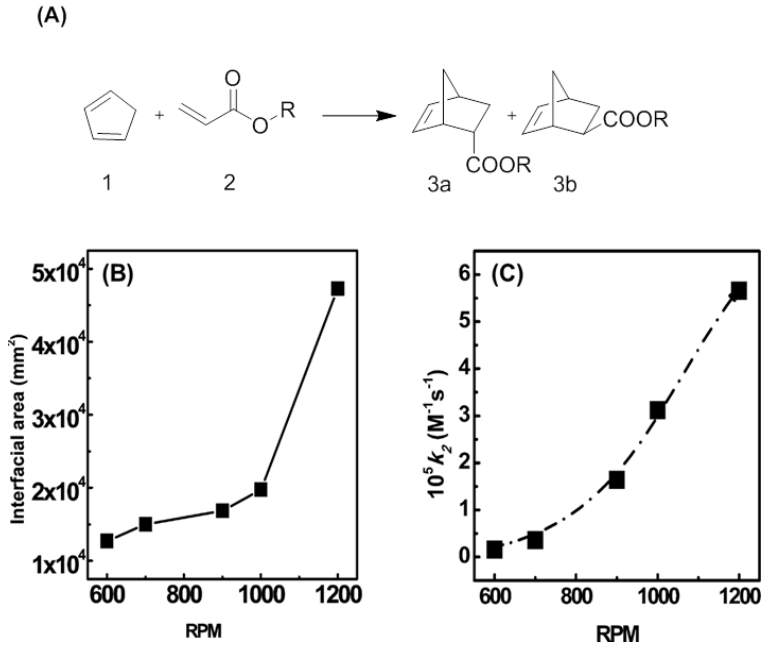

Figure 3: (A) Reaction performed by Manna and Kumar in the investigation of "on water" reactions; (B) the decrease of the interfacial are with the increase of the stirring rate resulted in the (C) increase of the kinetics. Adapted with permission from reference [105]. Copyright 2013 American Chemical Society.

Butler and Coyne have recently investigated the effects of protons and Li^+ ions in the aqueous phase and the presence of non-reacting competing hydrogen bond acceptor molecules in the organic phase on Huisgen cycloadditions.[106] Such hydrogen acceptor molecules in the organic phase caused an initial reduction of the reaction yield, but the further increase of the concentration did not produce a continuous effect. The authors conclude that for compounds with basic pK_a values (pK_a 3-5 of the conjugate acid) proton transfer across the water/organic interface is involved in the catalysis, while for weaker bases trans-phase H-bonding occurs. Another interesting approach to prove the vital importance of hydrogen bonds was the investigation of the "on water" reactions in D_2O instead of H_2O. The reaction between quadricyclane and dimethyl azodicarboxylate was completed in 10 min in a biphasic system with H_2O, while the same reaction was completed in 45 min in D_2O. Therefore, it seems to be clear that the presence of hydrogen bonds at the interfacial region is essential in the catalytic performance of such systems.

Sharpless and coworkers observed that reaction times in oil/water systems can decrease by a factor of 300 compared to solvent-free conditions. As already described, they termed these reactions "on water" reactions since only the existence of an interface seems

to be the cause of this acceleration.[103] Although the mechanism of these reactions is still unclear, the difference in kinetics between neat and "on water" reactions could be due to the unique nature of the oil-water boundary. As shown before, it was proposed by several authors that a structural change of the water at the interface compared to bulk could have the major influence.[107-109] Taking the results of Sharpless *et al.* as the basis for their theoretical models, Jung and Marcus calculated rate constants of a model reaction in bulk (neat), in homogeneous aqueous solution and in an oil/water emulsion.[110] The reaction is catalyzed by the OH-groups via the formation of hydrogen bonds. For the on-water reaction, rate enhancement of five orders of magnitude compared to the reaction in bulk, and of 600-fold compared to the aqueous solution were obtained. It was calculated that in every four interfacial water molecule there is a free OH group catalyzing reactions by forming in the organic phase hydrogen bonds with reagents in the transition state. In bulk water on the contrary, the reactants are surrounded by an H-bond network which has to be broken first to obtain a necessary number of OH-groups to catalyze a reaction as efficiently as in the on-water system (see Figure 4).

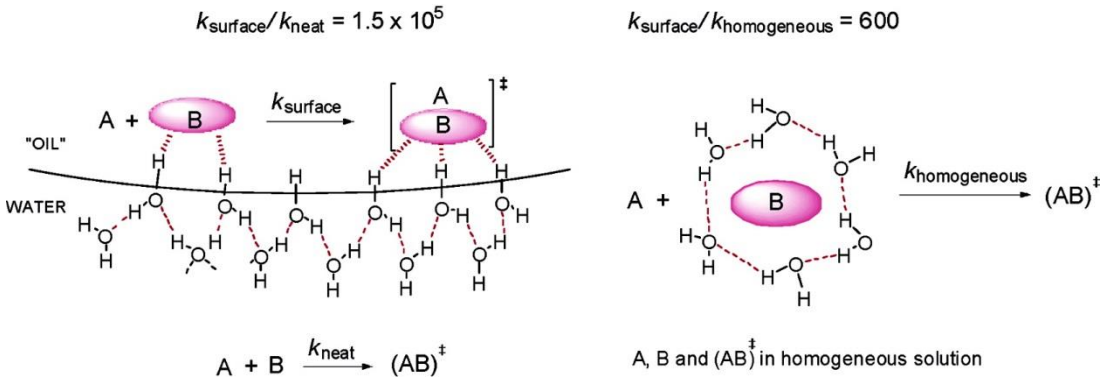

Figure 4: Scheme of the on-water catalysis and the catalysis in homogeneous solution. $k_{surface}$ is the rate constant of the interfacial reaction, $k_{homogeneous}$ of the reaction in water and k_{neat} is the rate constant of the reaction in bulk. Reproduced with permission from reference [110]. Copyright 2007 American Chemical Society.

This acceleration mechanism is of course not valid for every reaction. However, where this is the case, formation of an emulsion can be beneficial as shown in the following.

Organic syntheses "on water" have also been the topic of some reviews. The review of Chanda and Fokin provides an excellent overview about the diverse types of organic synthetic approaches that can be achieved using the "on water" protocol, including Diels-Alder reactions, 1,3-dipolar cycloadditions, cycloadditions of azodicarboxylates, Claisen rearrangement, nucleophilic substitution reactions, oxidation and reductions, etc.[23] One

topic not covered in this review is enzymatic catalysis at liquid-liquid interfaces. The principles of increased enzymatic activity in liquid interfaces have been described by Straathof.[111] The reasons of the interface influencing enzymatic system include, as pointed out by the author, higher concentration of the enzymes or the substrate at the interfacial region, and the activation of enzymes through specific interactions in the interfacial region. In the end of the following section, this will be covered in more detail.

The catalytic effect of interfaces is, as can be seen, a very important topic in nowadays organic synthesis. In order to achieve better results, the maximization of the surface interfacial area is required. In microchannel reactors, as an example, contact area and time between immiscible liquids can be increased, yielding better results than conventional stirring. Mikami and coworkers reported a dramatic increase in reactivity of Mukaiyama aldol reaction in a "fluorous nanoflow" system (nanoflow microreactor with fluorous lanthanide catalysts) (Figure 5) even at very low Lewis acid catalyst concentrations (less than 0.1 mM).[112] The reaction was complete within seconds of a biphasic contact time whereas under vigorous stirring, it required more than two hours and showed poor yields. A narrower width and a longer channel, thus a larger contact area, led to further improvement.

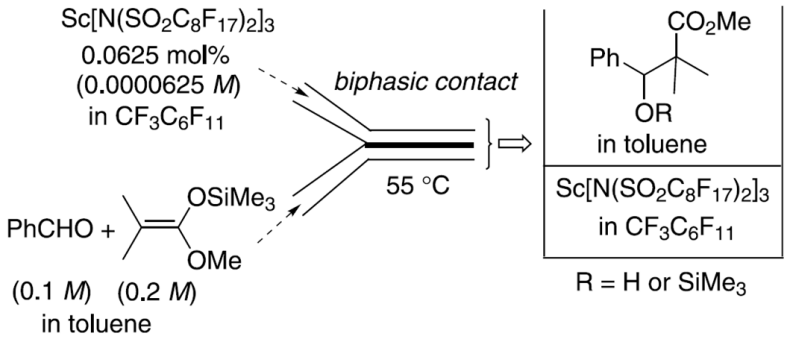

Figure 5: Mukaiyama aldol reaction in a "fluorous nanoflow" system. Reprinted with permission from reference [112]. Copyright 2003 Elsevier Ltd.

In the next section, diverse examples are covered, describing systems in which stable droplets are applied in order to increase the interfacial area.

1.1.2.2 Reactions at the droplet's interface

In general, synthesis of small molecules in disperse systems instead of bulk can lead in some cases to higher efficiency, such as high yields, reduced temperature, less

catalyst, due to the existence of a large interfacial area. Major advantages also comprise the direction of regio- and stereoselectivity, overcoming reagent incompatibility and rate enhancements.[24]

Using heterogeneous solvent systems forces molecules with polar and apolar groups to accumulate at the interface in analogy to surfactants. This can be used to induce formation of products with specific regioselectivity. In an early work, Jaeger and coworkers observed this phenomenon in a Diels Alder reaction of two hydrophobic molecules.[113] In pure organic solvents, both regioisomers were produced in the same amounts whereas in water a threefold excess of one isomer over the other was found. The excess was attributed to the micellar orientation of the two starting compounds in aqueous environment yielding predominantly one regioisomer. Similar observations were made by Wu *et al.* for the photocycloaddition of 9-substituted anthracenes (with polar or ionic substituents) in w/o microemulsions.[114] While in methylene chloride predominantly head-to-tail photocyclomers were obtained, in microemulsion exclusively head-to-head regioisomers were formed due to a pre-orientation of the substrate molecules at the interface (see Figure 6).

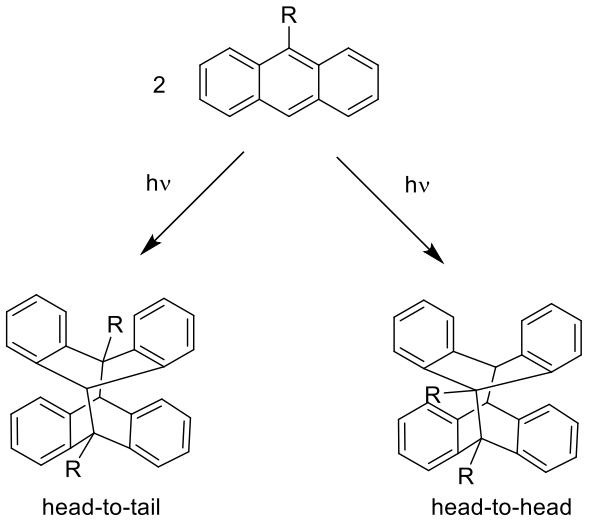

Figure 6: Photocycloaddition of 9-substituted anthracene.

Hayashi and coworkers reported successful cross-aldol reactions catalyzed by a proline-surfactant also acting as an organocatalyst with high diastereo- and enanioselectivites upon emulsification.[115] However, the role of water and emulsion formation was not clear from these results. For deeper insight, Zhong *et al.* used a similar amphiphilic organocatalyst in a w/o emulsion for the direct asymmetric aldol reactions

with cyclohexanone and different aldehydes (Figure 7).[116] Both a rate enhancement and higher stereoselectivity than in homogeneous media were observed. The authors attributed these findings to the large surface area created with the emulsion and the uniform distribution of the catalyst molecules creating a well-ordered two-dimensional chiral surface.

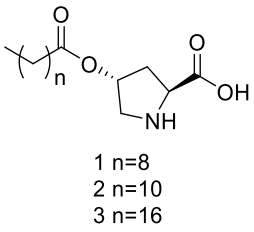

Figure 7: Structures of amphiphilic organocatalysts used in reference[116] for the asymmetric aldol reactions in emulsion.

Enantioselective enzymatic catalysis at the interface in miniemulsion has been reported for the preparation of optically active α- and β-amino acids at very high substrate concentrations (up to 800 g/L) and enantiomeric excess of >99% *ee*.[117]

Phase transfer catalysts facilitate reactions between reactants located in different phases. Typically, in liquid-liquid phase transfer catalysis (PTC) an anionic reactant is transferred from the aqueous phase to the organic phase by the catalyst, usually quaternary ammonium (e.g., tetrabutylammonium bromide, benzyltrimethylammonium chloride) or phosphonium salts (based on tributylphosphines) or crown ethers and cryptands (see Figure 8). In the organic phase, it can react with a lipophilic molecule. Due to a weaker solvation in the organic phase, the anions exhibit an enhanced nucleophilicity and are thus more reactive.

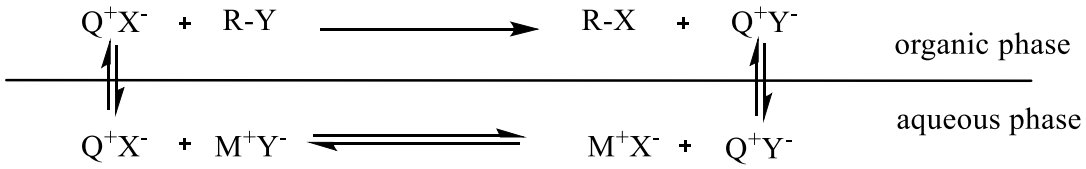

Figure 8: Schematic representation of phase transfer catalysis with Q+ as the quaternary ammonium cation, forming an ion pair with the anionic reactant X-. In the organic phase, it reacts with the substrate R-Y, yielding the product R-X and the anionic leaving group Y- which pairs with the catalyst. In the aqueous phase the leaving group is exchanged against another anionic reactant, completing the catalytic cycle.

Increasing the interfacial area between the two phases by emulsification can increase the reaction speed further. Rate enhancement was reported by Ooi and coworkers

for several alkylations of carbonyl substrates and epoxidations of ketones when ultrasonication was applied.[118] Similar observations were made for the saponification of vegetable oil, an industrially important reaction for the production of fatty acid salts.[119] By applying ultrasound (20 kHz) instead of the conventional agitation, the yield increased from 8% to 93%. The comparison of the cationic surfactants and phase transfer catalysts cetyl trimethylammonium bromide (CTAB), tetrabutylammonium bromide and benzyl triethylammonium bromide showed that CTAB was the most efficient. Due to the longer alkyl chains, it preferentially accumulates at the interface, lowers the surface tension and facilitates the formation of smaller droplets, resulting in higher contact area between water and the organic phase and thus more transfer possibilities.

Similarly to PTC, inverse phase transfer catalysis (IPTC) has also been developed.[120] Though not as commonly exploited as PTC, it further expands the potential use of phase transfer reactions. In IPTC, similar to PTC, a lipophilic substrate is transferred into the aqueous phase by the catalyst and the reaction takes place in the aqueous phase. Pyridine derivatives such as DMAP are popular catalysts due to their low cost. Also cyclodextrins,[121-122] calixarenes[123] and, as shown in the following example, surfactants are applicable as catalysts.

Boyer and coworkers used the surfactant dodecyltrimethylammonium bromide as catalysts for IPTC. They evaluated the influence of the stirring speed on the epoxidation of chalcone by hydrogen peroxide and observed two different mechanisms of reaction: at low stirring the reaction occurs via the inverse phase transfer catalysis (IPTC) while upon emulsion formation via ultrasonic stirring interfacial catalysis (IC) takes place.[124] In IPTC, the reaction takes place in micelles. In IC, the substrates react at the interface (Figure 9).

Under ultrasonic mixing, the reaction proceeded faster than under mechanical stirring, due to the production of a larger surface area. Furthermore, it was proven that under these conditions surfactants can be used in catalytic amounts since micelle formation is not necessary.

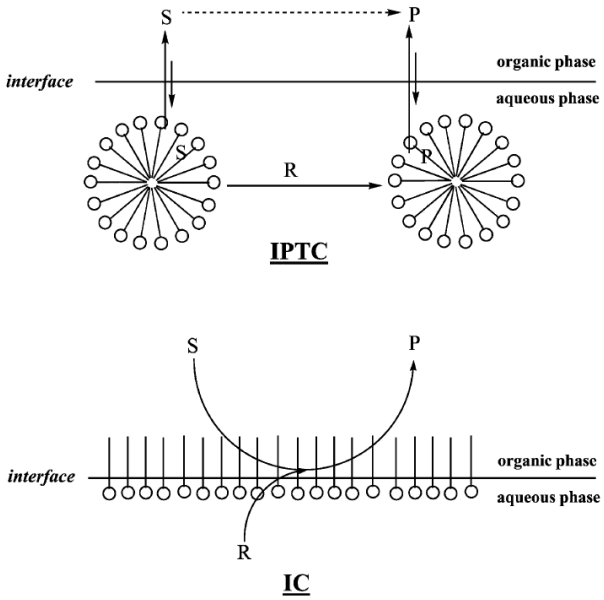

Figure 9: Principles of an inverse phase transfer catalysis (IPTC) and interfacial catalysis (IC) with a surfactant as catalyst (S: substrate, R: reactant, P: product). Reproduced with permission from reference [124]. Copyright 2002 Royal Society of Chemistry.

Besides using emulsification methods, an increase of the interface for a successful PTC reaction can be achieved by droplet-based microfluidics generating discrete droplets from femtoliter to nanoliter volumes in a continuous carrier phase. The exceptionally high surface-to-volume ratio and internal flow circulation enable an effective mass transfer and a rapid conversion. This has been shown for the synthesis of benzyl phenyl ether catalyzed by tetrabutylammonium bromide (see Figure 10).[125]

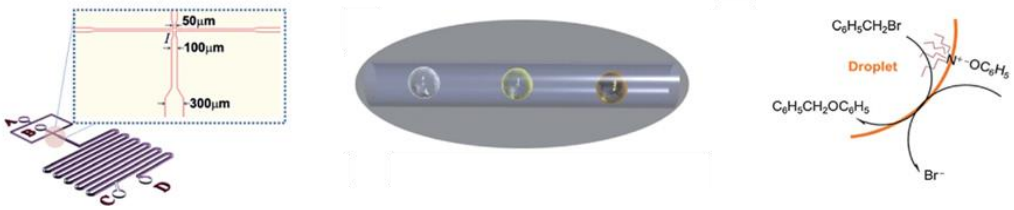

Figure 10: Schematic representation of PTC reaction in a droplet-based microfluidic device. From left to right: Overview of the microfluidic chip device, product formation by PTC while the organic droplets travel through water in the hydrophilic microchannels. Adapted with permission from reference [125]. Copyright 2012 Royal Society of Chemistry.

The examples above have shown that emulsion formation is beneficial for reactions with reagent incompatibility. However, PTC is often susceptible to a decrease in reactivity over time and respectively the yield as the phase transfer agent can partition completely into the organic phase forming an ion pair with the lipophilic anion. Consequently, the phase transfer agent stops carrying more anions from the aqueous phase to the organic phase for reaction. In this case, the use of microemulsions can be of advantage. In

microemulsion reactions, the substrates are not transferred from one medium to another, but rather, the reaction is confined at the oil-water interface. The interfacial area in microemulsions is very large and can reach values as high as 10^5 m^2/L.[126] Microemulsions can be applied both in combination with PTC, yielding even higher reaction rates, but even without it they can be superior to conventional biphasic reaction media.[127-129]

Microemulsions have been applied in several types of reactions such as nucleophilic substitution reactions,[130] esterifications,[131] alkylations,[132] and oxidations of hydrophobic substrates.[133-134]

Reagent incompatibility is a major issue for many organic reactions. When PTC is not possible, often polar aprotic solvents, such as DMSO or DMF are used. However, these solvents are difficult to remove and mostly toxic. Microemulsions and emulsions in general might be another approach for this problem.

For this reason, Jiang and Cai exploited the microemulsion for copper- and ligand-free Sonogashira reaction and the ligand-free Heck reaction of iodobenzene and styrene.[135-136] The microemulsion was beneficial for several reasons: surfactants stabilized the Pd nanoparticles acting as the catalyst but also enlarged the interfacial area, lowering mass transfer resistance. Water in the five-component microemulsion accelerated the Heck reaction promoting the migratory insertion step and provided overall a mild reaction environment with high conversion and selectivit. Zayas *et al.* performed the Heck reaction in miniemulsion resulting in high yields compared to neat toluene or DMF (99% in miniemulsion compared to 0% in toluene and 51% in DMF), and high control in stereoselectivity (>90% E-isomer).[137]

Dark-singlet oxidation of the poorly reactive species 1,4,5-trimethylnaphthalene in a three-liquid-phase microemulsion was performed with “balanced catalytic surfactants” based on double-tailed quaternary ammonium salts and molybdate counterions (see Figure 11).[134] The upper oil phase and the aqueous excess phase act as reservoirs for the reactants while the reaction itself takes place solely in the interface. This system benefits from the existence of these two interfaces as only there the reactants can meet.

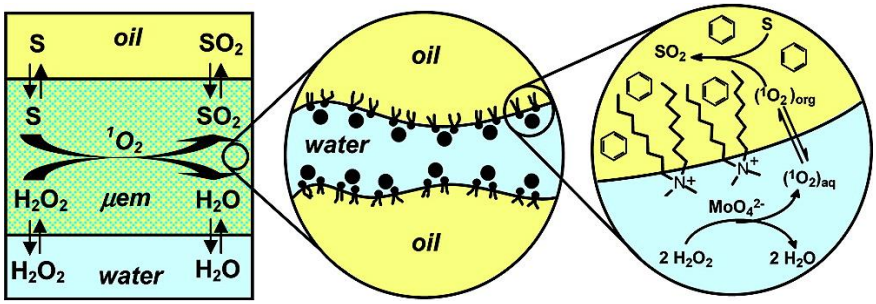

Figure 11: Schematic representation of dark singlet oxygenation of substrate S in a three-liquid-phase microemulsion. Reprinted with permission from reference [133]. Copyright 2008 American Chemical Society.

Engberts and coworkers observed an acceleration of a Diels Alder reaction between cyclopentadiene and *N*-ethylmaleimide in microemulsion with increasing water content compared to pure isooctane.[138] The rate enhancement was explained by hydrogen bond stabilization of the activated complex and enforced hydrophobic interactions.[139] An accelerating effect in microemulsion was also reported for 1,3-dipolar cycloaddition of benzonitrile oxide to *N*-ethylmaleimide by the same group.[140] An increase of the local concentration of the reactants due to confinement at the interface is one reason for the rate enhancement. Furthermore, electrostatic interactions with the negatively charged headgroups of the surfactant cause a destabilization of the negative charge of the benzonitrile oxide and favors the 1,3 dipolar cycloaddition (Figure 12).

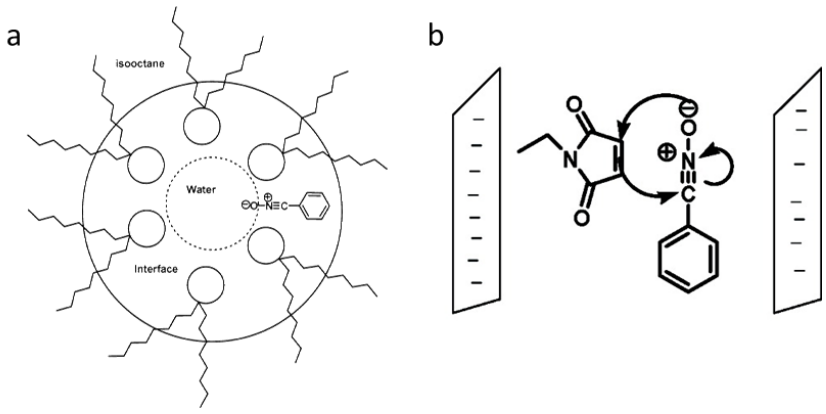

Figure 12: a.) Orientation of benzonitrile oxide in microemulsion; b.) destabilization of the negative charge of benzonitrile oxide due to the negatively charged environment causing reaction rate acceleration. Reproduced with permission from reference [140]. Copyright 2006 American Chemical Society.

Depending on the type of reaction, increasing the water ratio in a microemulsion and thereby changing the polarity of the interfacial zone, accelerates or impedes the reaction speed. Garcìa-Rìo *et al.* showed that for S_N1 type solvolysis reactions the intrinsic rate constant decreases with lowering the water ratio since the polarity of the interface also decreases.[141] S_N2 reactions, on the contrary, are accelerated due to a stronger

nucleophilicity of the interfacial water. The differences in kinetic behavior in the nucleophilic substitution of 4-*tert*-butylbenzyl bromide and potassium iodide in oil/water microemulsion was also attributed to role of water activity in the interfacial zone.[142] The reaction is assumed to occur only inside the surfactant layer and rates were dependent on the surfactant type. A possible explanation is that the sugar-based octyl glycoside as surfactant becomes more hydrated than dodecyl ethoxylate and thus the dielectrical constant changes in the interfacial zone. As already mentioned, the more polar reaction environment retards this type of S_N2 reaction. In a following study using ^{127}I NMR spectroscopy measurements, it was shown that there is a temperature-dependent accumulation of iodide at the oil/water interface.[143] In bulk, a rise in temperature accelerated the reaction. In microemulsion, however, a decrease at elevated temperatures was observed due to a decrease of iodide at the interface. The unexpectedly high reactivity in microemulsion could be therefore attributed to the accumulation of the iodide at the interface. With dodecyl ethoxylate as the surfactant, the iodide is less solvated at the interfacial layer, rendering it more nucleophilic.

Besides rate acceleration, the mechanism of a reaction can also be influenced by the microenvironment. Garcìa-Rìo and coworkers studied the kinetic behavior of butylaminolysis of 4-nitrophenyl caparate in bis(2-ethylhexyl) sulfosuccinate (AOT)/chlorobenzene/water microemulsions.[144] They observed a first and second order dependence on the butylamine concentration caused by the reaction pathways at the interface and in the continuous medium. This kinetic behavior was attributed to the rate-determining step of the reaction which differs at the interface from in bulk. At the interface the rate determining step is the formation of the addition intermediate whereas in the continuous phase, it is the base-catalyzed decomposition of this intermediate. For solvolysis of benzoyl halides, the same group observed that a change of water ratio in the microemulsion alters the mechanism of solvation by means of either an associative or dissociative pathway.[145-146] Mechanistic changes depending on the water ratio have also been reported for other solvolytic reactions, ester hydrolysis, and nucleophilic aromatic substitutions.[147-148]

Reactions confined at the interface are susceptible to changes of this interface. Increase or decrease of the droplet size as well as changes in the surface polarity by altering the solvent ratio or surfactant and co-surfactant concentrations influence the solubility of the reactants and the reaction kinetics. Shrikhande and coworkers showed that

for the condensation of benzaldehyde and acetone in cationic o/w microemulsion an increase of oil and co-surfactants ratio lowered the reaction rate.[149] This was correlated to an increase of droplet size and thereby less interfacial area. An increase of surfactant concentration also had a negative influence on the reaction rate since less space for the reactant at the interface is left. Additionally, the water content on the interface may increase with growing polarity and occupy the space. By this, the authors showed that the reaction takes place at the interface as otherwise these effects would not have been observed.

Similar findings were made for the furfural/cysteine reaction as a model for the Maillard reaction.[150] To understand and control the Maillard reaction is especially important for the food industry as it is involved in the process of flavor generation. Rate enhancement in o/w microemulsion compared to bulk water was found. It was suggested that the reaction is mainly compartmentalized at the interface rather than in the continuous medium since a change of the overall concentration of the reactants did not affect the rate. Furthermore, lower activation energies were determined for the o/w microemulsions compared to water and water/propylene glycol mixtures. The authors proposed that the interface could force the molecules to obtain already the specific configuration or orientation needed for reaction.

For biomolecular engineering, liquid-liquid interfaces constitute an interesting platform for various fields ranging from biomedical applications to food industry. Proteins adsorb spontaneously at the interface and the more rigid the ternary structure, the stronger interfacial networks are formed.[151] Upon adsorption, proteins partially unfold exposing residues which are inaccessible under normal conditions, for example, free thiol residues or hydrophobic patches. Proteins are thus used as surfactants in the food and cosmetics industry; native proteins typically do not possess surfactant properties, only the contact with an interface (water-air, or water-oil) leads to partial denaturation and rearrangement, allowing their use as surfactants. In nature, several enzymatic reactions, such as the digestion of fat, proceeding at the liquid-liquid interface, can be found. As already discussed, enlarging the surface can increase the reaction speed and efficiency. Furthermore, structural differences induced by the interface also play a role.

Upon confinement at the interface, it has been shown that lipase experiences an enhanced activity which could be the result of a rearrangement and displacement of the lid

covering the active site.[152] Maximal activity for lipases is observed in emulsions rather than in bulk media.[153-154] Nature has already recognized this, since most dietary fats are consumed in an emulsified form (milk) or emulsified in the mouth, stomach or intestine.[155] However, the structure of the lipid-water interface is also crucial for lipase activity.[156]

Obesity levels are increasing worldwide. Prolonging lipid digestion to reduce hunger and hence energy uptake could constitute an effective method for long-term weight reduction. For regulating lipase activity at the interface, a study of the efficiency and rate of lipolysis of olive oil was performed.[157] Therefore, the physicochemical nature of the interface at which this reaction occurs was altered by different kinds of lipids stabilizing the emulsion. While monogalactosyldiacylglycerol (MGDG) did not show any inhibitory effect, digalactosyldiacylglycerol (DGDG) slowed down the lipolysis. It was argued that the large digalactosyl headgroup of DGDG sterically hinders the adsorption of lipase and colipase at the interface. Incorporation of lecithin however, altered the organization of the closely packed structure of DGDG at the interface and interfered with the headgroup interactions, favoring lipolysis again (Figure 13). Additionally to these steric reasons, lecithin is assumed to facilitate the opening of the pancreatic lipase lid domain and to stabilize the active conformation.

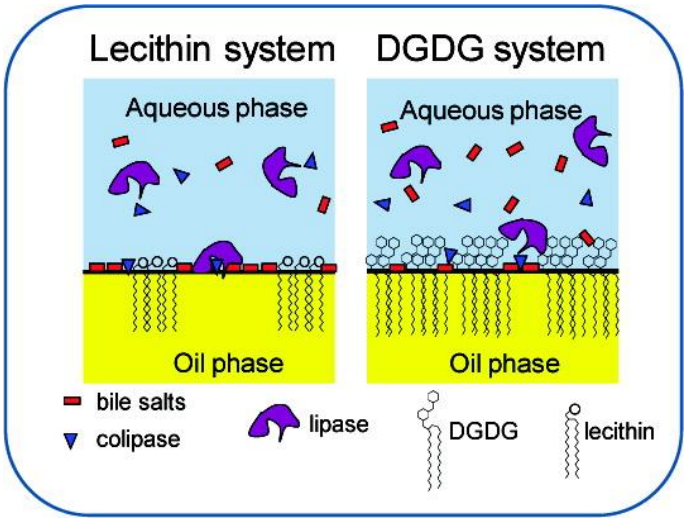

Figure 13: Schematic representation of lipolysis at the oil/water interface. Reprinted with permission from reference [157]. Copyright 2009 American Chemical Society.

Thus, by modifying the DGDG/lecithin ratio at the emulsion interface a regulation of lipolysis is possible, and these findings could contribute to the regulation of dietary fat uptake and the treatment of obesity.

1.1.3 Polymerizations at the droplet interface

Besides the synthesis of low molecular weight compounds, polymerizations can also be performed in a liquid-liquid biphasic reaction medium. In contrast to the examples mentioned above, polymerizations, especially chain-growth polymerization, are limited in two phases, due to transfer and termination reactions. This is especially obvious if water is one phase and cationic or anionic polymerizations are considered. Alternating radical copolymerization or metathesis polymerization tolerate water and are examples for beneficial properties of the interface to the product formation. With confinement to the interface not only more complex structures with stimuli responsiveness can be produced (as shown in the examples below) but also higher reaction rates and yields in aqueous emulsions have been reported in certain cases.[158] Interesting examples of interfacial polyreactions are polycondensations, such as Nylon synthesis (see above), and polyadditions, e.g. the cross-linking of multifunctional nucleophiles, such as starch, with diisocyanates forming nanocarriers (see below). This section will summarize the basic principles of different reaction types that can be conducted at the interface of two immiscible liquids including radical polymerizations, and polyadditions/ polycondensations. The current trends and challenges of each platform will also be discussed using selected examples.

1.1.3.1 Radical polymerization

While examples of ionic polymerization in dispersion and at the interface of immiscible liquids are quite scarce, a plethora of radical polymerizations in disperse phase can be found. For detailed discussions about radical emulsion polymerization, the reader should refer to the excellent and detailed review articles and literature therein covering the developments in the field of (controlled) radical polymerization in heterophase until 2008.[159-161]

A growing environmental concern and increasing application of polymers in pharmaceutical and medical fields are creating a demand for environmentally and chemically benign solvents.[162] As radical polymerizations are in general robust and proceed under “wet” conditions, they represent an attractive platform for performance in aqueous emulsion. Radical polymerizations in aqueous dispersions have therefore experienced rising interest for industrial production.

Free radical polymerization

In free radical polymerization, the alternating copolymerization in particular is an interesting example where the benefits of an interfacial reaction can be shown. Wu and coworkers synthesized aqueous-core capsules in an inverse emulsion by alternating copolymerization of hydrophobic maleate esters with hydrophilic poly(hydroxy vinyl ethers) analogous to classical interfacial polycondensation (see Figure 14).[163-164] The polymerization is constrained to proceed at the oil-water interface due to the low solubilities of the hydrophilic/hydrophobic monomers in the respective phase and the reluctance of each monomer to homopolymerize. Therefore, the conversion and the polymerization kinetics are limited by the monomer diffusion to the interface. Therefore, full conversion is only possible at low monomer concentrations having in turn an impact on the capsule shell thickness and permeability.

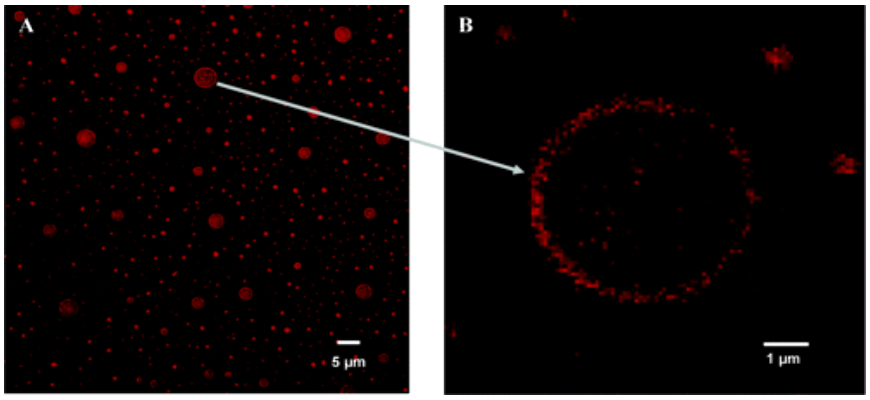

Figure 14: Top: Alternating interfacial free-radical polymerization of miniemulsion oil droplets (**I**) to form liquid-core polymer capsules (**II**) via (b) alternating copolymerization of dibutyl maleate (**1**) and hydrophilic PEG-divinyl ether **2**, initiated with surface active initiator **3** at the oil/water. Bottom: (A) Fluorescence image of dehydrated aqueous-core capsules. (B) Confocal image of the horizontal cross section of the particle shown by the arrow. Adapted with permission from references [163-164]. Copyright 2005,2006 American Chemical Society.

The main drawback of free radical polymerization in a disperse system remains the poor control over particle size and morphology. During the synthesis of capsules, for example, full particles are also obtained to a certain degree. This is caused by homogeneous nucleation occurring especially at high monomer concentrations. As showed by the example above, it is important to confine the reaction at the oil/water interface. Cao *et al*. observed that for polystyrene nanocapsules, the proportion of capsules over particles can be increased by using *N*-isopropyl acryl amide (NIPAM) as a comonomer and with reaction temperatures above the lower critical solution temperature (LCST) of polyNIPAM.[165] At the reaction temperature of 70 °C pNIPAM is neither soluble in water nor in oil and the pNIPAM oligomers phase separate at the oil droplet/ water interface and promote the interfacial free radical polymerization. The thermoresponsiveness of pNIPAM was also employed by Sun and Deng to synthesize hollow microspheres (see Figure 15).[166] An interfacial polymerization process was developed based on the property of pNIPAM to turn hydrophobic above the LCST and hydrophilic below this temperature. Therefore, the NIPAM monomer was first dissolved in the aqueous phase and a w/o emulsion with toluene was generated. A redox initiating system with benzoyl peroxide in the oil phase and tetraethylenepentamine in the water phase was used to generate free radicals at the oil/water interface. The polymerization of NIPAM thus started spontaneously at the interface. At reaction temperatures above the LCST, pNIPAM is insoluble in both phases and consequently a pNIPAM layer at the interface is formed. Divinylbenzene was then used to cross-link the pNIPAM layer. Thereby, thermoresponsive hollow microspheric structures were formed with diameters from 1 µm to 3 µm and wall thicknesses of 100 nm.

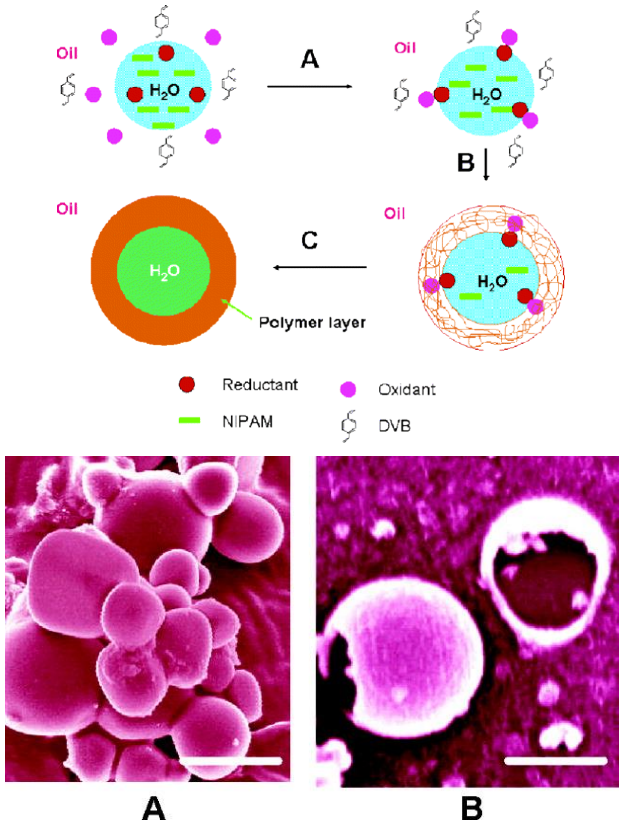

Figure 15: Top: Synthesis scheme of temperature sensitive hollow microspheres via free radical polymerization in inverse emulsion. Bottom: scanning electron microscopy images of pNIPAM microspheres; A: overview picture (scale bar 2 µm); B: cross section (scale bar 1 µm). Adapted with permission from reference [166]. Copyright 2005 American Chemical Society.

Sarkar and coworkers obtained polymer capsules with a hydrophobic poly(*tert*-butyl acrylate) shell and a hydrophilic poly(allylamine) interior by interfacial free radical polymerization in inverse miniemulsion.[167] In the water phase, hydrogen peroxide initiates the formation of a radical from the water soluble amine polymer. The macroradicals act as emulsifier molecules and assemble at the water/oil interface. The propagation reaction with the hydrophobic acrylate monomers occurs for this reason exclusively at the water/oil interface. With a difunctional cross-linker in the oil phase, narrowly dispersed polymer nanocapsules were obtained. Subsequent hydrolysis of the *tert*-butyl group under mild conditions allows the formation of an amphiphilic shell surface for further functionalization.

1.1.3.2 Polycondensation and polyaddition

Interfacial step-growth polymerization is one of the most applied approaches in the preparation of micro- and nanocapsules, going back to the early works of Chang for encapsulation of aqueous solutions of proteins within polymer shells.[168] Ideally for capsule

formation, the reaction of two monomers, each soluble in one phase of a biphasic system, begins at the interface of the two liquids and the resulting polymer is insoluble in either phase, precipitating at the interface, forming the capsule wall. Whereas, when the reaction locus is shifted to the droplet core, particles are obtained. It was proposed to divide the process of capsule formation by interfacial polycondensation in three steps: the initial polycondensation period, primary membrane formation and subsequent wall thickening.[169] The author proposes that shell properties can be influenced by variation of the solubility parameters in the system and swelling ability of the solvents for the forming polymer. Furthermore, the rate of precipitation of polymer chains, i.e., rate of polycondensation can control the shell morphology. A low rate of polymer precipitation leads to a more uniform and denser capsule wall. Further growth of the shell membrane is dependent on the diffusion of at least one of the monomers to the other.

For the development of capsules on a nanometer scale via interfacial polyreactions, miniemulsion has been used in diverse works, with both inverse and direct miniemulsions, and step-growth reaction approaches have been applied in the preparation of linear as well as cross-linked polymeric films at the interfacial region. Based on this strategy, the chemistry of polyurethanes and polyureas stands out. Crespy *et al*.[170] studied systematically the synthesis of polyurea, polythiourea and polyurethane nanocapsules by interfacial polycondensation and cross-linking reactions. They used an inverse miniemulsion to produce hollow nanocapsules (Figure 16A). The authors investigated the influence of the nature of the monomers and the continuous phase on the formation and morphology of the capsules. Control over size could be gained by the rate of addition of the second monomer. It was proposed that a slower addition could allow rearrangements in the conformation of the polymer forming the shell leading to larger hydrodynamic diameters. Besides, with control of the amount of the monomer in the disperse phase (in this case diethylenetriamine) the wall thickness was also controlled (Figure 16B and Figure 16C) and these capsules were further applied as nanoreactors in the reduction of silver nitrate.

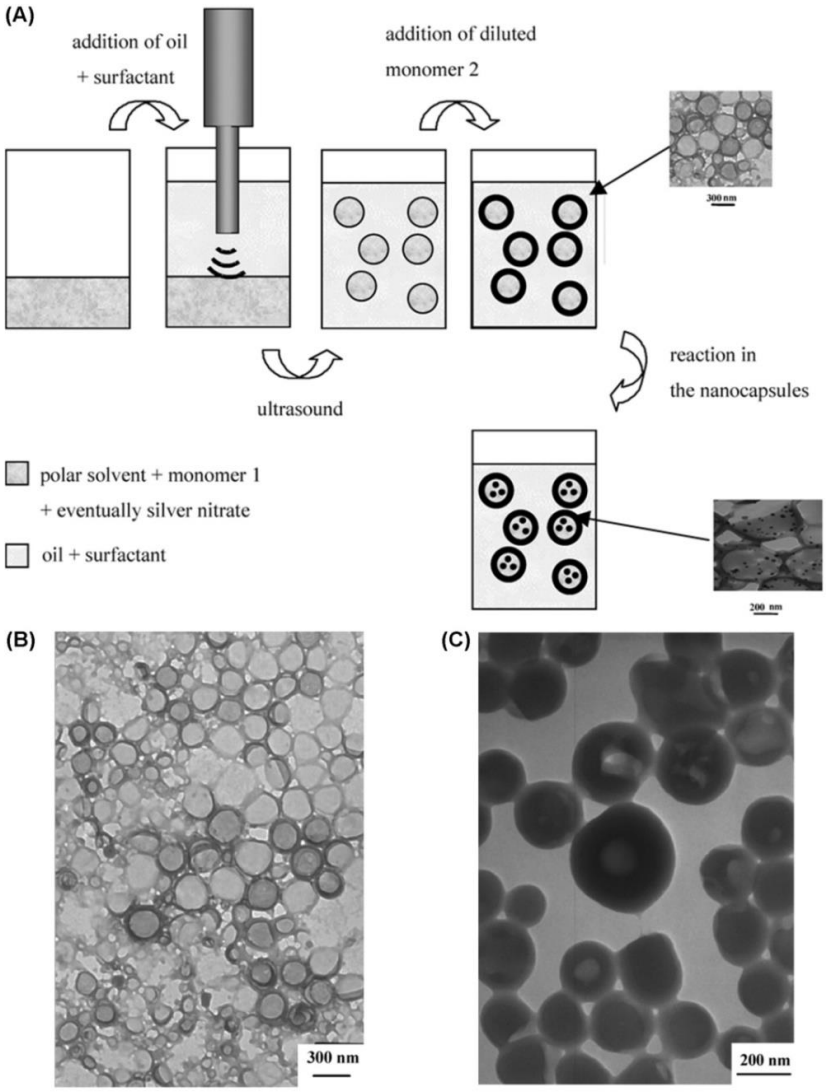

Figure 16: (A) Synthetic scheme applied in the production of polyurea, polythiourea and polyurethane nanocapsules in an inverse miniemulsion system, which could be further applied for reduction of silver nitrate; (B) polyurea nanocapsules and (C) polyurea nanocapsules produced with double amount of monomers in comparison to Figure 16B. The increase of the shell thickness is evidenced. Adapted with permission from reference [170]. Copyright American Chemical Society.

The kinetics of the polymeric shell formation by interfacial polycondensation has been discussed in the literature. Zhang *et al.* [171] evaluated the kinetics and modeled the formation of waterborne polyurethane shells in direct miniemulsions, relating diffusion processes through the formed polymer membrane and reactivity of the monomers. A schematic representation of the model is shown in Figure 17.

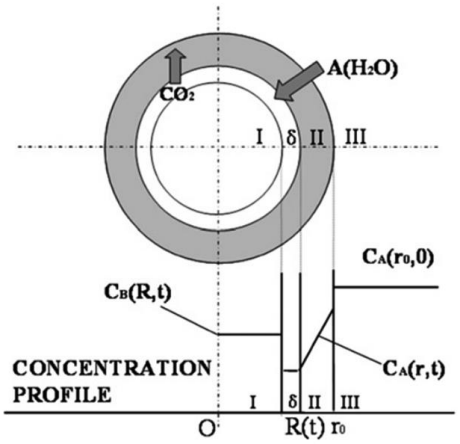

Figure 17: Schematic representation of the kinetic model applied by Zhang *et al.*[171] in the study of the kinetics of waterborne polyurethanes. The zone I is the capsule core, zone II is denominated as the capsule shell, zone III the aqueous solution and zone δ as the reaction zone. Reprinted with permission from reference [171]. Copyright 2012 Elsevier B.V.

While highly reactive aromatic isocyanates proved to exhibit a diffusion-controlled fast reaction, the moderate reactivity of aliphatic isocyanates resulted in a reaction-controlled process. More recently, Polenz *et al.*[172] used microfluidic polydimethylsiloxane devices to monitor the kinetics of reactions at the interface of emulsion droplets. The polyurea shell formation was followed using the droplet deformation as the analysis parameter. A microfluidic chip with a series of expansion-constriction chambers was used and provided the capacity to follow the shell formation with a time resolution of the order of milliseconds. Figure 18A shows the isocyanates, amines and surfactants used in this work and Figure 18B presents a general scheme of the procedure applied for the kinetics measurements.

This is a very interesting approach, firstly due to the time resolution obtained. The kinetics of polycondensations at the droplet interface is in general very fast and thus analysis techniques are limited. Furthermore, the authors conclude that different reactions laws are followed in direct and inverse systems and influence their behavior in relation to the concentration of both monomers and the reaction kinetics. While not providing an explanation, this work concludes that the component dissolved in the continuous phase has major influence in the reaction kinetics. The authors assume that the type of surfactant can also interfere by blocking the interface and interacting with the reactants. A reduction by a factor of 10 was observed with the use of sodium dodecylsulfate (HLB-value ~40) in comparison to a nonionic surfactant (Abil EM 90 with a HLB value of approximately 5).

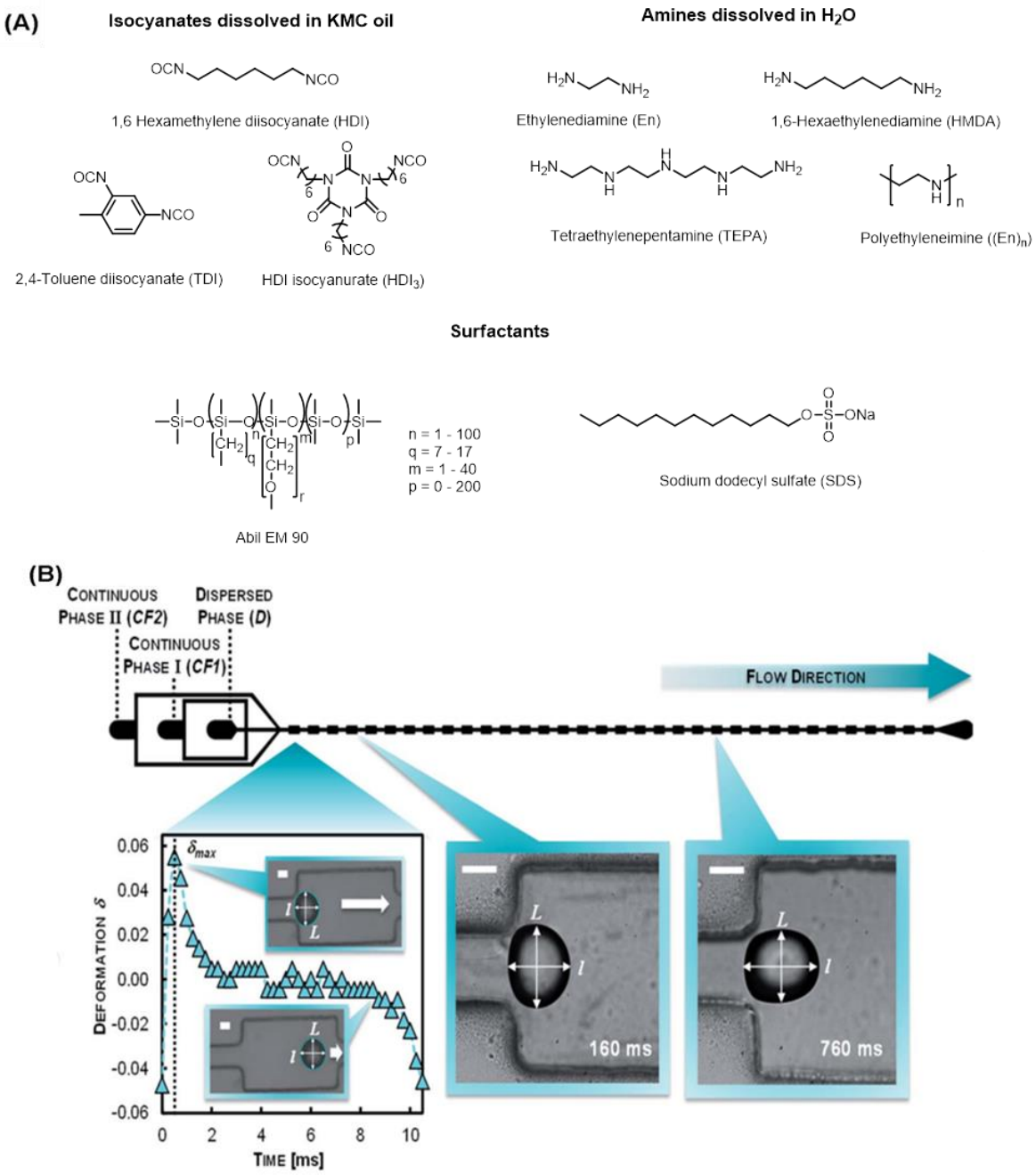

Figure 18: (A) Chemical structures of the monomers and surfactants applied in the study of microencapsulation dynamics of polyurea microcapsules; (B) Schematic representation of the microfluidic chip design for monitoring of the reactive encapsulation in direct and inverse emulsions and the measurement of the droplet deformation as a function of time. The scale bar is 50 µm. Reprinted with permission from reference [172].

Influences on the reaction kinetics of interfacial polycondensation reactions are a matter of discussion. Similarly to Polenz and coworkers, Wagh *et al.* performed an experimental study of polycondensation reactions at the oil/water interface for polyurea microcapsule production.[173] They observed a solvent dependency of the reaction kinetics, concluding that the reactions takes place on the organic solvent-side (i.e., from the disperse

phase) of the interface. Thus, the polarity of the organic solvent is responsible for rate acceleration.

Condensation reactions at the interface are suitable for a broad range of applications and capsule materials. For example, they have also been applied in the preparation of inorganic shells at the surface of droplets in miniemulsion. Fickert *et al.*[174] produced silica nanocapsules containing thiol or amine groups at the surface using a direct miniemulsion. Hydrolysis occurred at the interface between the continuous phase (water) and the droplets composed of the monomers for the silica shell formation. The droplets also contained self-healing agents which were still active after encapsulation.

Another important option for the production of polyurethane capsules, but with less side reactions and no polyurea formation, was achieved by the use of non-aqueous emulsions. Crespy and Landfester reviewed the use and preparation of non-aqueous (mini)emulsions and their possible applications.[175] The reaction between diisocyanates and diols was performed in inverse miniemulsions with a solution of the diol dissolved in formamide as the disperse phase and cyclohexane as the continuous phase. After the polyaddition at the interface, hollow morphologies were obtained (Figure 19A);[170] when the diols were purely used as the disperse phase, solid nanoparticles (Figure 19B) were prepared.[176] Besides the reduction of side reactions in hydrolysis-sensitive mixtures, non-aqueous emulsions can also be applied in polymerizations, which require high temperatures. For such application, ionic liquids, with their characteristic low vapor pressure and thermal stability, are perfect candidates to be one the components of the emulsion. Frank *et al.*[177] synthesized polyimide nanoparticles (Figure 19C) by the heterophase polycondensation of aromatic tetracarboxylic acids and diamines in an imidazolium-based ionic liquid as the continuous phase, being able to produce the miniemulsion without the need of a surfactant, due to the amphiphilic character of the ionic liquid. The authors prepared polyimide nanoparticles with average diameter of 100 nm and the synthesis was completed in 10 h at 190 °C.

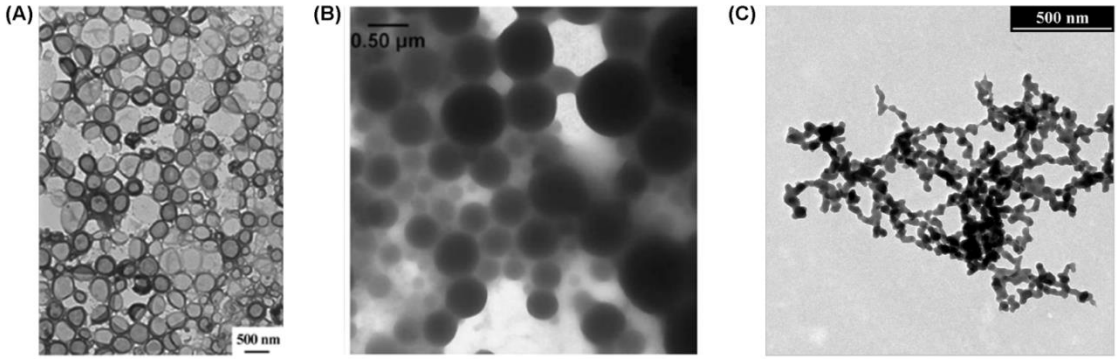

Figure 19: Examples of step-growth polymerizations performed in non-aqueous emulsions: (A) polyurethane nanocapsules (Reprinted with permission from reference [170]. Copyright 2007 American Chemical Society.) (B) nanoparticles (Reprinted with permission from reference[176]. Copyright 2011 Springer-Verlag) and (C) polyimide nanoparticles. (Reprinted with permission from reference [177]. Copyright 2009 American Chemical Society.).

The importance of the isocyanate chemistry at the interface in the preparation of nanocapsules is obvious by the number of different works found in the literature.[178-182] The highly reactive isocyanates enable a fast nucleophilic addition that occurs at the interface rather selectively to form hollow structures (compare above). Especially the polyaddition of 2,4-toluene diisocyanate (TDI) and different biopolymers in miniemulsion has been studied to generate nanocapsules for biomedical applications. Taheri et al.[183] produced hybrid nanocapsules based on starch and TDI as the cross-linker. The nanocapsules were loaded with silver nanoparticles (Figure 20) and had a mean diameter between 290 and 370 nm with different shell thicknesses, depending on the concentration of TDI. The nanocapsules showed effective antibacterial properties against *Staphylococcus epidermidis* and *Escherichia coli*.

Another example for a biopolymer used for the formation of nanocapsules by cross-linking with TDI is lignin (Figure 21). Hollow nanocapsules have been prepared, which were degraded in the presence of the enzyme laccase produced by certain fungi, generating a strategy for the development of delivery systems for agricultural applications.[184]

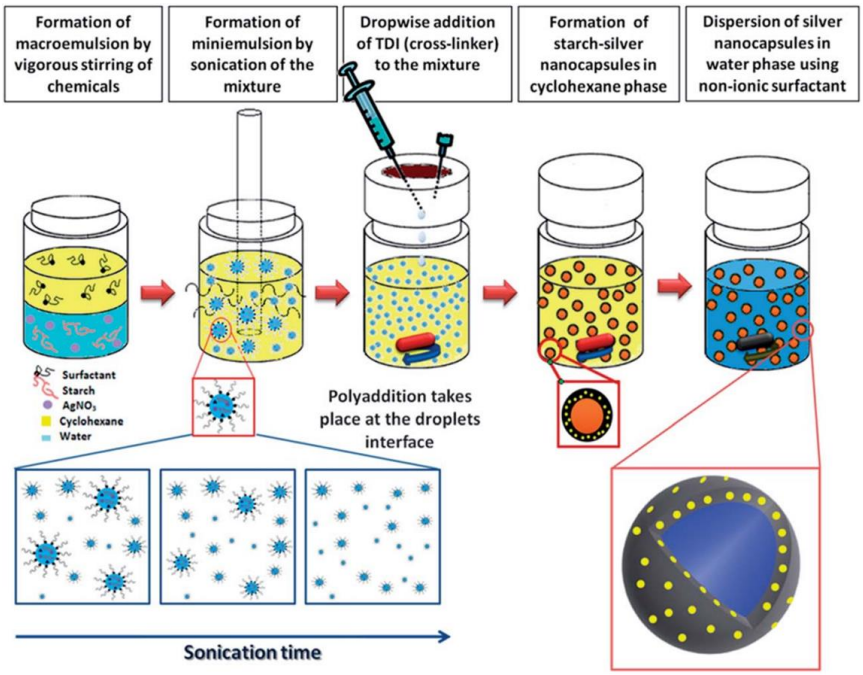

Figure 20: Schematic representation of the approach used by Taheri *et al*. for the preparation of starch nanocapsules loaded with silver nanoparticles. Reprinted with permission from reference [183].

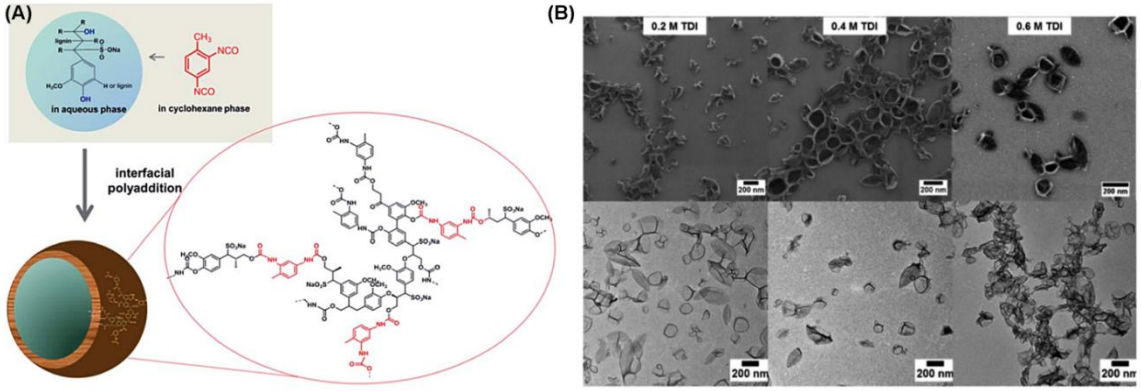

Figure 21: (A) Schematic representation of the synthetic protocol applied in the synthesis of lignin-based nanocapsules by Yiamsawas et al.; (B) SEM (top) and TEM (bottom) images of the lignin-based nanocapsules cross-linked with different amounts of 2,4-toluene diisocyanate (TDI). Reproduced with permission from reference [184].

1.1.4 Conclusion

Chemistry at interfaces evolved from the first nucleophilic addition conducted in heterophase 130 years ago to reactions “on water”, applications of phase transfer catalysts, nanoscale emulsions and bioorthogonal reactions that benefit from the interface of two immiscible liquids. In the near future, this reaction platform will definitively experience raising interest. In general, if a reaction can be conducted in two phases/at the interface to water, the amount of organic solvent can be reduced. This renders these reactions appealing for industry, not only to reduce organic waste, but also for efficient heat transfer

or the synthesis of water-soluble materials. Furthermore, with interfacial reactions complex architectures on micro/nanoscale become accessible which can be of advantage for the design of drug carriers. However, the increasing amount of biomolecules employed as efficient therapeutics requires also a growing variety in chemical reactions when nanocarriers for their encapsulation are constructed. Therefore, the development of new chemical reactions compatible or even reliable on the interface, being simultaneously inert to the functional groups of the cargo molecule is necessary. A possibility to achieve this is the use of bioorthogonal chemistry. In the following section, bioorthogonal reactions are reviewed in more detail. Besides a general overview of bioorthogonal chemistry, suitable reactions for applications at the liquid/liquid interface are emphasized.

1.2 Bioorthogonal Chemistry

A chemical reaction is orthogonal if a pair of substances reacts with each other but does not undergo a reaction with other substances present in the reaction medium. As mentioned above, these kinds of reactions are gaining increasing attention with regard to nanomedicine, especially for nanocarrier mediated drug transport, but also for imaging and selective labelling of biomolecules. The use of highly reactive substances for these applications is troublesome since the reactivity usually comes at the expense of selectivity. In the case of nanocarrier production, for example, unwanted side reactions with the cargo are likely (resulting in the deactivation thereof) if the cargo is carrying nucleophilic groups, which applies for many biomolecules such as proteins and siRNA. Before the commonly used bioorthogonal reactions are highlighted in the following, a short explanation for (bio)orthogonality is given.

A good example illustrating orthogonality is DNA. In DNA, adenine forms a base pair with thymine, cytosine only bonds with guanine. Base pairing in other combinations are energetically unfavorable.[185] Orthogonality is also present in case of reactions in a solvent, where the starting compounds do not react with the solvent molecules but solely with each other. Applied to biochemistry, a chemical reaction is considered bioorthogonal if it is inert against the native functional groups of biomolecules and does not interfere with natural processes in the biological system.[186] Additionally, since bioorthogonal chemistry is mostly used for protein or cell labeling (also *in vivo*), the reaction has to be non-toxic, proceed under physiological conditions and on a reasonable time scale at relatively low biomolecule concentration.[187]

Suitable bioorthogonal candidates employ functional groups that are not naturally occurring and have high reaction specificity towards each other. Excellent examples for that are organic azides and triaryl phosphines, which are used in the Staudinger ligation (Figure 22 *top*). The Staudinger ligation, developed in 2000 by Saxon and Bertozzi, is a modification of the classical Staudinger reaction (Figure 22 *bottom*).[188]

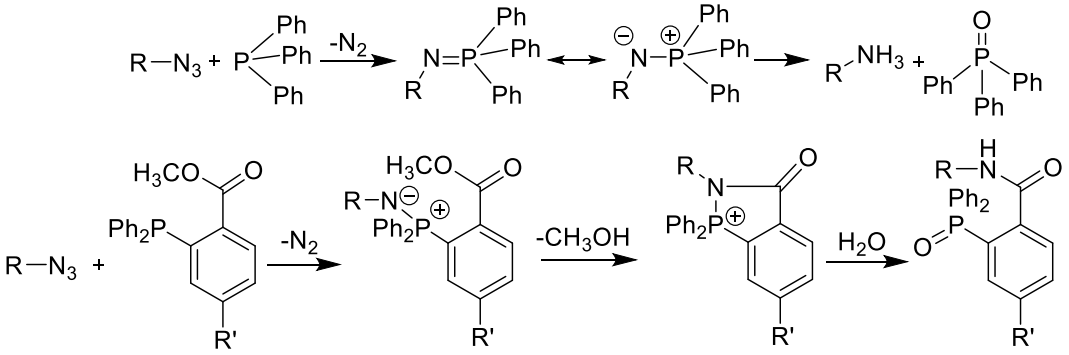

Figure 22: *Top*: classical Staudinger reaction. *Bottom*: Staudinger ligation.

In the Staudinger reaction, an azide reacts with a phosphine to form an aza-ylide. In the presence of water however, it hydrolyzes immediately to a primary amine and a phosphane oxide. To form a stable covalent bond, Saxon and Bertozzi introduced an electrophilic trap within the phosphine in form of a methyl ester to capture the nucleophilic aza-ylide by intramolecular cyclization. A further advancement is the traceless Staudinger ligation whereby the phosphane oxide is cleaved.[189] Being slower than other bioorthogonal chemistries, the Staudinger ligation nevertheless experiences continuous popularity especially for *in vivo* labeling owing to its remarkable chemoselectivity and mild reaction conditions.[190]

Various click reactions also fulfill the bioorthogonal conditions and are therefore used for protein/peptide or drug conjugation.[187] The term click chemistry introduced by Sharpless and coworkers describes a modular system wide in scope, where covalent linkage of molecules in a highly selective and high yielding manner is conducted in a one pot reaction.[191] Simple reaction conditions and product isolation, inoffensive and easily removable byproducts, as well as readily available starting materials and benign solvents are further characteristics of click reactions. To achieve a high selectivity towards a single product, the reaction should have a high thermodynamic driving force of greater than 84 kJ/mol. Several reaction types have been recognized to fulfill this requirement: nucleophilic ring-opening reactions of strained rings such as epoxides and aziridines;

cycloadditions of the Diels Alder type and especially the 1,3-dipolar cycloaddition reaction; additions to C-C multiple bonds such as oxidative additions, but also Michael additions; non-aldol type carbonyl chemistry, e.g., the formation of ureas, thioureas, oximes, hydrazones and amides.[192-193]

Azides are essentially absent in biological systems.[194] Furthermore, they are small and easy to introduce, stable under physiological conditions and highly reactive but simultaneously very selective.[195] Therefore, this moiety is frequently employed as the reporter tag for (bio)orthogonal reactions. The most famous example for this is the Huisgen dipolar cycloaddition of azides and alkynes termed as 'cream of the crop' of click reactions by Sharpless *et al.* (Figure 23).[191] Due to the almost full conversion, robustness and excellent functional group tolerance, this reaction has gained widespread use in chemistry and chemical biology. Under copper (I) catalysis a dramatic rate acceleration (reaction is then abbreviated as CuAAC) and full regioselectivity (only 1,4 triazoles are obtained) was achieved.[196]

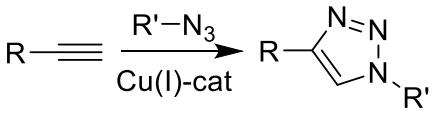

Figure 23: Azide-alkyne click reaction.

As a result of the high popularity of the CuAAC reaction, it is simply referred to it as 'The Click Reaction'.[192] Nevertheless, the toxicity of copper has hindered the use of CuAAC in living systems and has prompted researchers to look for alternatives.

Bertozzi and coworkers harnessed the ring strain of cyclooctynes to achieve a metal-free azide-alkyne reaction.[197] A series of cycloocytne derivatives have been investigated since then to accelerate the kinetics of this strain promoted cycloaddition (SPAAC). Besides fluorinated compounds, which are laborious to synthesize (8-12 steps), fusion of the cyclooctyne ring with two benzene rings (cf. Figure 24) leads to significant rate acceleration (2.3 M^{-1} s^{-1}, i.e. three orders of magnitude faster than the simple cyclooctyne).[198]

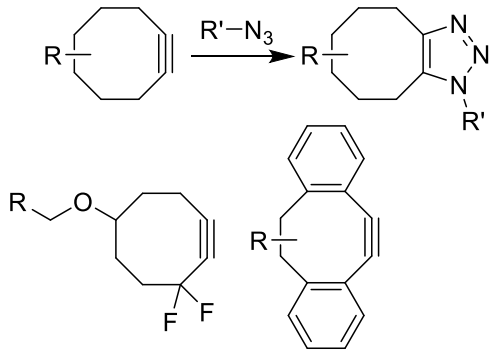

Figure 24: *Top*: strain-promoted cycloaddition reaction. *Bottom*: cyclooctyne derivatives for rate acceleration.

However, the low water solubility of the strained linkers, their accessibility and stability are still major issues. The increasing hydrophobicity was reported to cause non-specific binding to albumin and insertion into cell membranes.[199]

In addition to azides, cyclooctynes can also have other reaction partners such as nitrones, nitrile oxides, or diazo compounds with even higher rate constants of up to 50 M^{-1} s^{-1}.[200] However, the high reactivity results also in a poor stability in water, making an *in situ* generation of the dipole necessary.

Besides alkynes, strained alkenes can be used for bioorthogonal cycloadditions. In this category, the reaction of oxanorbornadienes with azides, inverse electron-demanding Diels-Alder reaction of tetrazines with *trans*-cyclooctenes or norbornenes and the 1,3-dipolar tetrazole-ene cycloaddition stand out (Figure 25).

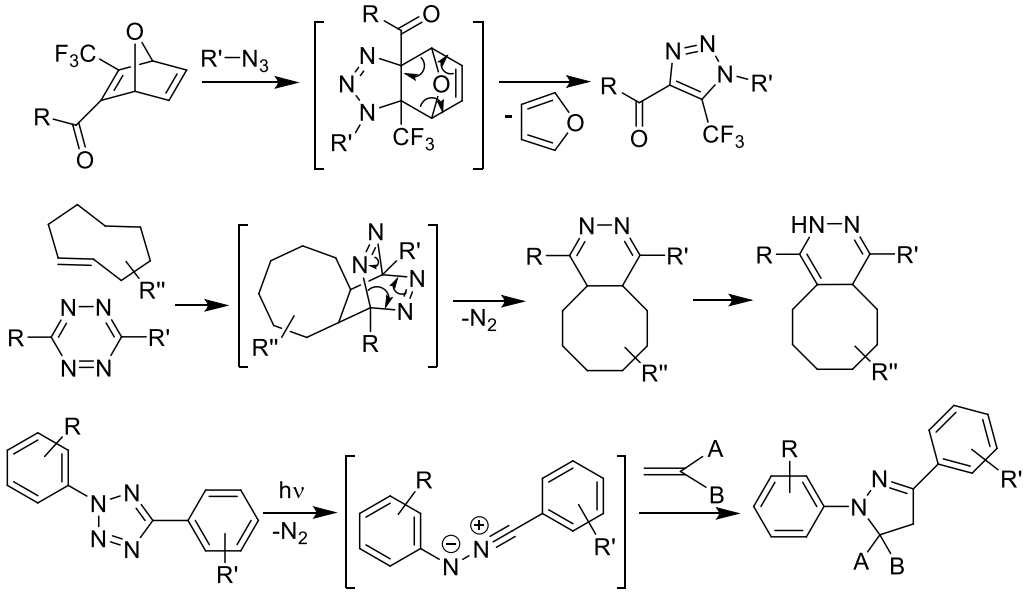

Figure 25: *Top*: reaction of oxanorbornadiene with azides. *Middle*: Inverse Diels-Alder reaction of tetrazines with trans-cyclooctenes. *Bottom*: 1,3-dipolar tetrazole-ene cycloaddition.

These reactions share the characteristics of rapid reaction kinetics. Second order rate constants (k_2) of up to $10x10^4$ M^{-1} s^{-1} for reactions of oxanorbornadienes with azides,[201] and up to $3.4x10^4$ M^{-1} s^{-1} for the tetrazole-ene cycloaddition have been reported.[202] The tetrazine *trans*-cyclooctene reaction is the fastest bioorthogonal reaction known so far with k_2 of $2.8x10^6$ M^{-1} s^{-1}.[203] However, the reactivity comes at the expense of the limited shelf life of *trans*-cyclooctenes. Therefore, norbornenes or cyclopropenes are considered as alternatives.[204-206] Among the reactions presented herein, the rapid kinetics, accessibility (price and synthesis pathway) and stability of the reagents were the reason to choose the bioorthogonal 1,3-dipolar tetrazole-ene cycloaddition reaction for nanocarrier synthesis presented in this work (cf. section 2.3).

Another mild bioorthogonal alternative is olefin metathesis with ruthenium catalysts.[207-209] However, for cellular applications, the efficient removal of the metal catalyst and the potential toxicity of residual amounts need to still be investigated attentively.

It has to be noted that the potential candidates for bioorthogonal chemistry can be further divided into *strictly* bioorthogonal and *effectively* bioorthogonal.[210] *Strictly* bioorthogonal reactions are not only inert against amine, hydroxyl, carboxyl or thiol groups but also against alkenes, amides, esters, disulfides and other functional groups present in biomolecules. However, reactions can be *effectively* biorthogonal, if they do not interfere with the native functionality of interest. For example, the thiol-ene click reaction is often counted as a bioorthogonal reaction, if no native thiol groups are present in the biomolecule or their modification does not restrict the function.[211] The condensation of aldehydes and ketones with hydrazides or alkoxyamines motifs is also listed as bioorthogonal.[186-187, 198, 212-213] On the cell surface native aldehydes and ketones are absent;[187] therefore, this reactions can be used for selective labeling. Intracellularly however, cross-reactivity with natural electrophiles, such as carbonyls from saccharides, renders this reaction not applicable. To conclude, these examples show that choosing the appropriate bioorthogonal chemistry for a given experiment from the vast variety available nowadays in the bioorthogonal toolkit can be sometimes challenging and has to be considered carefully according to the intended application.

1.2.1 1,3-Dipolar tetrazole-ene cycloaddition

The 1,3-dipolar cycloaddition of nitrile imine dipoles with alkene dipolarophiles belongs to the class of *effectively* bioorthogonal reactions. It is particularly attractive as it is a mild method, tolerant to a broad range of functional groups. The nitrile imine dipole can be generated either thermally above 150 °C[214] or by photolysis of tetrazoles. The 1,3-dipolar tetrazole-ene cycloaddition was described thoroughly by Huisgen and coworkers[215] in the 1960s, but found only recently a lot of attention as a powerful tool for biochemistry.

In contrast to the previous reports, it was found that for the photolytic activation a short irradiation with UV-light with low-intensity is already sufficient, rendering this reaction much milder than previously assumed.[216] Further, the reaction can be conducted in water and produces the fluorescent pyrazoline product in high yields and with high regioselectivities. The group of Lin systematically investigated the tetrazole-ene cycloaddition regarding reaction conditions and kinetics. Screening different solvents, they found out that the reaction is insensitive to solvent polarity, tolerant of protic solvents and can be conducted with equimolar concentrations of the reaction partners.[216] Electron deficient alkenes as dipolarophiles resulted in higher yields and faster conversion due to a lowering of the LUMO, enabling a better dipole HOMO-dipolarophile LUMO overlap.[217] Thus, irradiation times were lowered from initially 2 h to less than 1 min. In a following study, substitutions on the phenyl ring of the tetrazole were conducted to raise the HOMO energy level of the dipole, which further increases the reaction kinetics.

The exchange of electron withdrawing groups (EWG, e.g. CN, CO_2CH_3) against electron donating groups (EDG, e.g. CH_3, OCH_3, NH_2) as the X substituent (Figure 26) accelerated the reaction as expected. However, compared to the unsubstituted diphenyl tetrazole, the effect was less pronounced. An exchange of the Y substituent towards EDGs on the contrary, led to a significant increase of k_2 from 0.13 M^{-1} s^{-1} for the unsubstituted diphenyltetrazole to 0.79 M^{-1} s^{-1} for Y = NH_2. Additionally, the substituent effect was observed to be position dependent with substitution in the *para*-position resulted in the fastest rate constants.[218]

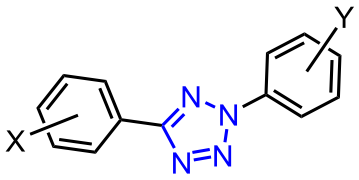

Figure 26: Diphenyltetrazole with substituents on the phenyl rings.

While photolytic activation of the first diaryl tetrazoles required UV light (254-365 nm, depending on the substitution)[219], subsequently tetrazole derivatives were developed enabling photoclick reactions with visible and infrared light. Terthiophene-tetrazoles are activatable with a 405 nm laser (Figure 27 *top*), while bithiophene-tetrazoles with extended π-systems at the C^5 position (Figure 27 *middle*) additionally generate red-fluorescent pyrazoline adducts upon reaction. Thereby, an interference caused by autofluorescence of living tissue is minimized.[220-221] The latest development are water-soluble naphthalene-tetrazoles activatable via a 700 nm near infrared laser (Figure 27 *bottom*). This two-photon-triggered photoclick chemistry allows a real-time, spatially controlled imaging of microtubules in live mammalian cells.[222] A drawback of these tetrazole-derivatives is that although the use of phototoxic UV-light is avoided, they are laborious to synthesize requiring 5-7 synthesis steps.

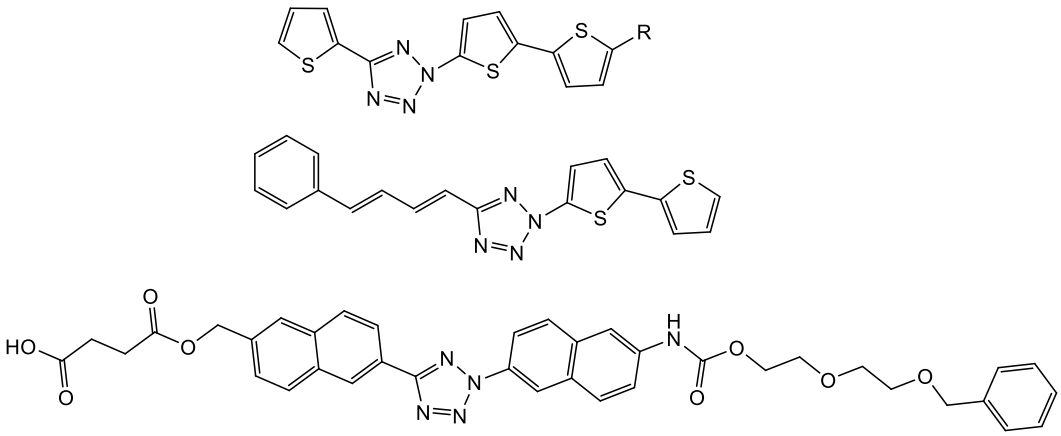

Figure 27: *top:* terthiophene-tetrazole, *middle:* phenylbutadiene-substituted bithiophene-tetrazole, *bottom:* tetrazole activatable with near infrared light.

Most publications with the tetrazole-ene photoclick chemistry report about selective labeling of proteins, and fluorescence imaging thereof frequently applied *in vitro*.[223-224] Furthermore, due to the self-fluorescence of the pyrazoline adduct, the tetrazole chemistry has been used for spatially resolved surface patterning[225] and polymerization reactions

yielding fluorescent polymers.[226] In this thesis, its application for bioorthogonal interfacial synthesis of nanocarriers is presented for the first time (cf. Section 2.3).

1.2.2 Bioorthogonal chemistry for nanocapsule synthesis

Bioorthogonal reactions are not only suitable for protein labeling, but can be used for the preparation of nanocarriers guaranteeing the encapsulation of sensitive biomolecules. Selected examples where bioorthogonal chemistry was used for nanocarrier preparation are given in the following.

Roux *et al.*[227] presented an approach for the preparation of glyco-nanocapsules using a copper catalyzed azide-alkyne (CuAAC) interfacial click approach in miniemulsion (cf. Figure 28). In this work, 6,6'-diazido-6,6'-dideoxysucrose was reacted with bis(propargyloxy)butane in a direct miniemulsion by the copper-catalyzed Huisgen-cycloaddition. The reaction was conducted with and without the use of microwave heating to increase the kinetics of the reaction and nanocapsules with an average mean diameter of 200 nm with mygliol as a core were prepared.[227] In this way, hydrophilic cargo can be encapsulated in the carrier systems. Besides the fact that the monomers and the core of the formulation were biocompatible, the use of the copper catalyst can be regarded as a potential drawback of this strategy as mentioned before.[228]

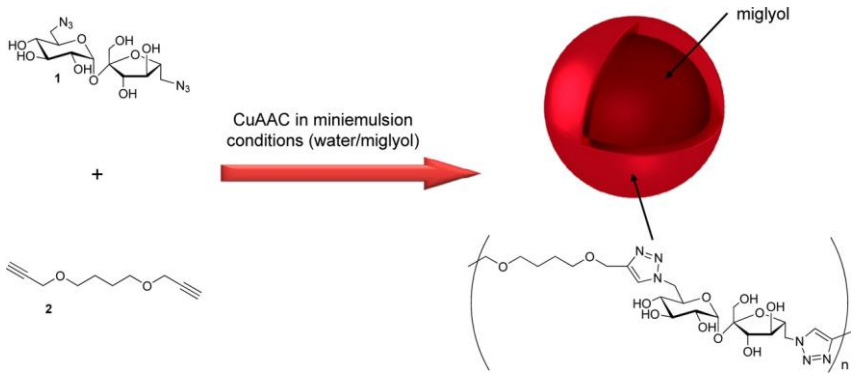

Figure 28: CuAAC polyaddition of 6,6'-diazido-6,6'-dideoxysucrose (1) with bis(propargyloxy)butane (2) for the formation of glyco-nanocapsules in miniemulsion. Adapted with permission from reference [227]. Copyright 2012 American Chemical Society.

Siebert *et al.*[29] used a copper-free alkyne-azide click reaction at the interface of inverse miniemulsion droplets for the preparation of nanocapsules relying on electron deficient alkynes (Figure 29). The approach yielded polymers with molecular weights up to M_w 33,600 g mol^{-1} in miniemulsion (lower than the ones obtained in the solution approach (M_w 45,500 g mol^{-1})) and nanocapsules with mean diameters of ca. 280 nm were obtained. Copper-free alkyne-azide click reactions are generally dependent of temperature

and relatively high temperatures are necessary for satisfactory kinetics (50 °C in this work). This can be problematic when sensitive compounds such as proteins or siRNA are encapsulated.

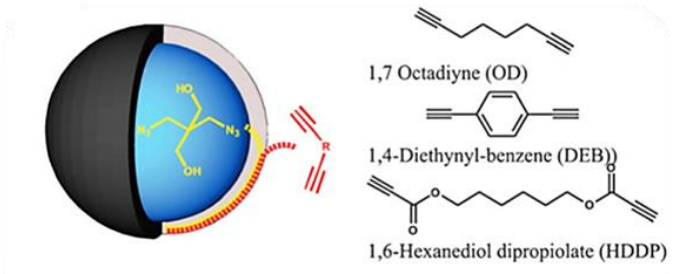

Figure 29: (A) Schematic representation of the alkyne-azide polyaddition approach studied by Siebert *et al.*[29] between the diazide 2,2-bis(azidomethylene)-1,3-propanediol (BAP) and the alkynes 1,7-octadiyne (OD), 1,4-diethynyl-benzene (DEB) and the activated alkyne 1,6-hexanediol dipropriolate (HDDP). Reproduced with permission from reference [29].

However, studies of the cycloaddition reaction kinetics at the interface in miniemulsion performed by ^{1}H NMR demonstrated the acceleration of the kinetics (Figure 30).[229] This effect was attributed to the increase of the local concentrations at the droplet's interface, allowing the use of lower temperatures (25 °C).

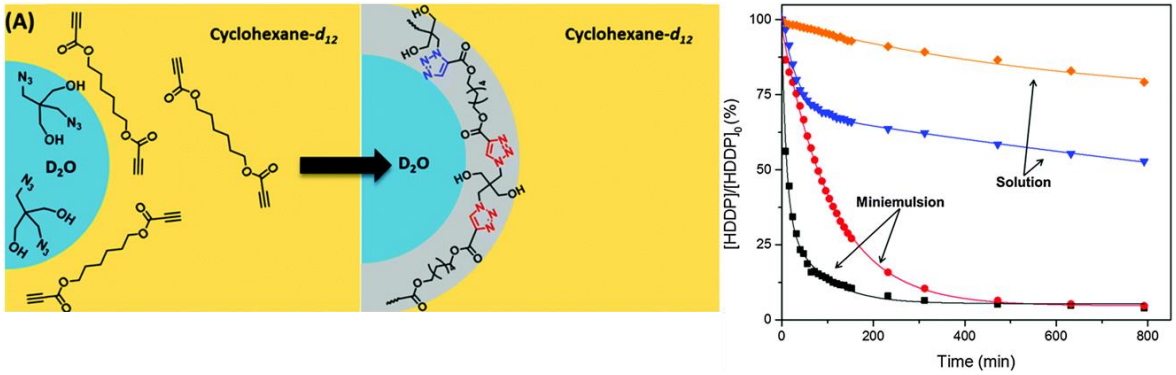

Figure 30: (left) Schematic representation of the polymerizable system investigated in the analysis of the kinetics of Cu-free alkyne-azide cycloadditions in inverse miniemulsion; (right) Curves obtained for the consumption of the monomer 1,6-hexanediol dipropiolate against time, monitored through ^{1}H NMR measurements at 298 K and 323 K in an inverse miniemulsion system (red and black curves) and in solution (DMSO-d_6, orange and blue curves). Reproduced with permission from reference [229].

The increase of the local concentration was used to explain the effect on the kinetics of other cycloaddition reactions based on the concepts described in the so-called pseudo-phase model. Engberts *et al.*[140] studied the 1,3-dipolar cycloaddition between benzonitrile oxide and *N*-ethylmaleimide in microemulsions, observing an 150-fold and 35-fold increase of the reaction kinetics in comparison to the same reaction in pure isooctane or water, respectively, which were used for the preparation of the

microemulsion. The authors attributed the increase to two factors: local concentration increase as well as electrostatic interactions due to the head groups of the ionic surfactant. In the case of the click chemistry presented in Figure 30, the use of a nonionic surfactant avoids the influence of charges in the reaction mechanism. In such a situation, only the increase of the local concentration is capable to explain the increase of the overall consumption of the monomer in the continuous phase.

Besides the Huisgen cycloaddition, other click reactions at the interface allow the preparation of nanocapsules in miniemulsion, e.g. the thiol-ene polyaddition. Paiphansiri and coworkers[230] produced glutathione-responsive DNA-based nanocapsules by the thiol-disulfide exchange and the thiol-ene click reaction. These nanocapsules for theranostic applications were biodegradable and fluorescently labeled (Figure 31).

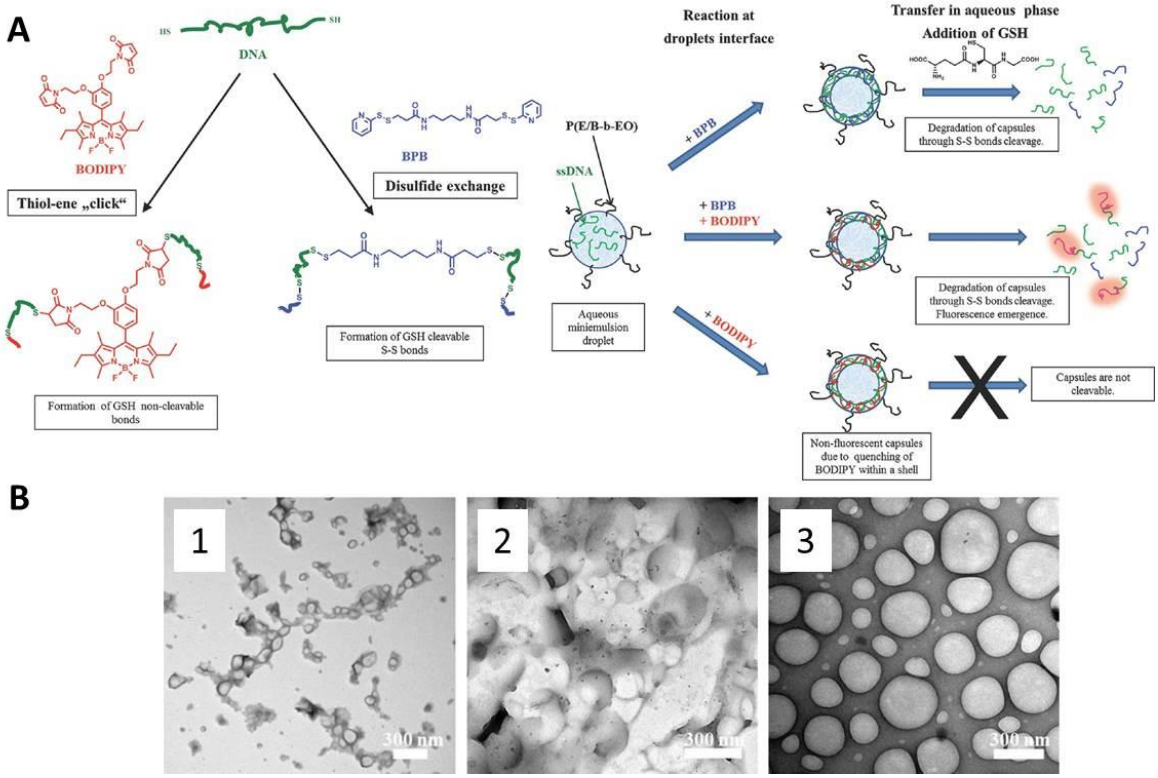

Figure 31: (A) Schematic representation of the synthetic approach used for the preparation of the different functional monomers and the DNA-based nanocapsules using a thiol-ene "click" reaction approach at the interface; (B) TEM images from dichloromethane phase: B-1 with BPB monomer only; B-2 with BPB and BODIPY monomer; B-3 with only BODIPY monomer. Reproduced with permission from reference [230]. Copyright 2014 John Wiley & Sons Inc.

The development of metathesis reactions in the presence of water could open up the way to synthesize polar polymers and biomolecules besides advantages in terms of security, economy and environmental friendliness. Reported reactions in the presence of water still proceed mostly inside the organic phase (see minireview[158]), and the catalysts

are designed to tolerate water. Nevertheless, since this reaction is considered as bioorthogonal, it makes olefin metathesis a tool of high interest for the development of new nanocapsules for biomedical applications.

Malzahn and coworkers[231] presented a bioorthogonal interfacial olefin cross metathesis for the preparation of hollow dextran-alkylphosphate nanocapsules (Figure 32). The olefin metathesis is a reaction which can be performed at mild conditions and the use of phosphate-cross-linkers also offers the possibility of further addition of functionalities to the polymeric shell, as for example the addition of fluorescent units. EDX and ICP-OES analysis revealed efficient removal of the ruthenium catalyst (which is only soluble in the continuous phase).

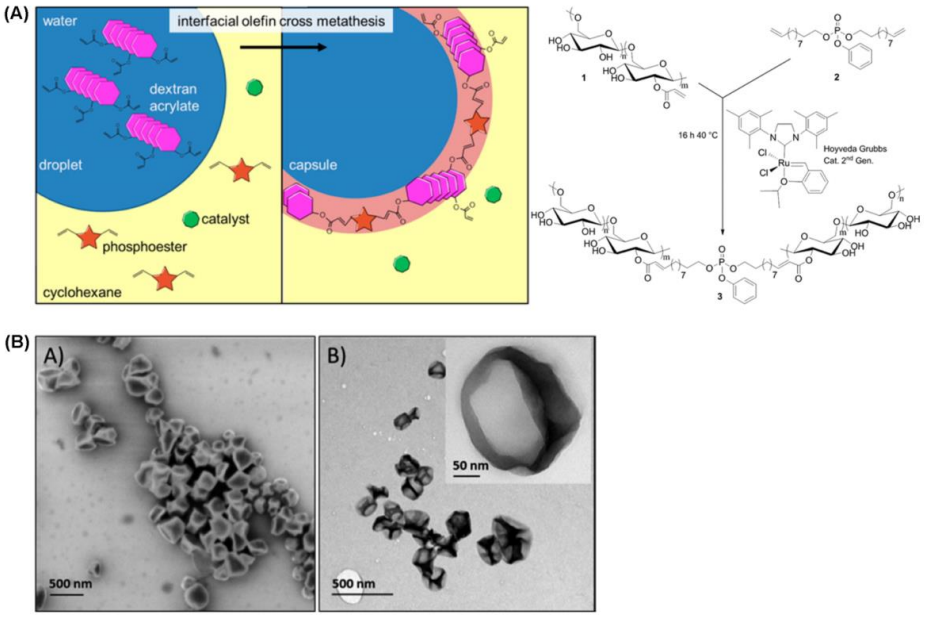

Figure 32: (A) Schematic representation of the interfacial olefin cross metathesis strategy applied by Malzahn *et al*.[231] (B) TEM micrographs of the dextran-based nanocapsules obtained through interfacial olefin cross metathesis. Adapted with permission from reference . Copyright 2014 American Chemical Society.

Ring-opening cross-metathesis at toluene/water interface was used by Breitenkamp and Emrick to synthesize microcapsules from amphiphilic graft copolymers (Figure 33).[232] Due to the amphiphilic nature of the shell material, the capsules are able to swell both in water and in organic solvent. Similarly to the example above, incorporation of a fluorescent monomer enabled the visualization of the capsules by fluorescence confocal microscopy and showed a strong preference of the graft copolymer for the interface (Figure 33, *right*).

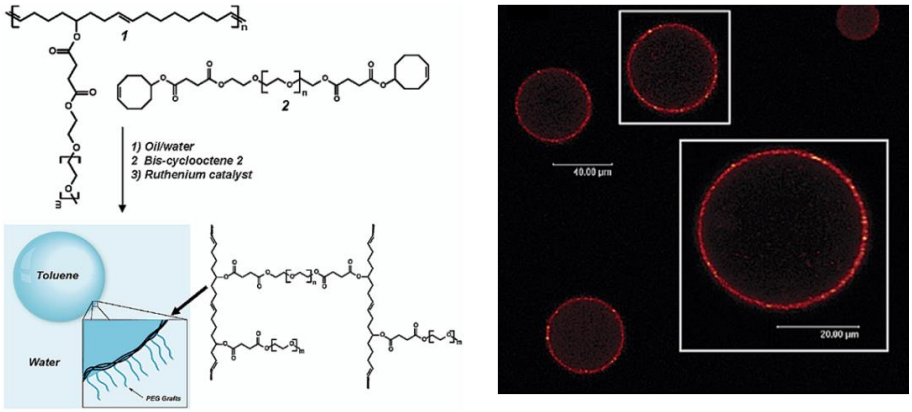

Figure 33: *left*: principle of the ring opening cross-metathesis presented by Breitenkamp and Emrick[232]; *right*: confocal laser scanning micrograph cross-section of microcapsules. Reprinted with permission from reference [232]. Copyright 2003 American Chemical Society.

"Tagged" ruthenium catalysts were developed to achieve certain affinity to the reaction media and even be soluble in the aqueous phase, and surface-active catalysts could expand the possibilities for metathesis reactions at the oil/water interface further.[233-235]

2. Results and Discussion

This chapter is structured as follows. The feasibility to prepare nanocarriers out of proteins is presented in the first section. These first protein nanocarriers or nanocontainers were composed of easily available model proteins, such as albumins. With these nanocontainers insights on colloidal properties, biological behavior and general suitability of protein nanocarriers as drug delivery vehicles were obtained. The gained knowledge was used to promote these efficient carrier systems to a cargo itself by using the HCV nonstructural protein 5A (NS5A) for protein nanocarrier formation for nanovaccination. The results of this approach are described in the second section of this chapter. The idea and its limitations, to avoid additional carrier material in general and use the active compound itself instead is described briefly in section 2.3, with nanocarriers from the drug dexamethasone. Finally, an alternative synthesis pathway is presented in section 2.4 bearing the potential to encapsulate sensitive cargo inside protein nanocarriers.

2.1 Albumin nanocontainers

In this section, the synthesis of nanocontainers entirely composed of albumin proteins using an interfacial polyaddition reaction is presented. Parts of the content have been previously published in the paper "Biodegradable Protein Nanocontainers" by Piradashvili *et al*., *Biomacromolecules*, **2015**, *16*, 815-821. Adapted with permission from reference [236]. Copyright 2015 American Chemical Society.

2.1.1 Motivation

In the field of targeted drug delivery, the design of nanocarriers is particularly interesting as these systems open up ways of directed and personalized medication with reduction of side effects.[237-238] Drug delivery vehicles should protect sensitive cargo and be able to transport safely the medication to the pathological site overcoming biological barriers within the body.[4, 239] Additionally, a facile, controlled and naturally driven way of release must be guaranteed once the target site is reached.[240] Thus, nanocontainers for the use as drug carriers have to meet certain requirements such as low toxicity, high loading efficiency and a sustained release.[241]

Several efforts have been undertaken to provide such drug delivery systems with materials which are known for their biocompatibility and -degradability such as

poly(lactide-*co*-glycolide)s (PLGA) or poly(lactone)s.[242-243] However, these materials still remain a foreign compound within a biological system exhibiting certain drawbacks as, for example, a fast clearance by the immune system or toxicity, low pH of the degradation products.[244-245] Nanocontainers based on biopolymers such as polysaccharides[178, 246-247] and proteins,[248-249] on the contrary, have been proven to be more effective because they often show a higher drug-loading capacity and a better biocompatibility compared to the synthetic ones.[246]

Proteins are particularly interesting as they are easily accessible, water-soluble, biodegradable and in general associated with low toxicity.[247, 250-251] Moreover, due to their defined molecular weight and known primary structure, further chemical modifications are possible.[10-11, 252] In recent studies, for example, the chemotherapeutic agent paclitaxel was bound to albumin nanoparticles (*nab*-paclitaxel), increasing the efficacy of the drug compared to solvent-based formulations and lowering the side effects.[253]

Herein, the synthesis of nanocontainers composed exclusively of bovine serum albumin (BSA) or ovalbumin (OVA) is shown. The nanocontainers were prepared via the inverse miniemulsion technique (see Figure 34).

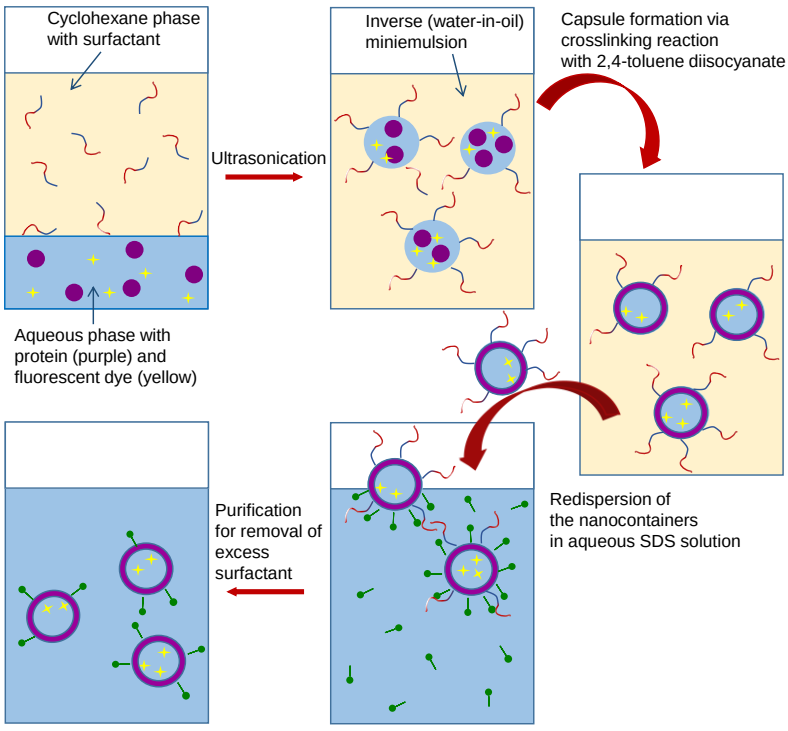

Figure 34: Synthetic procedure for protein nanocontainers via the miniemulsion process.

This process enables the production of stable capsules in size ranges of 50-500 nm via a polyaddition reaction at the interface of stable nano-sized droplets in emulsion.[254-256]

The advantage of this method is that with water representing the dispersed phase, it is possible to encapsulate water-soluble compounds with high loading efficiency.[257] Additionally, via functional groups on the nanocontainer surface (such as hydroxyl or amino moieties), the nanocontainers can be further modified, e.g. with antibodies, for targeting of specific organs or cell types.[258-260] Polysaccharide-based nanocarriers, for example, functionalized with antibodies and adjuvants were taken up more efficiently by Kupffer cells and dendritic liver cells compared to the untargeted constructs.[260] Polyurethane nanocapsules with an amino-functionalized surface showed an increased uptake by HeLa cells demonstrating their potential use as biocarriers.[261]

In the present study, BSA and OVA were chosen as model proteins. These proteins are well studied, easily available, exhibit a wide acceptance in pharmaceutical industry and are already used in several drug delivery systems.[11, 262-264] A representative from serum albumins was chosen as these proteins are the most abundant plasma proteins in mammals and play an important role in the transport of small molecules due to the extraordinary high ligand binding capacity.[10, 265] BSA nanoparticles can be used as suitable agents for liver-targeting drug delivery systems. It was found that BSA nanoparticles prepared via the pH-coacervation method and loaded with the anticancer drug methotrexate exhibited a significant higher accumulation in the murine liver, lung and spleen compared to the free drug.[266] Furthermore, studies have shown that nanoparticles modified with serum albumin have less undesired interactions in serum and thus can be used as suitable agents for gene therapy.[267-268]

As BSA is extracted from bovine blood and can therefore be, despite purification, contaminated with pathogens, ovalbumin is preferentially used for medical testing.[269] Especially for immunization experiments, ovalbumin is widely used as a model antigen for vaccine studies. OVA and BSA share a number of common properties, including low toxicity, and they are biodegradable, chemically rather stabile and capable to stabilize emulsions.[10]

Protein nanocontainers were characterized regarding their composition, formation kinetics and morphology. The loading efficiency by encapsulating the dye SR101 as a hydrophilic drug model was studied along with the degradation of PNCs by proteolysis both in a cell-free assay and in a dendritic cell culture system. Further, the uptake of the PNCs in dendritic cells was examined and in addition, the behavior of the PNCs in human

blood plasma was investigated. By encapsulation of multiple cargos the potential of PNCs for co-delivery of several drugs, an important factor for drug delivery applications, was evaluated.

2.1.2 Synthesis of protein nanocontainers

Protein nanocontainers were synthesized by a polyaddition reaction at the interface of nanodroplets in water-in-oil miniemulsion. For the stabilization of the droplets, the oil-soluble block copolymer poly((ethylene-*co*-butylene)-*b*-(ethylene oxide) P((E/B)-*b*-EO) was used as the surfactant.

The isocyanate groups of the crosslinker 2,4- toluene diisocyanate (TDI) react with the nucleophilic groups of the respective protein (hydroxyls and amines) which results in the formation of water-insoluble nanocontainers with a dense and cross-linked polypeptide shell. In Figure 35, the ATR-IR spectra are shown which were recorded over 24 h reaction time for the OVA-PNCs. As can be seen in the inset, the isocyanate stretching vibrations appear at 2265 cm^{-1} when TDI is added at t = 1 min. Over time, as the reaction proceeds, the intensity of the band decreases and after 24 h the N=C=O groups cannot be detected any more. Thus, the majority of the isocyanate groups were converted to urea and urethane linkages, predominantly by reaction with amines from the protein but also reactions with TDI itself cannot be excluded.

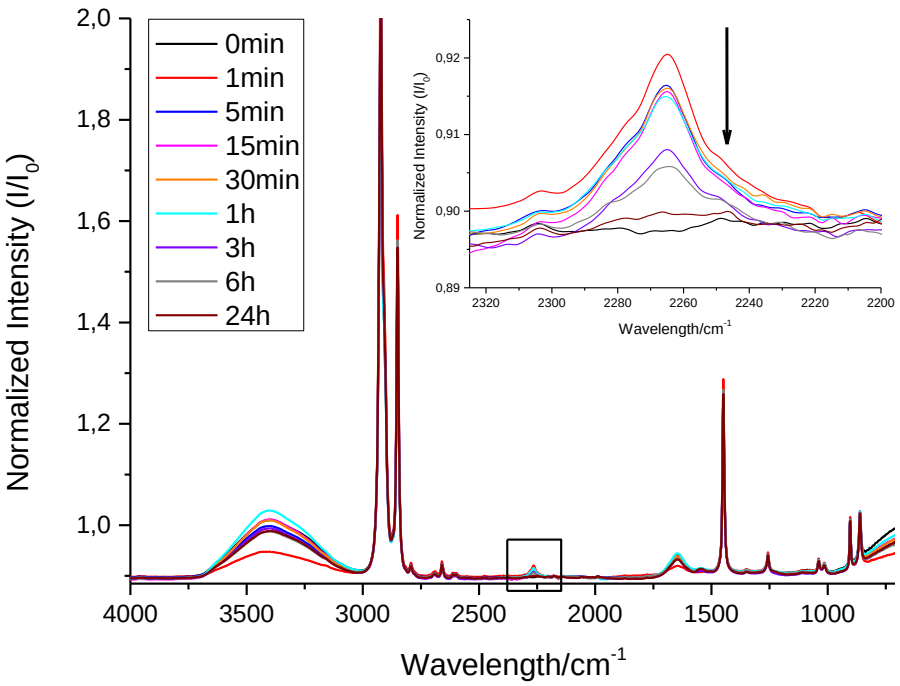

Figure 35: Normalized ATR-IR spectra of OVA-nanocontainers recorded over time. The area where the isocyanate vibration bands appear is shown enlarged in the inset. The arrow indicates the decrease of this band over time as free isocyanate groups are consumed.

SEM and TEM images confirm the core-shell morphology of the obtained PNCs (see Figure 36). For studies of cellular uptake and degradation, the OVA-PNCs were modified with fluorescent dyes cy5, CellTracker CMFDA (CT) and fluorescently labeled ovalbumin (DQ) (see below).

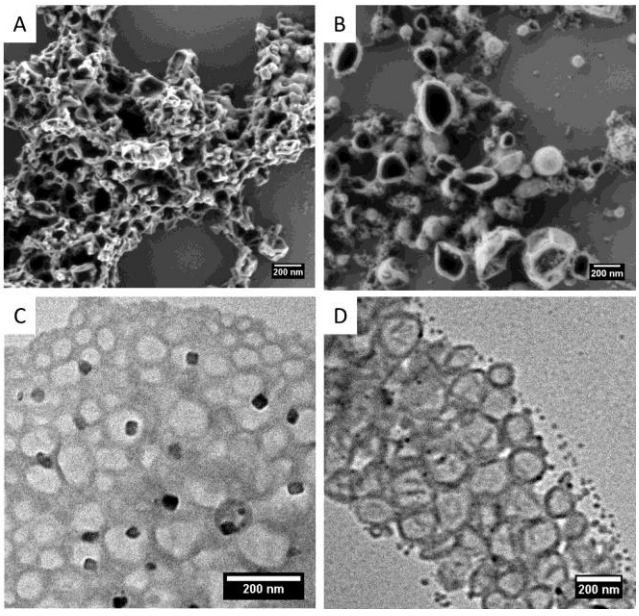

Figure 36: top: Scanning electron microscopy (SEM) images of A: BSA-nanocontainers; B: OVA-nanocontainers; bottom: Transmission electron microscopy (TEM) images of C: BSA-nanocontainers (black spots: NaCl crystals); D: OVA-nanocontainers

The average size of the particles was determined via dynamic light scattering (DLS) and the data is shown in Table 1. PNCs with a diameter of ca. 200 nm were obtained which were redispersed in aqueous SDS solution. After purification zeta potentials in the range of -10 to -20 mV were measured (see Table 1). The negative values are due to the residual negatively charged anionic surfactant used for stabilization of the particles during the redispersion process.

Table 1: Characterization of the protein nanocontainers.

Sample	Average diameter [nm] in cyclohexane (PDI)	Average diameter [nm] in water (PDI)	ζ [mV]
OVA-cy5	261 (0.10)	260 (0.39)	-19±4
OVA-DQ	263 (0.20)	285 (0.29)	-16±4
OVA-CT	221 (0.36)	229 (0.44)	-12±6
BSA	220 (0.04)	190 (0.32)	-18±5

2.1.3 Quantification of residual surfactants

Surfactants are essential for stabilization of the protein nanocontainer dispersion. However, a low surfactant amount is preferential, in order to minimize potential effects caused by the surfactants, especially for biological applications. Nevertheless, a complete removal is not advisable in most cases as it results in instability of the dispersion and aggregation of the nanocontainers.

For PNC synthesis, P((E/B)-*b*-EO) was used for stabilization of the aqueous droplets in the oil phase. The structure of this surfactant is shown in Figure 37.

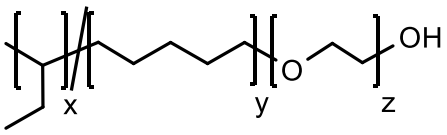

Figure 37: Structure of the surfactant poly((ethylene-*co*-butylene)-*b*-(ethylene oxide) P((E/B)-*b*-EO).

Prior to PNC transfer to the aqueous phase, the dispersion was centrifuged three times and the supernatant was exchanged with pure cyclohexane. The surfactant amount in the raw and purified OVA-PNC dispersions as well as in the three supernatants was determined via ^{1}H-NMR using DMF as internal standard and monitoring the signals of the ethylene oxide block. In Figure 38, the amount of P((E/B)-*b*-EO) from each step is depicted. It decreases with every purification cycle until in the final purified PNC dispersion only 11% of the initial P((E/B)-*b*-EO) amount is present.

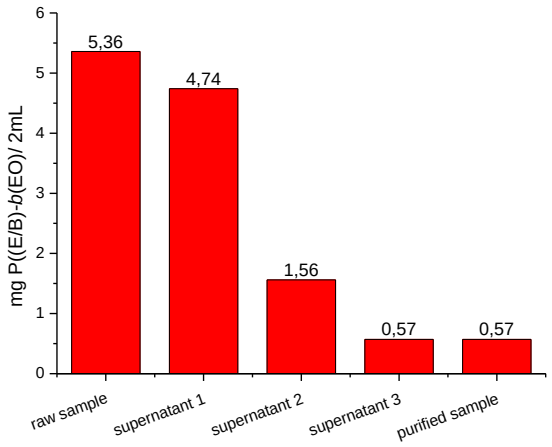

Figure 38: Amount of P((E/B)-b-EO)in OVA-PNC dispersion and supernatants determined via ^{1}H-NMR.

For the transfer of the PNCs from the organic to the aqueous phase, sodium dodecyl sulfate (SDS) was used. Similarly to P((E/B)-*b*-EO), SDS was removed via centrifugation. The residual amount of SDS in the nanocontainer dispersion was quantified via a method developed by Rusconi et al. using stains-all dye.[270] This quick and sensitive method was chosen since it allows quantification on microliter scale and is specific to SDS. The free dye shows a major absorption band at 510 nm, which decreases upon SDS addition whereas absorption maxima of the dye-SDS complex appear at 438 nm and 453 nm (Figure 39).

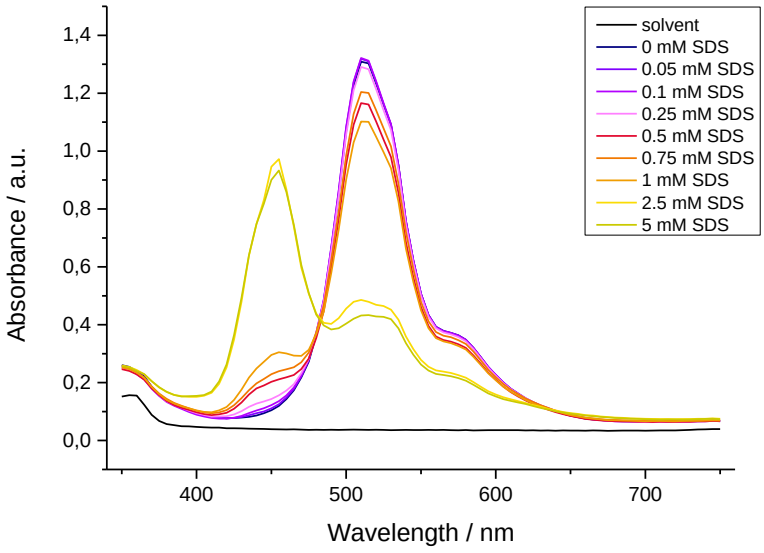

Figure 39: Absorbance spectra of stains-all dye upon SDS addition.

The best linearity is given at 438 nm, therefore this local maximum is used for quantification. Visually, after every purification step a gradual color change from yellow over orange to purple occurs upon SDS reduction as can be seen in Figure 40.

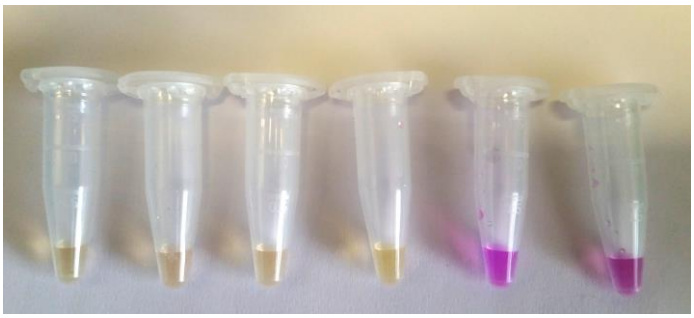

Figure 40: From left to right: stains all dye with raw sample, supernatant 1, supernatant 2, supernatant 3, supernatant 4, clean sample.

Figure 41 depicts the SDS amount of every purification step. In the purified PNC dispersion, which is used in the subsequent biological experiments, 4% of the initial SDS amount remained, i.e. 0.06 g/L from the initial 1.5 g/L.

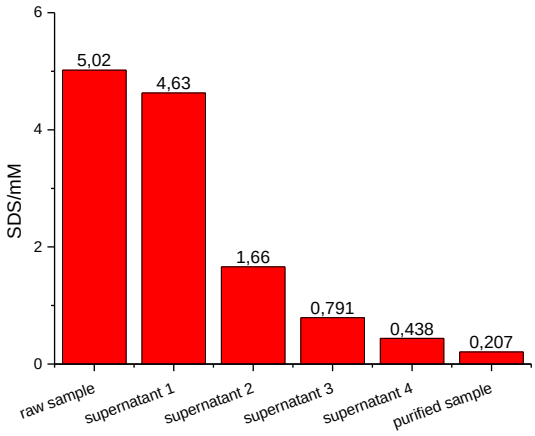

Figure 41: Amount of SDS in aqueous OVA-PNC dispersion before and after purification and in the supernatants of every purification step.

2.1.4 Encapsulation efficiency

Encapsulation efficiency is an essential characteristic determining the value of PNCs as drug delivery systems. Therefore, the fluorescent, hydrophilic dye sulforhodamine 101 (SR101) was chosen as a water-soluble drug representative (Figure 42).

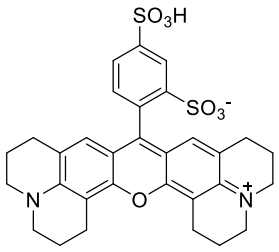

Figure 42: Structure of sulforhodamine SR101.

The advantage of SR101 is that it does not influence the crosslinking reaction.[257] Notably, SR101 is a relatively small molecule (1.0-1.4 nm),[271] enabling the assessment of the endurance and the shell density. Additionally, due to its fluorescence, the leakage of the nanocontainers can be easily determined by measuring the residual fluorescence intensity in the aqueous phase after removal of the PNCs. The resulting values were correlated with the initial amount of the encapsulated dye. A release over time was also monitored by measuring the change in fluorescence intensity over a period of 22 days (t = 0 days is 12 h after redispersion) (Figure 43). For both protein nanocontainers very high encapsulation efficiencies were detected with 88% for BSA-PNCs and 97% for OVA-PNCs. After redispersion into water, an initial leakage (less than 10%) was detected. However, it reached a plateau after 8 days indicating that in the remaining observation period only very limited release of the encapsulated dye took place.

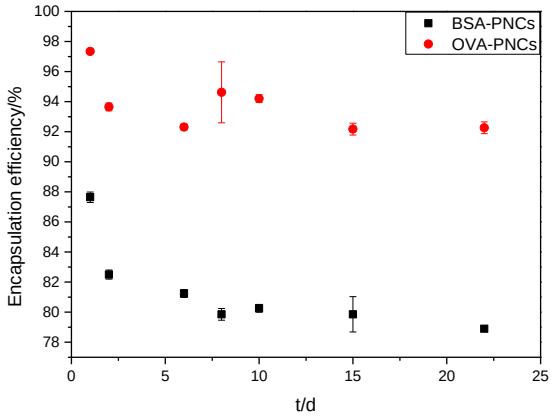

Figure 43: Encapsulation efficiencies and density measurements for PNCs in aqueous dispersion (measured via fluorescence of SR101). Depicted values were determined through two experiments with three single measurements per sample.

After 22 days, a total leakage of 8.7% for BSA-PNCs and 5.1% for OVA-PNCs compared to the initial value was observed. Thus, both PNCs, especially OVA-PNCs, can

be used to encapsulate hydrophilic molecules stressing the density of the synthesized shell, which impedes the diffusion of the encapsulated compound.

2.1.5 Interaction with blood plasma

The aggregation behavior of the PNCs in blood plasma was studied via DLS by applying the method after Rausch et al.[272] For light scattering experiments, the protein to PNC ratio was set constant to the *in vivo* experiments. Figure 44 displays the self-autocorrelation function of the plasma/PNC mixture, which can be perfectly described by the so-called force fit. This means that the sum of the individual correlation functions with the known parameters of the two compounds (plasma/PNC) is kept fixed and the intensity contributions for plasma and PNC are the only fit parameters.[272] The result indicates that no sizes larger than the largest size of either plasma or PNCs are formed in the mixture.

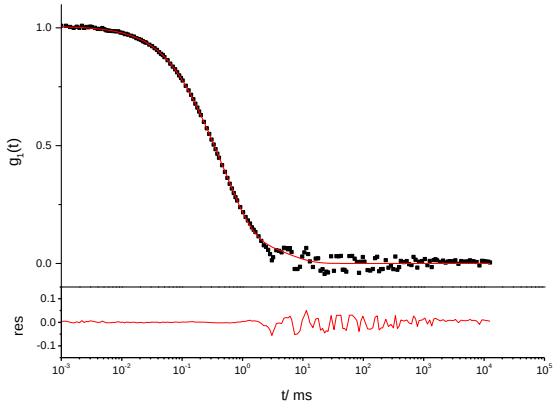

Figure 44: Self-autocorrelation function of the plasma/OVA-nanocapsule mixture. Black squares depict the data points of the plasma/OVA-nanocapsule mixture. The red curve represents the force fit of the mixture and the residue of the fit. Scattering angle 60°, T = 20 °C.

It has to be noted that the presented method is not able to detect changes in the size distribution caused by a monolayer of proteins on the nanoparticle surface.[273]

2.1.6 Intracellular uptake

Intracellular uptake of OVA-PNCs was analyzed by an *in vitro* cell culture system using human monocyte-derived dendritic cells (moDCs) due to their capability to phagocytize particles in the nanometer range. In addition, dendritic cells are specialized antigen presenting cells that play a role in the induction of immune responses[274]. Confocal laser scanning microscopy (CLSM) revealed an intracellular uptake of cy5-labeled OVA-PNCs by moDCs after incubation for 24 h rather than just adherence to the plasma membrane (Figure 45 A). Furthermore, the uptake of OVA-cy5 by moDCs was quantified using flow cytometry after co-incubation for 24 h. Figure 45 B shows a concentration-

dependent increase from 16.8% of PNC^+ moDCs up to 87.4% for 7.5 µg/mL and 100 µg/mL OVA-cy5, respectively, documenting an efficient uptake of PNCs by moDCs *in vitro*.

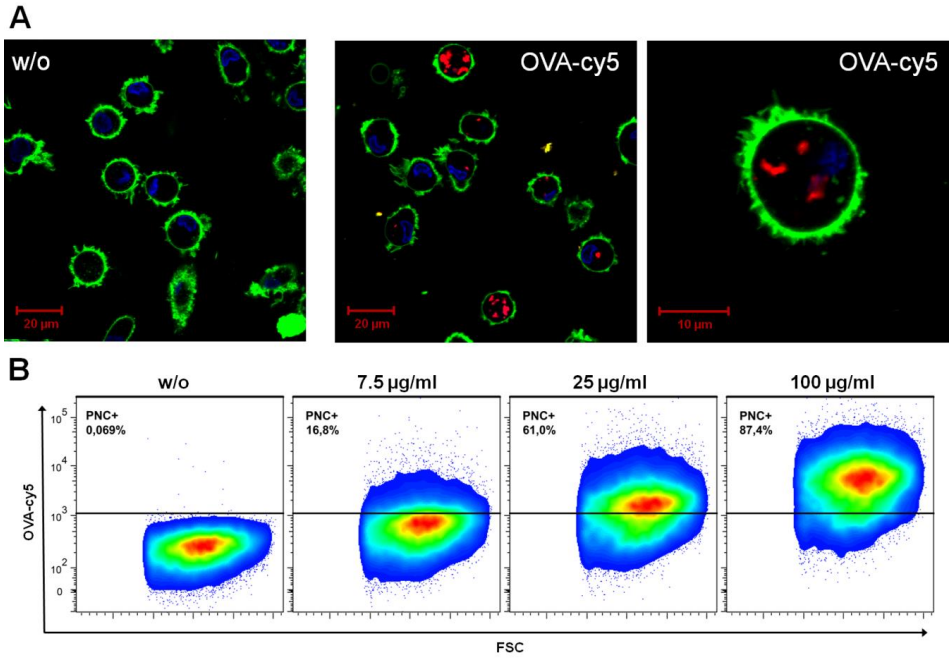

Figure 45: Confocal laser scanning microscopy images (A) and dot plots obtained by flow cytometry (B) of moDCs incubated without or with different concentration of OVA-cy5 PNCs for 24 h. (A) Plasma membrane was stained with CellMask Orange (green), nuclei were stained with Hoechst 33342 (blue), OVA-PNCs were labeled with cy5 (red). (B) moDCs that incorporated PNCs were quantified and indicated with "PNC+". Measurements were performed by M. Fichter.

2.1.7 Cytotoxicity

In order to examine a potential toxicity of the PNCs, human moDCs were coincubated with OVA-cy5 PNCs with concentrations from 2.5 µg/mL to 100 µg/mL for 24 h. As can be seen in Figure 46, no cytotoxicity could be detected. This finding suggests, that potential toxic substances used for the synthesis of PNCs, do not exceed critical concentrations in the resulting nanocontainer dispersion.

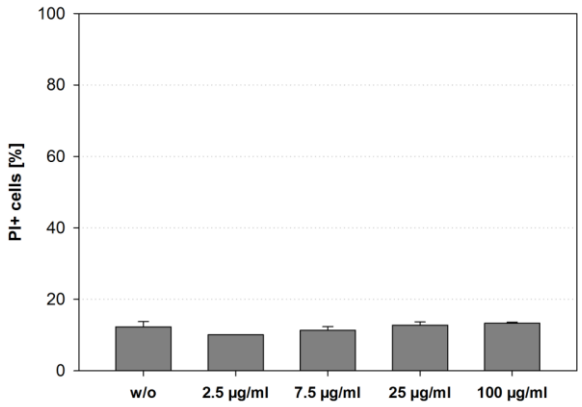

Figure 46: Toxicity analysis of OVA-cy5 PNCs coincubated with moDCs for 24h. Cells were stained with propidium iodide (PI) and dead moDCs are displayed as PI^+. Measurements were performed by M. Fichter.

2.1.8 Enzymatic degradation

The degradation of OVA-PNCs was studied with a method resembling physiologically occurring biodegradation. Accordingly, OVA-PNCs were loaded with the fluorescent markers DQ ovalbumin (DQ) and CellTracker CMFDA (CT), which do not emit fluorescence signals in their natural states. DQ ovalbumin is composed of the protein ovalbumin, which is conjugated to multiple BODIPY molecules leading to a quenching of fluorescence. Proteolytic degradation of the protein into BODIPY-labeled peptides however, leads to a restoration of fluorescence.[275] CellTracker CMFDA is a low-molecular weight fluorescent dye of about 465 Da that is colorless and non-fluorescent (structure of CT see Figure 47).

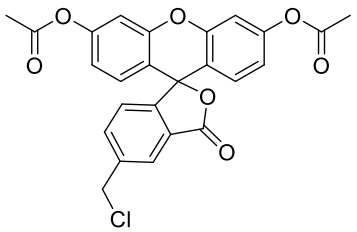

Figure 47: Structure of the fluorescent dye CellTracker CMFDA.

Upon cleavage of acetate groups by esterases the resulting product is activated and can emit fluorescence signals. Due to its esterase activity, [276] we chose the serine protease trypsin as the enzyme for the degradation of both substrates, DQ ovalbumin as well as CellTracker CMFDA.

The diagrams in Figure 48 show the increase in fluorescence intensity of the aqueous surrounding immediately after addition of trypsin both for DQ ovalbumin and for

CT-modified OVA-PNCs. The controls without trypsin display no change in intensity. Thus, the release of PNC content is dependent on proteolytic degradation of the capsule shell.

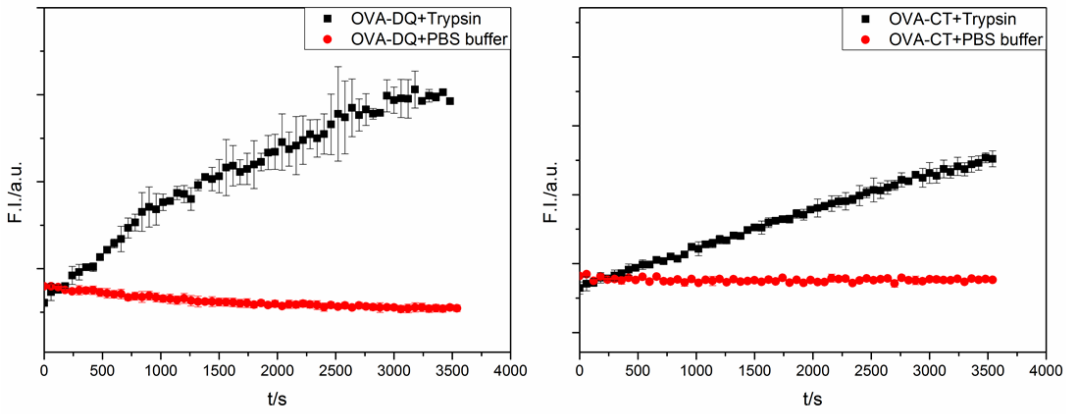

Figure 48: Time-dependent change of fluorescence intensity due to trypsin degradation of DQ ovalbumin (A) and CellTracker-labeled OVA-PNCs (B).

These results demonstrate that despite cross-linking of the proteins by urethane and urea linkages and the resulting conformational changes, PNCs are still accessible to proteolytic degradation by proteases.

In order to confirm these observations in an *in vitro* setting, cell-culture experiments using human monocyte-derived dendritic cells co-cultured with OVA-DQ PNCs were performed. This experimental approach revealed an intracellular release of DQ ovalbumin (Figure 49) after co-incubation for 24 h.

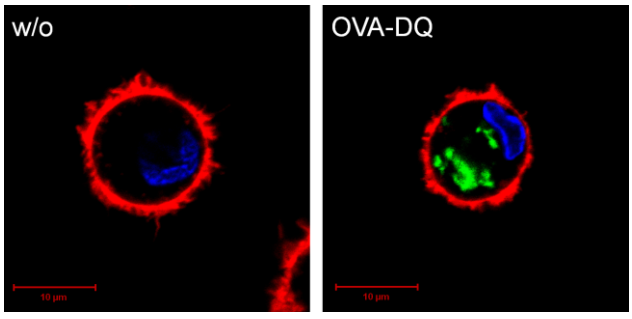

Figure 49: Confocal laser scanning microscopic images of moDCs incubated with (right) or without (left) OVA-DQ PNCs for 24 h (plasma membrane was stained with CellMask Orange (red), nuclei were stained with Hoechst 33342 (blue) and OVA-DQ PNCs were stained with DQ ovalbumin (green)). Measurements were performed by M. Fichter.

A further proof that the degradation process is an enzymatic one after an active cellular uptake, the cell experiments were repeated at two different temperatures. At 4 °C,

where the enzymatic activity and endocytosis is decreased, the mean fluorescence intensity of the DQ-ovalbumin degradation products measured by FACS is lower than at 37 °C (Figure 50 A), and even not observable by CLSM, respectively (Figure 50 B). This experiment shows that PNC uptake by cells is an active process (endocytic pathway) and proteolytic degradation starts inside the cell.

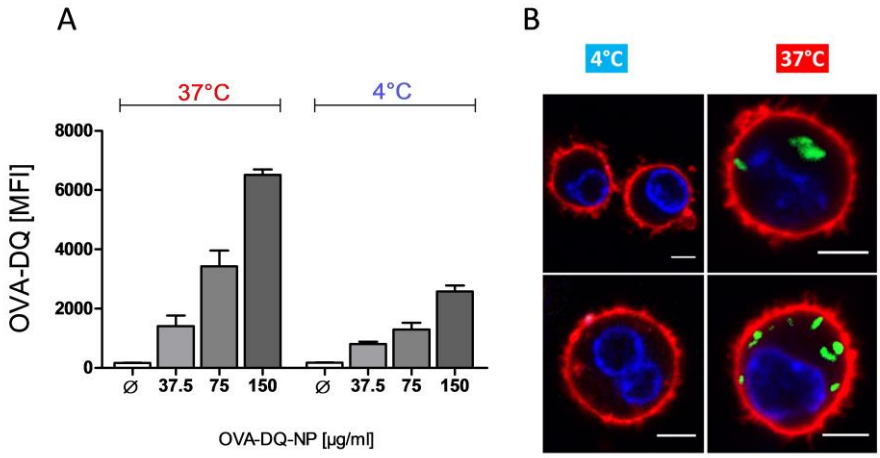

Figure 50: A: Bone marrow derived dendritic cells incubated with OVA-DQ PNCs at 4 °C and 37 °C, respectively. A: Mean fluorescence intensity (MFI) of DQ-ovalbumin degradation products measured by FACS. B: CLSM images thereof. Plasma membrane was stained with CellMask Orange (red), nuclei were stained with Hoechst 33342 (blue) and OVA-DQ PNCs were stained with DQ ovalbumin (green)). Measurements were performed by D. Paßlick.

Thus, protein nanocontainers are, despite their polymeric form, still recognized by proteases and prone to enzymatic degradation, being thereby suitable as biodegradable drug delivery vehicles.

2.1.9 Ovalbumin nanocontainers as adjuvant delivery systems

Aside from model drugs testing the PNC's encapsulation efficiency and degradation behavior, nanocontainers can be also loaded with actual active components. Therefore, two adjuvants were encapsulated in OVA PNCs. For the development of a nanoparticle-based vaccine, it is crucial for its effectiveness that a nanocontainer is able to carry all essential base components together, namely antigen and adjuvant. Especially the transport of adjuvants to the respective cellular receptors in this manner is beneficial since the adjuvants are usually not membrane permeable. Resiquimod (R848) used herein is an immunostimulant and is known to provoke an increased expression of certain dendritic cell surface proteins, which are essential for the mediation of T cell-based immune responses.[277] Muramyl dipeptide (MDP) is a peptidoglycan fragment with potent adjuvant activity.[278] The structures of both adjuvants are depicted in Figure 51.

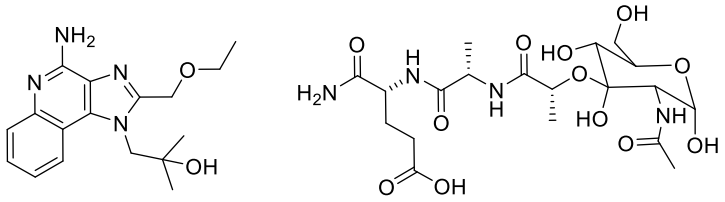

Figure 51: Structures of R848 (left) and MDP (right).

Four different PNC formulations were synthesized. All OVA-PNCs were loaded with the cy5 dye for imaging. The PNCs were further loaded with either R848 or MDP. Additionally, PNCs with both R848 and MDP encapsulated were prepared to enhance the efficacy of the adjuvants for inducing adaptive T cell responses due to synergistic effects.[279-280] OVA-cy5 PNCs without adjuvants served as the control. In Table 2, the size and zeta potential of the carriers is shown and the amounts of adjuvants used per synthesis. The molar amounts of adjuvants used differ since R848 is only soluble in DMSO and an equimolar amount to MDP would require the replacement of the water phase by DMSO resulting in the precipitation of OVA. Therefore, the maximum possible amount of DMSO, and thus R848, was used so that the other components of the aqueous phase remained soluble. This is not critical since R848 and MDP bind to different receptors in the cell and have thus different signaling pathways.[277, 281] An influence of the cargos on PNC size or stability was not observed. The PNCs with adjuvants were slightly larger after synthesis than the standard OVA-cy5 PNCs. After transfer to the aqueous phase however, this difference was evened out.

Table 2: Size and zeta potential of OVA PNCs used for adjuvants delivery.

Sample	Ø [nm] (PDI) in cyclohexane	Ø [nm] (PDI) in water	ζ [mV]	Amount of adjuvants used in synthesis [10^{-6} mol]
OVA-cy5	256 (0.16)	348 (0.47)	-26 ± 5	-
OVA-R848	331 (0.21)	335 (0.43)	-32 ± 6	2.23
OVA-MDP	268 (0.15)	404 (0.39)	-27 ± 6	5.08
OVA-MDP/R848	302 (0.21)	338 (0.13)	-31 ± 4	5.08 (MDP) / 2.23 (R848)

The core-shell morphology of the PNCs was confirmed by electron microscopy imaging. A representative image of the PNCs is shown in Figure 52.

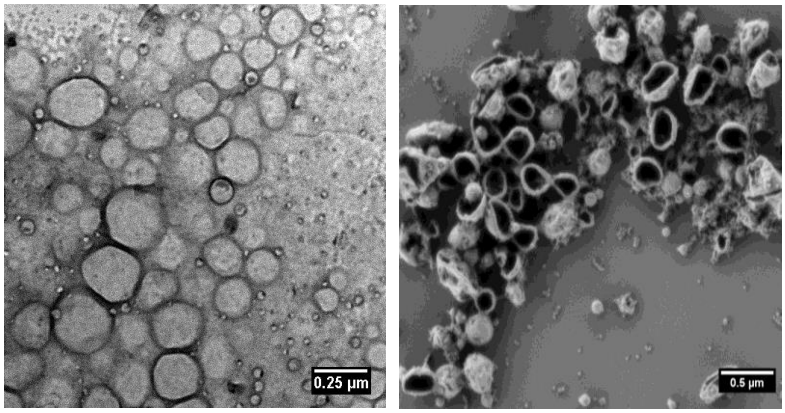

Figure 52: Transmission (left) and scanning (right) electron microscopy images of OVA-MDP/R848.

These results show that the loading of OVA-PNCs with multiple cargos is feasible and that they do not affect the formation of a core-shell morphology.

In the following, the biological impact of the adjuvants-loaded PNCs is described briefly. All biological experiments were carried out by D. Paßlick.

The OVA-PNCs were incubated with bone marrow derived dendritic cells (BMDCs) for 24 h. The stimulatory capacity of the adjuvants was evaluated based on surface activation marker expression, i.e. of cell surface proteins such as CD80 and CD86. This was determined by flow cytometry. To verify that the adjuvants were encapsulated and the results are not due to free adjuvants in the nanocontainer solution, the supernatants of the dispersion were examined as well. In Figure 53, the results are shown.

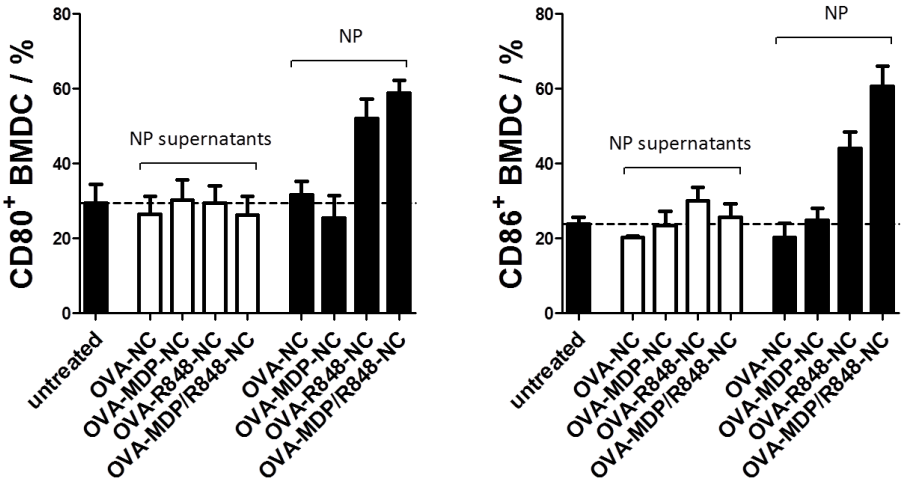

Figure 53: Assessment of the influence of adjuvants-loaded OVA-PNC on BMDCs by functional assay. To detect potential free adjuvants (MDP, R848) in the PNC dispersion, BMDC (2x105 cells) were treated both with different types of OVA-PNC (100 µg/ml) as indicated, and with their supernatants for 24 h. Afterwards, the frequencies of BMDCs positive for the maturation markers CD80 and CD86 were measured by flow cytometry. The results are displayed relative to the untreated control (mean ± SEM; n=2). The experiments were performed by D. Paßlick.

OVA-cy5 PNCs and the MDP-loaded PNCs showed no immunomodulatory effect on BMDCs, while OVA-R848 (50 and 100 µg/ml) led to a moderate upregulation of the surface markers. Compared to the OVA-PNCs with single adjuvants, the combination of MDP plus R848 in OVA-PNCs increased the expression of CD80 and CD86 in a superadditive manner. These results show that the capability of PNCs to be loaded with multiple cargos is of great advantage. This ability can be crucial for applications where combination medication is necessary.

The potential of OVA-MDP/R848 PNCs to stimulate efficiently BMDCs was also assessed by proinflammatory cytokine measurements. The supernatants of BMDC samples treated with OVA-MDP/R848 PNCs for 24h contained high concentrations of the pro-inflammatory cytokines IL-1β, IL-6, TNF-α, and IL-12 compared with unstimulated BMDCs and with BMDC that were treated with OVA-PNC formulations with single adjuvants loading (Figure 54). A strong upregulation of proinflammatory cytokines was observed with the co-delivery of both adjuvants by OVA-MDP/R848 PNCs.

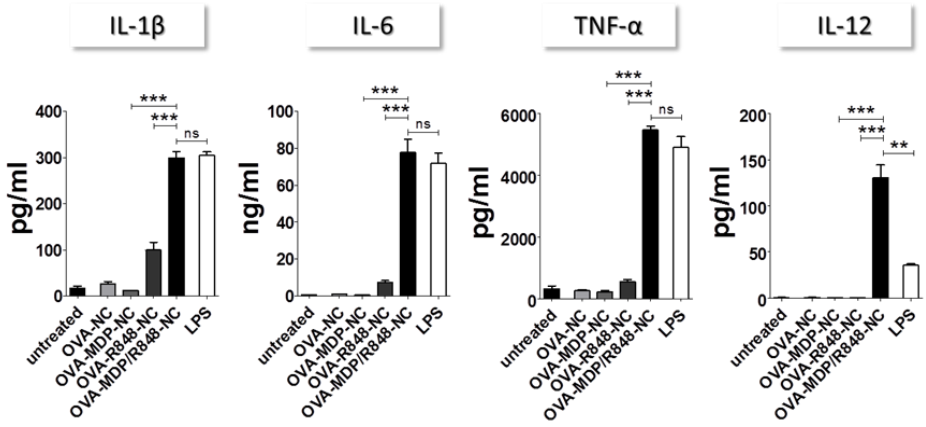

Figure 54: Upregulation of pro-inflammatory cytokines after stimulation with adjuvant-loaded ovalbumin-nanocontainers. BMDC (2x105 cells/mL) were incubated with differentially loaded OVA-PNC formulations (1-100 µg/mL) or LPS (100 ng/mL) as a control for 24h. Cytokine (IL-1β, IL-6, TNF-α, and IL-12) contents of differentially treated BMDC were analyzed by Cytometric Bead Array (CBA) (mean ± SEM; n=3). *p < 0.05, **p < 0.01, ***p < 0.001. All experiments were performed by D. Paßlick.

These results demonstrate the suitability of protein-based nanocontainers engineered to co-deliver adjuvants to induce adaptive T cell responses. The new delivery concept introduced herein has the perspective to develop multi-functionalized nanovaccines for DC-focused immunotherapy. Nanocarriers with a shell composed of tumor-related proteins and loaded with the adjuvant combination MDP/R848 may induce potent anti-tumor T cell responses as exemplified in this study.

2.1.10 Conclusion

Nanocontainers composed of albumin proteins were successfully synthesized using an inverse miniemulsion protocol. The PNCs have a dense shell and possess loading capabilities between 79-92% which were determined by encapsulation of the hydrophilic dye SR101 as model substance. PNCs subjected to human blood plasma showed no aggregation behavior. In order to determine the biodegradability, PNCs were treated with the serine protease trypsin. A successful degradation was observed through the release of fluorescent markers incorporated both in the PNC shell and in core. Importantly, PNCs were efficiently taken up by DCs, resulting in intracellular cleavage of PNCs and subsequent release of protein content. PNCs bear the potential for the application in vaccine development as a delivery system for both antigens and adjuvants. The method of synthesis is transferable to other proteins - a topic discussed in the following section.

2.2 Nanocarriers from hepatitis C virus for vaccination

In this section, the synthesis of polymeric nanocarriers exclusively composed of hepatitis C virus non-structural protein 5A (NS5A) is presented showing the versatility of protein nanocarriers: in contrast to the approach presented in section 2.1, here the container shell itself constitutes the drug. Its carrier function is at the same time exploited to co-deliver imaging agents and adjuvants. In the following, nanocarrier delivery to the liver as the primary organ affected by HCV infection, and the induction of intrahepatic immunity is discussed. The content has been previously published in the paper "Polymeric hepatitis C virus non-structural protein 5A nanocapsules induce intrahepatic antigen-specific immune responses" by Fichter, Piradashvili *et al.*, *Biomaterials* **2016**, *108*, 1-12. Adapted with permission from reference [282]. Copyright 2016 American Chemical Society. All biological experiments were performed by M. Fichter.

2.2.1 Motivation

The hepatitis C virus is a globally prevalent pathogen with over 185 million infected people worldwide.[283] About 50-80% of acute HCV infections become chronic, associated with the development of severe liver diseases including cirrhosis and hepatocellular carcinoma.[284] HCV infections and associated secondary liver diseases lead to 350,000 deaths per year.[285] The development of effective prophylactic vaccines against HCV remains a great challenge due to the extraordinary high degree of genetic diversity of HCV (cf. Figure 55), additionally diminishing the success of treatment approaches against chronic infections.[286]

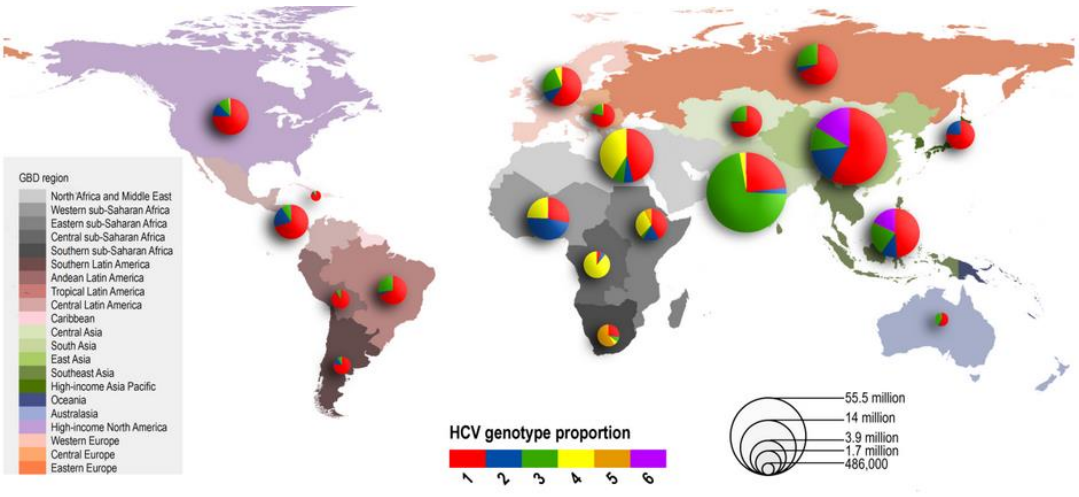

Figure 55: Relative prevalence of each HCV genotype by global burden of disease (GBD) region. Size of pie charts is proportional to the number of seroprevalent cases. Reprinted with permission from reference [283]. Copyright 2014 John Wiley and Sons.

Current standard care of treatment dramatically improved with the introduction of direct acting antivirals (DAAs) in 2011, increasing the efficacy with simultaneously lower adverse effects.[287] However, the costly treatment of DAAs, side effects and the risk of reinfection in regions with high prevalence of HCV (cf. Figure 55) is a major issue, especially for developing countries.[288] Additionally, the high mutation rates of HCV, promoting the development of DAA-resistant strains, show the urgent need for the development of a prophylactic vaccine against HCV.[289]

The induction of antigen-specific immunity in the liver is impeded by the extreme tolerogenicity of this highly immunological organ. Studies have shown that for an effective viral clearance strong and sustained $CD4^+$ and $CD8^+$ T cell responses towards HCV antigens are necessary.[290-291] Therefore, a targeted delivery of antigens to liver-resident antigen-presenting cells, such as dendritic or Kupffer cells, together with an adjuvant is a promising approach to induce intrahepatic T cellular immunity.

The HCV nonstructural protein 5A (NS5A), used in this study, is a critical component for HCV replication and involved in immune evasion modulating the physiology of the host cell.[286] NS5A-based immunogens for the development of vaccines against HCV have been subject of intensive research in recent years.[292-293] The induction of T cell-mediated immune responses by dendritic cell-based vaccination requires an efficient antigen loading of dendritic cells (DCs).[293] A promising approach for this purpose is the use of nanocarriers entirely composed of NS5A protein. NS5A nanocarriers (NS5A NCs) presented herein inherently provide a high antigen loading efficacy. Furthermore, NS5A NCs preferentially accumulate in liver DCs and Kupffer cells after intravenous administration. They enable a prolonged antigen presentation and can co-deliver DC maturation stimuli, such as the adjuvants monophosphoryl lipid A (MPLA),[294-295] promoting T_h1-directed immune responses. In contrast to polymeric nanocarriers with additional compounds as carrier scaffold, these nanovaccine formulations can avoid unintended side effects and unspecific immune responses caused by foreign carrier substances. In the present study, the potential of NS5A antigen nanocarriers to induce intrahepatic T cellular immunity *in vitro* and *in vivo* was evaluated in a mouse model.

2.2.2 NS5A nanocarrier synthesis

HCV NS5A expression was performed in the yeast *Pichia pastoris* with a total yield of approx. 50 mg and a purity of over 98% measured by SDS-PAGE and silver

staining. The amount of obtained protein enabled the synthesis of multiple batches of NS5A nanocarriers in course of the experiments, as only 6.25 mg were needed per synthesis. The amount of protein required for synthesis was scaled down compared to OVA-PNCs. Many experiments (for example, immunization with the nanocarriers) were conducted over several weeks. Therefore, to avoid difficulties due to ageing of the samples over time we decided to synthesize small batches upon need. However, each batch was analyzed thoroughly to ensure reproducibility before it was used for biological experiments.

Fluorescently labeled NS5A nanocarriers were synthesized in an inverse miniemulsion. The polyaddition reaction at the oil/aqueous nanodroplet interface of TDI with the NS5A protein resulted in hollow nanocarrier formation. The obtained core-shell morphology was confirmed by scanning electron microscopy (SEM) and transmission electron microscopy (TEM). Representative images are displayed in Figure 56. A slight swelling of nanocarriers after transfer into the aqueous phase occurred documented DLS (Table 3). Due to this swelling process, the carrier shell became softer and was less stable under high vacuum conditions than carriers from the cyclohexane phase leading to a more collapsed and flattened morphology in the SEM image of the aqueous phase (Figure 56C).

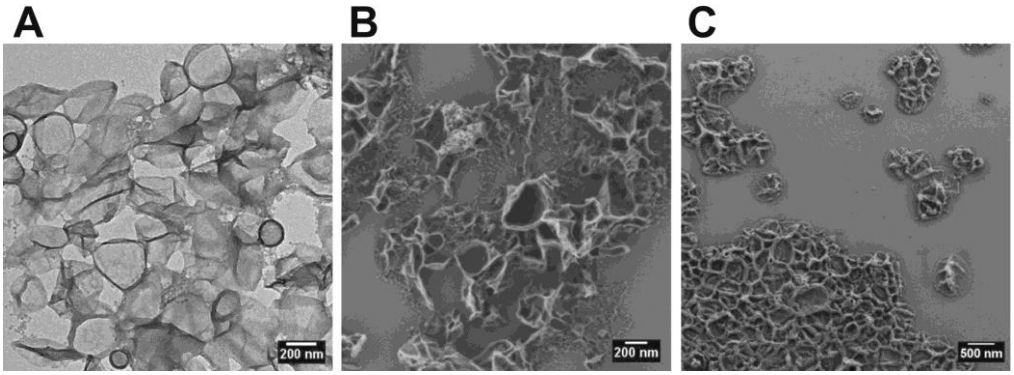

Figure 56: Characterization of NS5A-NCs by electron microscopy. (A) transmission electron microscopy (TEM) image of NS5A nanocarriers in cyclohexane phase, (B) scanning electron microscopy image (SEM) of nanocarriers in cyclohexane phase, (C) SEM image of nanocarriers from the aqueous phase.

Dynamic light scattering was used to determine the size of the nanocarriers. The cy5-labeled NS5A nanocarriers had an average diameter of 409 nm in the cyclohexane phase and 428 nm in the aqueous dispersion after purification (Table 3). No aggregation or flocculation was detected at any steps during synthesis and NCs remained stable at 4 °C under constant stirring.

Table 3: Characterization of NS5A nanocarriers.

Formulation	Size		ζ [mV]	Estimated percentage of	
	in cyclohexane [nm] / PDI	in H_2O [nm] / PDI		NS5A / OVA [wt-%]	MPLA [wt-%]
NS5A-NCs	409 / 0.32	428 / 0.15	-31 ± 7	16.0 ± 1.5	-
NS5A+MPLA-NCs	-	451 / 0.22	-39 ± 7	-	0.66 ± 0.12
OVA-NCs	324 / 0.24	408 / 0.55	-32 ± 6	36.5 ± 0.9	-

Residuals of the negatively charged anionic surfactant, used for stabilization during the transfer of the nanocarriers from the organic to the aqueous phase, accounted for the negative zeta potential of -31 mV. The amphiphilic MPLA was adsorbed onto the nanocarriers in defined quantities. A loading capacity (LC) with MPLA of 0.66 wt-% was documented using a limulus amebocyte lysate assay. This finding is comparable to a LC of up to 0.86% after incorporation of MPLA in PLGA nanoparticles as reported recently.[296] MPLA adsorption resulted in a slight size increase of the NCs from 428 nm to 452 nm and in a decrease of zeta potential due to the phosphate moiety of MPLA molecules. Nanocarriers based on ovalbumin (OVA) were synthesized as described in section 2.1 and applied as negative control in immunization studies.

2.2.3 Toxicity of NS5A nanocarriers

The prepared nanocarrier formulations showed no significant toxicity profile even at concentrations of up to 100 µg/mL (Figure 57).

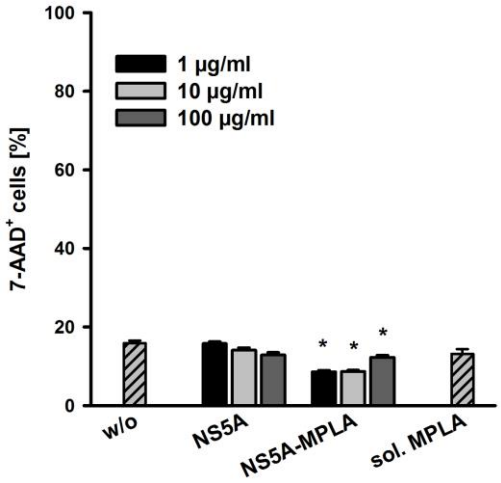

Figure 57: Toxicity of NS5A nanocarrier formulations was documented by 7-AAD-staining and subsequent flow cytometric analysis. NPCs were coincubated with NS5A- or NS5A+MPLA-NCs at different concentrations (1, 10, 100 µg/mL) for 24 hours. Data represent the mean ± SD of four independent experiments conducted with n = 3. All conditions were compared to the negative control (without stimulation) and significance was given with $P < 0.05$ (*) (One way ANOVA). The measurements were performed by M. Fichter.

This finding indicates that sufficient removal of potentially toxic residual substances, needed during synthesis and redispersion, took place. Mice injected with NS5A-NCs developed no clinical symptoms at all, whereas application of MPLA-coated NCs was accompanied by a mild fatigue with a short duration of about 2 h. This observation corresponds to slightly increased side effects observed for the MPLA-supplemented hepatitis B virus vaccine (Fendrix®).[297]

2.2.4 NC uptake *in vitro*

In order to enhance the frequency of dendritic cells in the liver, mice were pre-treated with a plasmid encoding the human Fms-like tyrosine kinase 3 ligand (hFlt3l). Uptake of NS5A nanocarriers by non-parenchymal liver cells (NPCs) derived from hFlt3l-treated mice was evaluated by two methods. First, confocal laser scanning microscopy (CLSM) verified intracellular uptake of NCs by phagocytosis excluding adhesion to the cell membrane. Figures 58 A and B clearly document the intracellular localization of cy5-labeled NS5A nanocarriers (red) after cocultivation with NPCs for 3 h *in vitro*. None of the analyzed cells displayed signs of plasma membrane adherence. Internalized NCs displayed a dense fluorescence signal and seemed to be localized in the endo-lysosomal compartment.

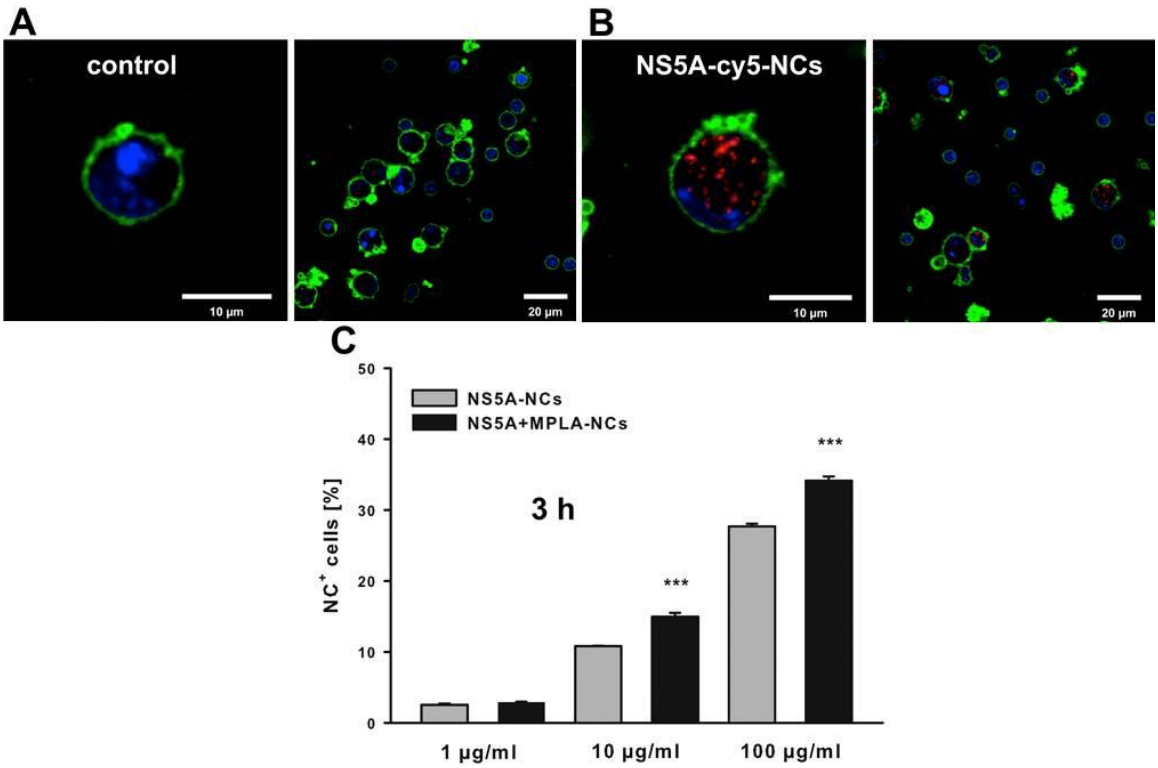

Figure 58: **(**A, B) Confocal laser scanning microscopy was performed in order to document the uptake of NS5A-NCs (red) by NPCs (B). Cells incubated without nanocarriers served as negative control (A). Plasma membrane was stained with CellMask Orange (green) and nuclei were stained using Hoechst 33342 (blue). (C) Flow cytometric analysis was performed to quantify the uptake of different concentrations (1, 10, or 100 µg/mL) of NS5A- or NS5A+MPLA-NCs by NPCs after 3 h of coincubation. Data shown in Figure 58 C are expressed as mean ± SD representing five independent experiments conducted with n = 3. Comparisons between NS5A- and NS5A+MPLA-NCs were performed using a non-paired Student's t-test. Significance was given with $P < 0.01$ (**); $P < 0.001$ (***).The measurements were performed by M. Fichter.

Flow cytometric analysis revealed a concentration-dependent increase in NC^+ NPCs from 2.5% to 27.7% by incubation with 1 µg/mL or 100 µg/mL for 3 h, respectively (Figure 58C). Prolonged incubation up to 24 h did not significantly augment the percentage of NC ingesting NPCs in comparison to the 3 h incubation period (data not shown), probably due to a phagocytic saturation after 3 h of incubation. Surface modification of NS5A-NCs with MPLA induced a significantly enhanced uptake for NC concentrations of 10 µg/mL and 100 µg/mL from 10.8% to 15.0% and 27.7% to 34.1%, respectively. These findings agree with several studies describing the importance of combining antigens along with adjuvants in nanoparticle-based immunization approaches.[298-301]

2.2.5 *In vivo* uptake of nanocarriers in the liver

A beneficial *in vivo* uptake of nanocapsules was reported after surface-functionalization with MPLA.[260] Therefore, the deposition of NS5A nanocarrier formulations with and without MPLA in the liver was evaluated after intravenous injections.

For nanocarrier visualization *in vivo*, the use of infrared fluorescent dyes are of advantage since in the near infrared region the autofluorescence of tissue and organs is low and thus the signal-to-noise ratio is higher.[302] Therefore, the IRdye 800 CW with λ_{ex} = 778 nm, λ_{em} = 794 nm was used. To find the optimal amount of dye for encapsulation to be detectable via the IVIS SpectrumCT imager, OVA nanocarriers were used for evaluation. In Table 4, the synthesized OVA-PNCs are shown. 19.3 nmol of IR dye used for OVA-IR1 corresponds to the amount of cy5 dye used for the visualization of cellular uptake. As shown in Figure 59, this is also the optimal concentration to be detectable by the IVIS SpectrumCT imager. A higher concentration does not enhance the radiant efficiency possibly due to quenching effects also reported in literature.[303] Thus, for NS5A nanocarriers the amount of IR dye used for OVA-IR1 was chosen and adjusted according to the synthesis on small scale.

Table 4: OVA-PNCs loaded with different concentrations of IRdye 800 CW.

Sample	Amount of dye/synthesis [nmol]	Ø [nm] (PDI) after synthesis
OVA-IR1	19.3	250 (0.12)
OVA-IR2	38.6	275 (0.25)
OVA-IR3	9.6	345 (0.25)
OVA-IR4	4.8	425 (0.23)

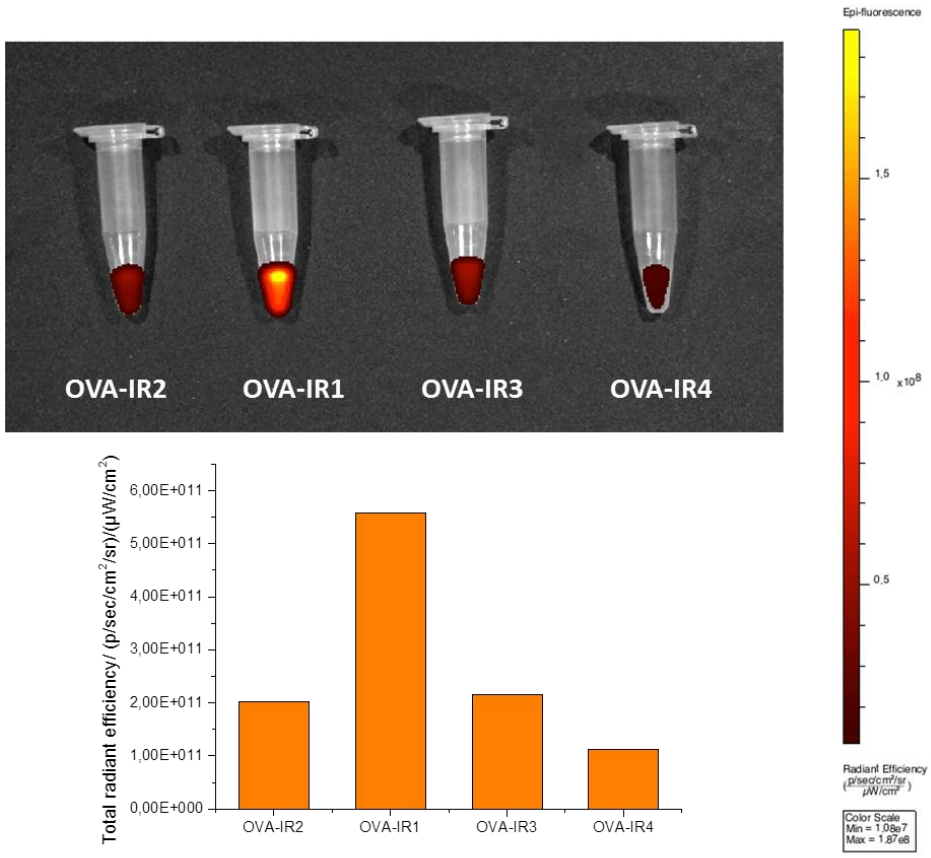

Figure 59: Fluorescence intensity of OVA PNCs loaded with IRdye 800 CW recorded by the IVIS SpectrumCT imager. The measurement was performed by M. Fichter.

In vivo imaging analysis was performed at different time points following intravenous administration of NS5A- or NS5A+MPLA-NCs. In Figure 60A and C a preferential deposition of nanocarriers in the liver can be seen.

Ex vivo imaging of organs isolated 4 h after NC injection confirmed an almost exclusive accumulation of both NC formulations in the liver, while a very weak signal was observed originating from the spleen (Figure 60B). Quantification of fluorescence intensities originating from isolated liver revealed a significant increase in NC accumulation of approx. 37% after functionalization with MPLA (Figure 60D). In the lung, no accumulation of NCs was detectable.

As can be seen in Figure 60E, intracellular cytokine staining of NPCs after intravenous administration of NS5A+MPLA-NCs showed an increase in IL-12p70^{+}, IL-6^{+}, and in double positive CD11c^{+} NC ingesting cells in comparison to the application of NS5A-NCs without adjuvant. This is an essential prerequisite for the induction of intrahepatic cellular immune responses.

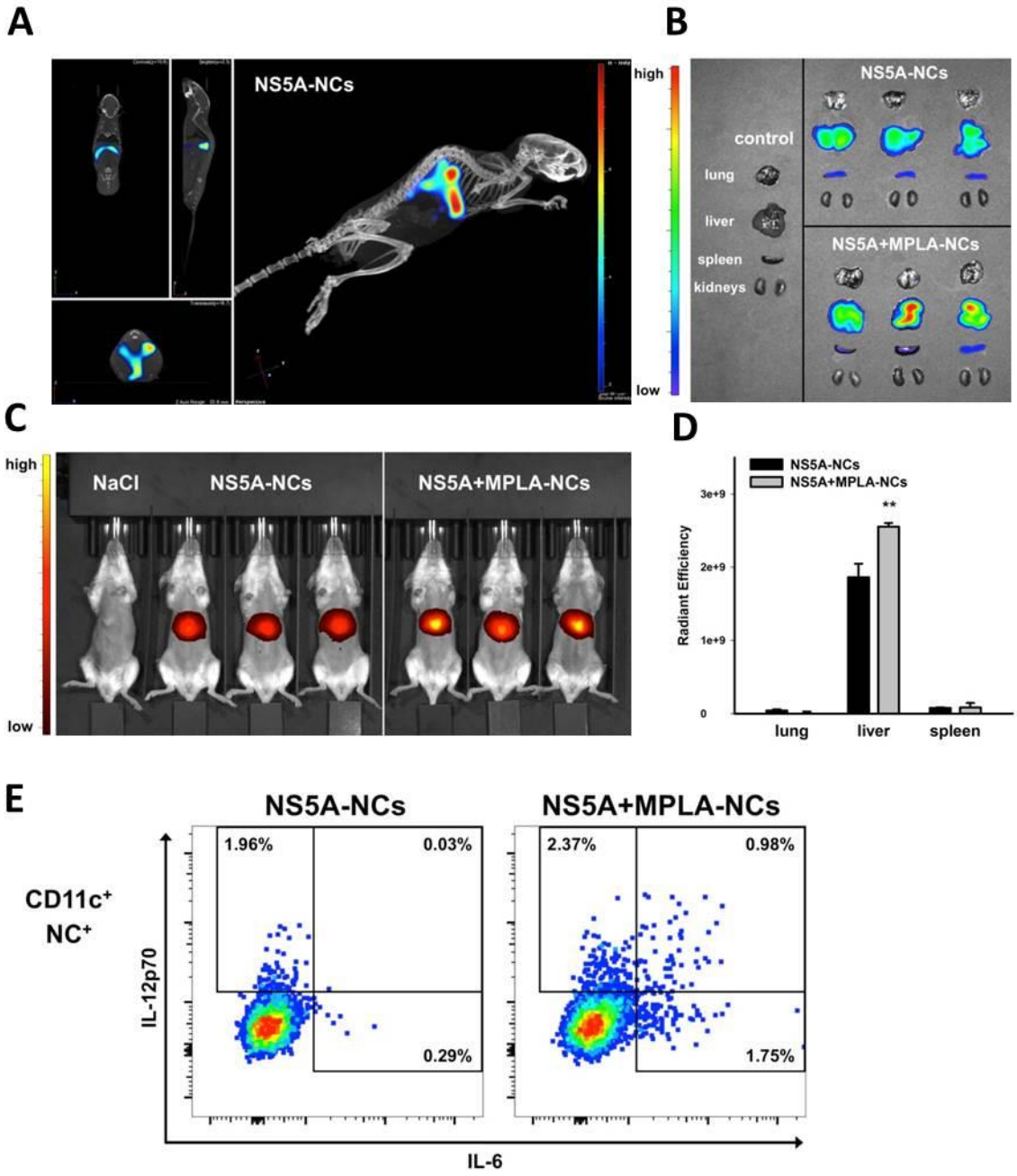

Figure 60: *In vivo* imaging of NS5A- and NS5A+MPLA-NCs labeled with IRdye 800CW was performed at different time points (30 min / 1 h / 2 h / 3 h / 4 h) after intravenous injection into B6N-Tyrc-Brd/BrdCrCrl albino mice (n = 3). Comparisons between NS5A- and NS5A+MPLA-NCs were performed using a non-paired Student's t-test and significance was given with $P < 0.05$ (*). (A) representative image of an albino mouse 4 h after injection of NS5A-NCs analyzed using fluorescence intensity tomography and 3D reconstruction. Coregistration of bones and fluorescence signals are depicted. (B) epi-illumination image of mice 4 h after NC injection. (C, D) *ex vivo* imaging of isolated organs 4 h after NC injection. Comparisons between NS5A- and NS5A+MPLA-NCs were performed using a non-paired Student's t-test and significance was given with $P < 0.01$ (**). (G) intracellular cytokine staining of IL-12p70 and IL-6 after intravenous administration of NCs and flow cytometric analysis of CD11c+ NC+ NPCs. Cells were isolated 4 h after injection and additionally incubated with GolgiPlug for 16 h prior to analysis. Representative dot plots are shown. The measurements were performed by M. Fichter and G. Kuhn.

2.2.6 Immunization with NS5A-NCs

Evaluation of anti-HCV NS5A immune responses was based on previous studies demonstrating that the resolution of HCV is accompanied with intrahepatic T_h1-directed immune responses. The focus of this study was the evaluation of cellular immune responses localized in the liver. Hence, concentrations of IFNγ and IL-2 were measured in culture supernatants of NPCs isolated from livers of immunized mice following stimulation with different concentrations of NS5A. Figure 61 A and B shows an increase in IL-2 and IFNγ secretion by NPCs derived from livers of mice that were vaccinated with NS5A+MPLA-NCs. Additional adjuvant supplementation with αCD40 further enhanced this effect. The immunization with OVA+MPLA-NCs, serving as an antigen control, did not induce any significant cytokine secretion. Splenocytes isolated from immunized mice displayed a similar pattern in terms of IFNγ secretion (Figure 61C). NS5A-NCs without adjuvant showed a slight, concentration-dependent increase in IFNγ and IL-2 levels. The secretion of IFNγ and IL-2 in the absence of IL-4 after restimulation with NS5A suggests the induction of a T_h1-directed immune response.

These findings were confirmed by intracellular cytokine staining represented by an elevated frequency of IFNγ-producing NPCs from 0.03%, 0.15%, and 0.05% up to 0.44% (NS5A-NCs), 0.54% (NS5A+MPLA-NCs), and 0.47% (NS5A+MPLA-NCs + αCD40), respectively (Figure 61D).

In order to determine humoral immune responses, serum titers of NS5A-specific antibodies were measured (Figure 61E). Immunization with MPLA-adjuvanted NS5A-NCs led to a substantial production of antigen-specific antibodies, while NS5A-NCs without MPLA or OVA+MPLA-NCs did not induce considerable titers.

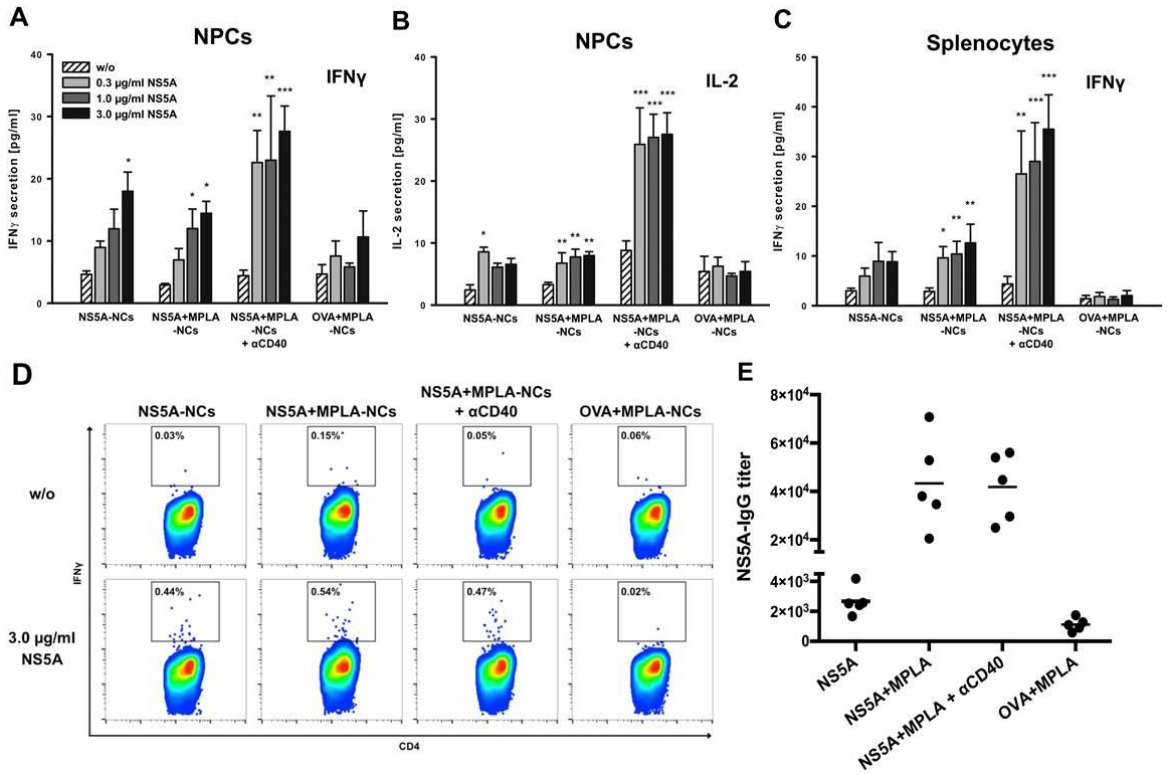

Figure 61: NPCs and splenocytes obtained from mice immunized three times with different NC formulations were cultured with recombinant HCV NS5A at indicated concentrations. (A-C) Culture supernatants were collected after 24 h; IFNγ and IL-2 concentrations were quantified by an enzyme-linked immunosorbent assay. (D) NPCs were cultured for a total of 16 h, in the presence of GolgiPlug during the last 4 h, following intracellular cytokine staining of IFNγ and flow cytometric analysis. (E) Antibody responses were evaluated after serum collection from immunized mice. NS5A-specific antibody titers were determined using an enzyme-linked immunosorbent assay. Data represent the means ± SD derived from five mice. All conditions were compared to the negative control (without stimulation) or to the OVA+MPLA-NCs group for antibody responses and significance was given with $P < 0.05$ (*), $P < 0.01$ (**), $P < 0.001$ (***) (One way ANOVA). The measurements were performed by M. Fichter.

2.2.7 Conclusion

In this proof-of-concept study, polymeric nanocarriers synthesized exclusively of the HCV-specific NS5A antigen and functionalized with the adjuvant MPLA proved the capability to target liver-resident antigen-presenting cells leading to their efficient maturation and activation. The induction of intrahepatic cellular immunity and humoral responses after immunization provides the basis for the development of vaccines tackling liver-associated pathogens such as hepatitis C virus or Malaria parasites.

2.3 Dexamethasone nanocarriers

The synthesis of nanocarriers composed of and loaded with the pharmaceutical drug dexamethasone is discussed in this section. Based on the results presented in the previous section, our aim was to compose a drug delivery vehicle where the drug is both cargo and carrier. In this manner, additional carrier substances potentially interfering with the mode of action of the drug and causing immunological effects by themselves could be avoided.

2.3.1 Motivation

Dexamethasone is a synthetic glucocorticoid with anti-inflammatory and immunosuppressive properties. A systemic administration of dexamethasone results in severe adverse effects such as hypertension, gastrointestinal perforation, an enhanced risk of gastric ulcer, and psychological diseases.[304-306] A targeted delivery of this compound to cell lines regulating inflammation bears the potential to avoid or minimize these side effects. For this purpose, the encapsulation of dexamethasone in polymeric nanocarriers has been studied by many research groups. Dexamethasone was encapsulated in PLGA microparticles,[307] liposomes,[308] and by our group into hydroxyethyl starch nanocapsules.[309] Based on these promising results *in vitro* we decided to pursue this topic towards *in vivo* experiments by using nanocarriers composed of dexamethasone with no additional carrier material. To exclude unintended immune responses we wanted to omit the use of proteins or other biodegradable polymers.

2.3.2 Dexamethasone nanocarrier synthesis

Dexamethasone is not soluble in water. For the nanocarrier synthesis in miniemulsion as described in section 2.1.2 with TDI as the cross-linker, we decided to use a water-ethanol mixture as the aqueous phase. However, to find the right ratio of water to ethanol for the dexamethasone not to precipitate during synthesis turned out to be challenging and no nanocarriers were obtained (Figure 62). The resulting structures are due to phase separation and precipitation during synthesis.

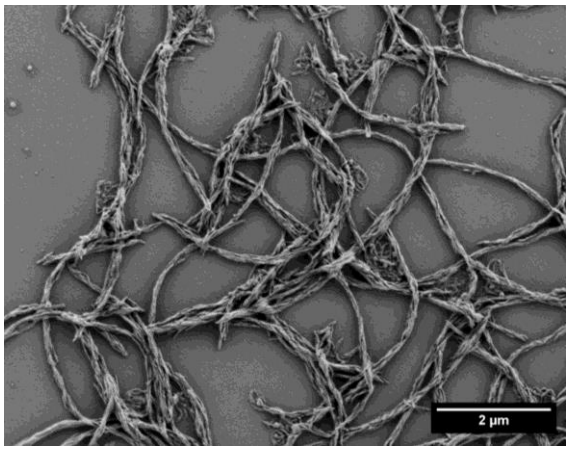

Figure 62: SEM image of dexamethasone sample synthesized in miniemulsion with water/ethanol mixture for the aqueous phase.

For this reason, we decided to change to a water-soluble dexamethasone derivative, the dexamethasone 21-phosphate disodium salt (Figure 63) which is also commercially available as Fortecortin®. Dexamethasone 21-phosphate disodium salt (DXM) is a prodrug and is converted to dexamethasone in the body by enzymatic cleavage of the phosphate ester.[310-311] For the polyaddition reaction with TDI at the interface, the molecule has only two hydroxyl groups, a secondary and a tertiary alcohol (depicted in red), which are far less reactive than primary alcohols or amines. Compared to proteins, DXM is thus less suitable for cross-linking with TDI and has a much lower molecular weight. The results of this circumstance will be discussed in subsection 2.3.3.

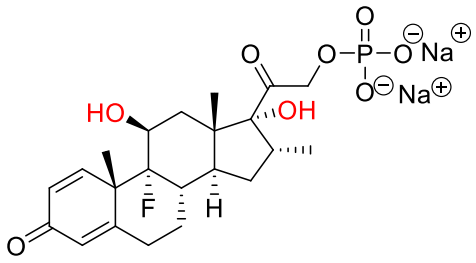

Figure 63: Structure of dexamethasone 21-phosphate disodium salt (DXM).

Surface tension measurements showed that DXM is surface active (at a concentration of 25 mg/mL in water the surface tension at 20 °C is γ = 58 mN/m cf. literature value[312] for water: γ = 72 mN/m) and despite the poor prerequisites regarding the structure, stable nanocarriers with core-shell morphology were formed (Figure 64).

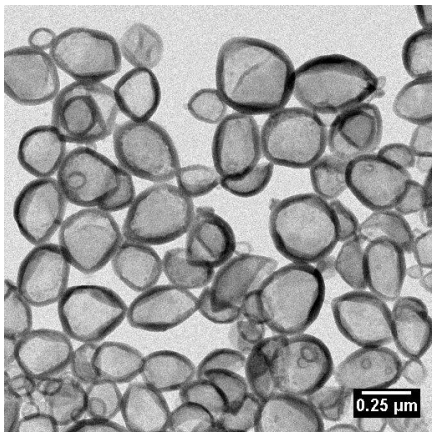

Ø [nm] (PDI) in cyclohexane	Ø [nm] (PDI) in water	ζ [mV]
335 (0.13)	405 (0.43)	-46 ± 13

Figure 64: TEM image of DXM-nanocarriers, their average size determined by DLS and zeta potential.

The negative zeta potential after purification in this case is predominantly caused by the negatively charged phosphate group of DXM. It was tried to transfer the DXM nanocarriers to the aqueous phase without SDS for stabilization. While the stability of the dispersion was not satisfactory and agglomeration occurred, the zeta potential was with -41 mV ± 9 mV in the same range as with the usual transfer procedure with SDS. A successful removal of excess SDS was verified by the stains-all assay described in section 2.1.3 (cf. experimental part).

In contrast to the reported procedure, [309] equimolar amounts of TDI can be used respective to the two hydroxyl groups of DXM. In this case, no isocyanate stretching vibration at 2274 cm^{-1} is detected by IR spectroscopy measurements after synthesis (Figure 65, cf. DXM-10 vs. DXM-13). Thus, the isocyanate groups are mostly converted to urethane linkages over time (and urea, due to reaction of TDI with itself, which cannot be excluded).

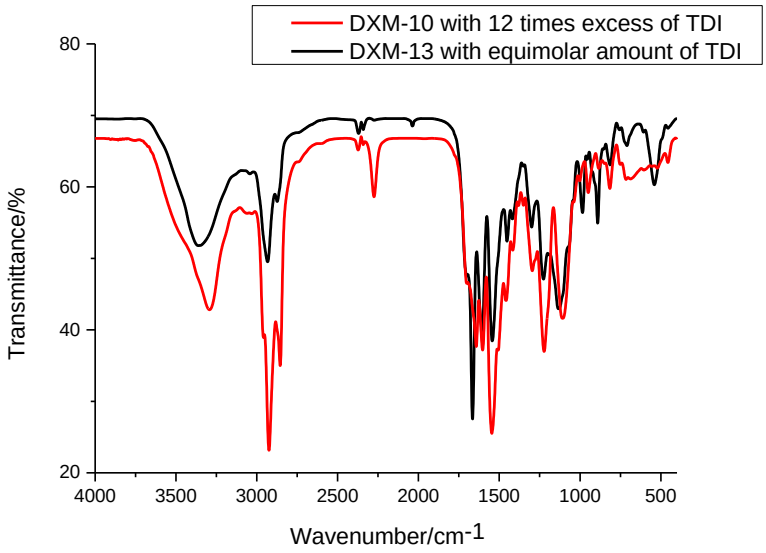

Figure 65: FT-IR spectrum of DXM nanocarriers with excess TDI synthesized as reported in literature (in red)[309] and with equimolar amounts of TDI respective to the hydroxyl groups of DXM (in black).

2.3.3 Dexamethasone quantification

To examine the biological impact of DXM-nanocarriers knowledge of the amounts of encapsulated and free dexamethasone in the nanocarrier dispersion as well as the dexamethasone amount incorporated in the shell is crucial. Furthermore, it is important to know whether the nanocarrier shell itself can have an influence on the results, i.e. if the polymerized DXM is involved in the metabolism.

In the beginning, a quantification of soluble DXM in the nanocarriers was challenging. DXM absorbs at 240 nm in the UV/vis spectrum. At this wavelength, the absorbance of TDI is present as well, preventing a quantification of DXM via this method. Next, we thought to use ^{31}P-NMR but the samples were not concentrated enough for these measurements. Finally, HPLC was applied for quantification. Both, supernatants obtained during nanocarrier purification as well as the filtered solution from the nanocarrier dispersion were examined. As depicted in Figure 66, the largest amount of soluble DXM is detected in the supernatant from the first purification step and a low amount in the purified nanocarrier dispersion used for biological analysis.

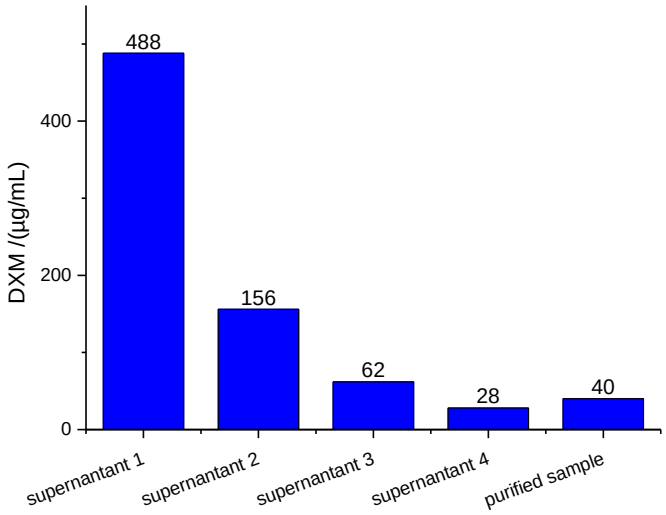

Figure 66: DXM amounts determined via HPLC in nanocarrier dispersion and in its supernatants obtained during purification.

It has to be noted that from this measurement set-up it is not clear whether the soluble DXM from the nanocarrier dispersion detected by HPLC is outside the nanocarriers or inside and released when the dispersion is filtered prior to analysis. DXM-nanocarriers cannot be degraded by trypsin like protein nanocontainers to release their content. Therefore, after synthesis and transfer to water, ultrasound was applied on the DXM-nanocarriers to break the shell. Figure 67 shows DLS measurements of the sample before and after treatment with ultrasound.

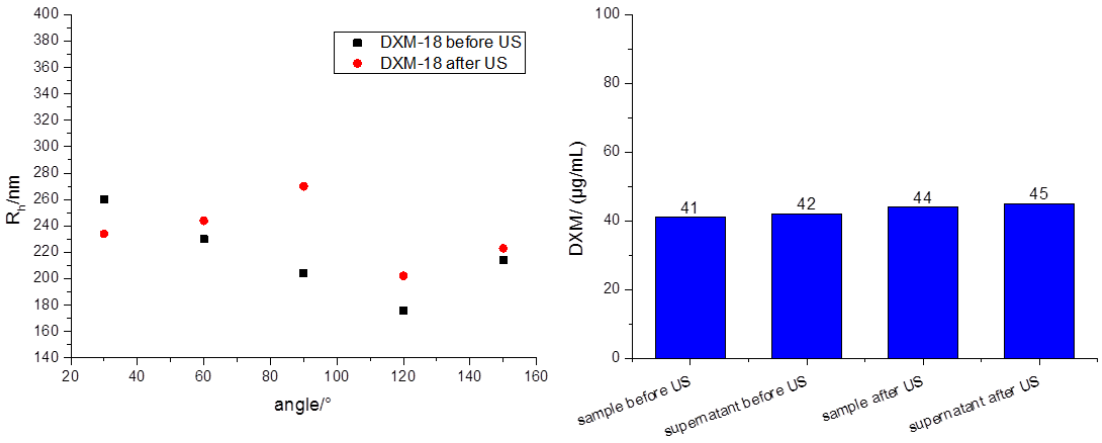

Figure 67: *left:* Hydrodynamic radii of DXM-nanocarriers before and after treatment with ultrasound determined by DLS. *Right:* DXM quantification via HPLC for DXM-nanocarriers and their supernatants before and after ultrasound treatment.

As can be seen, there is no difference in size before and after ultrasound treatment. DXM quantification via HPLC showed also no significant difference in the detected DXM amounts before and after ultrasonification (Figure 67, *right*). Furthermore, it can be seen

that the DXM amount in the supernatants of these samples is the same as in the nanocarrier dispersion. Thus, we can conclude that although the nanocarriers are very stable against breakage via ultrasound, their shell is not dense enough and they have poor encapsulation efficiency. These findings are in accordance to the consideration in the beginning. Neither has DXM enough functional groups for multiple cross-linking points nor has it a high molecular weight to form a dense shell. Due to the premature leakage of DXM from the core, these nanocarriers show the same adverse effects as with intravenous application of soluble DXM. Exemplarily, this is shown on the examination of the thymus weight after repeated administration of both soluble DXM and DXM nanocarriers over 10 days in mice. Systemic administration of corticosteroids leads to a decrease of the thymus weight,[313] observed in this case for both systems (Figure 68).

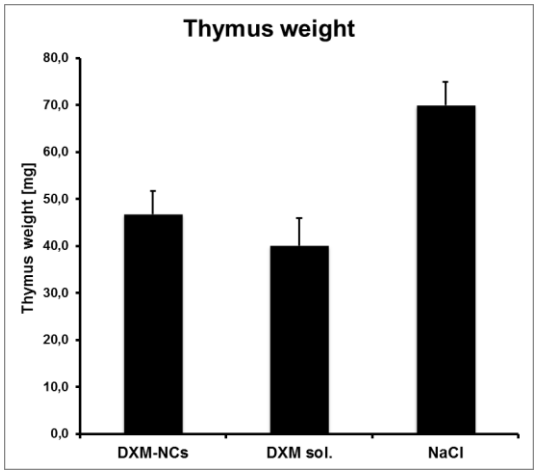

Figure 68: Thymus weight after administration of soluble DXM and DXM nanocarriers in mice for 10 days. Administration of NaCl served as the control. These experiments were performed by M. Fichter.

Although it was assumed that the polymerized DXM-nanocarrier shell is not biologically active, this had to be verified. Therefore, full (nano)particles were synthesized from the polymerized DXM-nanocarrier shell material by the solvent evaporation method.[314] In this case, a direct miniemulsion is generated, i.e. with an aqueous solution as the continuous phase. The dispersed phase is composed of an organic solvent, here chloroform, in which the polymer should be well dissolved. Upon heating, the organic solvent starts to evaporate and with the polymer being insoluble in water, it precipitates at the oil/water interface forming spherical particles. In Figure 69, SEM-images of these particles are presented. As shown in the inset, spherical microparticles were formed from agglomerated hollow nanocarriers. The remaining nanocarrier morphology is still

observable. Thus, the polymeric nanocarriers were not fully dissolved in chloroform but merely swollen by the organic solvent.

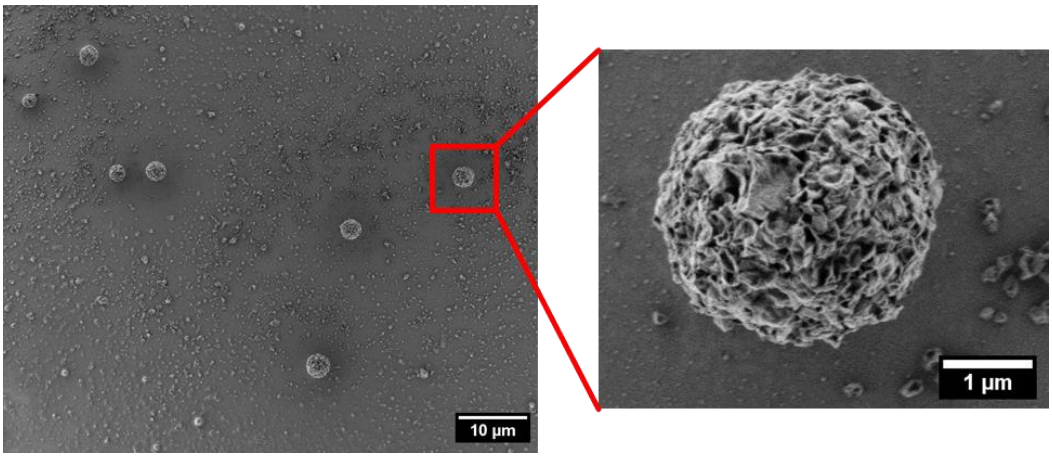

Figure 69: SEM image of DXM-particles obtained by solvent-evaporation. From the inset the remaining morphology of the nanocarriers forming the particles is observable.

Analysis of the dispersion regarding the DXM content via HPLC revealed a residual DXM amount of 0.68 µg/mL. As expected, these particles were not biologically active. Thus, only the soluble DXM is responsible for the biological response and not the polymerized DXM-shell material.

2.3.4 Conclusion

The results of this section showed that a synthesis of hollow nanocarriers out of the pharmaceutical drug dexamethasone by the polyaddition reaction with TDI in miniemulsion is feasible. Thus, the use of additional substances for the formation of the drug delivery vehicle could be avoided. However, a quantification of the free DXM amount present in the nanocarrier dispersion revealed a poor encapsulation capacity compared to protein nanocontainers. Although stable nanocarriers were obtained, the carrier shell was not dense enough to prevent leakage of soluble DXM from the core. This resulted in systemic side effects upon *in vivo* application similar to an administration of soluble DXM. In conclusion, for a successful nanocarrier formation, the molecule intended as carrier material should ideally have both a high molecular weight and multiple functional groups suitable for cross-linking. Therefore, in case of DXM, the use of other carrier substances should be considered. They provide good encapsulation efficiency and, in case of the proteins, a good degradation profile. Drug delivery to the targeted cell lines can be achieved avoiding both the side effects of soluble DXM and a potential accumulation of the polymeric DXM-shell material in the body.

2.4 Photoclick tetrazole-ene chemistry for protein nanocarriers allows the survival of functional antitumor drugs

As we have seen in the previous sections, TDI is a powerful cross-linking agent for nanocarrier formation by reaction with nucleophilic groups of the carrier material. However, the encapsulation of sensitive drugs retaining their bioactivity by this method can be challenging since TDI does not react selectively and can cross-link the cargo as well. In general, the encapsulation of biomolecules as pharmaceuticals and their selective release is a challenging topic in current drug delivery design. As pointed out in section 1.2.2, established protocols following bioorthogonal approaches mostly rely on metal-catalyzed reactions to build the primarily synthetic vehicles.

Triggered by light, the mild tetrazole-ene cycloaddition enables the preparation of protein nanocarriers (PNCs) preserving at the same time the bioactivity of sensitive cargos. This catalyst-free reaction was designed to take place at the interface of aqueous nanodroplets in miniemulsion to produce self-fluorescent, core-shell PNCs with over 90% encapsulation efficiency.

Together with the thorough colloidal analysis of the PNCs, their stability in human blood plasma and the detailed protein corona composition, these results underline the high potential of such naturally derived drug delivery vehicles.

Parts of this section have been submitted for publication.

2.4.1 Motivation

Bioorthogonal chemistry is an efficient strategy for selective protein labeling, polymer conjugation, and surface modification.[187, 213, 225] In this study, the bioorthogonal 1,3-dipolar tetrazole-ene cycloaddition chemistry was used for the interfacial cross-linking reaction to synthesize biodegradable nanocarriers out of naturally occurring proteins for drug delivery.

For the application of nanocarriers for biomedical purposes, it is essential that the shell material is biocompatible and degradable within the body without producing toxic side products. Many polymers used for this purpose fulfill the first aspect but often fail for the latter.[315-316] Therefore, proteins from the abundant albumin family can be advantageous over synthetic materials since the body is acquainted with processing these substances which make them ideal for degradable drug delivery vehicles.[6, 317-318]

Hollow nanocarriers have furthermore the advantage to protect the payload from the outer environment, and they can be designed to release their cargo with certain stimuli, such as pH, temperature, enzymes or redox potential.[21, 319-323] Hollow nanocarriers are most frequently synthesized by forced polymerization at the droplet's interface in miniemulsion.[17] Successful nanocarrier formation in inverse miniemulsion has been reported by reactive, but rather unselective compounds such as isocyanates[170, 183] making the encapsulation of biopolymers, due to unwanted side reactions, difficult.

Thus, these kinds of reactions do not allow the encapsulation of sensitive biological cargos such as enzymes, siRNA, or proteins, since the electrophilic isocyanates will react with the payload and eventually deactivate it partially or completely. An attractive strategy for successful encapsulation of biomolecules and therapeutic substances is the application of bioorthogonal chemistry.[187, 210, 324] Ruthenium-catalyzed olefin cross-metathesis[207, 232] and copper-catalyzed azide-alkyne interfacial click reaction[227] have been reported as bioorthogonal and mild alternatives to isocyanates for the preparation of nanocarriers. Nevertheless, these reactions depend on the use of potentially toxic transition metal catalysts.

In the class of bioorthogonal reactions, the tetrazole-ene 1,3-dipolar cycloaddition between a diphenyltetrazole and a dipolarophile, reported first by Huisgen in 1967,[215] stands out. In recent years, this method was established as an efficient bioorthogonal ligation technique by Lin and coworkers and termed "photoclick-reaction", since it is induced by UV-light.[198, 216, 223] Irradiation with a low-powered UV-lamp is sufficient for the diaryltetrazole to undergo a cycloreversion, releasing nitrogen and generating a nitrile imine dipole, which readily reacts with an olefin as dipolarophile.[223] The tetrazole-ene cycloaddition is claimed to be one of the fastest bioorthogonal reactions, which is an ideal prerequisite for an interfacial reaction.[224] In addition, it proceeds at ambient conditions (in water, at physiological pH, at room temperature), does not require metal catalysts and yields a fluorescent product.[226, 325]

In this work, instead of simple protein ligation, the tetrazole chemistry and the proteins ovalbumin (OVA) and human serum albumin (HSA) were exploited for the preparation of hollow nanocarriers. The proteins were modified with tetrazole groups (acting as A_n-type monomer) and for cross-linking, a difunctional oil-soluble norbornene derivative was chosen as the B_2-type monomer, due to the high reactivity of the strained olefins.[326] The encapsulation of a hydrophilic compound into the non-toxic protein nanocarriers (PNCs) was proven to be efficient (encapsulation efficiency 91%).

Furthermore, the PNC interaction with human blood plasma and the proteolytic degradation are shown. Due to the self-fluorescence of the pyrazoline product, experiments for cellular uptake of the PNCs were performed without the need of an additional fluorophore. To verify that the PNCs are taken up by dendritic cells and degraded intracellularly, resiquimod (R848) was encapsulated. R848 is an immunostimulant which has antitumor and antiviral properties (structure cf. Figure 51).[277]

As the receptor for R848 is located in the endosomes of dendritic cells, an upregulation of the surface proteins, like CD86, after stimulation with the R848-loaded nanocarriers indicates their successful uptake and release from the PNCs with a preserved functionality of R848. The results for the survival and intracellular release of an active drug makes the PNCs synthesized by the light-triggered tetrazole-chemistry a general platform for the design of new drug delivery vehicles.

2.4.2 Tetrazole synthesis

Upon irradiation with UV-light, tetrazole derivatives release nitrogen and then react with olefins.[217, 222] In dependence on the side groups, the tetrazoles show an enhanced or decreased reactivity towards double bonds. For example, the introduction of electron donating substituents such as methoxy groups or amines in the aromatic ring in the para position leads to rate acceleration due to lifting of the HOMO of the dipole.[218] However, the availability of the compounds, ease of synthesis and most importantly, of further modifications should be considered. For the synthesis of the 2,5 disubstituted tetrazole, two different synthesis methods found in literature were considered. The classical pathway, developed in the 1970s, employs the coupling reaction of arylhydrazone derivatives with diazonium salts.[327-328] In contrast to this three-step synthesis, in 2012 Han *et al.* developed a simple one-pot reaction by the so-called aerobic oxidative coupling of N-H free tetrazoles with boronic acids under Cu_2O-catalysis (Figure 70).[329-330]

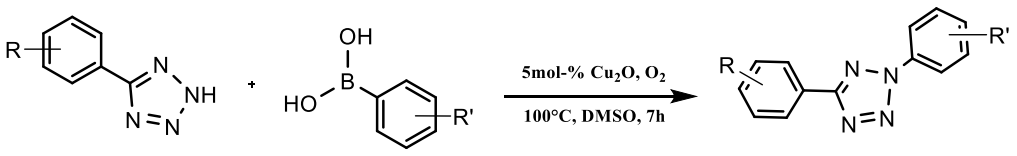

Figure 70: Synthesis scheme for 2,5 disubstituted tetrazole after Han *et al.*[329]

We chose to synthesize by the method of Han *et al.* a tetrazole compound with either carboxyl or hydroxyl moieties allowing an attachment to other molecules via esterification reactions. To verify that this method is working, we synthesized first 4-(5-phenyl-2H-tetrazol-2-yl)phenol already reported by this group (Figure 71).[329] The

molecule was successfully obtained (for details see section 3.4). However, several attempts to attach this tetrazole to various acids or acid chlorides (succinic acid via DCC/DMAP, EDC/DMAP, succinyl chloride and phenyldichlorophosphate with Cs_2CO_3) failed due to hydrolysis of the obtained ester during work-up. Therefore, we decided to synthesize the 4-(5-phenyl-2H-tetrazol-2-yl)benzoic acid, which has not yet been reported before via this synthesis method.

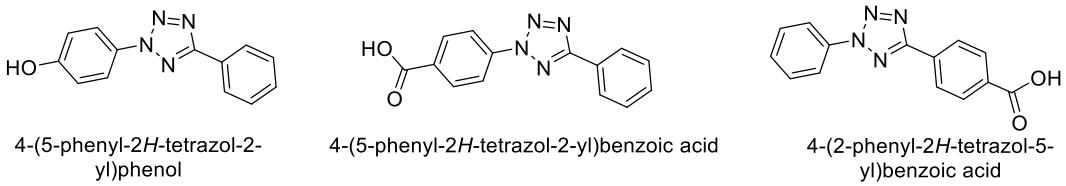

Figure 71: Structures of tetrazoles synthesized in this work.

The molecule was obtained successfully. In Figure 72, the NMR spectrum is shown. For the correct signal assignment and for the proof that the benzoic acid moiety is truly attached to the tetrazole, a $^{1}H^{15}N$ HMBC measurement was performed. In Figure 73, the long range coupling signals from the neighboring protons from the benzoic acid moiety and the tetrazole-nitrogen at position 1 are shown. This confirms that the desired product was obtained.

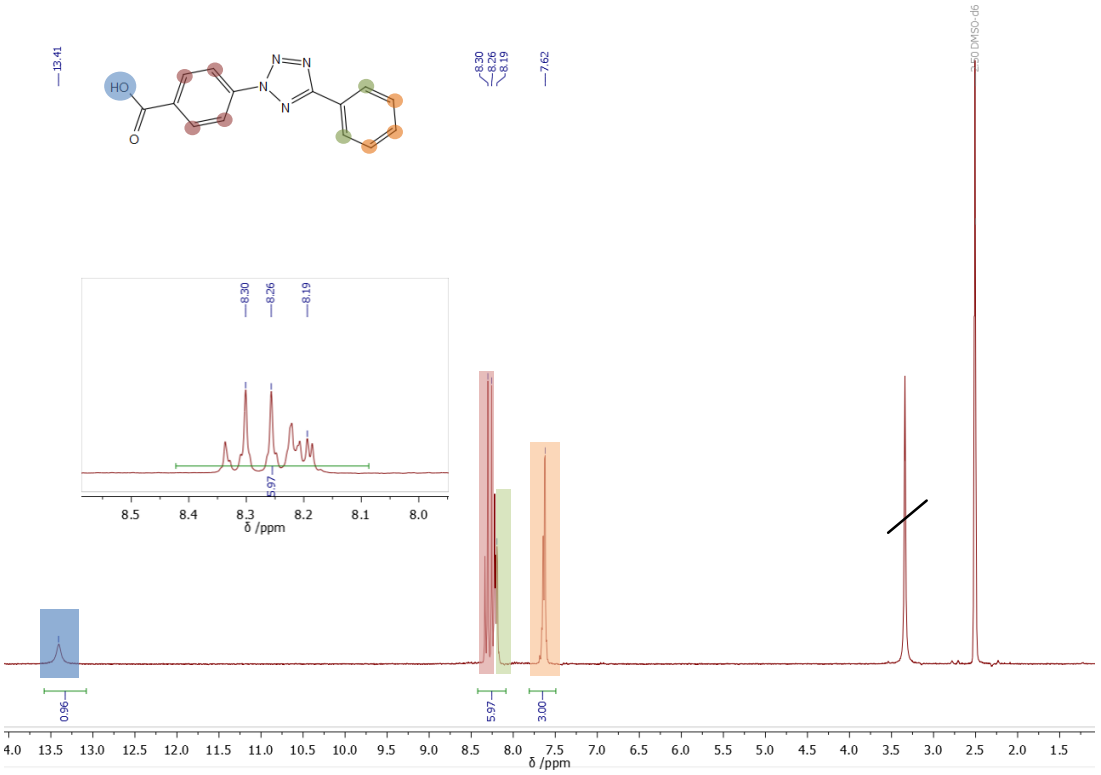

Figure 72: ^{1}H NMR spectrum of 4-(5-phenyl-2H-tetrazol-2-yl)benzoic acid (250 MHz, 298K, DMSO-d_6).

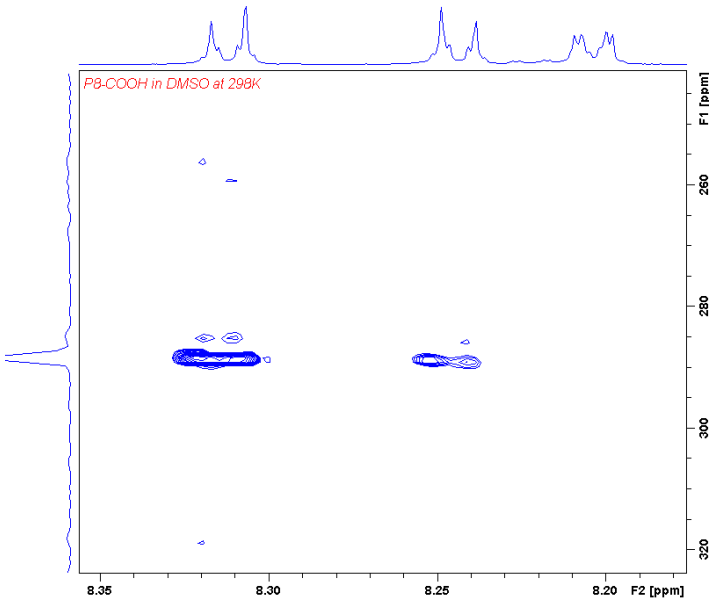

Figure 73: $^{1}H^{15}N$ HMBC spectrum of 4-(5-phenyl-2H-tetrazol-2-yl)benzoic acid (850 MHz, 298K, DMSO-d_6).

However, despite successful synthesis for several times, the reproducibility of this pathway was not satisfactory and the yield could not be increased above 41%. Since the complete mechanism of this reaction is still under investigation, an analysis of potential reasons for the failure in synthesis was difficult to perform.

For this reason, we decided to employ the classical method of synthesis to obtain reproducibly and in high yields (91%) 4-(2-phenyl-2*H*-tetrazol-5-yl) benzoic acid (TET). It carries the benzoic acid group at the 5-position in contrast to the prior one (Figure 71) and it allows us similarly to attach it easily to other compounds.

2.4.3 Coupling reactions of the tetrazole

Initially, the idea for nanocarrier synthesis was to use the tetrazole as the cross-linker in the organic phase and introduce for the counterpart acrylate moieties to the carrier material, i.e. to the water-soluble proteins. Therefore, a bifunctional cross-linker was synthesized by Steglich esterification of TET with 1,6 hexanediol and a trifunctional cross-linker by reaction of TET with trimethylolpropane.However, these compounds turned out to be unsuitable for the intended use as cross-linkers since they were only slightly soluble in chloroform and dichloromethane and insoluble in any other organic solvent. For this reason, we decided to reverse the whole system, attach TET to the proteins and use in the organic phase cross-linkers bearing reactive double bonds.

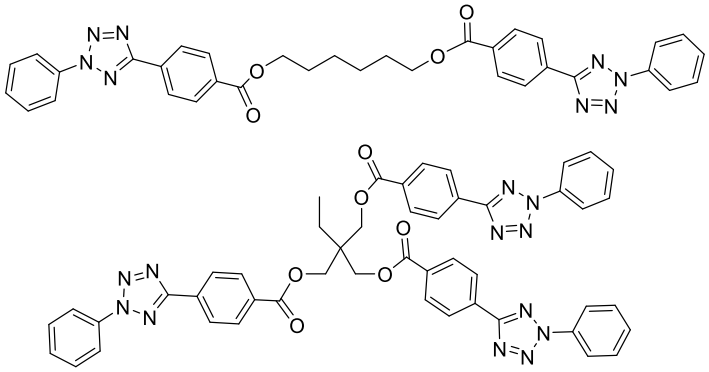

Figure 74: Structures of bifunctional and trifunctional tetrazole cross-linkers.

TET was attached to OVA and HSA by Steglich amidation. The degree of functionalization was determined by UV/vis measurements. By this method, a TET/protein ratio of 13:1 for OVA and of 12:1 for HSA was determined (cf. Table 8 and Figure 95 in section 3.4.3.4). Due to the decrease in hydrophilicity for the proteins after TET-conjugation, we decided not to increase the degree of modification further. By LC-MS/MS analysis changes in protein primary structure upon conjugation were detected. For analysis, the TET-modified proteins were digested and peptide fragments were analyzed. Peptide regions containing modified residues cannot be digested. By comparing the identified peptides of unmodified and modified proteins, we were able to identify distinct peptide regions which contain modified residues. The protein sequence of HSA, of OVA and of the modified proteins is shown in Figure 75. Since the modified proteins were used as nanocarrier material not aiming to preserve the native state, detailed analyses of protein secondary and ternary structures were not performed.

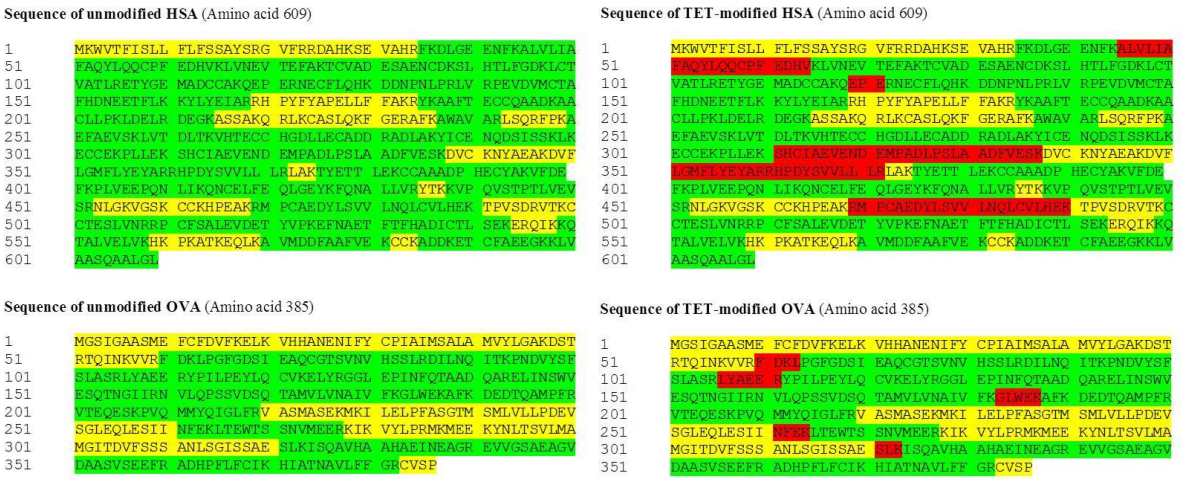

Figure 75: Protein sequence analysis by LC-MS/MS. Peptides identified both in unmodified and modified proteins are highlighted in green. Peptide regions which differ in sequence are marked in red and unidentified regions in yellow. The measurements were performed by J. Simon.

2.4.4 Choice of cross-linker

Recently, the bioorthogonality of the tetrazole-ene cycloaddition has been doubted, since the nitrile imine intermediate can also react with strong nucleophiles under certain conditions.[331-334] Nevertheless, the use of highly reactive dipolarophiles such as strained norbornene derivatives and the confinement of the reaction at the interface of two liquids can decrease the probability for cross-reactivity. Since tetrazoles react readily with strained double bonds,[326] we prepared difunctional norbornene cross-linkers (Figure 76). Norbornenes are advantageous over other strained ring systems such as cycloocytnes which are laborious to synthesize. Initially, 1,6-hexanediol was chosen as the spacer (cross-linker DN1) as it provides enough hydrophobicity for the cross-linker to be soluble in the oil phase and allows sufficient distance between the norbornenes to avoid steric hindrance. 1,4-benzenedimethanol (cross-linker DN2) and acetylenedicarboxylic acid (cross-linker DN3) were chosen as more rigid structures, and in case of the alkyne to have an additional functionality for post-modification. The triethylene glycol chain for cross-linker DN4 was thought to introduce amphiphilicity and thereby the preference for the interface. However, synthesis of nanocarriers with DN4 was not reproducible, which is possibly the result of the cross-linker being too hydrophilic for a successful interfacial reaction. Cross-linker DN5 with the disulfide bond introduces an additional potential cleavage point for subsequent drug release from the protein nanocarriers.

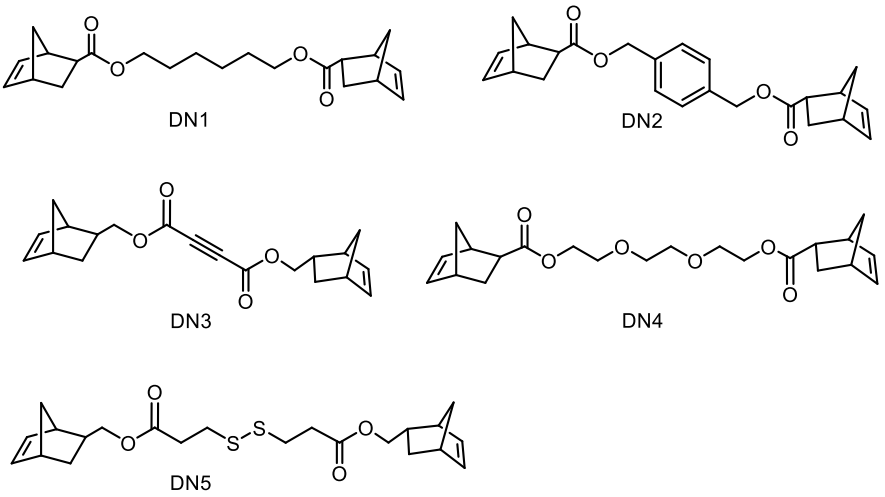

Figure 76: Structures of dinorbornene cross-linkers.

2.4.5 Protein nanocarrier synthesis

The protein nanocarriers (PNCs) were prepared by an interfacial cross-linking reaction in a water-in-oil miniemulsion. In Figure 78b, the mechanism of cross-linking is shown. The TET-conjugated proteins (OT stands for ovalbumin-TET conjugates, HT for HSA-TET) were dissolved in chloride-free aqueous buffer (due to the inhibitory effect of chloride on the cycloaddition reaction).[202] Cyclohexane, containing the surfactant P((E/B)-*b*-EO) was used as the organic phase and the mixture was homogenized by ultrasound to obtain stable aqueous nanodroplets. By addition of dinorbornene cross-linker to the miniemulsion and irradiation of the mixture with UV light (254 nm), the reaction at the oil/water interface between the TET moieties and the cross-linker was triggered leading to the formation of a core-shell morphology (Figure 78d and Figure 79 for all cross-linkers).

Initially, the reaction was performed in a petri-dish with the UV lamp placed on top to allow the emulsion to have sufficient contact with the UV-light (Figure 77).

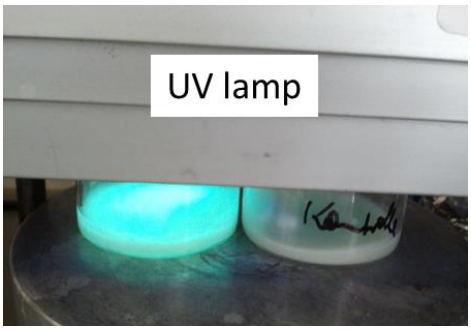

Figure 77: Experimental set-up for the photoclick reaction. Two petri dishes with emulsion (*left*: sample with cross-linker, *right*: control sample without cross-linker) are placed onto a magnetic stirring plate and the UV lamp is placed on top.

However, this led to a fast evaporation of the cyclohexane and required a careful monitoring of the emulsion not to dry out. An advanced set-up is depicted in Figure 78c. To avoid unnecessary evaporation of cyclohexane but guarantee at the same time an irradiation of the whole emulsion, a peristaltic pump was used. It transports the emulsion through a long quartz tube irradiated with a low-power UV-lamp placed in front of it.

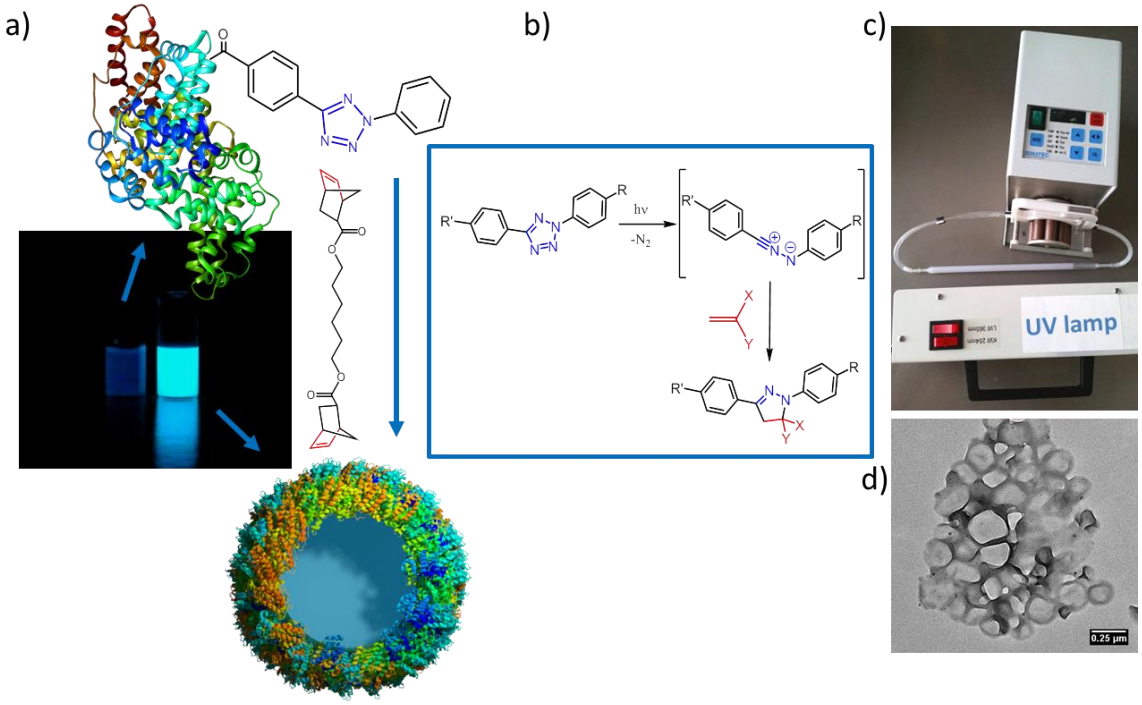

Figure 78: Preparation of protein nanocarriers (PNCs). a) Non-fluorescent protein-TET conjugates were cross-linked by dinorbornene in inverse miniemulsion to obtain self-fluorescent protein nanocarriers. b) Reaction mechanism of the bioorthogonal UV-light induced 1,3 dipolar tetrazole-ene cycloaddition. c) Experimental setup with a peristaltic pump pumping the emulsion through a quartz cuvette with the UV lamp placed in front. d) TEM image of the PNCs.

After synthesis and purification, PNCs were transferred into water. Their diameter from DLS was about 300 nm with a zeta potential of about -30 mV (Table 5).

Table 5: Size of PNCs (OT for OVA-TET, HT for HSA-TET conjugates) determined by dynamic light scattering (DLS) after synthesis, and after transfer to the aqueous phase and their Zeta-potential.

Sample	Ø [nm] (PDI) in cyclohexane	Ø [nm] (PDI) in water	ζ [mV]
OT-DN1	290 (0.17)	291 (0.17)	-37 ±12
OT-DN2	203 (0.20)	319 (0.28)	-31 ±11
OT-DN3	329 (0.25)	506 (0.36)	-29 ±13
HT-DN1	285 (0.25)	315 (0.30)	-30 ±10
HT-DN2	297 (0.27)	380 (0.30)	-29 ± 8
HT-DN3	257 (0.17)	355 (0.31)	-37 ±15

The PNCs in TEM (Figure 79) appear smaller compared to the values from DLS which can be attributed to their soft shell, leading to shrinkage upon drying and under high-vacuum conditions.

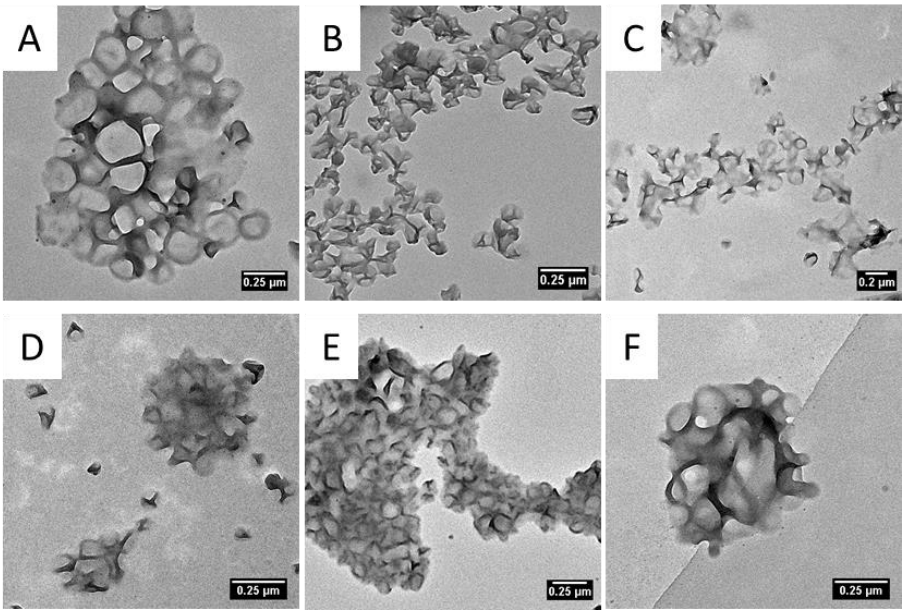

Figure 79: Transmission electron microscopy images of PNCs. A: OT-DN1, B: OT-DN2, C: OT-DN3, D: HT-DN1, E: HT-DN2, F: HT-DN3.

2.4.6 Fluorescence properties useful for detection of cellular uptake

Upon reaction, the appearance of fluorescence, not existing before, was observed (Figure 80 for comparison of HT-PNCs and OT-PNCs and fluorescence spectra in Figure 81). This is typical for the formed pyrazoline cycloadduct.[198] A more intensive fluorescence was detected with human serum albumin, especially with DN2. This can possibly be due to quenching effects of the pyrazoline in the OVA PNCs. Per 12.5 mg protein used in the PNC synthesis, the molar amount of OVA is higher than that of HSA ($2.9 \cdot 10^{-7}$ mol compared to $1.9 \cdot 10^{-7}$ mol). Thus, also the TET amount in the reaction mixture is approximately 1.7 times higher with OVA-TET conjugates than for HSA-TET if we consider the modification degrees of 13 TET/mol for OVA and 12 TET/mol for HSA.

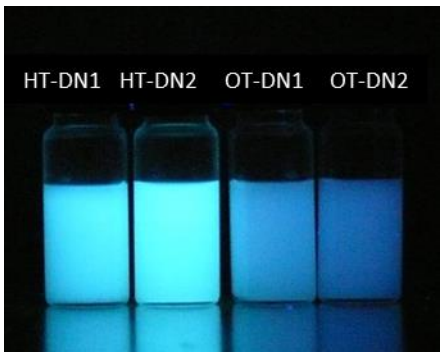

Figure 80: Nanocarriers out of HSA-TET conjugate (HT) with DN1 and DN2: HT-DN1, HT-DN2; and nanocarriers out of OVA-TET conjugate (OT) with DN1 and DN2: OT-DN1, OT-DN2. Samples show fluorescence after synthesis when irradiated with a 365nm UV-lamp.

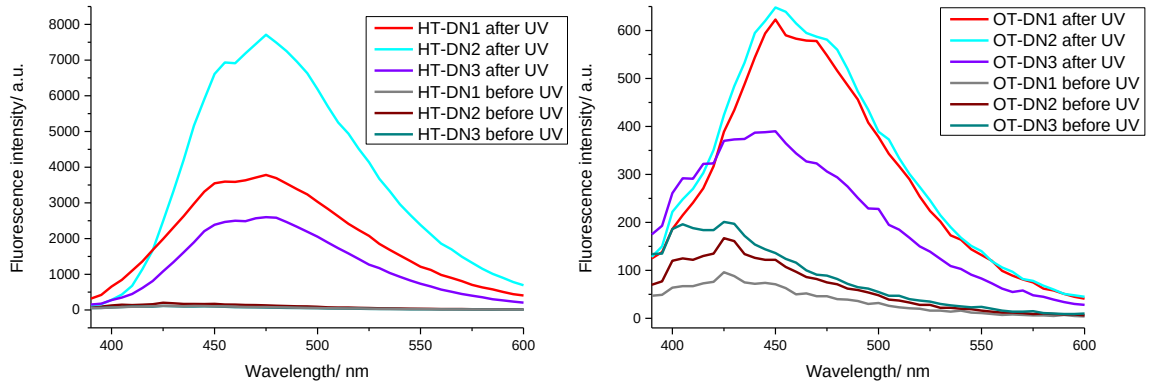

Figure 81: Fluorescence spectra of PNC solution in cyclohexane before and after irradiation.

For studies of cellular uptake of nanocarriers, usually labelling with a fluorophore is necessary. Fluorescent dyes, for example cyanine dyes, are frequently encapsulated in nanocontainers.[178, 335] With the nanocarriers reported herein, the need for these additional substances, which are usually quite expensive, can be bypassed or additional dyes (with different colors or intracellular density) can be incorporated. Since the pyrazoline cycloadduct is fluorescent by itself, the uptake by monocyte derived dendritic cells (moDCs) was studied without the use of an additional dye. PNC uptake by moDCs was analyzed after co-incubation for 24 h *in vitro*. Flow cytometry revealed a percentage of internalized HT-DN3 NCs of 8.7%, while HT-DN1 and HT-DN2 PNCs displayed an enhanced uptake by moDCs with a frequency of about 31% and 24%, respectively (Figure 82). Moreover, analysis of median fluorescence intensities (MFI) of moDCs documented an increase by co-incubation with HT-DN1 (MFI: 3740) and HT-DN2 (MFI: 3560) PNCs compared to HT-DN3 PNCs (MFI: 2515). The percentage of OT-DN PNC ingesting moDCs was significantly reduced (OT-DN1: 0.09%; OT-DN2: 0.46%; OT-DN3: 0.44%). However, a weak shift of median fluorescence intensities of moDCs was detected with OT-DN PNCs compared to the negative control. The successful uptake of OVA nanocarriers of similar size and by the same cell lines has already been reported in section 2.1. Therefore, little uptake in this case compared to HSA is predominantly caused by the weak fluorescence of the OVA nanocarrier formulations reaching the lower limit of detection by the flow cytometer.

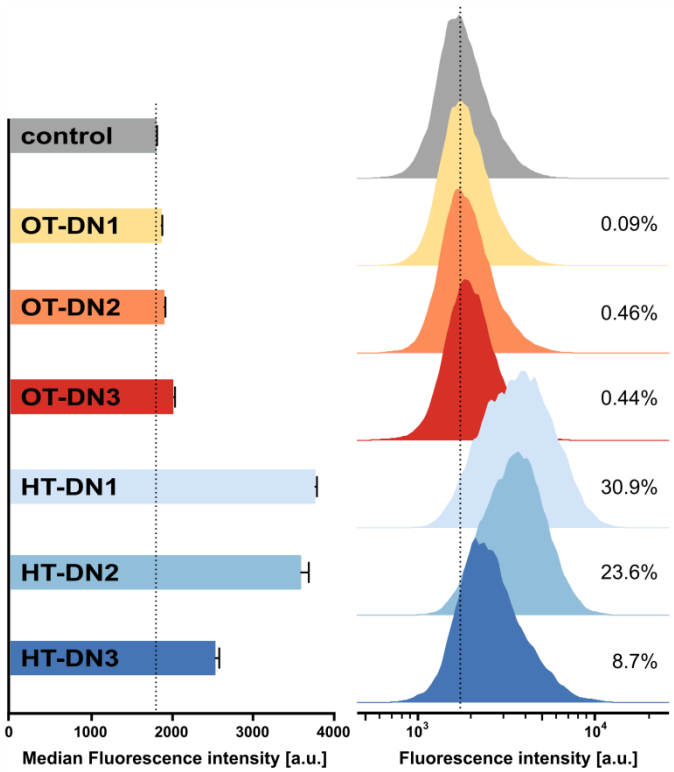

Figure 82: Uptake of protein nanocarriers by moDCs *in vitro* was analyzed by flow cytometry. Left: Quantification of PNC uptake based on the median fluorescence intensities of moDCs (n=3). Right: Representative histograms showing the shift of moDC fluorescence after internalization of PNCs. Frequencies of PNC+ moDCs are indicated. Dotted lines indicate a MFI of 1800. Data represent mean ± SD of three independent experiments conducted with n = 3. M. Fichter performed the experiments.

2.4.7 Encapsulation efficiency and enzymatic degradation

The PNCs were loaded with the hydrophilic and low molecular weight sulforhodamine SR101 as model drug to assess the encapsulation efficiency of the PNCs for their potential application as drug carriers. Leakage of the dye over a period of up to 78 days was recorded by measuring the fluorescence intensity of the aqueous supernatant after removal of the PNCs by centrifugation (Figure 83). By comparing the measured values with the amount of initially used dye, an encapsulation efficiency of over 91%, which remains constant over time, was established.

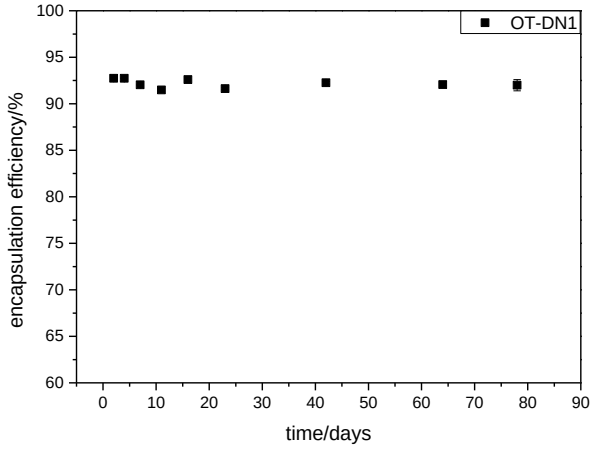

Figure 83: Encapsulation efficiency of OT-DN1 PNCs determined by measurement of the fluorescence intensity of sulforhodamine SR101 dye. Day 2 as the starting day means 36 h after transfer of the PNCs from the organic to the aqueous phase. The experiment was conducted twice with two single measurements per sample.

A major feature of protein nanocarriers is their potential to (bio-)degrade into low molecular weight fragments which can be cleared from the body by using naturally occurring enzymes. To prove that the cross-linked PNCs can be cleaved by proteases, DQ-ovalbumin was encapsulated in OT-DN1 and HT-DN1 PNCs. DQ-ovalbumin is a commercial, self-quenched fluorescent marker, consisting of ovalbumin conjugated with several BODIPY molecules. Upon proteolytic degradation, green fluorescence (λ_{em} = 515 nm) can be detected. The DQ-ovalbumin-loaded PNC dispersions in PBS buffer (at pH = 7.4) do not show any change in fluorescence over several hours. After the addition of the serine protease trypsin, an instantaneous increase in fluorescence intensity can be detected (Figure 84). The fluorescence increases over time as trypsin degrades the PNCs and thus more dye is released.

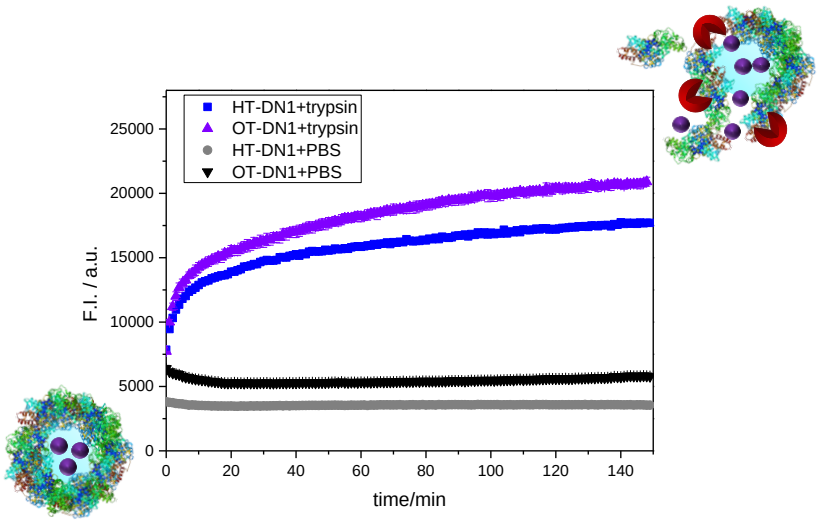

Figure 84: Biodegradability of the nanocarriers: change of fluorescence intensity over time of OT-DN1 and HT-DN1 PNCs containing DQ-ovalbumin and incubated with trypsin or PBS buffer at pH 7.4, 37 °C for 2.5 h.

Similarly, the proteolytic degradation was also verified by encapsulation and release of CdTe quantum dots, proving the versatility of the process to encapsulate various cargo molecules and particles (Figure 85).

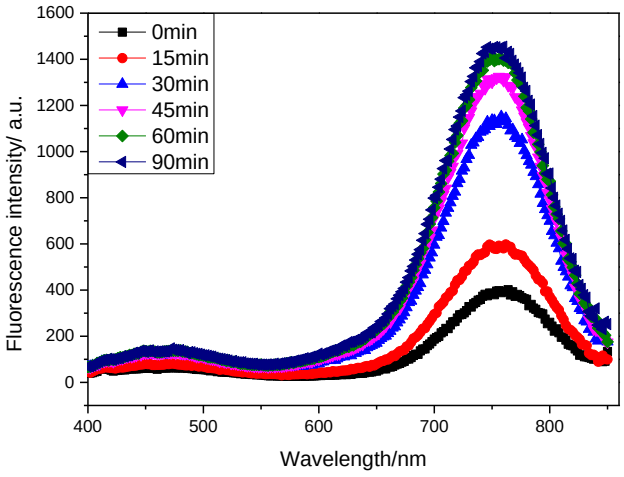

Figure 85: Fluorescence spectra of HT-DN1 PNC supernatant with hydrophilic, carboxyfunctionalized CdTe quantum dots recorded with an excitation wavelength of 364 nm. 0 min is before trypsin addition.

2.4.8 Loading of PNCs with R848

The encapsulation of the immunostimulant R848 into the PNCs offers the opportunity to prove the intracellular PNC uptake and degradation in a functional manner. R848 is recognized by the highly specific toll-like receptor 7, localized in the endosomes, and induces an upregulation of specific surface proteins on the corresponding cells of the immune system, such as dendritic cells.[277, 336] These proteins are necessary and essential for the activation of T cells and therefore for all adaptive immune reactions against tumors

and pathogens.[337] Thus, to develop its stimulatory potential, R848 has to reach the endosomally localized receptor. For this reason, unstimulated bone marrow derived dendritic cells (BMDCs) were treated with different doses (0.1-100 µg/mL) of HT-DN1 and OT-DN1 loaded with R848 for 24 h. Lipopolysaccharide (LPS), an immunostimulant, whose receptor is located on the dendritic cell surface, was used as the common immunological positive control. Afterwards, BMDCs were harvested and the CD86 expression was measured by flow cytometry. OT-DN1-R848 and HT-DN1-R848, respectively, induced a dose dependent upregulation of the dendritic cell surface protein CD86 (Figure 86). Compared to the untreated samples, the CD86 expression was strongly enhanced by the R848-loaded nanocarriers, especially with 10-100 µg/mL. The dose dependent stimulatory effect of the PNCs illustrates that the TET-chemistry does not restrict R848 in its biological activity and an intracellular degradation of the PNCs is feasible.

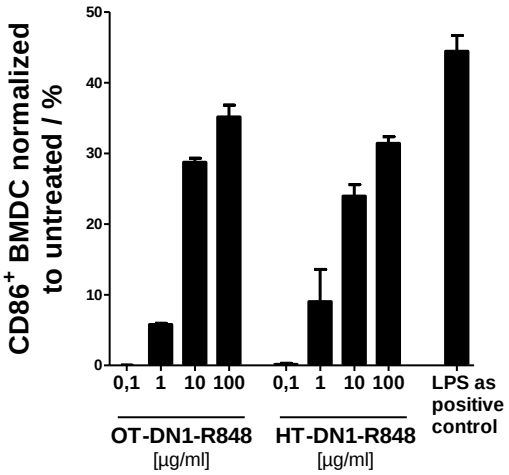

Figure 86: Upregulation of CD86 expression by bone marrow derived dendritic cells (BMDCs) upon treatment with PNCs loaded with R848 indicating a successful intracellular cleavage of the PNCs. Lipopolysaccharide (LPS) as positive control was used. D. Paßlick performed the experiments.

2.4.9 Cytotoxicity analysis

For the successful biomedical application of nanocarriers, it is essential to understand their behavior in physiological fluids such as blood plasma. Interactions of blood proteins with nanocarriers can dramatically alter their physicochemical properties and highly influence the further biological fate. It is crucial that the drug delivery vehicles are non-toxic and, for intravenous administration, do not aggregate in blood. Human monocyte derived dendritic cells (moDCs) were incubated with 1 to 100 µg/L of OT-DN1 and HT-DN1 nanocarriers for 24 h. Propidium iodide staining did not reveal any increase in cytotoxicity even at the highest concentration of PNCs (Figure 87).

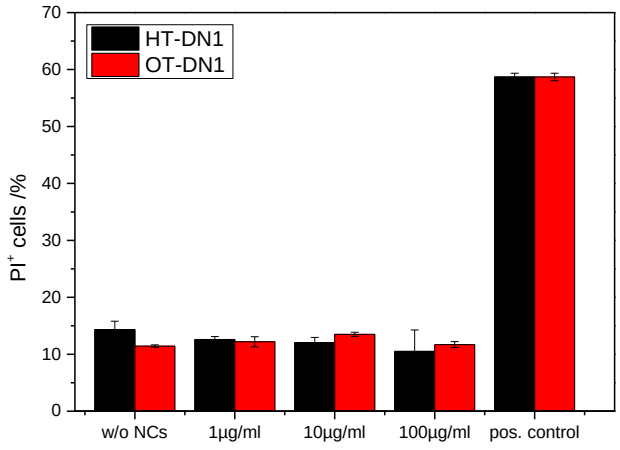

Figure 87: Toxicity analysis of OT-DN1 and HT-DN1 PNCs incubated with human moDCs for 24 h. Dead moDCs are displayed as PI^+, obtained after staining with propidium iodide. A. Pietrzak-Nguyen performed these experiments.

2.4.10 Interaction of PNCs with human blood plasma

The PNCs were further directly introduced to human blood plasma. With dynamic light scattering measurements we proved that PNCs remained stable in human blood plasma and do not aggregate (Figure 88).

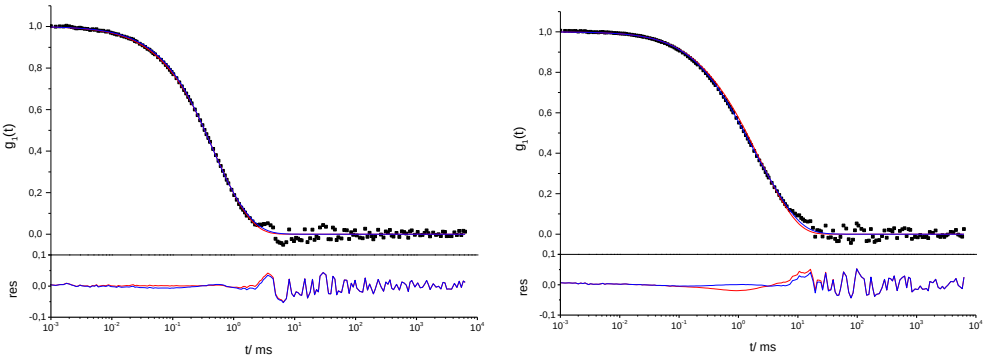

Figure 88: Dynamic light scattering measurement of PNCs in human blood plasma after a method developed by Rausch et al.[272] Self-autocorrelation function of the mixture of PNCs with human blood plasma (left: with HT-DN1, right: OT-DN1). The data points in black derive from the PNC/plasma mixture. The red curve represents the force fit and its residue without the intensity contribution from aggregates. It fits well with the blue curve which considers intensity contribution from aggregates. The measurement was performed at an angle of 90° and 37 °C.

In addition, incubation with human blood plasma altered the zeta-potential of PNCs, indicating protein adsorption (Table 6).

Table 6: Zeta-potential of PNCs (OT for OVA-TET, HT for HSA-TET conjugates) after transfer to the aqueous phase and purification and zeta-potential of these samples after incubation in human blood plasma.

Sample	ζ [mV]	ζ [mV] in plasma
OT-DN1	-37 ±12	-14±4
HT-DN1	-30±10	-16±5

For qualitative and quantitative characterization of the protein corona of the nanocarriers in human blood plasma, we applied SDS-PAGE and liquid chromatography coupled to tandem mass spectrometry (LC-MS/MS). It was found that the composition of the protein corona of PNCs highly depends on the shell material of the nanocarrier (Figure 89 B). In addition, the protein corona strongly differs from the native abundance of proteins in the human blood plasma (exemplarily shown for HSA in Figure 89 A, Lane 1 vs. Lane 4).

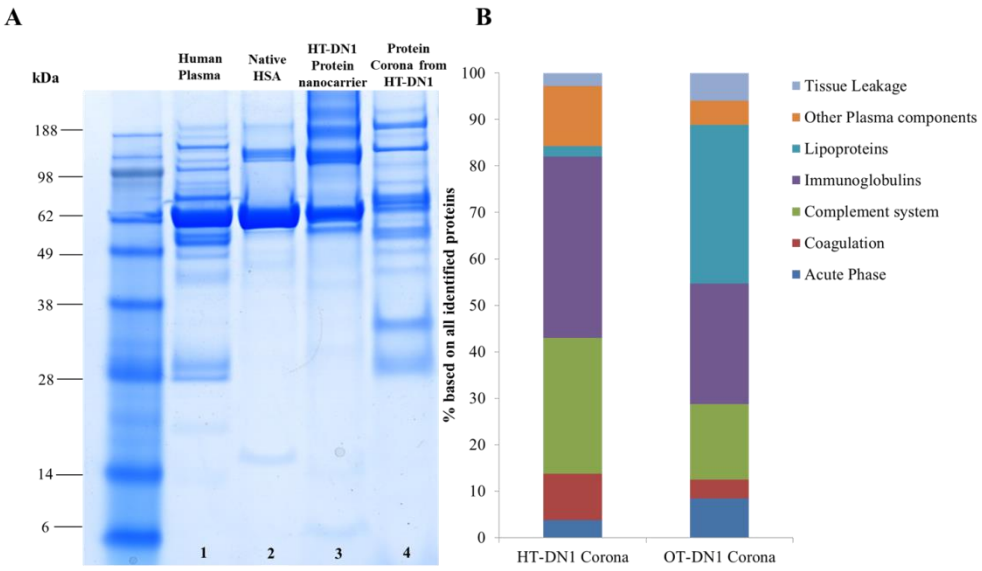

Figure 89: Interaction of PNCs with human blood plasma. Protein nanocarriers were incubated with human plasma (1 h, 37 °C). To remove unbound and loosely proteins, PNCs were centrifuged (20000 g, 30 min) and the remaining supernatant was discharged. This procedure was repeated three times. Bound proteins were eluted form nanocarriers with lysis buffer and analyzed by SDS-PAGE (A) and LC-MS/MS (B). These experiments were performed by J. Simon.

The identified proteins were classified into six major classes: PNCs prepared from HSA carry a protein corona strongly enriched with immunoglobulins and proteins from the complement system (Figure 89 B). In contrast, a great amount of lipoproteins (e.g. clusterin, ApoAIV) are adsorbed on OT-DN1-PNCs which are of importance to obtain a stealth behavior in *in vivo* applications.[338-339] Interestingly, by comparing the protein coronas of nanocarriers synthesized by the interfacial polyaddition reaction with TDI (as

described in section 2.1) with the PNCs by photoclick chemistry presented here, no significant differences were found. As can be seen in Figure 90, the formation of the protein corona does not depend on the cross-linker which was used for the nanocarrier synthesis but is predominantly governed by the type of protein.

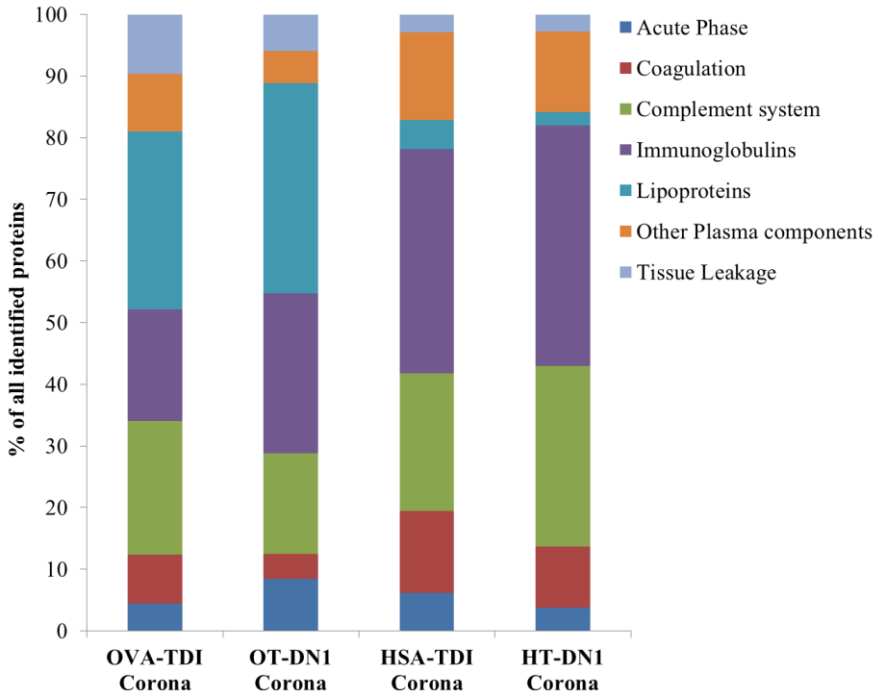

Figure 90: Protein corona composition in dependence of the cross-linker used for PNC synthesis. This experiment was performed by J. Simon.

A detailed overview of all identified proteins is summarized in the experimental section 3.4.3.7.

These results further render the use of proteins as the building material for nanocarriers interesting, as it allows the tailoring of the protein corona in blood and should enable us to control selective targeting *in vivo*, eventually.

2.4.11 Raman spectroscopy for cross-linker DN3

As mentioned in section 2.4.4, the introduction of a triple bond into the cross-linker opens up the way for post-modification of the PNCs.

Chemical analysis of the PNC composition by common analytical methods is difficult. Either a technique is not applicable due to the insolubility of the PNCs, or the proteins interfere with the moieties of interest and the influences of the respective compounds are difficult to separate. To verify the presence of the alkyne bond in the

PNCs, a complexation reaction thereof with octacarbonylcobalt was applied. First reported by Greenfield *et al.* in 1956,[340] this reaction can be used for the quantitative and qualitative analysis of alkyne moieties.[341] Octacarbonylcobalt forms a complex with alkynes by replacing the two bridge carbonyls in a quantitative manner. Upon complexation, the appearance of an absorption band around 350 nm can be observed.[341] Due to the low stability of octacarbonyldicobalt towards oxidation, the reaction was performed under inert conditions. A successful complexation, i.e. an appearance of an absorption band at 365 nm was observed. However, despite several efforts, the reaction mixture was not stable enough to give reasonable and reproducible results regarding a quantification of the triple bonds present in the PNCs.

Therefore, to verify additionally that the triple bond is present in the compounds, Raman spectroscopy measurements were performed. While IR spectroscopy requires a change in the dipolar momentum during a vibrational mode, for Raman spectroscopy, a change in polarization is needed. As a consequence, Raman spectroscopy is perfectly suited for easily polarizable transitions.[342] For symmetrically disubstituted alkynes, Raman spectroscopy is a sensitive tool since the triple bond vibrations yield a characteristic signal with high intensity.

First, a spectrum of acetylenedicarboxylic acid, the starting compound for the DN3 cross-linker, was recorded to have a reference spectrum (Figure 91). Then, DN3 and HT-DN3 were measured in order to verify the presence of the triple bond in the cross-linker and in the nanocarriers. Each spectrum was baseline-corrected. The original spectra can be viewed in the appendix. The complete Raman-spectroscopic analysis of all compounds is not part of this work. It is used to show the presence of the triple bond.

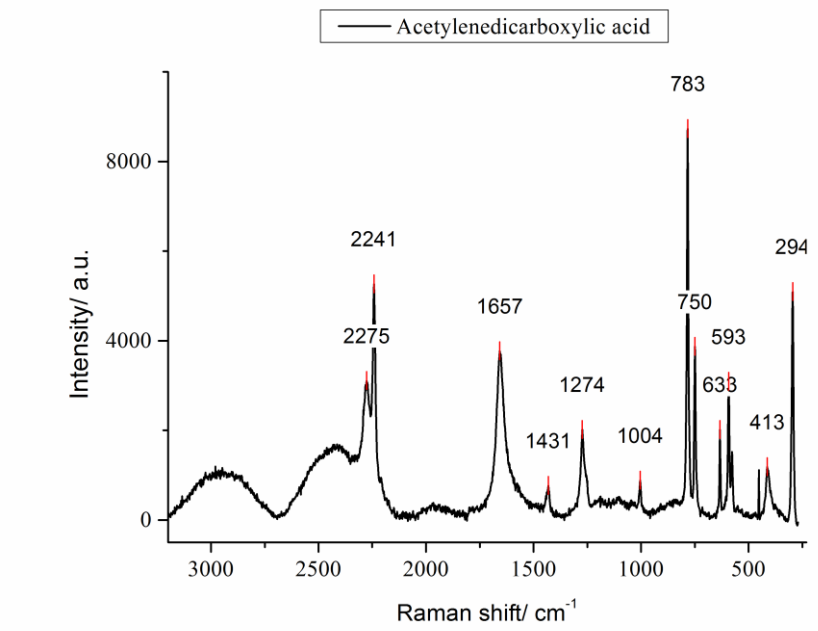

Figure 91: Raman-spectrum of acetylenedicarboxylic acid.

The peaks in Figure 91 are correlated to the characteristic oscillations given in Table 7.

Table 7: Peak assignment for Figure 91.

Wavenumber [cm^{-1}]	Signal intensity	Mode
294	s	γ(C≡CCO_2H)
413	m	δ(COOH)
593	m	γ(CCO)
633	m	δ(COOH)
750	s	δ(CCO)
783	s	ν(C-COOH)
1004	w	ν(C-O)
1274	s	ν(C-O)
1431	w	δ(OH)
1657	s	ν(C=O)
2241	s	ν(C≡C)
2275	s	ν(C≡C)

The band of interest appears at about 2275 cm^{-1}. A signal in this area also should be found in the spectra of DN3 and HT-DN3. The three spectra are shown in Figure 92.

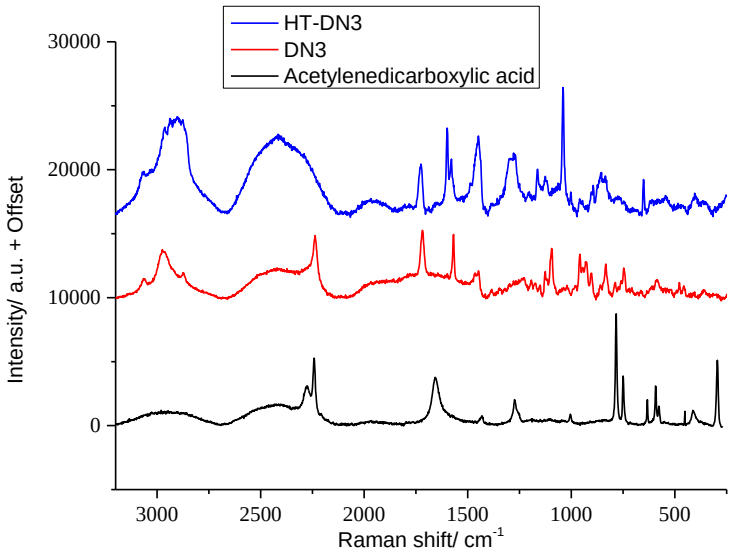

Figure 92: Raman-spectra of HT-DN3, DN3 and acetylenedicarboxylic acid

The band derived from the alkyne is present in the spectrum of DN3. The spectrum of the nanocarriers however, does not show this signal. It seems that the band is overlaid by other signals. According to literature, the ammonium group of α-aminoacids and thiol groups show a band appearing between 2500 cm^{-1} and 2000 cm^{-1}.[343-344]

For this reason, to prevent that the signals of the triple bond are overlaid by the signals of the α-aminoacid or thiol groups, toluene-2,4-diisocyanate (TDI) was added to the nanocarrier dispersion to react with the ammonium and thiol groups. Afterwards, a spectrum was recorded again which is shown in Figure 93.

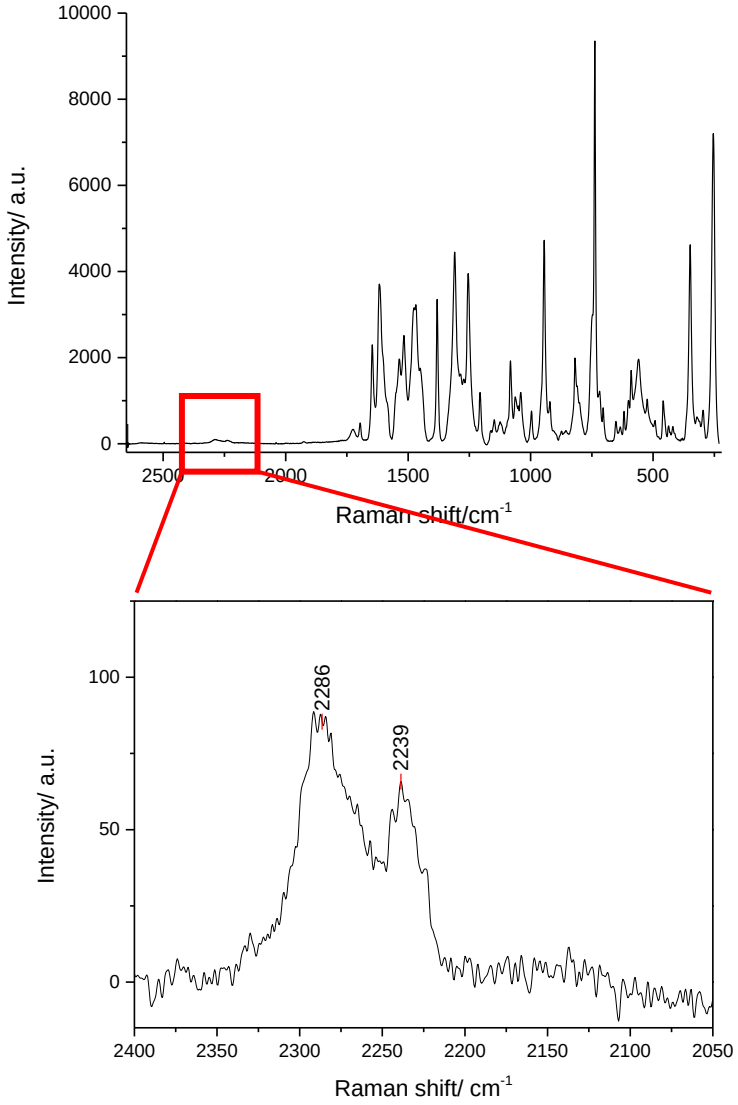

Figure 93: Raman-spectrum of HT-DN3 treated with TDI**.** Top: whole spectrum, bottom: *ν*(C≡C) transition.

The bands at 2286 cm^{-1} and 2238 cm^{-1} in Figure 93 are in good accordance with the double peak in Figure 91. Thus, the triple bond seems to be present in the nanocarriers, even if the intensity is low. The low intensity of the Raman-bands of the C-C triple bond can be explained with the low concentration of these in the nanocarriers, since the Raman scattering intensity is proportional to the amount of scattering centres.[345]

2.4.12 Conclusion

In summary, we developed a robust and successful synthesis method for the preparation of biodegradable protein nanocarriers which are taken up by dendritic cells and release an active drug intracellularly. The bioorthogonal 1,3-dipolar tetrazole-ene cycloaddition was adjusted precisely at the interface of nanodroplets in miniemulsion to

generate crosslinked protein nanocarriers by low-intensity UV-light in 30 min at ambient conditions. The nanocarriers were self-fluorescent enabling a monitoring of cellular uptake without additional fluorophores. A high drug payload of more than 90% was achieved. The non-toxic PNCs were stable in blood plasma and were enzymatically degradable. They released their intact cargo only after proteolytic cleavage of the shell which was shown by encapsulation of the immunostimulant R848 into the PNCs. Proteins are ideal non-toxic and biodegradable building blocks to be combined with the bioorthogonal TET chemistry. A facile modification of the cross-linkers by introducing additional functionalities allow for further customization. This unique combination, suitable for a great variety of proteins, offers us a diverse tool to design drug delivery vehicles for the encapsulation of sensitive drugs.

3. Experimental Part

3.1 Experimental details for Section 2.1

3.1.1 Materials

All chemicals and materials were used as received. Bovine serum albumin (>96% purity) and albumin from chicken egg white (grade VII) were purchased from Sigma Aldrich as well as 2,4-toluene diisocyanate (TDI) and dimethylsulfoxide (DMSO) (>99%) and the stains-all dye. Cyclohexane (HPLC grade) and the osmotic reagent sodium chloride were purchased from VWR. The block copolymer poly((ethylene-*co*-butylene)-*b*-(ethylene oxide) P(E/B)-*b*-EO) used as the oil soluble surfactant was synthesized as described in literature[346] and consists of a poly((ethylene-co-butylene) block (NMR: M_n = 3,900 g/mol) and a poly(ethylene oxide) block (NMR: M_n = 2,700 g/mol). The anionic surfactant sodium dodecyl sulfate (SDS) was purchased from Alfa Aesar. The sodium chloride solution (NaCl 0.9%) was purchased from B. Braun. CellTracker™ Green CMFDA and DQ™ ovalbumin (D-12053) were purchased from Molecular Probes. Sulforhodamine 101 (SR101) was purchased from BioChemica, Aldrich. The cy5-labeled oligonucleotide with the sequence cy5-CCA CTC CTT TCC AGA AAA CT-3′ was synthesized by Thermo Scientific. Muramyl dipeptide (MDP) and resiquimod (R848) were obtained from Invivogen. Amicon Ultra-2 centrifugal filter devices and the GS200 nm filters were purchased from Merck Millipore (100,000 nominal molecular weight limit (NMWL)). The human blood plasma, prepared according to the standard guidelines, was obtained from the University Clinic of Mainz (Germany). Due to the high variation of protein composition of different patients a pool of plasma obtained by the mixture of serum of several healthy donors was used for all measurements. Demineralized water was used for all experiments. For cell experiments, Histopaque-1077 from Sigma Aldrich was used. CD14 microbeads were purchased from Miltenyi Biotec, X-Vivo 15 medium from Lonza and GM-CSF and IL-4 from ImmunoTools. Propidium iodide solution was purchased from eBiosciences. The magnesium and calcium free phosphate-buffered saline, Hoechst 33342 and CellMask Orange were purchased from Life Technologies.

3.1.2 Instrumentation

For ultrasonication, a Branson Sonifier W-450-Digital was used with a ½" tip, operating under ice cooling for 3 min at 70% amplitude with pulse cycles of 20 s sonication and 10 s pauses.

For centrifugation, the Sigma 3 k-30 from Sigma Centrifuges, UK was used.

Morphological studies were performed with transmission electron microscopy (TEM) and scanning electron microscopy (SEM). For the measurements, one drop of diluted PNC dispersion was placed either onto a silica wafer (for SEM) or onto a 300 mesh carbon-coated copper grid (for TEM) and allowed to dry under ambient conditions. The SEM measurements were performed with a 1530 Gemini LEO (Zeiss) field emission microscope, with an accelerating voltage of 170 V. For TEM measurements, Jeol 1400 transmission electron microscope was used with an accelerating voltage of 120 kV.

The average size and size distribution of the PNCs were measured via dynamic light scattering (DLS) at 25 °C using a Nicomp 380 submicron particle sizer (Nicomp Particle Sizing Systems, USA) at an angle of 90 °.

ATR-IR measurements were performed with the PerkinElmer Spectrum BX FT-IR spectrometer and the spectrum was recorded between 4000 and 400 cm^{-1}. For the measurements, one drop of the liquid sample was placed onto the ATR crystal.

Zeta potential measurements were performed in 10^{-3} M potassium chloride solution at pH 6.8 and 25 °C with Malvern Zeta sizer (Malvern Instruments, U.K.).

All dynamic light scattering experiments in human blood plasma were performed on a commercially available instrument from ALV GmbH consisting of a goniometer and an ALV-5000 multiple-tau full-digital correlator with 320 channels. A helium-neon laser (JDS Uniphase with a single mode intensity of 25 mW operating at a laser wavelength of λ_0 = 632.8 nm) was used as the light source. All solutions for light scattering experiments were prepared in dust-free quartz light scattering cuvettes (inner diameter 18 mm, Hellma, Müllheim), which were cleaned prior to use with distilled acetone.

Fluorescence intensity measurements were performed with the Infinite M1000 plate reader from Tecan, Austria using 96-well plates.

Flow cytometric analysis of PNC^+ moDCs was performed on the BD LSR II flow cytometer (BD Biosciences).

Confocal laser scanning microscopy was performed on the Zeiss LSM 710 NLO.

3.1.3 Methods

3.1.3.1 Protein Nanocontainer (PNC) synthesis

The protein nanocontainers were prepared adopting a previously described procedure from Landfester *et al.* using a polyaddition reaction in an inverse miniemulsion process.[347] First, 50 mg of the appropriate protein were dissolved in 0.5 g demineralized water and 7.2 mg NaCl were added to the mixture. 35.7 mg of surfactant P((E/B)-*b*-EO) were dissolved in 7.5 g of cyclohexane and the mixture was added drop-wise to the stirred aqueous solution. The so prepared pre-emulsion was homogenized by ultrasound as described above. A solution of 10.7 mg P((E/B)-*b*-EO) and 3 mg TDI in 5 g of cyclohexane was then added drop-wise over a period of two minutes to the miniemulsion and the mixture was allowed to stir at 25 °C for additional 24 h.

The synthesized PNCs were purified by repetitive centrifugation (3 times for 20 min, RCF 1664) to remove the excess of the surfactant and re-dispersed in pure cyclohexane. For transfer into the aqueous phase, 500 µL of PNC dispersion in cyclohexane were added drop-wise to 5 g of an aqueous SDS solution (0.1 wt-%) under mechanical stirring and the samples were subjected afterwards to a ultrasound bath for 3 min at 25 °C (25 kHz). Subsequently, the samples were stirred open for 24 h at 25 °C to evaporate cyclohexane. To remove the excess SDS, the dispersion was further purified via Amicon Ultra-2 centrifugal filter (3 times for 20 min, RCF 1664) or 2 mL centrifuge tubes, respectively.

3.1.3.2 Modification of PNCs for biological analysis

For the measurement of cellular uptake, the PNCs were loaded with the cy5-labeled oligonucleotides by using 130µL of the fluorophore dissolved in PBS and 0.370 g of distilled water proceeding as described above.

The PNCs modified with DQ ovalbumin were synthesized by the addition of 300 µL of a DQ ovalbumin solution in PBS buffer (with a concentration of 1 mg/mL) to the aqueous phase. PNCs labeled with CellTracker CMFDA were synthesized by addition

of 160 µL of CellTracker CMFDA (with a concentration of 1 mg/mL in DMSO) to the aqueous phase and proceeding as described above.

For loading of the nanocontainers with R848 and MDP, respectively, 70 µL R848 (10 mg/mL in DMSO) and 250 µL MDP (10 mg/mL in water) were used and the amount of water reduced accordingly to maintain 500 µL of total volume.

3.1.3.3 Measurements in human blood plasma

The PNCs were measured in PBS buffer solution at physiological pH (7.4) and salinity (0.152 M). For measurements of nanocontainer-plasma mixtures, 10 µL of PNC dispersion (0.2%) was pipetted unfiltrated into the light scattering cuvette containing 200 µL undiluted human plasma which was filtered into the cuvette through a GS200 nm filter. The protein/PNC ratio was kept constant to the respective *in vivo* experiments (600 mg protein per mg PNC). The mixture was then diluted up to 1 mL total sample volume by filtering PBS into the light scattering cuvette. For DLS analysis of the nanocontainers alone, 10 µL of the PNC solution (0.2%) was added (without filtration) in 990 µL of filtered PBS. Plasma alone was prepared adding 800 µL of PBS to maintain the same dilutions.

After mixing, the samples were incubated for 20 min on a shaker at room temperature (20 °C) prior to the measurement. All DLS measurements were performed at 20 °C.

3.1.3.4 Determination of PNC permeability and encapsulation efficiency.

The permeability of the PNC-shell was studied by encapsulation of the fluorescent dye SR 101 which shows an absorption maximum at 550 nm and an emission maximum at 605 nm. 0.5 mg of SR101 was mixed with the aqueous phase and the reaction was carried out as described above. After re-dispersion in the aqueous SDS solution, the PNCs were sedimented by centrifugation with the Amicon Ultra-2 centrifugal filter devices and the fluorescence intensity of the permeate was measured by a plate reader. The encapsulation efficiency was calculated by correlating the obtained fluorescence intensity to the intensity of the starting concentration of SR101. To determine the permeability, the experiment was repeated over a given period and the fluorescence signal was compared to the initial value. The experiment was conducted two times with three single measurements.

3.1.3.5 Intracellular uptake of PNCs.

Human monocyte-derived dendritic cells (moDCs) were generated as previously described.[348] Briefly, peripheral blood mononuclear cells (PBMCs) were isolated from buffy coats of healthy human donors upon informed consent using density gradient centrifugation. Subsequently, $CD14^+$ monocytes were isolated using the magnetic-activated cell sorting technique and CD14 microbeads. Purified $CD14^+$ monocytes were cultured in X-Vivo 15 medium supplemented with L-glutamine, 100 U/mL penicillin, 100 µg/mL streptomycin, 200 U/mL GM-CSF and 200 U/mL IL-4 for 6 days. After 6 days of culture immature moDCs were collected and co-cultured with 25 µg/mL cy5-labeled OVA PNCs in 8-well chamberslides (ibidi) for 24 h at 37 °C. Nuclei were stained with 2 µg/mL Hoechst 33342 for 30 min and 4 µg/mL CellMask Orange was added immediately before analysis for plasma membrane staining. In order to evaluate intracellular uptake of OVA PNCs by moDCs, confocal laser scanning microscopy was performed.

In addition, PNC-uptake was quantified using flow cytometry. Therefore, immature moDCs were co-cultured with or without various concentrations of cy5-labeled OVA PNCs (7.5 / 25 / 100 µg/mL) for 24 h.

3.1.3.6 Biodegradability of PNCs

The degradation of DQ ovalbumin and CellTracker CMFDA-labeled PNCs was studied with the serine protease trypsin. A concentration of 2 mg/mL trypsin was used and the measurements were performed in PBS buffer. Control measurements of the PNCs in PBS buffer were carried out additionally. The changes in fluorescence intensity were recorded over 1 h at 37 °C. In addition, the biodegradability of PNCs was evaluated using a cell culture system as described above. MoDCs were co-incubated with or without 25 µg/mL OVA-DQ PNCs for 24 h, subsequently stained with Hoechst 33342 and CellMask Orange and analyzed by confocal laser scanning microscopy.

3.1.3.7 Toxicity evaluation of PNCs.

Human moDCs were cultured in presence of different concentrations of OVA-cy5 PNCs (2.5 / 7.5 / 25 / 100 µg/mL) or without PNCs for 24 h, as described above. Subsequently, moDCs were harvested and incubated with 10 µL propidium iodide solution for 2 min in order to stain nuclei of dead cells, followed by flow cytometric analysis.

3.1.3.1 Cell experiments with BMDCs

Bone marrow-derived dendritic cells (BMDCs) were differentiated from bone marrow progenitors (BM cells) of 8- to 10-week-old C57BL/6 mice as first described by Scheicher *et al.*[349] and modified by Gisch *et al.*[350] Briefly, the bone marrow was obtained by flushing the femur, tibia, and hip bone with Iscove's Modified Dulbecco's Medium (IMDM) containing 5% FCS (Sigma-Aldrich, Deisenhofen, Germany) and 50 µM β-mercaptoethanol (Roth, Karlsruhe, Germany). For the BMDC stimulation analysis via flow cytometry, the bone marrow cells (2 x 105 cells/1.25 mL) were seeded in 12 well suspension culture plates (Greiner Bio-One, Frickenhausen, Germany) with culture medium (IMDM with 5% FCS, 2 mM L-Glutamine, 100 U/mL penicillin, 100 µg/mL streptomycin (all from Sigma-Aldrich), and 50 µM β-mercaptoethanol), supplemented with 5% of GM-CSF containing cell culture supernatant derived from X63.Ag8-653 myeloma cells stably transfected with a murine GM-CSF expression construct.[351] On day 3, 500 µL of the same medium was added into each well. On day 6, 1 mL of the old medium was replaced with 1 mL fresh medium per well. On day 7, BMDCs were treated with nanocarrier formulations and LPS (positive control) as indicated in the figure legends. Before usage, all nanoparticle solutions were analyzed for endotoxin contaminations by limulus amebocyte lysate (LAL) assay (Thermo Fisher Scientific, Waltham, USA) according to the manufacturer's instructions. To analyze the expression of the BMDC surface maturation marker CD86, BMDCs were harvested and washed in staining buffer (PBS/2% FCS). To block Fc receptor-mediated staining, cells were incubated with rat anti-mouse CD16/CD32 Ab (clone 2.4G2), purified from hybridoma supernatant, for 15 min at room temperature. After that, the cells were incubated with phycoerythrin (PE)-conjugated anti-CD86 (clone GL-1) and PE-Cy7-labelled anti-CD11c (clone N418) (all from eBioscience, San Diego, USA) for 30 min at 4 °C.

To detect cell-nanoparticle-interaction and to analyze the expression of DC surface maturation markers, BMDCs were harvested and washed in staining buffer (phosphate buffer saline [PBS]/2% FCS). To block Fc receptor-mediated staining, cells were incubated with rat anti-mouse CD16/CD32 Ab (clone 2.4G2), purified from hybridoma supernatant, for 15min at room temperature. After that, the cells were incubated with eFluor450-conjugated Ab specific for MHC class II I-Ab,d,q/I-Ed,k (clone M5/114.15.2), fluorescein isothiocyanate (FITC)-labelled Ab directed at CD80 (clone 16-10A1), phycoerythrin (PE)-conjugated anti-CD86 (clone GL-1), and allophycocyanin (APC)-,

FITC- or PE-Cy7-labelled anti-CD11c (clone N418) (all from eBioscience, San Diego, USA) for 30 min at 4 °C. To analyze the importance of C-type lectin receptors for the binding/uptake of OVA-nanocapsules, the cells were alternatively incubated with PE-Cy7-labelled anti-DEC-205 (clone 205yekta), PE-labelled anti-Dectin-1 (clone bg1fpj), FITC-conjugated anti-DC-SIGN (clone MMD3) (all from eBioscience) and Brilliant Violet 421-conjugated anti-CD206 (clone C068C2) (Biolegend) for 30 min at 4 °C. Samples were measured with a BD FACS Canto II flow cytometer equipped with BD FACSDiva software (BD Biosciences). Data were generated based on defined gating strategies and analyzed using FlowJo software (FlowJo, Ashland, USA).

Cytokine levels in BMDC culture medium and BMDC/T cell co-culture supernatants were analyzed using a Cytometric Bead Array (CBA) (BD Biosciences). The following cytokines were measured: IL-1β, IL-5, IL-6, IL-10, IL-12p70, IL-17, interferon gamma (IFN-γ), and tumor necrosis factor alpha (TNF-α). The assay was performed according to the manufacturer's instructions.

3.2 Experimental details for Section 2.2

3.2.1 Nanocarrier synthesis and characterization

3.2.1.1 Materials

Cyclohexane (HPLC grade – VWR, Radnor, USA) and 2,4-toluene diisocyanate (TDI - Sigma-Aldrich, St. Louis, USA) were used for NC synthesis. The block copolymer poly((ethylene-*co*-butylene)-*b*-(ethylene oxide) P((E/B)-*b*-EO) consisting of a poly((ethylene-co-butylene) block (NMR: M_n = 3,900 g/mol) and a poly(ethylene oxide) block (NMR: M_n = 2,700 g/mol) was used as oil soluble surfactant and was synthesized according to previously published methods.[346] The anionic surfactant sodium dodecyl sulfate (SDS - Alfa Aesar, Heysham, U.K.) was used for redispersion of NCs. The cy5-labeled oligonucleotide with the sequence cy5-CCA CTC CTT TCC AGA AAA CT-3′ (Thermo Scientific, Waltham, USA) and IR dye 800CW (LI-COR Biosciences, Lincoln, USA) were used for detection of NCs.

3.2.1.2 Instrumentation

Ultrasonication was performed using the Branson Sonifier W-450-Digital and a microtip operating under ice cooling for 3 min at 70% amplitude with a pulse regime of 20 s sonication and 10 s pauses.

Sample purification was performed with the centrifuge Sigma 3 k-30 (Osterode am Harz, Germany). The Jeol 1400 transmission electron microscope (Freising, Germany) with an accelerating voltage of 120 kV was used for morphological studies. Sample preparation was performed by placing 20 µL of diluted NC dispersion onto a 300 mesh carbon-coated copper grid allowing to dry under ambient conditions. Scanning electron microscopy (SEM) measurements were performed with a 1530 Gemini LEO (Zeiss, Oberkochen, Germany) field emission microscope, using an accelerating voltage of 170 V. Sample preparation was performed as described above using silicon wafers instead of copper grids as substrate.

The average size and size distribution of the NS5A-NCs were determined via dynamic light scattering (DLS) at 25 °C using a Nicomp 380 submicron particle sizer (Nicomp Particle Sizing Systems, Port Ritchey, USA) at an angle of 90°.

Zeta potential was measured in 10^{-3} M potassium chloride solution at pH 6.8 and 25°C with the Malvern Zeta sizer (Malvern Instruments, Malvern, U.K.).

Quantification of MPLA adsorbed onto NS5A-NCs was performed using a Limulus Amebocyte Lysate (LAL) assay (#HIT302, Hycult Biotech, Uden, The Netherlands) according to manufacturer´s instructions. Two-fold serial dilutions of NS5A+MPLA-NCs (0.54 wt-%) in endotoxin-free water (1:1000 - 1:16.000) were analyzed. NS5A-NCs without MPLA served as reference. Loading capacity (LC) of MPLA was calculated by the ratio of the mass of adsorbed MPLA over the total mass of NCs.

3.2.1.3 Synthesis of NS5A nanocarriers

NS5A nanocarriers were synthesized adapting a modified procedure from Baier et al. in an inverse miniemulsion using a polyaddition reaction at the droplets interface for cross-linking.[236] A mixture of 125 µL of the NS5A solution (6.25 mg) and 33 µL (31.9 µg) of cy5-labeled oligonucleotides dissolved in PBS constituted the aqueous phase. For labeling with IRdye 800CW, 15 µL were added to the aqueous phase. Separately, 9 mg of the surfactant P((E/B)-*b*-EO) were dissolved in 1.88 g of cyclohexane and the mixture was added to the aqueous phase under stirring. The mixture was homogenized by ultrasound. To a solution of 2.7 mg P((E/B)-*b*-EO) in 1.25 g cyclohexane, 1.5 mg 2,4-toluene diisocyanate (TDI) was added. The mixture was added dropwise to the miniemulsion and the reaction proceeded overnight at 25 °C under stirring.

Subsequently, repetitive centrifugation (3 times for 20 min, 1,700 x g) and exchange of the upper phase with pure cyclohexane was performed to remove excess surfactant. In order to transfer NCs into the aqueous phase, 500 µL of the dispersion was added in 100 µL steps to 5 mL of an aqueous solution containing 0.1 wt-% sodium dodecyl sulfate (SDS). The mixture was subjected to an ultrasound bath for 5 min at 25 °C (25 kHz). The samples were stirred open for 24 h at 25 °C to remove cyclohexane. Repetitive centrifugation (4 times for 15 min, 1,800 x g) and exchange of the supernatant with aquapure water was applied for the removal of excess SDS.

Adsorption of MPLA onto the NC surface was performed using a slightly modified method as described previously.[260] Briefly, 1 mg of a NS5A-NC dispersion was mixed with 24 µL of MPLA/DMSO solution (0.1 wt-%) and stirred for 1 day at 4 °C. Afterwards, NCs were washed with ultrapure water two times by centrifugation at 2.500 x g for 15 min in order to remove residues of MPLA. Finally, the supernatant was removed and the NCs were redispersed in 0.9% NaCl.

3.2.2 Biological analysis

3.2.2.1 Mice

Six to 8-week old female C57BL/6J and B6N-Tyr$^{c\text{-}Brd}$/BrdCrCrl albino mice were obtained from Harlan Laboratories (Indianapolis, USA) and from the Transgenic Facility Mainz (Mainz, Germany), respectively. All mice were kept under a 12 h dark, 12 h light cycle (with food and water supply ad libitum) in the animal facility of the Translational Animal Research Center, University Medical Center Mainz, Germany. The animals were treated in accordance with NIH publications entitled “Principles for Use of Animals” and “Guide for the Care and Use of Laboratory Animals”. All protocols have been approved by the local Animal Care and Use Committee (“Landesuntersuchungsamt Rheinland-Pfalz”).

3.2.2.2 Expansion of the dendritic cell population *in vivo*

The dendritic cell population in the livers of mice was expanded *in vivo* via hydrodynamic tail vein injections using methods previously described.[260, 352-353] Briefly, 10 µg of the plasmid pUMVC3-hFLex (Vector Core Laboratory, University of Michigan, USA) encoding the secreted portion of the human Fms-like tyrosine kinase 3 ligand (hFlt3l) was dissolved in 2 mL of 0.9% NaCl and injected into tail veins of mice within 5 s. The injection was repeated on day 6; on day 12, pre-treated mice were employed for subsequent studies.

3.2.2.3 Isolation of non-parenchymal liver cells and splenocytes

The non-parenchymal liver cells (NPCs) of pre-treated mice, mainly consisting of dendritic cells, Kupffer cells, and lymphocytes, were isolated from livers as described previously.[309, 354] Splenocytes were isolated following dissection of spleens. Single cell suspensions were prepared using a 70-µm nylon cell strainer.

3.2.2.4 Cultivation of non-parenchymal liver cells and splenocytes and stimulation with nanocarriers

Isolated non-parenchymal liver cells and splenocytes were cultured at 1 x 10^6 cells/mL in culture medium composed of HEPES-buffered RPMI 1640 medium supplemented with 10 vol-% FCS, 2 mM L-glutamine, 100 U/mL penicillin, 100 µg/mL streptomycin, 1 vol-% non-essential amino acids, 1 mM sodium pyruvate and 50 µM 2-mercaptoethanol. In order to determine the influence of nanocarriers upon NPCs, different concentrations (1 / 10 / 100 µg/mL) of NS5A- or NS5A+MPLA-NCs were added to the culture medium. Applied NC concentrations were based on the total mass of the respective NC formulation. Cells were cultured for 3 h or 24 h and analyzed for NC uptake and cytokine production (intracellular cytokine staining - ICCS) as described below. Culture supernatants were obtained after 24 h incubation and analyzed in terms of cytokine secretion levels by NPCs.

3.2.2.5 Confocal laser scanning microscopy

Confocal laser scanning microscopy (CLSM) was performed in order to visualize intracellular uptake of NS5A-NCs using a Zeiss LSM 710 NLO (Oberkochen, Germany). NPCs (5 x 10^5 per well) were cultured in 8-well chamber slides (#80827, ibidi, Martinsried, Germany) at 37 °C for 24 h in the presence of 10 µg/mL cy5-labeled NS5A nanocarriers. Nuclei were stained with 2 µg/mL Hoechst 33342 (Life Technologies, Carlsbad, USA) for 30 min. Plasma membrane staining was achieved by adding 4 µg/mL CellMask Orange (Life Technologies, Carlsbad, USA) 5 min prior to analysis.

3.2.2.6 Effects of NCs after *in vivo* injection

For *in vivo* experiments 300 µg NS5A- or NS5A+MPLA-NCs were suspended in 300 µL NaCl 0.9% and intravenously injected into tail veins. Mice injected with 300 µL vehicle (0.9% NaCl) served as a negative control. NPCs from NC-treated mice were isolated 4 h after injection as described in 2.2.4 and analyzed for NC uptake and cytokine production determined by ICCS.

In vivo imaging studies were performed in order to analyze the biodistribution of NCs. Therefore, B6N-Tyr$^{c\text{-}Brd}$/BrdCrCrl albino mice were depilated at the abdominal and thoracic zone and the corresponding dorsal areas. NS5A- or NS5A+MPLA-NCs (300 µg) labeled with IR dye 800CW (LI-COR Biosciences) were injected intravenously and mice were analyzed at time points 30 min, 1 h, 2 h, 3 h, and 4 h using the IVIS SpectrumCT imager (PerkinElmer, Waltham, USA) and the Living Image software 4.5. Isolation of organs (lung, liver, spleen, kidneys) was performed 4 h after injection following ex vivo imaging in order to verify the organ distribution of NCs.

3.2.2.7 Flow cytometry and intracellular cytokine staining

Flow cytometric analysis was performed according to previously published methods using the multi-channel flow cytometer BD LSR II (BD Biosciences, San Jose, USA) equipped with FACSDiva software (BD Biosciences, San Jose, USA).[309, 352] Briefly, NPCs were incubated with 5 µg of anti-mouse CD16/32 (clone 2.4G2, rat isotype) for 15 min at 4 °C in order to block unspecific antibody binding by Fc receptors. Subsequently, NPCs were stained for 30 min with antibodies specific for CD45 (V450 – clone 30-F11), CD11c (PE-Cy7 – N418), F4/80 (FITC – BM8), CD4 (APC-Cy7 – GK1.5), CD40 (PerCP-CF710 – 1C10), CD80 (FITC – 16-10A1) or CD86 (PE-Cy7 – GL1). For intracellular cytokine stainings (ICCS), isolated NPCs were cultured for 16 h in culture medium supplemented with or without different NC formulations or different concentrations of NS5A (immunization readouts). A protein transport inhibitor containing Brefeldin A (GolgiPlug - BD Biosciences, San Jose, USA) was added after 3 h of incubation in order to inhibit cytokine secretion. Cells were then harvested, fixed and permeabilized using a cytofix/cytoperm kit (BD Pharmingen, San Jose, USA) and additionally incubated with anti-mouse interleukin-6 (PE – MP5-20F3), IL-12p70 (V450 – C15.6) or IFNγ (APC – XMG1.2) followed by flow cytometric analyses.

3.2.2.8 Quantification of cytokine secretion

Quantification of cytokine secretion by NPCs was performed using a cytometric bead array kit (BD CBA Mouse Inflammation Kit, BD Biosciences, San Jose, USA) in accordance with manufacturer´s instructions followed by data analysis using FCAP 3.0 software (SoftFlow, Inc., Pecs, Hungary). Cytokines secreted by NPCs and splenocytes derived from immunized mice were determined using commercial enzyme-linked immunosorbent assays (Read-Set-Go, eBioscience, San Diego, USA) measuring IFNγ, IL-2, and IL-4 according to manufacturer´s instructions.

3.2.2.9 Immunization

Following expansion of DCs *in vivo*, groups of 5 mice each were immunized as follows: (i) NS5A-NCs, (ii) NS5A+MPLA-NCs, (iii) NS5A+MPLA-NCs + αCD40, (iv) OVA+MPLA-NCs. Mice were inoculated intravenously three times at 2-week intervals with 50 µg of NCs each. In the case of group (iii), 50 µg αCD40 was injected intraperitoneally at each immunization as a positive control. One week after the final inoculation, mice were sacrificed and NPCs and splenocytes were isolated for subsequent analyses.

3.2.2.10 Sera collection and humoral immune response

Sera of immunized mice were collected by cardiac puncture and subsequent centrifugation at 10,000 x g for 5 min. Quantification of NS5A-specific antibody titers in serum samples was assessed by ELISA. Therefore, high binding microtiter plates (Greiner Bio-One, Kremsmünster, Austria) were coated with 10 µg/mL NS5A dissolved in 100 mM sodium bicarbonate buffer (pH 9.6) over night at 4 °C. Unspecific binding of antibodies was blocked by incubation with 5 wt-% bovine serum albumin for 1 h followed by a 2 h incubation of two-fold serial dilutions of serum samples. NS5A-specific antibodies present in sera were labeled with a goat anti-mouse IgG-peroxidase (1:2,000 in PBS - #A4416, Sigma-Aldrich, St. Louis, USA) for 2 h. Visualization of NS5A antibodies was achieved by incubation with TMB substrate for 10 min followed by subsequent absorbance measurements at 450 nm.

3.2.2.11 Statistical analysis

Experiments were performed in triplicates and analyzed using SigmaPlot 11 software (Systat Software, Inc., Erkrath, Germany) and GraphPad Prism 6.0 (GraphPad Software, Inc., La Jolla, USA). For comparisons between two groups only, a non-paired Student's *t*-test was performed (* $P < 0.05$; ** $P < 0.01$; *** $P < 0.001$). When more than two groups were compared to each other, a one way ANOVA test or a Kruskall-Wallis test were performed followed by a Holm-Sidak or Tukey posthoc test procedure, respectively, in order to determine which groups differed significantly.

3.3 Experimental details for section 2.3

3.3.1 Materials

All chemicals and materials were used as received. Dexamethasone 21-phosphate disodium salt was purchased from Alfa Aesar. Dexamethasone and 2,4-toluene

diisocyanate (TDI), chloroform (HPLC grade) and stains-all dye were purchased from Sigma Aldrich. Cyclohexane (HPLC grade) and the osmotic reagent sodium chloride were purchased from VWR. The block copolymer poly((ethylene-*co*-butylene)-*b*-(ethylene oxide) P(E/B)-*b*-EO) used as the oil soluble surfactant was synthesized as described in literature[346] and consists of a poly((ethylene-co-butylene) block (NMR: M_n = 3,900 g/mol) and a poly(ethylene oxide) block (NMR: M_n = 2,700 g/mol). The anionic surfactant sodium dodecyl sulfate (SDS) was purchased from Alfa Aesar.

3.3.2 Instrumentation

For miniemulsion preparation, the Branson Sonifier W-450-Digital was used with a ½" tip, operating under ice cooling for 3 min at 70% amplitude with pulse cycles of 20 s sonication and 10 s pauses. For breakage of the nanocarriers after synthesis, the ⅛" tip was used, with operation conditions of 5 min, 70% amplitude, 20 s sonication, 10 s pause. Lost volume of water due to evaporation was replaced.

For purification, the Sigma 3 k-30 centrifuge from Sigma Centrifuges, UK was used.

Morphological studies were performed with transmission electron microscopy (TEM) and scanning electron microscopy (SEM) as described in the sections above.

The average size and size distribution of the nanocarriers were determined via dynamic light scattering (DLS) at 25 °C using a Nicomp 380 submicron particle sizer (Nicomp Particle Sizing Systems, USA) at an angle of 90 °.

FT-IR measurements were performed with the PerkinElmer Spectrum BX FT-IR spectrometer and the spectrum was recorded between 4000 and 400 cm^{-1}. For the measurements, sample were freeze-dried and pressed with KBr to a pellet.

Zeta potential measurements were performed in 10^{-3} M potassium chloride solution at pH 6.8 and 25 °C with Malvern Zeta sizer (Malvern Instruments, U.K.).

Surface tension measurements were performed with the ring tensiometer DCAT 21 from DataPhysics at 20°C.

For HPLC analysis, all samples were filtered gently through a 0.45 µm filter. The HPLC from Agilent Technologies 1200 Series operating at 20 °C was used. For detection of DXM at 240 nm, the DAD detector was used. An Agilent Eclipse plus C18 column was

used with a flow rate of 1 mL/min. The gradient was composed of acetonitrile/water+0.1% trifluoroacetic acid (starting with 20%:80% and reaching 100% acetonitrile after 10 min).

3.3.3 Methods

3.3.3.1 Nanocarrier synthesis

DXM-nanocarriers were synthesized as described in the prior sections. Briefly, 100 mg of DXM were dissolved in 500 µL demineralized water together with 7.5 mg NaCl. The cyclohexane phase added to the mixture consisted of 35.8 mg of surfactant P((E/B)-*b*-EO) dissolved in 7.5 g of cyclohexane. The mixture was homogenized by ultrasound as described above. A solution of 10.7 mg P((E/B)-*b*-EO) and 34 mg TDI in 5 g of cyclohexane was then added drop-wise to the miniemulsion and the mixture was allowed to stir overnight at 25 °C.

The synthesized PNCs were purified by repetitive centrifugation (3 times for 20 min, RCF 1664) to remove the excess of the surfactant and re-dispersed in pure cyclohexane. For transfer into the aqueous phase, 600 µL of nanocarrier dispersion in cyclohexane were added drop-wise to 5 g of an aqueous SDS solution (0.1 wt-%) subjected to an ultrasound bath for 3 min at 25 °C (25 kHz). Subsequently, the samples were stirred open for 24 h at 25 °C to evaporate cyclohexane. To remove excess SDS, the dispersion was purified by centrifugation and replacement of the supernatant by demineralized water (4 times for 15 min, RCF 1817) in 2 mL centrifuge tubes. The residual amount of SDS was quantified using the stains-all dye (Figure 94).

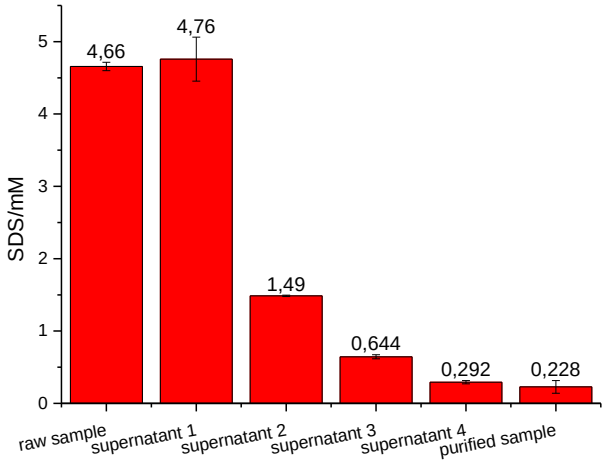

Figure 94: SDS quantification for DXM nanocarriers with stains-all dye.

3.3.3.2 Nanoparticle synthesis by solvent evaporation

After purification of DXM-nanocarriers in the cyclohexane phase, they were freeze-dried. 20 mg of freeze-dried carrier material were dissolved in 2.5 g chloroform. All undissolved residuals were removed by filtration. The organic phase was added to 10 mL of an aqueous solution of SDS (2 g/L) and stirred vigorously at 1250 rpm for 1 h in a closed vial. The pre-emulsion was subjected to ultrasound for 3 min (70% amplitude, 30 s sonication, 10 s pause). Afterwards, the emulsion was stirred at 40°C at 500 rpm overnight in an open vial to evaporate the chloroform. Finally, the dispersion was dialyzed for 5 days with frequent water exchange to remove excess SDS and any residual soluble DXM.

3.3.3.3 Biological analysis

Six week old female C57BL/6J mice were obtained from Harlan Laboratories (Indianapolis, USA), respectively. All mice were kept under a 12 h dark, 12 h light cycle (with food and water supply ad libitum) in the animal facility of the Translational Animal Research Center, University Medical Center Mainz, Germany. The animals were treated in accordance with NIH publications entitled “Principles for Use of Animals” and “Guide for the Care and Use of Laboratory Animals”. All protocols have been approved by the local Animal Care and Use Committee (“Landesuntersuchungsamt Rheinland-Pfalz”). 8 mice were used per group. Over a period of 10 days, 60µg DXM-NCs per 20g body weight and 3µg soluble DXM per 20g body weight, respectively, were applied intravenously per day. The control group was treated with NaCl. On day 10, the mice were sacrificed and the thymus isolated to determine its weight.

3.4 Experimental details for section 2.4

3.4.1 Materials

All chemicals and materials were used as received. Human serum albumin (>97% purity) and albumin from chicken egg white (grade VI) were purchased from Sigma Aldrich as well as benzene, 2,4-toluene diisocyanate (TDI), dimethylsulfoxide (DMSO) (>99%), 4-formylbenzoic acid (97%), benzenesulfonohydrazide (98%) and 5-norbornene-2-carboxylic acid (98%, *endo/exo* mixture), 5-norbornene-2-methanol (98%, *endo/exo* mixture), acetylenedicarboxylic acid (95%) 1,6-hexanediol (99%) and 1,4-benzenedimethanol (99%) and the stains-all dye. Cyclohexane (HPLC grade) and HCl (37%) were purchased from VWR. The block copolymer poly((ethylene-*co*-butylene)-*b*-(ethylene oxide) P((E/B)-*b*-EO) used as the oil soluble surfactant was synthesized as

described in literature[346] and consists of a poly((ethylene-*co*-butylene) block (NMR: M_n = 3,900 g/mol) and a poly(ethylene oxide) block (NMR: M_n = 2,700 g/mol). The anionic surfactant sodium dodecyl sulfate (SDS) was purchased from Alfa Aesar. DQ™ ovalbumin (D-12053) was purchased from Molecular Probes and hydrophilic CdTe quantum dots from PlasmaChem. Sulforhodamine 101 (SR101) was purchased from BioChemica, Aldrich. Amicon Ultra-2 centrifugal filter devices were purchased from Merck Millipore (100,000 nominal molecular weight limit (NMWL)). The human blood plasma, prepared according to the standard guidelines, was obtained from the University Clinic of Mainz (Germany). Due to the high variation of protein composition of different patients, a pool of plasma obtained by the mixture of serum of several healthy donors was used for all measurements. For cell experiments, Histopaque-1077 and Hank´s Balanced Salt Solution from Sigma Aldrich was used. Magnetic cell separator (MACS) was obtained from Miltenyi Biotec. Propidium iodide solution was purchased from eBiosciences. The immunostimulant lipopolysaccharide (LPS) and R848 were obtained from Invivogen (Toulouse, France). The magnesium and calcium free phosphate-buffered saline, was purchased from Life Technologies. Demineralized water was used for all experiments.

3.4.2 Instrumentation

For ultrasonication, a Branson Sonifier W-450-Digital was used with a ½" tip, operating under ice cooling for 3 min at 70% amplitude with pulse cycles of 20 s sonication and 10 s pauses.

Sigma 3 k-30 from Sigma Centrifuges, UK was used for centrifugation.

Morphological studies were performed with transmission electron microscopy (TEM). For the measurements, 20 µL of diluted PNC dispersion was placed onto a 300 mesh carbon-coated copper grid and allowed to dry under ambient conditions. The TEM measurements were performed with a Jeol 1400 transmission electron microscope was used with an accelerating voltage of 120 kV.

The average size and size distribution of the PNCs were measured via dynamic light scattering (DLS) at 25 °C using a Nicomp 380 submicron particle sizer (Nicomp Particle Sizing Systems, USA) at an angle of 90°.

For Zeta potential measurements in 10^{-3} M potassium chloride solution at pH 6.8 and 25 °C, the Malvern Zeta sizer (Malvern Instruments, U.K.) was used.

All dynamic light scattering experiments in human blood plasma were performed on a commercially available instrument from ALV GmbH consisting of a goniometer and

an ALV-5000 multiple-tau full-digital correlator with 320 channels. A helium-neon laser (JDS Uniphase with a single mode intensity of 25 mW operating at a laser wavelength of λ_0 = 632.8 nm) was used as the light source. All solutions for light scattering experiments were prepared in dust-free quartz light scattering cuvettes (inner diameter 18 mm, Hellma, Müllheim), which were cleaned prior to use with distilled acetone.

Fluorescence intensity and absorbance measurements were performed with the Infinite M1000 plate reader from Tecan, Austria using 96-well plates.

UV/Vis spectroscopy was performed with a PerkinElmer Lambda 25 spectrophotometer.

For nuclear magnetic resonance (NMR) analysis, ^{1}H and ^{13}C NMR spectra were recorded with Bruker Avance spectrometers operating with 250, 300, 500 and 700 MHz frequencies. Deuterated chloroform or deuterated DMSO was used as the solvent.

Raman spectroscopy was performed on a Bruker Senterra Raman microscope and on a homebuilt setup within a Horiba iHr550 spectrograph, an Horiba Symphony II CCD camera with liquid nitrogen cooling and a 633 nm HeNe laser in an excitation- and detection angle of 55°.

Flow cytometric analysis was performed with a BD FACS Canto II flow cytometer equipped with BD FACSDiva software (BD Biosciences). Data were analyzed using FlowJo software (FlowJo, Ashland, USA) and are presented as means ± SEM of the values (GraphPad Software, La Jolla, USA).

3.4.3 Methods

3.4.3.1 Synthesis of 4-(5-phenyl-2H-tetrazol-2-yl)phenol and of 4-(5-phenyl-2H-tetrazol-2-yl)benzoic acid

The tetrazoles were synthesized according to the procedure decribed by Han et al.[329] For 4-(5-phenyl-2H-tetrazol-2-yl)phenol, 0.804 g (5.5 mmol) of 5-phenyl tetrazole was added to a Schlenck tube together with 1.517 g (11 mmol) of 4-hydroxyphenylboronic acid and 10 mol-% Cu_2O respective to the tetrazole. 40 mL DMSO were added as the solvent. The mixture was stirred at 100 °C for 7 h under oxygen atmosphere. Afterwards, the mixture was cooled to room temperature, diluted with 200 mL EtOAc and washed with 50 mL 1 M HCl and three times with 50 mL of water. The organic phase was dried over $MgSO_4$ and concentrated under reduced pressure. The product was purified by column chromatography (PE: EtOAc 1:1). Yield: 1.18 g (4.9 mmol, 90%). ^{1}H NMR (250 MHz,

DMSO-d6) δ: 10.25 (s, 1H, OH), 8.16 - 8.13 (m, 2H, C_6H_5), 7.93 (dd, J = 9.0 Hz, 2H, C_6H_4), 7.63 – 7.58 (m, 3H, C_6H_5), 7.03 - 6.99 (dd, J = 9.0 Hz, 2H, C_6H_4).

For 4-(5-phenyl-2H-tetrazol-2-yl)benzoic acid, 0.292 g (2 mmol) of 5-phenyl tetrazole and 0.664 g (4 mmol) of 4-carboxyphenylboronic acid were used with 16 mL DMSO, 10 mol-% Cu_2O and 0.48 mL of pyridine and proceeded as described above. After the reaction, the micture was diluted with 150 mL of EtOAc and washed two times with 15 mL 1 M HCl and four times with 25 mL water. The mixture was dissolved in 1 M NaOH and the product precipitated with 1 M HCl. After drying, a white precipitate was obtained. Yield: 0.219 g (0.82 mmol, 41%). ^{1}H NMR (250 MHz, DMSO-d6) δ: 13.41 (s, 1H, COOH), 8.42 – 8.09 (m, 6H, C_6H_4, C_6H_5), 7.63 (m, 3H, C_6H_5).

3.4.3.2 Synthesis of 4-(2-phenyl-2H-tetrazol-5-yl)benzoic acid (TET).

The synthesis of TET was achieved in three steps, following previously reported procedures.[325, 327] In the first step, benzenesulfonohydrazide (1.72 g, 10.0 mmol) was added to 1.5 g (10.0 mmol) 4-formylbenzoic acid in 100 mL EtOH and the mixture stirred for 30 min. The resulting hydrazone adduct was precipitated with 200 mL DI-water, filtered and dried overnight. Yield: 2.74 g (9.13 mmol, 91.3%). Next, the diazonium salt was prepared by dissolving 0.79 g (11.4 mmol) $NaNO_2$ in 4.6 mL water and adding it to a cooled mixture of 1.05 g (11.4 mmol) aniline in 18 mL water/EtOH (1:1) with 3 mL conc. HCl. The obtained diazonium salt was added dropwise to the hydrazone dissolved in 68 mL pyridine and cooled with an ice-salt-bath to -20 °C. The mixture was stirred for 6 h and extracted afterwards for three times with 150 mL EtOAc. The organic solution was washed with 100 mL 3 M HCl. After removal of the solvent, the product was isolated by recrystallization from hot EtOH. Yield: 2.23 g (8.35 mmol, 91.5%). ^{1}H NMR (250 MHz, DMSO-d6) δ: 13.28 (s, 1 H, COOH), 8.30 (d, J = 8.5 Hz, 2 H, C_6H_4), 8.23 – 8.10 (m, 4 H, C_6H_4, C_6H_5), 7.76 – 7.58 (m, 3 H, C_6H_5) ppm. Respective spectra can be found in the appendix.

3.4.3.3 TET-crosslinker synthesis

For the Steglich esterification of TET with 1,6-hexanediol, 0.869 g (3.26 mmol) of TET and 153.8 g (0.87 mmol) were dissolved together with 40 mg DMAP (10 mol-% respective to TET) in 100 mL DCM and cooled to 0 °C. After dissolution of the compounds, 0.75 g (3.9 mmol) of 1-ethyl-3-(3-dimethylaminopropyl)carbodiimide (EDC) were added. The mixture was stirred overnight and allowed to warm to room temperature.

Afterwards, the product was isolated by recrystallization from hot THF. Yield: 0.36 g (0.59 mmol, 67%). ^{1}H NMR (250 MHz, Chloroform-d) δ: 8.34 – 8.31 (d, J = 8.7 Hz, 4H, C_6H_4), 8.22 – 8.18 (m, 8H, C_6H_4, C_6H_5), 7.62 – 7.49 (m, 6H, C_6H_5), 4.40 (t, J = 6.5 Hz, 4H, O-CH_2), 1.90 – 1.84 (m, 4H, O-CH_2-CH_2), 1.60 – 1.54 (m, 4H, CH_2).

The trifunctional cross-linker was synthesized by using 0.5 g (1.88 mmol) TET and 0.084 g (0.63 mmol) trimethylolpropane in 45 mL of DCM with 23 mg (0.188 mmol) DMAP and 441 mg (2.3 mmol) EDC proceeding as described above. The product was isolated by column chromatography (PE:EtOAc 2:1). Yield: 0.34 g (0.39 mmol, 61%). 1H NMR (250 MHz, Chloroform-d) δ: 8.39 – 8.04 and 7.68 – 7.43 (m, 27H, C_6H_4, C_6H_5), 4.62, 4.49 (s, 6H, OCH_2), 1.68 (q, J = 7.5 Hz, 2H, CH_2), 1.06 (t, J = 7.5 Hz, 3H, CH_3).

3.4.3.4 Coupling of 4-(2-phenyl-2H-tetrazol-5-yl)benzoic acid to proteins

For the coupling reaction of 4-(2-phenyl-2*H*-tetrazol-5-yl)benzoic acid to ovalbumin and human serum albumin, 500 mg of the respective protein were dissolved in 5 mL of DMSO. TET and about 10 mol-% DMAP respective to the TET amount were added and the mixture stirred until a homogeneous solution was obtained. In the next step, equivalent amounts of 1-ethyl-3-(3-dimethylaminopropyl)carbodiimide (EDC) respective to TET were added and the reaction was allowed to proceed under ambient conditions for 48 h. The product was precipitated with 50 mL i-PrOH, filtered and dissolved in water. The side-products were removed by dialysis for 4 days (MWCO 1000 Da) under frequent water exchange. After lyophilization, approximately 430 mg of the product was obtained. The amount of TET/protein was determined by UV/vis spectroscopy in DMSO, using the absorption maximum of TET in DMSO at 280 nm for calibration (Figure 95) and unmodified proteins as blanks to exclude their contribution to the absorption intensity. The amounts used for the reaction and the obtained degrees of modification are depicted in Table 8.

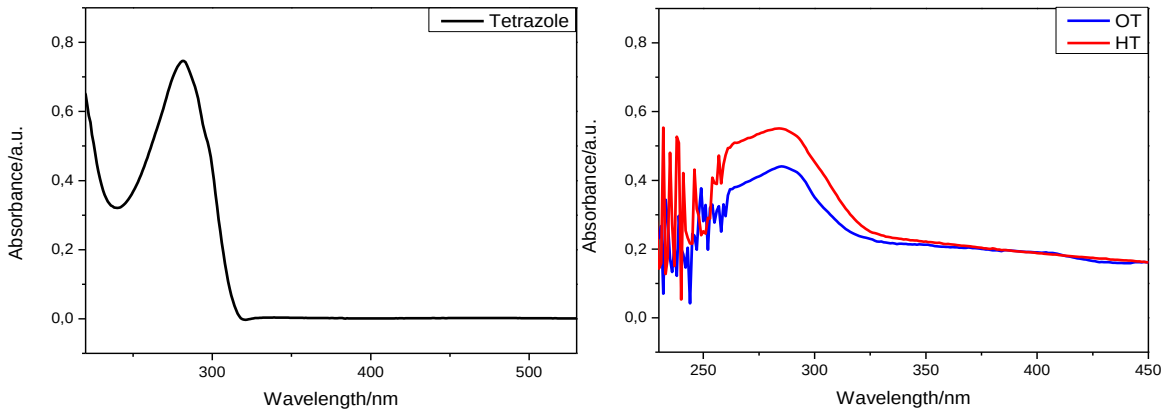

Figure 95: left: absorption spectrum of TET, right: absorption spectra of TET-coupled proteins after blanking with native proteins to exclude their contribution to the absorption intensity (OT for OVA-TET, HT for HSA-TET).

Table 8: Reagents used for protein modification with TET

	Protein/ mol	TET/ mol	DMAP/ mol	EDC/ mol	Spectroscopically determined amount of TET/mol protein
OVA	$1.17 \cdot 10^{-5}$	$2.34 \cdot 10^{-4}$	$2.34 \cdot 10^{-5}$	$2.34 \cdot 10^{-4}$	13
HSA	$7.53 \cdot 10^{-6}$	$1.51 \cdot 10^{-4}$	$1.51 \cdot 10^{-5}$	$1.51 \cdot 10^{-4}$	12

3.4.3.1 Synthesis of dinorbornene cross-linkers

Dinorbornene cross-linker were synthesized by esterification reaction of a dialcohol (diacid) with a respective norbornene-acid or –alcohol (cf. Table 9). The starting compounds were dissolved in 200 mL of benzene, pTsOH was used in catalytic amounts and the mixture was stirred at 100 °C under reflux using a Dean-Stark apparatus. Afterwards, the product was washed twice with 30 mL saturated $NaHCO_3$ solution and twice with 30 mL of water to remove the unreacted acid. In case of DN3, the product was washed twice with conc. HCl and water, respectively. The products were purified after solvent removal by column chromatography (PE:EtOAc 3:1, R_F values: DN1:0.71, DN2: 0.57, DN3: 0.61, DN4: 0.64, DN5: 0.70)) and verified by TLC prior to NMR analysis.

Table 9: Amounts of dialcohol and diacid used for cross-linker synthesis.

Cross-linker	Type of acid	Amount of acid/ g [mmol]	Type of alcohol	Amount of alcohol/ g [mmol]	Yield/ g [mmol]/ %
DN1	5-norbornene-2-carboxylic acid	8.05 [58.3]	1,6-hexanediol	2.28 [19.3]	3.5 [9.88]/ 51
DN2	5-norbornene-2-carboxylic acid	10.0 [72.4]	1,4-benzenedimethanol	3.33 [24.1]	6.3 [16.6]/ 69
DN3	acetylenedicarboxylic acid	1.64 [14.4]	5-norbornene-2-methanol	4.76 [38.3]	1.5 [4.5]/ 31
DN4	5-norbornene-2-carboxylic acid	10.0 [72.4]	triethylene glycol	3.62 [24.1]	4.4 [11.3]/ 47
DN5	3,3'-Dithiodipropionic acid	1.42 [6.75]	5-norbornene-2-methanol	2.51 [20.2]	1.0 [2.30]/ 34

DN1: ^{1}H NMR (700 MHz, $CDCl_3$) δ 6.24 – 5.85 (m, 4 H, CH=CH), 4.20 – 3.88 (m, 4 H, OCH_2), 3.20 – 2.90 and 2.21 (m, 6 H, CH), 1.90 (m, 2 H, CH_2), 1.74 – 1.28 (m, 14 H, CH_2, CH) ppm. ^{13}C NMR (176 MHz, $CDCl_3$) δ 176.26 – 174.76 (C=O), 137.99 – 132.29 (C=C), 64.31 – 64.07 (C-O), 49.59 (CH-COO), 46.58 – 25.61 (C_{aliph}) ppm. FT-IR ν=3061 (=CH), 2970 (C-H), 2869 (CH_2), 1732 (C=O), 1178 (C-O) cm^{-1}. Respective spectra can be found in the appendix.

DN2: ^{1}H NMR (500 MHz, $CDCl_3$) δ 7.80 – 7.30 (m, 4H, C_6H_4), 6.23 – 5.83 (m, 4H, CH=CH), 5.23 – 5.00 (m, 2H, OCH_2) and 4.70 and 4.56 (s, 2H, OCH_2), 3.23 – 2.92 (m, 5.5H, CH), 2.27 (m, 0.5H, CH), 1.93 (m, 2H, CH_2), 1.54 – 1.26 (m, 6H, CH_2) ppm. ^{13}C NMR (176 MHz, $CDCl_3$) δ 176.09 – 174.60 (C=O), 138.20 – 135.80 (C=C), 132.36 – 127.95 ($C=C_{arom}$), 65.97 – 65.73 (CH_2-O), 49.73 – 29.35 (C_{aliph}) ppm. FT-IR ν=3061 (C=H), 2974 (C-H), 2869 (CH_2), 1732 (C=O), 1517 ($C=C_{arom}$), 1170 (C-O) cm^{-1}.

DN3: ^{1}H NMR (500 MHz, $CDCl_3$) δ 6.28 – 5.83 (m, 4H, CH=CH), 4.41 – 3.73 (m, 4H, O-CH_2), 2.96 – 2.65 (m, 4H, CH), 2.44 (m, 1H, CH_{en}), 1.87 (m, 1.4H, CH_{2en}), 1.78 (m, 1.4H, CH_{ex}), 1.53 – 1.04 (m, 7H, CH_2,CH), 0.56 (m, 1H, CH_{2en}) ppm. ^{13}C NMR (126 MHz, $CDCl_3$) δ 152.30 (C=O), 138.40 – 132.32 (C=C), 75.20 (C≡C), 71.31 – 70.74 (CH_2-O),

49.83-29.35 (C_{aliph}) ppm. FT-IR ν=3061 (C=H), 2963 (C-H), 2869 (CH_2), 1724 (C=O), 1252 (C-O) cm^{-1}.

DN4: ^{1}H NMR (250 MHz, $CDCl_3$) δ 6.30 – 5.83 (m, 4H, CH=CH), 4.31 – 4.07 (m, 4H, $COOCH_2$), 3.77 – 3.57 (m, 8H, CH_2-O), 3.27 – 2.82 and 2.29 – 2.16 (m, 6H, CH), 1.99 – 1.77 and 1.56 – 1.19 (m, 8H, CH_2) ppm. ^{13}C NMR (176 MHz, $CDCl_3$) δ 176.09 – 174.57 (C=O), 137.93 – 132.21 (C=C), 77.16 – 69.12 (CH_2-O), 63.13 (CH_2-O-C=O), 49.46 – 29.12 (C_{aliph}) ppm. FT-IR ν=3061 (C=H), 2970 (C-H), 2873 (CH_2), 1732 (C=O), 1181 (C-O) cm^{-1}.

DN5: ^{1}H NMR (300 MHz, $CDCl_3$) δ 6.27 – 5.85 (m, 4H, CH=CH), 4.23 – 3.63 (m, 4H, O-CH_2), 2.98 – 2.68 (m, 12H, CH, S-CH_2CH_2), 2.45 – 2.32 (m, 1H, CH_{en}), 1.90 – 1.65 (m, 2H, CH_{2en}), 1.50 – 1.01 (m, 7H, CH_2,CH), 0.55 (m, 1H, CH_{2en})ppm. ^{13}C NMR (176 MHz, $CDCl_3$) δ 171.73 – 171.61 (C=O), 137.65 – 132.12 (C=C), 77.21 – 76.84 (C-S), 68.94-68.27 (C-O), 49.39 (CH-COO), 44.96 – 29.00 (C_{aliph}) ppm. FT-IR ν=3058 (C=H), 2960 (C-H), 2865 (CH_2), 1731 (C=O), 1167 (C-O) cm^{-1}.

3.4.3.2 Protein Nanocarrier (PNC) synthesis

First, 12.5 mg of the TET-functionalized protein were dissolved in 0.25 g buffer (Na_2HPO_4/KH_2HPO_4 at pH 7.6). In case of encapsulation of R848, 50 µL with a concentration of 10 mg/mL in DMSO was added to the aqueous solution. 17.9 mg of surfactant P((E/B)-*b*-EO) were dissolved in 3.75 g of cyclohexane and the mixture was added drop-wise to the stirred aqueous solution. The pre-emulsion was homogenized by ultrasound. A third solution containing of 1.0 mg P((E/B)-*b*-EO) and 0.5 g of cyclohexane and a 100-fold molar excess (to TET in the system) of the dinorbornene cross-linker was then added drop-wise to the stirred miniemulsion. The mixture was transferred to a quartz glass tube attached to a peristaltic pump with a flow rate of 2.5 mL/min. The miniemulsion was irradiated with a hand-held UV lamp at 254 nm for 30 min.

After preparation, the PNCs were purified by repetitive centrifugation (3 times for 20 min, RCF 1664) to remove excess surfactant and cross-linker and re-dispersed in pure cyclohexane. For transfer into the aqueous phase, 500 µL of PNC dispersion from the cyclohexane phase were added drop-wise to 5 g of an aqueous SDS solution (0.1 wt-%) under mechanical agitation in an ultrasound bath over 3 min at 25 °C (25 kHz). Subsequently, the samples were stirred in open vials for 24 h at 25 °C to evaporate cyclohexane. For removal of excess SDS, the dispersion was purified via Amicon Ultra-2 centrifugal filters (3 times for 20 min, RCF 1664) and redispersed in DI-water. The

successful removal of excess SDS could be monitored by the concentration-dependent color change of stains-all dye (see Figure 96).[270]

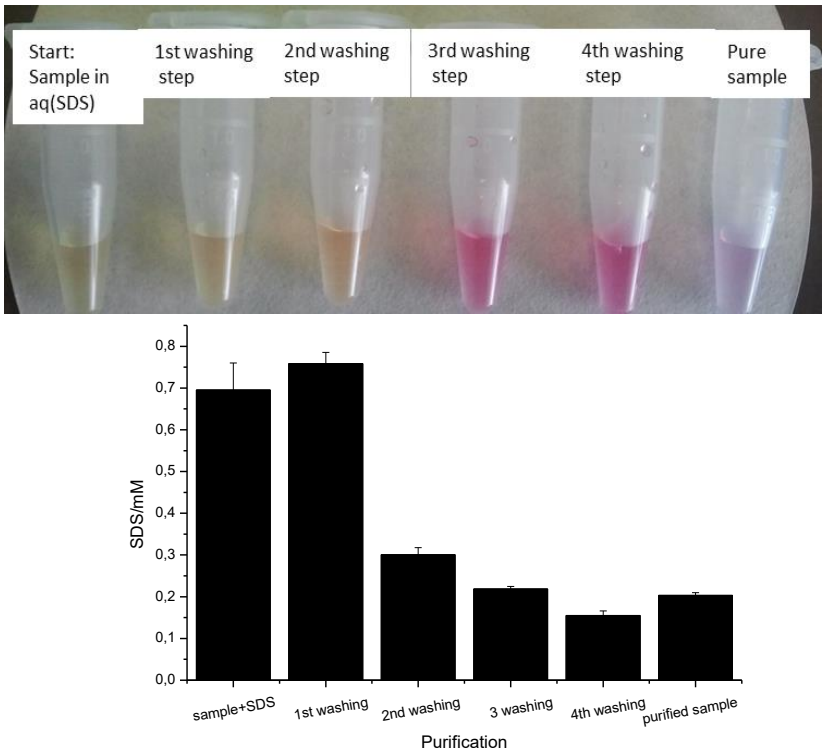

Figure 96: SDS quantification of OT-DN1 with stains-all dye. Top: colorimetric change of the dye from yellow (high SDS content) to purple (low SDS content). Bottom: SDS amount in the unpurified and purified sample and in the respective supernatants.

3.4.3.3 Determination of PNC permeability and encapsulation efficiency

The permeability of the PNC-shell was studied by encapsulation of the fluorescent dye SR101 which shows an absorption maximum at 550 nm and an emission maximum at 605 nm. Since UV light contributes to bleaching of the dye, a calibration curve was recorded by treating the dye solution with UV-light, using the same conditions as for PNC synthesis. 0.54 mg of SR101 was mixed with the aqueous phase and the reaction was carried out as described above. After re-dispersion in the aqueous SDS solution, the PNCs were sedimented by centrifugation with the Amicon Ultra-2 centrifugal filter devices and the fluorescence intensity of the permeate was measured at the plate reader. The encapsulation efficiency was calculated by correlating the obtained fluorescence intensity to the intensity of the starting concentration of SR101. To determine the permeability, the experiment was repeated over a given period and the fluorescence signal was compared to the initial value. The experiment was conducted two times with three single measurements.

3.4.3.4 Biodegradability of PNCs

The degradation of DQ ovalbumin labeled PNCs (encapsulation of 150 µL with a concentration of 1mg/mL in PBS) was studied with the serine protease trypsin. 20 µL of trypsin with a concentration of 0.5 mg/mL in PBS buffer were added to 100 µL PNC dispersion. Control measurements of the PNCs in PBS buffer were carried out additionally. The changes in fluorescence intensity were recorded over 2.5 h at 37 °C. For the proteolytic release of hydrophilic CdTe quantum dots, 3 mg of the quantum dots were encapsulated in HT-DN1. After purification and transfer to water, the PNC dispersion was treated with trypsin (amounts as above), aliquots were taken over time, centrifuged for 10 min and the supernatant was used for measurement. The control measurement (0 min) was performed by adding water instead of trypsin.

3.4.3.5 Toxicity evaluation of PNCs

Human monocyte-derived dendritic cells (moDCs) were generated as previously described.[348] Briefly, adult peripheral blood mononuclear cells (PBMCs) were isolated from fresh buffy coats, obtained from healthy voluntary donors upon informed consent (University of Mainz, Germany), by centrifugation through Histopaque®-1077 density gradient media for 20 min at 900 x g and 20 °C. The interphase consisting of PBMCs was subsequently extracted and washed with Hank´s Balanced Salt Solution. $CD14^+$ monocytes were isolated from the PBMC fraction by positive selection using CD14 MicroBeads, MACS LS columns and a magnetic cell separator in accordance with the manufacturer's instructions. Purified $CD14^+$ monocytes were cultured in X-Vivo 15 medium supplemented with L-glutamine, 100 U/mL penicillin, 100 µg/mL streptomycin, 200 U/mL GM-CSF and 200 U/mL IL-4 for 6 days. Subsequently, immature moDCs were collected and co-cultured in presence of different concentrations of the PNCs (1.0 / 10 / 100 µg/mL) or without PNCs for 24 h. Subsequently, moDCs were harvested and incubated with 10 µL propidium iodide solution for 2 min in order to stain nuclei of dead cells, followed by flow cytometric analysis.

3.4.3.6 Dynamic Light Scattering in human blood plasma

For stability measurements in human blood plasma, first DLS analysis of the pure PNCs was performed by dilution of 100 µL of PNC dispersion with 1 mL filtered PBS buffer solution at physiological pH (pH 7.4) and salinity (0.125 M). For the measurement of PNCs in human blood plasma, 100 µL of the PNC dispersion were added to 1 mL plasma filtered through a 0.2 µm GS filter and the mixture was incubated at 37 °C for

30 min. DLS analysis of plasma was performed similarly to maintain the same dilutions. All DLS measurements were performed at 37 °C.

3.4.3.7 Protein corona analysis

Human blood plasma was obtained from the Department of Transfusion Medicine Mainz from healthy donors. To remove any aggregated plasma samples were centrifuged for 30 min at 20000 g before usage.

Protein nanocarriers (1 mg) were incubated with human blood plasma (1 mL) for 1 h at 37 °C with constant agitation (300 rpm). Unbound proteins were removed via centrifugation at 20000 g for 30 min. The remaining nanocarrier pellet was re-suspended in PBS (1 mL) and washed by three centrifugation steps (20000 g, 30 min). After the last washing step, protein nanocarriers bound with proteins were re-suspended in urea-thiourea buffer (7 M urea, 2 M thiourea, 4% CHAPS) and bound proteins were quantified by Pierce assay and identified with SDS-PAGE and LC-MS/MS.

SDS-PAGE. Protein solutions (6 µg in 26 µL total volume) were added to LDS NuPAGE sample buffer (4 µL) and NuPAGE sample reducing agent (10 µL). This mixture (total volume: 40 µL) was heated up for 10 min at 70 °C, loaded onto a 10% NuPAGE bis-tris gel (10-well) in a chamber with NuPAGE MES SDS running buffer and SeeBlue Plus2 prestained standard as protein marker. Proteins were separated at 100 V for 1 h and washed with distilled water. Gels were stained with Simply Blue^{TM} for at least 4 h and de-stained with distilled water overnight.

Protein quantification. Protein concentration were quantified with the Pierce 660 nm protein assay (Thermo Scientific; Germany) according to manufacturer's instructions and bovine serum albumin (Serva, Germany) was used a standard. Absorption was measured at 660 nm at the plate reader.

In solution digestion. Tryptic digestion was performed after the protocol of Tenzer *et al.*[355] with the following adjustments. Proteins were precipitated overnight using ProteoExtract protein precipitation kit (CalBioChem) according to the manufacturer's instructions. The resulting protein pellet was isolated via centrifugation (14000 g, 10 min) and washed twice with washing buffer (500 µL, CalBioChem). The resulting protein pellet was re-suspended in RapiGest SF (Waters Cooperation) dissolved in 50 mM ammonium bicarbonate (Sigma) and incubated at 80 °C for 15 min. Proteins were reduced by adding dithiothreitol (Sigma) to gain a final concentration of 5 mM and incubated for 45 min at 56 °C. For alkylation, iodoacetoamide (final concentration 15 mM, Sigma) was added and

the solution was incubated in the dark for 1 h. Tryptic digestion with a trypsin:protein ratio of 1:50 was carried out over 14 h at 37 °C. The reaction was quenched by adding 2 µL hydrochloric acid (Sigma). To remove degradation products of RapiGest SF, peptide samples were centrifuged (14.000 g, 15 min) and the remaining supernatant containing digested peptides was applied to LC-MS/MS.

Liquid-chromatography mass-spectrometry (LC-MS) analysis. For absolute quantification, peptide samples were spiked with 25 fmol/µL of Hi^3 EColi Standard (Waters Cooperation), applied to a C18 nanoACQUITY Trap Column (5 µm, 180 µm x 20 mm,) and separated on a C18 analytic reversed phase column (1.7 µm, 75 µm x 150 mm) using a nanoACQUITY UPLC systems. The mobile system consisted of phase (A) 0.1% (v/v) formic acid in water and phase (B) acetonitrile with 0.1% (v/v) formic acid. The flow rate was set to 300 µL/min and with a gradient of 2 – 37% mobile phase (A) to (B) over 70 min. As a reference component, Glu-Fibrinopeptide (150 fmol/µL, Sigma) was infused at a flow rate of 500 µL/min. Eluted peptides were infused into a Synapt G2Si (Waters).

The mass spectrometer was operated in resolution mode performing data-independent acquisition (MS^E) and electrospray ionization (ESI) was performed in positive ion mode with nanoLockSpray source. Data acquisition was carried out over 90 min with a mass to charge range (m/z) over 50-2000 Da, scan time of 1 s and ramped trap collision energy from 20 to 40 V. Data processing was conducted with MassLynx 4.1 and proteins were identified with Progenesis QI for Proteomics Version 2.0 with continuum data using a reviewed human data base (Uniprot). The peptide sequence of ovalbumin (chicken) and Hi^3 Ecoli standard (Chaperone protein CLpB, Waters Cooperation) was added to the database for absolute quantification. Data was processed with high energy, low energy and peptide intensity values of 120, 25, and 750 counts. For protein and peptide identification, the following search criteria were applied: one missed cleavage, maximum protein mass 600 kDa, fixed carbamidomethyl modification for cysteine, variable oxidation for methionine and protein false discovery rate of 4%. Two assigned peptides and five assigned fragments are required for protein identification and three assigned fragments are necessary to identify a peptide. Further, peptides with a score below 4 were excluded and based on the TOP^3/Hi^3 approach[356] the absolute amount of each protein in fmol was generated. A detailed list of 20 major identified proteins in each sample is provided in Table 10.

Table 10: Detailed description of the protein corona composition (20 major proteins) of OT-DN1 and HT-DN1 PNCs.

Description (% based on all identified proteins)	OT-DN1
Clusterin	23.26
Ig kappa chain C region	7.93
Fibronectin	7.94
Apolipoprotein A-IV	8.32
Ig mu chain C region	5.85
Complement C1q subcomponent subunit C	4.59
Serum albumin	3.65
Complement C1q subcomponent subunit B	3.16
Ig gamma-1 chain C region	2.54
Zinc finger protein basonuclin-2	2.53
Ig lambda-3 chain C regions	2.14
Ig gamma-2 chain C region	1.96
Complement factor H	1.56
Actin, cytoplasmic 2	1.64
Ig alpha-1 chain C region	1.48
Complement C1q subcomponent subunit A	1.38
Apolipoprotein A-I	1.3
Fibrinogen beta chain	1.27
Complement C3	1.21

Description (% based on all identified proteins)	HT-DN1
Ig kappa chain C region	12.14
Ig mu chain C region	10.81
Serum albumin	4.55

C4b-binding protein alpha chain	3.94
Complement C1q subcomponent subunit C	8.72
Fibrinogen beta chain	2.04
Complement factor H	2.15
Ig gamma-1 chain C region	2.51
Complement C1q subcomponent subunit B	5.14
Fibrinogen gamma chain	1.7
Ig lambda-3 chain C regions	2.7
Fibrinogen alpha chain	1.04
Fibronectin	3.22
Ig gamma-2 chain C region	1.79
Complement C3	1.96
Immunoglobulin lambda-like polypeptide 5	1.36
Ig gamma-3 chain C region	1.16
Complement C1q subcomponent subunit A	2.35
Ig heavy chain V-III region	1.05
Platelet-activating factor acetylhydrolase IB subunit beta	1.52

3.4.3.8 Cell experiments

Bone marrow-derived dendritic cells (BMDCs) were differentiated from bone marrow progenitors (BM cells) of 8- to 10-week-old C57BL/6 mice as first described by Scheicher *et al.*[349] and modified by Gisch *et al.*[350] Briefly, the bone marrow was obtained by flushing the femur, tibia, and hip bone with Iscove's Modified Dulbecco's Medium (IMDM) containing 5% FCS (Sigma-Aldrich, Deisenhofen, Germany) and 50 µM β-mercaptoethanol (Roth, Karlsruhe, Germany). For the BMDC stimulation analysis via flow cytometry, the bone marrow cells (2 x 105 cells/1.25 mL) were seeded in 12 well suspension culture plates (Greiner Bio-One, Frickenhausen, Germany) with culture

medium (IMDM with 5% FCS, 2 mM L-Glutamine, 100 U/mL penicillin, 100 µg/mL streptomycin (all from Sigma-Aldrich), and 50 µM β-mercaptoethanol), supplemented with 5% of GM-CSF containing cell culture supernatant derived from X63.Ag8-653 myeloma cells stably transfected with a murine GM-CSF expression construct.[351] On day 3, 500 µL of the same medium was added into each well. On day 6, 1 mL of the old medium was replaced with 1 mL fresh medium per well. On day 7, BMDCs were treated with nanocarrier formulations and LPS (positive control) as indicated in the figure legends. Before usage, all nanoparticle solutions were analyzed for endotoxin contaminations by limulus amebocyte lysate (LAL) assay (Thermo Fisher Scientific, Waltham, USA) according to the manufacturer's instructions. To analyze the expression of the BMDC surface maturation marker CD86, BMDCs were harvested and washed in staining buffer (PBS/2% FCS). To block Fc receptor-mediated staining, cells were incubated with rat anti-mouse CD16/CD32 Ab (clone 2.4G2), purified from hybridoma supernatant, for 15 min at room temperature. After that, the cells were incubated with phycoerythrin (PE)-conjugated anti-CD86 (clone GL-1) and PE-Cy7-labelled anti-CD11c (clone N418) (all from eBioscience, San Diego, USA) for 30 min at 4 °C.

4. Summary and Conclusion

In this thesis, interfacial reactions in inverse miniemulsions were employed to develop nanoscale drug delivery vehicles composed of proteins. It was shown that these protein nanocarriers are versatile, regarding the choice of protein as well as the cross-linking chemistry, and allow us to prepare biodegradable carriers which can be loaded with sensitive drugs.

Initially, the abundant albumins, i.e. ovalbumin and bovine serum albumin, were used as carrier material to prove the feasibility of conducting an interfacial polyaddition reaction to obtain protein nanocarriers with core-shell morphology and to thoroughly study them. The inverse miniemulsion was used to generate nanocarriers with an aqueous core intended for the encapsulation of water-soluble pharmaceuticals and imaging agents. Electron microscopy confirmed the core-shell morphology while the encapsulation of a fluorescent dye showed that a dense shell was obtained with a leakage of less than 10% for OVA-nanocarriers. Furthermore, the protein nanocarriers were efficiently taken up by dendritic cells and did not agglomerate upon incubation with blood plasma as verified by DLS. This is a crucial feature with regard to their intravenous administration as drug delivery vehicles. An additional important benefit of the protein nanocarriers compared to other polymeric systems is their biodegradability. Exposed to proteases both in a cell-free assay as well as *in vitro*, the nanocarriers were cleaved releasing their cargo. Thus, despite cross-linking by 2,4-toluene diisocyanate, the proteins were still recognized by cells and degraded proteolytically. The application of protein nanocarriers for drug delivery was tested by encapsulation of two adjuvants used for vaccination. These experiments showed that multiple compounds could be encapsulated at the same time in the nanocarriers and successfully released intracellularly - an important feature for nanovaccine design.

These findings let us draw the conclusion that the cross-linking reaction with TDI could also be applicable to other proteins than albumins as far as reactive amino acids residues are present. Therefore, the focus was set on proteins with therapeutic potential. For the immunization against the hepatitis C virus, a targeted delivery of antigens to liver-resident antigen-presenting cells to induce intrahepatic T cellular immunity is a promising approach. However, for the induction of T cell-mediated immune responses an efficient antigen loading of dendritic cells (DCs) is necessary. As we have seen that albumin nanocarriers are successfully ingested and degraded by DCs, we used the non-structural

protein 5A (NS5A) from the hepatitis C virus for protein nanocarrier production. These NS5A nanocarriers enabled both an antigen delivery by the carrier shell material itself and a co-delivery of adjuvants by physical adsorption. Additionally, due to the hollow morphology, the introduction of imaging agents was possible allowing the localization of the nanocarriers *in vivo* after intravenous administration. These experiments showed that the NS5A nanocarriers were almost exclusively accumulated in the liver. In nanoparticle-based immunization approaches, a combination of antigens along with adjuvants yields the most pronounced effects. Our study confirmed these findings as NS5A nanocarriers in combination with the adjuvants led to an enhanced uptake by DCs and a substantial production of antigen-specific antibodies. Taken together these results proved the capability of protein nanocarriers to act by themselves as antigen delivery systems and target liver-resident antigen-presenting cells. The efficient maturation and activation of DCs shows the potential for protein nanocarrier based vaccination.

An approach to synthesize nanocarriers out of other pharmaceutical substances than proteins was shown exemplarily with dexamethasone. Similarly to the NS5A nanocarriers, the use of foreign material was omitted in order to be able to study the biological effects of dexamethasone nanocarriers alone without interference from other compounds. Although nanocarriers were formed successfully after reaction with TDI, their shell was not dense enough to prevent premature leakage of free dexamethasone leading to systemic side effects. These results showed that for a successful nanocarrier preparation for drug delivery purposes, high molecular weights and multiple cross-linking sites are needed. Proteins fulfill these requirements and provide furthermore biodegradability through enzymatic cleavage, while polymeric dexamethasone bears the risk of accumulation in the body.

Besides the variation of nanocarrier shell material, i.e. the choice of protein in accordance to the intended use, it was shown herein that also the cross-linking chemistry can be varied. Instead of the rather unselective 2,4-toluene diisocyanate as the cross-linker, the use of bioorthogonal reactions was envisioned to facilitate the encapsulation of sensitive cargo. Several bioorthogonal reactions were presented in the introduction. The 1,3-dipolar tetrazole-ene reaction presented itself as very suitable because it shows sufficiently high reaction rates for interfacial reactions and has stable and easily obtainable reagents and intermediates for the inverse miniemulsion conditions. Thus, coupling of the tetrazole moiety to OVA and HSA, and using bifunctional norbornene derivatives as dipolarophiles for the 1,3-dipolar cycloaddition resulted in the development of protein

nanocarriers capable to encapsulate molecules maintaining their functionality. Similarly to the previous nanocarrier systems, they were proteolytically degradable releasing the intact cargo after cellular uptake. Additionally, the formed pyrazoline adduct was responsible for the self-fluorescence of these protein nanocarriers making the use of additional fluorophores for visualization negligible.

In conclusion, this thesis demonstrated the versatility of proteins as complex molecular building blocks for the preparation of protein nanocarriers and their benefits for the application as drug delivery vehicles. Furthermore, it was shown for the first time that the bioorthogonal tetrazole-ene cycloaddition can be conducted as an interfacial reaction in miniemulsion providing thus an alternative way for nanocarrier synthesis.

In the future, a targeted delivery to other organs or cell lines by coupling of specific antibodies on the nanocarrier surface or the introduction of stealth properties through PEGylation could be applicable. A controlled and triggered release by incorporation of specific cleavage points is a further possibility to tailor the nanocarriers according to their intended use. As we have seen, protein nanocarriers allow a co-delivery of different substances. Thus, the simultaneous transport of multiple therapeutic drugs with the same carrier could allow a combination therapy, could help to enhance the efficacy of treatment or to overcome multidrug resistance. Besides nanovaccination, the treatment of tumors and genetic diseases by systemic nucleic acid or enzyme delivery through these nanocarriers are additional aspects for future research. Regarding the bioorthogonal chemistry, the use of tetrazole-derivatives activatable at longer wavelengths than the UV region is appealing to enable a co-delivery of different imaging agents. Furthermore, the reaction of tetrazines with strained double bonds, the fastest bioorthogonal reaction so far, could be an interesting alternative to the tetrazole photoclick reaction if applicable at the interface.

Appendix

List of Abbreviations

a.u.	arbitrary unit
ATR-IR	attenuated total reflection- infrared spectroscopy
BCA	bicinchoninic acid
BMDC	bone marrow derived dendritic cell
BSA	bovine serum albumin
CD	cluster of differentiation
CLSM	confocal laser scanning microscopy
CT	CellTracker CMFDA
CTAB	cetyl trimethylammonium bromide
CuAAc	copper-catalyzed azide-alkyne cycloaddition
DAA	direct antiviral drug
DC	dendritic cell
DGDG	digalactosyldiacylglycerol
DLS	dynamic light scattering
DMAP	4-dimethylaminopyridine
DMF	dimethyl formamide
DMSO	dimethyl sulfoxide
DN1	6-(((1R,4R)-bicyclo[2.2.1]hept-5-ene-2-carbonyl)oxy)hexyl (1S,2S,4S)-bicyclo[2.2.1]hept-5-ene-2-carboxylate
DN2	4-((((1R,4R)-bicyclo[2.2.1]hept-5-ene-2-carbonyl)oxy)methyl)benzyl (1S,2S,4S)-bicyclo[2.2.1]hept-5-ene-2-carboxylate
DN3	1-(((1R,4R)-bicyclo[2.2.1]hept-5-en-2-yl)methyl)4-(((1S,2S,4S)-bicyclo[2.2.1]hept-5-en-2-yl)methyl)but-2-ynedioate
DN4	2-(2-(2-(((1R,4R)-bicyclo[2.2.1]hept-5-ene-2-carbonyl)oxy)ethoxy)ethoxy)ethyl (1S,2S,4S)-bicyclo[2.2.1]hept-5-ene-2-carboxylate
DN5	((1R,4R)-bicyclo[2.2.1]hept-5-en-2-yl)methyl 4-((3-(((1S,2R,4S)-bicyclo[2.2.1]hept-5-en-2-yl)methoxy)-3-oxopropyl)disulfanyl)butanoate
DXM	dexamethasone
EDC	1-ethyl-3-(3-dimethylaminopropyl)carbodiimide
EDG	electron donating group
EDX	energy-dispersive X-ray spectroscopy
EtOAc	ethyl acetate
EWG	electron withdrawing group
FT-IR	fourier transform infrared spectroscopy
h	Planck constant
HCV	hepatitis C virus
HEPES	4-(2-hydroxyethyl)-1-piperazineethanesulfonic acid
HLB	hydrophilic lipophilic balance
HMBC	heteronuclear multiple bond correlation

HOMO	highest occupied orbital
HPH	high-pressure homogenizer
HPLC	high-performance liquid chromatography
HSA	human serum albumin
HT	human serum albumin coupled to TET
IC	interfacial catalysis
ICCS	intracellular cytokine staining
ICP-OES	inductively coupled plasma optical emission spectrometry
IFNγ	interferon gamma
IL	interleukin
iPrOH	isopropyl alcohol
IPTC	inverse phase transfer catalysis
k_2	second order rate constant
LAL	limulus amebocyte lysate
LC	loading capacity
LC-MS/MS	liquid chromatography coupled to tandem mass spectrometry
LCST	lower critical solution temperature
LPS	lipopolysaccharide
LUMO	lowest occupied orbital
MDP	muramyl dipeptide
MFI	median fluorescence intensity
MGDG	monogalactosyldiacylglycerol
moDC	monocyte-derived dendritic cell
MPLA	monophosphoryl lipid A
MWCO	molecular weight cut-off
NC	nanocarrier
NIPAM	*N*-isopropyl acrylamide
NMR	nuclear magnetic resonance
NPC	non-parenchymal liver cell
NS5A	non-structural protein 5A
OT	ovalbumin coupled to TET
OVA	ovalbumin
P(E/B)-*b*-EO)	poly-((ethylene-*co*-butylene)-*b*-(ethyleneoxide)
PAGE	polyelectrolyte gel electrophoresis
PBS	phosphate-buffered saline
PDI	polydispersity index
PE	petrol ether
PEG	poly(ethylene glycol)
PI	propidium iodide
PLGA	poly(lactic-*co*-glycolic acid)
PNC	protein nanocontainer/carrier
PTC	phase transfer catalysis
R848	resiquimod
RT	room temperature
SD	standard deviation
SDS	sodium dodecyl sulfate
SEM	scanning electron microscopy

siRNA	small interfering ribonucleic acid
SPAAc	strain-promoted azide-alkyne cycloaddition
SR101	sulforhodamine SR101
TDI	2,4-toluene diisocyanate
TEM	transmission electron microscopy
TET	4-2-(2-Phenyl-2H-tetrazol-5-yl)benzoic acid
TLC	thin-layer chromatography
UV	ultra violet
ν	wavenumber

Spectra

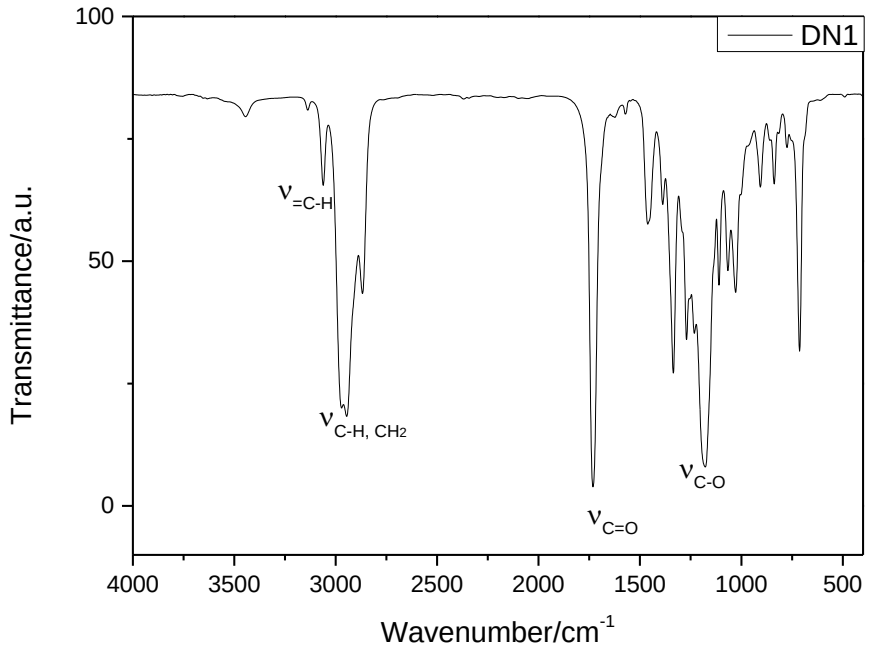

Figure 97: FT-IR spectrum of dinorbornene cross-linker DN1.

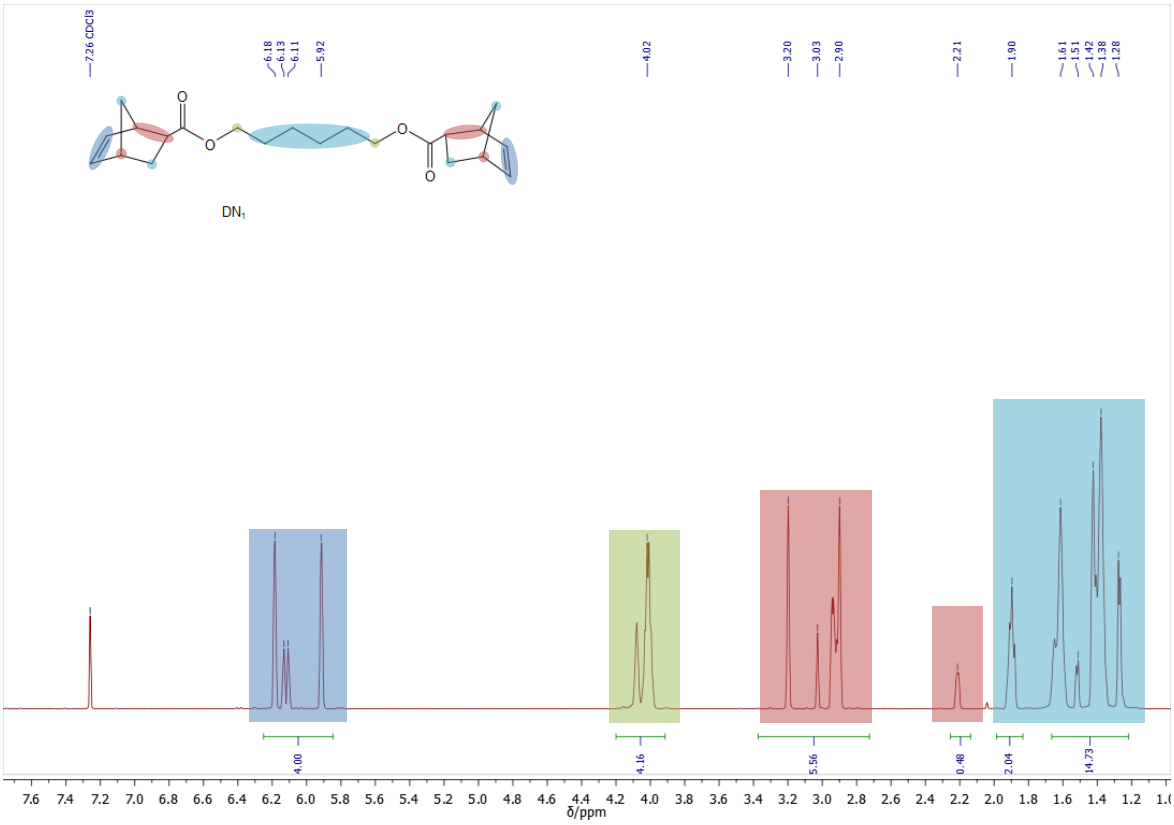

Figure 98: ^{1}H NMR spectrum of DN1 (700 MHz, 298K, $CDCl_3$).

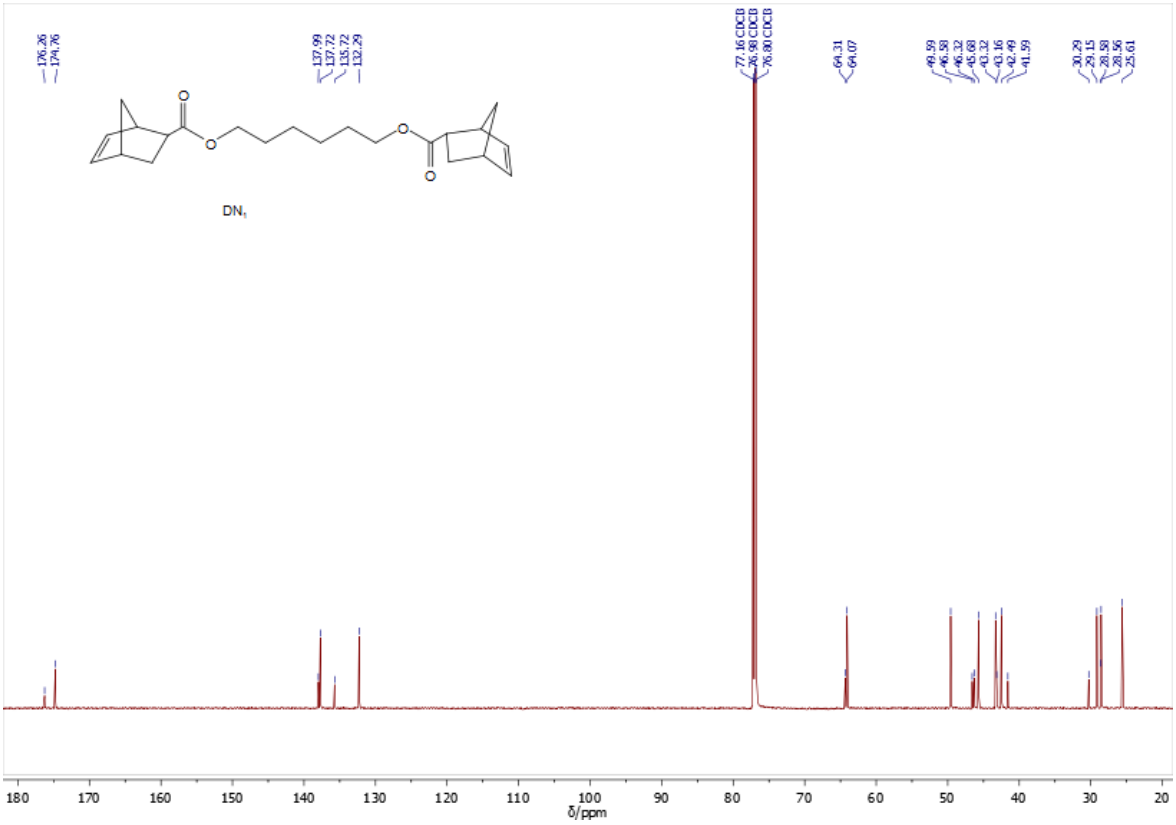

Figure 99: ^{13}C NMR spectrum of DN1 (176 MHz, 298 K, $CDCl_3$).

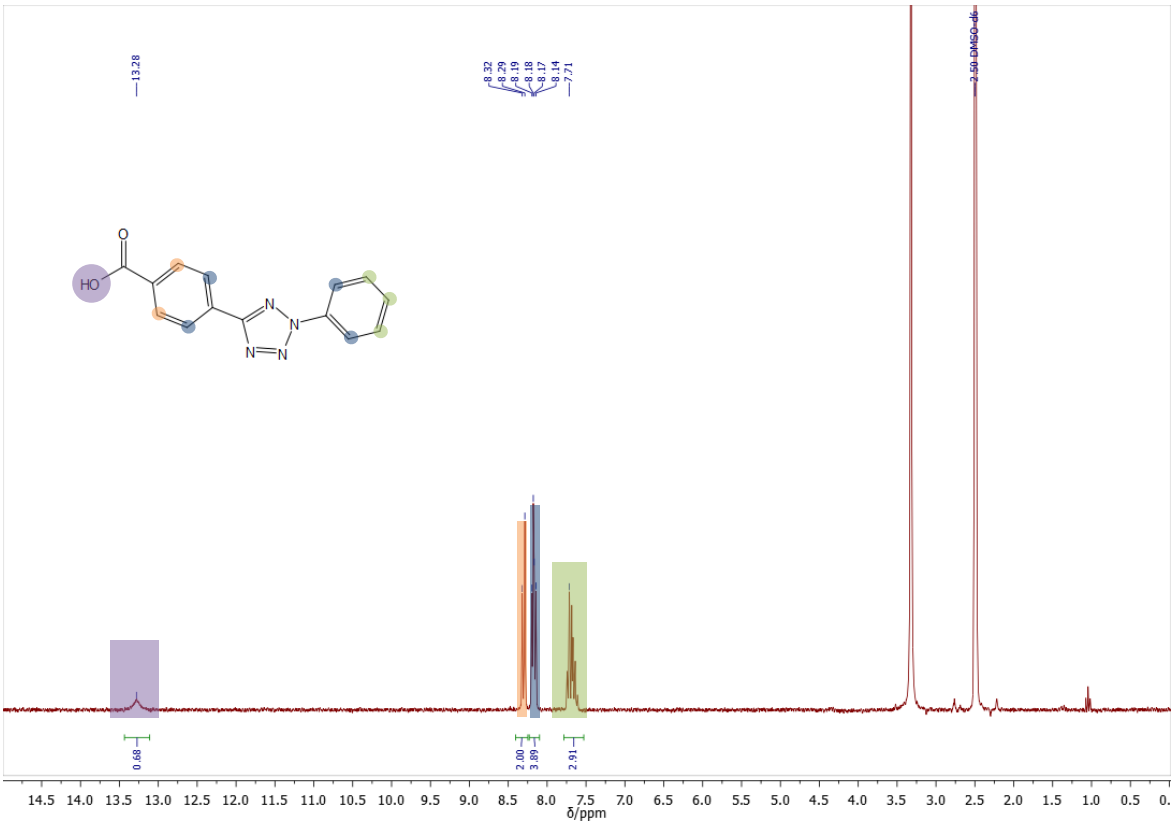

Figure 100: ^{1}H NMR spectrum of 4-(2-phenyl-2*H*-tetrazol-5-yl)benzoic acid (250 MHz, 298 K, DMSO-d_6).

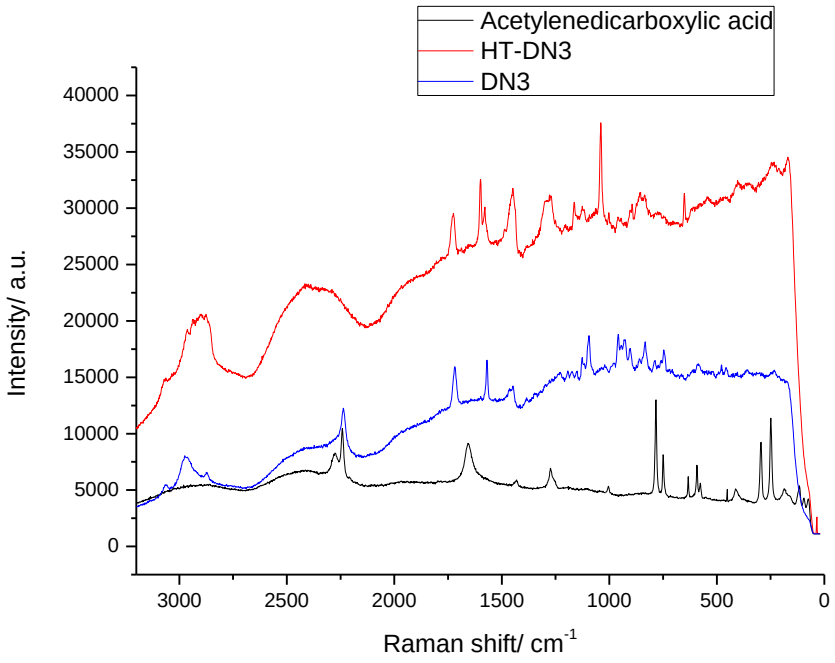

Figure 101: Raman-spectra presented in section 2.4.11 without baseline correction.

References

1. K. Shao, S. Singha, X. Clemente-Casares, S. Tsai, Y. Yang, P. Santamaria, *ACS Nano* **2014**, *9*, 16-30.
2. M. W. Tibbitt, J. E. Dahlman, R. Langer, *JACS* **2016**, *138*, 704-717.
3. T. Sun, Y. S. Zhang, B. Pang, D. C. Hyun, M. Yang, Y. Xia, *Angew. Chem. Int. Ed.* **2014**, *53*, 12320-12364.
4. V. P. Torchilin, *Eur. J. Pharm. Sci.* **2000**, *11, Supplement 2*, S81-S91.
5. R. Wang, P. S. Billone, W. M. Mullett, *J. Nanomater.* **2013**, *2013*, 1.
6. A. O. Elzoghby, W. M. Samy, N. A. Elgindy, *J. Control. Release* **2012**, *161*, 38-49.
7. B. Elsadek, F. Kratz, *J. Control. Release* **2012**, *157*, 4-28.
8. F. Kratz, *J. Control. Release* **2008**, *132*, 171-183.
9. M. Fasano, S. Curry, E. Terreno, M. Galliano, G. Fanali, P. Narciso, S. Notari, P. Ascenzi, *IUBMB life* **2005**, *57*, 787-796.
10. A. O. Elzoghby, W. M. Samy, N. A. Elgindy, *J. Control. Release* **2012**, *157*, 168-182.
11. M. J. Hawkins, P. Soon-Shiong, N. Desai, *Adv. Drug Del. Rev.* **2008**, *60*, 876-885.
12. L. Yang, F. Cui, D. Cun, A. Tao, K. Shi, W. Lin, *Int. J. Pharm.* **2007**, *340*, 163-172.
13. D. N. Kapoor, F. V. Manvi, R. C. Doijad, S. Dhawan, *PDA J. Pharm. Sci. Technol.* **2008**, *62*, 111-124.
14. F.-Q. Li, H. Su, J. Wang, J.-Y. Liu, Q.-G. Zhu, Y.-B. Fei, Y.-H. Pan, J.-H. Hu, *Int. J. Pharm.* **2008**, *349*, 274-282.
15. C. R. Bertozzi, *Acc. Chem. Res.* **2011**, *44*, 651-653.
16. C. P. Ramil, Q. Lin, *Chem. Commun.* **2013**, *49*, 11007-11022.
17. K. Piradashvili, E. M. Alexandrino, F. R. Wurm, K. Landfester, *Chem. Rev.* **2016**, *116*, 2141-2169.
18. C. W. Hume, U.S. Patent 2, 130, 947, 1938. .
19. W. H. Carothers, U.S. Patent 2, 130, 523, 1938.
20. C. W. Hume, U.S. Patent 2, 130, 948, 1938.
21. K. Landfester, A. Musyanovych, V. Mailander, *J. Polym. Sci., Part A: Polym. Chem.* **2010**, *48*, 493-515.
22. M. Antonietti, K. Landfester, *Prog. Polym. Sci.* **2002**, *27*, 689-757.
23. A. Chanda, V. V. Fokin, *Chem. Rev.* **2009**, *109*, 725-748.
24. K. Holmberg, *Curr. Opin. Colloid Interface Sci.* **2003**, *8*, 187-196.
25. A. G. Volkov, *Liquid Interfaces In Chemical, Biological And Pharmaceutical Applications*, CRC Press, **2001**.
26. L. Shui, J. C. Eijkel, A. van den Berg, *Adv. Colloid Interface Sci.* **2007**, *133*, 35-49.
27. C. Rao, K. Kalyanikutty, *Acc. Chem. Res.* **2008**, *41*, 489-499.
28. J. P. Ge, W. Chen, L. P. Liu, Y. D. Li, *Chem. Eur. J.* **2006**, *12*, 6552-6558.
29. J. M. Siebert, G. Baier, A. Musyanovych, K. Landfester, *Chem. Commun.* **2012**, *48*, 5470-5472.
30. S. L. Anna, N. Bontoux, H. A. Stone, *Appl. Phys. Lett.* **2003**, *82*, 364-366.
31. T. Fu, Y. Ma, D. Funfschilling, C. Zhu, H. Z. Li, *Chem. Eng. Sci.* **2010**, *65*, 3739-3748.
32. P. Heunemann, S. Prévost, I. Grillo, C. M. Marino, J. Meyer, M. Gradzielski, *Soft Matter* **2011**, *7*, 5697-5710.
33. G. T. Vladisavljević, N. Khalid, M. A. Neves, T. Kuroiwa, M. Nakajima, K. Uemura, S. Ichikawa, I. Kobayashi, *Adv. Drug Del. Rev.* **2013**, *65*, 1626-1663.
34. E. Piacentini, E. Drioli, L. Giorno, *J. Membr. Sci.* **2014**, *468*, 410-422.
35. G. Vladisavljević, I. Kobayashi, M. Nakajima, *Microfluid. Nanofluid.* **2012**, *13*, 151-178.
36. S. Sugiura, M. Nakajima, M. Seki, *Langmuir* **2002**, *18*, 5708-5712.
37. D. Crespy, K. Landfester, *Beilstein J. Org. Chem.* **2010**, *6*, 1132-1148.
38. N. Anton, J.-P. Benoit, P. Saulnier, *J. Control. Release* **2008**, *128*, 185-199.
39. S. A. Vitale, J. L. Katz, *Langmuir* **2003**, *19*, 4105-4110.

40. P. Fernandez, V. André, J. Rieger, A. Kühnle, *Colloids Surf. Physicochem. Eng. Aspects* **2004**, *251*, 53-58.
41. Q. Yuan, R. A. Williams, N. Aryanti, *Adv. Powder Technol.* **2010**, *21*, 599-608.
42. J.-C. Baret, *Lab Chip* **2012**, *12*, 422-433.
43. I. Kobayashi, M. Nakajima, S. Mukataka, *Colloids Surf. Physicochem. Eng. Aspects* **2003**, *229*, 33-41.
44. M. T. Guo, A. Rotem, J. A. Heyman, D. A. Weitz, *Lab Chip* **2012**, *12*, 2146-2155.
45. W. Wang, M.-J. Zhang, L.-Y. Chu, *Curr. Opin. Pharmacol.* **2014**, *18*, 35-41.
46. O. J. Dressler, R. M. Maceiczyk, S.-I. Chang, A. J. deMello, *J. Biomol. Screen.* **2014**, *19*, 483-496.
47. S.-Y. Teh, R. Lin, L.-H. Hung, A. P. Lee, *Lab Chip* **2008**, *8*, 198-220.
48. S. Haeberle, R. Zengerle, *Lab Chip* **2007**, *7*, 1094-1110.
49. S. Xu, Z. Nie, M. Seo, P. Lewis, E. Kumacheva, H. A. Stone, P. Garstecki, D. B. Weibel, I. Gitlin, G. M. Whitesides, *Angew. Chem.* **2005**, *117*, 734-738.
50. P. Garstecki, H. A. Stone, G. M. Whitesides, *Phys. Rev. Lett.* **2005**, *94*, 164501.
51. T. Nisisako, *Chem. Eng. Technol.* **2008**, *31*, 1091-1098.
52. L. Shang, Y. Cheng, J. Wang, H. Ding, F. Rong, Y. Zhao, Z. Gu, *Lab Chip* **2014**, *14*, 3489-3493.
53. R. K. Shah, H. C. Shum, A. C. Rowat, D. Lee, J. J. Agresti, A. S. Utada, L.-Y. Chu, J.-W. Kim, A. Fernandez-Nieves, C. J. Martinez, *Mater. Today* **2008**, *11*, 18-27.
54. N.-N. Deng, C.-L. Mou, W. Wang, X.-J. Ju, R. Xie, L.-Y. Chu, *Microfluid. Nanofluid.* **2014**, *17*, 967-972.
55. G. T. Vladisavljević, B. Wang, M. M. Dragosavac, R. G. Holdich, *Colloids Surf. Physicochem. Eng. Aspects* **2014**, *458*, 78-84.
56. M. Marquis, J. Davy, B. Cathala, A. Fang, D. Renard, *Carbohydr. Polym.* **2015**, *116*, 189-199.
57. S. Guo, T. Yao, X. Ji, C. Zeng, C. Wang, L. Zhang, *Angew. Chem.* **2014**, *126*, 7634-7639.
58. Y. Cheng, C. Zhu, Z. Xie, H. Gu, T. Tian, Y. Zhao, Z. Gu, *J. Colloid Interface Sci.* **2014**, *421*, 64-70.
59. J. Wang, D. Yu, H. Jing, J. Tao, *Chem. Eng. Res. Des.* **2014**, *92*, 2223-2230.
60. I. U. Khan, L. Stolch, C. A. Serra, N. Anton, R. Akasov, T. F. Vandamme, *Int. J. Pharm.* **2015**, *478*, 78-87.
61. P. W. Chen, J. Brignoli, A. R. Studart, *Polymer* **2014**.
62. I. Polenz, S. S. Datta, D. A. Weitz, *Langmuir* **2014**, *30*, 13405-13410.
63. P. W. Chen, G. Cadisch, A. R. Studart, *Langmuir* **2014**, *30*, 2346-2350.
64. C.-H. Chen, R. K. Shah, A. R. Abate, D. A. Weitz, *Langmuir* **2009**, *25*, 4320-4323.
65. T. JunáHuang, *Lab Chip* **2012**, *12*, 2097-2102.
66. A. Andar, R. Hood, W. Vreeland, D. DeVoe, P. Swaan, *Pharm. Res.* **2014**, *31*, 401-413.
67. D. van Swaay, A. deMello, *Lab Chip* **2013**, *13*, 752-767.
68. S. H. Kim, J. W. Kim, D. H. Kim, S. H. Han, D. A. Weitz, *Small* **2013**, *9*, 124-131.
69. C. Martino, T. Y. Lee, S.-H. Kim, *Biomicrofluidics* **2015**, *9*, 024101.
70. T. Schneider, D. R. Burnham, J. VanOrden, D. T. Chiu, *Lab Chip* **2011**, *11*, 2055-2059.
71. S. Zeng, X. Liu, H. Xie, B. Lin, in *Microfluidics*, Springer, Berlin Heidelberg, **2011**, pp. 69-90.
72. S. Sugiura, T. Kuroiwa, T. Kagota, M. Nakajima, S. Sato, S. Mukataka, P. Walde, S. Ichikawa, *Langmuir* **2008**, *24*, 4581-4588.
73. S. Sugiura, M. Nakajima, M. Seki, *J. Am. Oil Chem. Soc.* **2002**, *79*, 515-519.
74. I. Kobayashi, K. Uemura, M. Nakajima, *Colloids Surf. Physicochem. Eng. Aspects* **2007**, *296*, 285-289.
75. I. Kobayashi, K. Uemura, M. Nakajima, *Langmuir* **2006**, *22*, 10893-10897.
76. F. Leal-Calderon, V. Schmitt, J. Bibette, *Emulsion science: basic principles*, Springer Science&Business Media, **2007**.
77. K. Schroen, S. Sahin, K. van Dijke, S. van der Graaf, M. Zijffers-Steegmans, T. Krebs, R. Boom, in *Encyclopedia of microfluidics and nanofluidics*, Springer, Germany, **2014**.
78. S. Sugiura, M. Nakajima, S. Iwamoto, M. Seki, *Langmuir* **2001**, *17*, 5562-5566.

79. S. Sugiura, M. Nakajima, M. Seki, *Langmuir* **2002**, *18*, 3854-3859.
80. S. Sugiura, M. Nakajima, J. Tong, H. Nabetani, M. Seki, *J. Colloid Interface Sci.* **2000**, *227*, 95-103.
81. I. Kobayashi, M. Nakajima, K. Chun, Y. Kikuchi, H. Fujita, *AlChE J.* **2002**, *48*, 1639-1644.
82. S. Souilem, I. Kobayashi, M. A. Neves, L. Jlaiel, H. Isoda, S. Sayadi, M. Nakajima, *Food Res. Int.* **2014**, *62*, 467-475.
83. M. A. Neves, I. Kobayashi, M. Nakajima, in *ASME 2013 11th International Conference on Nanochannels, Microchannels, and Minichannels*, American Society of Mechanical Engineers, **2013**, pp. 1-7.
84. S. Souilem, I. Kobayashi, M. Neves, S. Sayadi, S. Ichikawa, M. Nakajima, *Food and Bioprocess Technology* **2014**, *7*, 2014-2027.
85. A. M. Chuah, T. Kuroiwa, I. Kobayashi, M. Nakajima, *Colloids Surf. Physicochem. Eng. Aspects* **2014**, *440*, 136-144.
86. N. Khalid, I. Kobayashi, M. A. Neves, K. Uemura, M. Nakajima, H. Nabetani, *Colloids Surf. Physicochem. Eng. Aspects* **2014**, *459*, 247-253.
87. J. Wu, Q. Fan, Y. Xia, G. Ma, *Chem. Eng. Sci.* **2014**.
88. A. Nazir, K. Schroën, R. Boom, *J. Membr. Sci.* **2010**, *362*, 1-11.
89. G. T. Vladisavljević, R. A. Williams, *Adv. Colloid Interface Sci.* **2005**, *113*, 1-20.
90. C. Charcosset, *J. Food Eng.* **2009**, *92*, 241-249.
91. A. K. Pawlik, I. T. Norton, *J. Food Eng.* **2013**, *114*, 530-537.
92. F. Qi, J. Wu, T. Yang, G. Ma, Z. Su, *Acta Biomater.* **2014**, *10*, 4247-4256.
93. S. Slomkowski, V. Alemán José, G. Gilbert Robert, M. Hess, K. Horie, G. Jones Richard, P. Kubisa, I. Meisel, W. Mormann, S. Penczek, F. T. Stepto Robert, in *Pure Appl. Chem., Vol. 83*, **2011**, p. 2229.
94. D. Crespy, K. Landfester, *Beilstein J. Org. Chem.* **2010**, *6*, 1132-1148.
95. D. J. McClements, *Soft Matter* **2012**, *8*, 1719-1729.
96. S. Abbas, K. Hayat, E. Karangwa, M. Bashari, X. Zhang, *Food Eng. Rev.* **2013**, *5*, 139-157.
97. M. Manea, A. Chemtob, M. Paulis, J. C. de la Cal, M. J. Barandiaran, J. M. Asua, *AlChE J.* **2008**, *54*, 289-297.
98. H.-J. Butt, K. Graf, M. Kappl, in *Physics and Chemistry of Interfaces*, Wiley-VCH Verlag GmbH & Co. KGaA, **2004**, pp. 4-25.
99. G. B. Kauffman, *J. Chem. Educ.* **1988**, *65*, 803.
100. C. Schotten, *Berichte der deutschen chemischen Gesellschaft* **1884**, *17*, 2544-2547.
101. E. Baumann, *Berichte der deutschen chemischen Gesellschaft* **1886**, *19*, 3218-3222.
102. R. Breslow, *Acc. Chem. Res.* **1991**, *24*, 159-164.
103. S. Narayan, J. Muldoon, M. Finn, V. V. Fokin, H. C. Kolb, K. B. Sharpless, *Angew. Chem. Int. Ed.* **2005**, *44*, 3275-3279.
104. J. E. Klijn, J. B. F. N. Engberts, *Nature* **2005**, *435*, 746-747.
105. A. Manna, A. Kumar, *J. Phys. Chem. A* **2013**, *117*, 2446-2454.
106. R. N. Butler, A. G. Coyne, *J. Org. Chem.* **2015**, *80*, 1809-1817.
107. Y. R. Shen, V. Ostroverkhov, *Chem. Rev.* **2006**, *106*, 1140-1154.
108. P. Perera, K. Fega, C. Lawrence, E. Sundstrom, J. Tomlinson-Phillips, D. Ben-Amotz, *Proceedings of the National Academy of Sciences of the United States of America* **2009**, *106*, 12230-12234.
109. Y. Ni, S. M. Gruenbaum, J. L. Skinner, *Proceedings of the National Academy of Sciences of the United States of America* **2013**, *110*, 1992-1998.
110. Y. Jung, R. A. Marcus, *JACS* **2007**, *129*, 5492-5502.
111. A. J. Straathof, *Biotechnol. Bioeng.* **2003**, *83*, 371-375.
112. K. Mikami, M. Yamanaka, M. N. Islam, K. Kudo, N. Seino, M. Shinoda, *Tetrahedron* **2003**, *59*, 10593-10597.
113. D. A. Jaeger, J. Wang, *Tetrahedron Lett.* **1992**, *33*, 6415-6418.
114. D.-Y. Wu, L.-P. Zhang, L.-Z. Wu, B.-j. Wang, C.-H. Tung, *Tetrahedron Lett.* **2002**, *43*, 1281-1283.

115. Y. Hayashi, S. Aratake, T. Okano, J. Takahashi, T. Sumiya, M. Shoji, *Angew. Chem. Int. Ed.* **2006**, *45*, 5527-5529.
116. L. Zhong, Q. Gao, J. Gao, J. Xiao, C. Li, *J. Catal.* **2007**, *250*, 360-364.
117. H. Gröger, O. May, H. Hüsken, S. Georgeon, K. Drauz, K. Landfester, *Angew. Chem. Int. Ed.* **2006**, *45*, 1645-1648.
118. T. Ooi, E. Tayama, K. Doda, M. Takeuchi, K. Maruoka, *Synlett* **2000**, *2000*, 1500-1502.
119. M. H. Entezari, A. Keshavarzi, *Ultrason. Sonochem.* **2001**, *8*, 213-216.
120. L. J. Mathias, R. A. Vaidya, *JACS* **1986**, *108*, 1093-1094.
121. A. R. Abreu, I. Costa, C. Rosa, L. M. Ferreira, A. Lourenço, P. P. Santos, *Tetrahedron* **2005**, *61*, 11986-11990.
122. J. Chief Elk, I. Benjamin, *Langmuir* **2015**, *31*, 5086-5092.
123. M. Baur, M. Frank, J. Schatz, F. Schildbach, *Tetrahedron* **2001**, *57*, 6985-6991.
124. B. Boyer, A. Hambardzoumian, J.-P. Roque, N. Beylerian, *J. Chem. Soc., Perk. Trans. 2* **2002**, 1689-1691.
125. J. Ji, Y. Zhao, L. Guo, B. Liu, C. Ji, P. Yang, *Lab Chip* **2012**, *12*, 1373-1377.
126. M.-J. Schwuger, K. Stickdorn, R. Schomaecker, *Chem. Rev.* **1995**, *95*, 849-864.
127. T. Wielpütz, T. Sottmann, R. Strey, F. Schmidt, A. Berkessel, *Chem. Eur. J.* **2006**, *12*, 7565-7575.
128. M. Häger, K. Holmberg, *Chem. Eur. J.* **2004**, *10*, 5460-5466.
129. T. Hamerla, M. Schwarze, R. Schomäcker, *Chem. Ing. Tech.* **2012**, *84*, 1861-1872.
130. K. K. Ghosh, M. L. Satnami, *Colloids Surf. Physicochem. Eng. Aspects* **2006**, *274*, 125-129.
131. L. Jing, X. J. Li, Y. C. Han, Y. Chu, *Colloids Surf. Physicochem. Eng. Aspects* **2008**, *326*, 37-41.
132. G. Bode, M. Lade, R. Schomäcker, *Chem. Ing. Tech.* **1999**, *71*, 877-881.
133. V. Nardello-Rataj, L. Caron, C. Borde, J.-M. Aubry, *JACS* **2008**, *130*, 14914-14915.
134. L. Caron, V. Nardello, J. Mugge, E. Hoving, P. L. Alsters, J.-M. Aubry, *J. Colloid Interface Sci.* **2005**, *282*, 478-485.
135. J.-Z. Jiang, Y.-A. Wei, C. Cai, *J. Colloid Interface Sci.* **2007**, *312*, 439-443.
136. J.-Z. Jiang, C. Cai, *J. Colloid Interface Sci.* **2006**, *299*, 938-943.
137. H. A. Zayas, D. Valade, Z. Jia, M. J. Monteiro, *Aust. J. Chem.* **2012**, *65*, 1090-1094.
138. J. B. F. N. Engberts, E. Fernández, L. García-Río, J. R. Leis, *J. Org. Chem.* **2006**, *71*, 4111-4117.
139. H. Lü, X. An, J. Yu, X. Song, *J. Phys. Org. Chem.* **2012**, *25*, 1210.
140. J. B. F. N. Engberts, E. Fernández, L. García-Río, J. R. Leis, *J. Org. Chem.* **2006**, *71*, 6118-6123.
141. L. Garcia-Rio, J. R. Leis, E. Iglesias, *J. Phys. Chem.* **1995**, *99*, 12318-12326.
142. M. Häger, U. Olsson, K. Holmberg, *Langmuir* **2004**, *20*, 6107-6115.
143. M. Häger, F. Currie, K. Holmberg, *Colloids Surf. Physicochem. Eng. Aspects* **2004**, *250*, 163-170.
144. L. García-Río, J. C. Mejuto, M. Pérez-Lorenzo, *J. Phys. Chem. B* **2006**, *110*, 812-819.
145. L. García-Rio, J. R. Leis, J. C. Mejuto, *Langmuir* **2003**, *19*, 3190-3197.
146. L. García-Río, J. Leis, *Chem. Commun.* **2000**, 455-456.
147. E. Fernández, L. García-Río, M. Méndez-Pérez, P. Rodríguez-Dafonte, *J. Phys. Chem. B* **2009**, *113*, 8828-8834.
148. M. A. López-Quintela, C. Tojo, M. Blanco, L. G. Rio, J. Leis, *Curr. Opin. Colloid Interface Sci.* **2004**, *9*, 264-278.
149. J. J. Shrikhande, P. A. Hassan, R. V. Jayaram, *Colloids Surf. Physicochem. Eng. Aspects* **2010**, *370*, 64-71.
150. A. Yaghmur, A. Aserin, A. Abbas, N. Garti, *Colloids Surf. Physicochem. Eng. Aspects* **2005**, *253*, 223-234.
151. L. He, A. F. Dexter, A. P. Middelberg, *Chem. Eng. Sci.* **2006**, *61*, 989-1003.
152. H. González-Navarro, L. Braco, *Biotechnol. Bioeng.* **1998**, *59*, 122-127.
153. H. Chahinian, L. Nini, E. Boitard, J.-P. Dubès, L. Sarda, L.-C. Comeau, *Lipids* **2000**, *35*, 919-925.

154. L. Nini, L. Sarda, L.-C. Comeau, E. Boitard, J.-P. Dubès, H. Chahinian, *Biochim. Biophys. Acta* **2001**, *1534*, 34-44.
155. P. J. Wilde, B. S. Chu, *Adv. Colloid Interface Sci.* **2011**, *165*, 14-22.
156. P. Reis, K. Holmberg, H. Watzke, M. E. Leser, R. Miller, *Adv. Colloid Interface Sci.* **2009**, *147–148*, 237-250.
157. B.-S. Chu, G. T. Rich, M. J. Ridout, R. M. Faulks, M. S. J. Wickham, P. J. Wilde, *Langmuir* **2009**, *25*, 9352-9360.
158. D. Burtscher, K. Grela, *Angew. Chem. Int. Ed.* **2009**, *48*, 442-454.
159. P. B. Zetterlund, Y. Kagawa, M. Okubo, *Chem. Rev.* **2008**, *108*, 3747-3794.
160. J. K. Oh, *J. Polym. Sci., Part A: Polym. Chem.* **2008**, *46*, 6983-7001.
161. M. F. Cunningham, *Prog. Polym. Sci.* **2008**, *33*, 365-398.
162. S. Belbekhouche, T. Hamaide, V. Dulong, L. Picton, D. Le Cerf, J. Desbrières, *Polym. Int.* **2013**, *62*, 1617-1623.
163. D. Wu, C. Scott, C. C. Ho, C. C. Co, *Macromolecules* **2006**, *39*, 5848-5853.
164. C. Scott, D. Wu, C.-C. Ho, C. C. Co, *JACS* **2005**, *127*, 4160-4161.
165. Z. H. Cao, G. R. Shan, N. Sheibat-Othman, J. L. Putaux, E. Bourgeat-Lami, *J. Polym. Sci., Part A: Polym. Chem.* **2010**, *48*, 593-603.
166. Q. Sun, Y. Deng, *JACS* **2005**, *127*, 8274-8275.
167. D. Sarkar, J. El-Khoury, S. T. Lopina, J. Hu, *Macromolecules* **2005**, *38*, 8603-8605.
168. T. M. S. Chang, *Science* **1964**, *146*, 524-&.
169. R. Arshady, *J. Microencapsul.* **1989**, *6*, 13-28.
170. D. Crespy, M. Stark, C. Hoffmann-Richter, U. Ziener, K. Landfester, *Macromolecules* **2007**, *40*, 3122-3135.
171. Q. Zhang, Y. Shi, X. Zhan, F. Chen, *Colloids Surf. Physicochem. Eng. Aspects* **2012**, *393*, 17-26.
172. I. Polenz, Q. Brosseau, J.-C. Baret, *Soft Matter* **2015**, *11*, 2916-2923.
173. S. J. Wagh, S. S. Dhumal, A. K. Suresh, *J. Membr. Sci.* **2009**, *328*, 246-256.
174. J. Fickert, P. Rupper, R. Graf, K. Landfester, D. Crespy, *J. Mater. Chem.* **2012**, *22*, 2286-2291.
175. D. Crespy, K. Landfester, *Soft Matter* **2011**, *7*, 11054-11064.
176. C. Herrmann, D. Crespy, K. Landfester, *Colloid. Polym. Sci.* **2011**, *289*, 1111-1117.
177. H. Frank, U. Ziener, K. Landfester, *Macromolecules* **2009**, *42*, 7846-7853.
178. G. Baier, A. Musyanovych, M. Dass, S. Theisinger, K. Landfester, *Biomacromolecules* **2010**, *11*, 960-968.
179. H. Freichels, M. Wagner, P. Okwieka, R. G. Meyer, V. Mailaender, K. Landfester, A. Musyanovych, *J. Mater. Chem. B.* **2013**, *1*, 4338-4348.
180. E.-M. Rosenbauer, M. Wagner, A. Musyanovych, K. Landfester, *Macromolecules* **2010**, *43*, 5083-5093.
181. L. Spernath, S. Magdassi, *Polym. Adv. Technol.* **2011**, *22*, 2469-2473.
182. B. Kang, P. Okwieka, S. Schöttler, S. Winzen, J. Langhanki, K. Mohr, T. Opatz, V. Mailänder, K. Landfester, F. R. Wurm, *Angew. Chem. Int. Ed.* **2015**, 7463-7440.
183. S. Taheri, G. Baier, P. Majewski, M. Barton, R. Forch, K. Landfester, K. Vasilev, *J. Mater. Chem. B.* **2014**, *2*, 1838-1845.
184. D. Yiamsawas, G. Baier, E. Thines, K. Landfester, F. R. Wurm, *RSC Advances* **2014**, *4*, 11661-11663.
185. J. Kuriyan, B. Konforti, D. Wemmer, *The molecules of life: Physical and chemical principles*, Garland Science, UK, **2012**.
186. D. M. Patterson, L. A. Nazarova, J. A. Prescher, *ACS Chem. Biol.* **2014**, *9*, 592-605.
187. E. M. Sletten, C. R. Bertozzi, *Angew. Chem. Int. Ed.* **2009**, *48*, 6974-6998.
188. E. Saxon, C. R. Bertozzi, *Science* **2000**, *287*, 2007-2010.
189. S. S. van Berkel, M. B. van Eldijk, J. van Hest, *Angew. Chem. Int. Ed.* **2011**, *50*, 8806-8827.
190. M. Köhn, R. Breinbauer, *Angew. Chem. Int. Ed.* **2004**, *43*, 3106-3116.
191. H. C. Kolb, M. G. Finn, K. B. Sharpless, *Angew. Chem. Int. Ed.* **2001**, *40*, 2004-2021.
192. J. E. Moses, A. D. Moorhouse, *Chem. Soc. Rev.* **2007**, *36*, 1249-1262.

193. H. C. Kolb, K. B. Sharpless, *Drug Discov. Today* **2003**, *8*, 1128-1137.
194. R. J. Griffin, in *Prog. Med. Chem., Vol. Volume 31* (Eds.: G. P. Ellis, D. K. Luscombe), Elsevier, **1994**, pp. 121-232.
195. R. Breinbauer, M. Köhn, *ChemBioChem* **2003**, *4*, 1147-1149.
196. L. Liang, D. Astruc, *Coord. Chem. Rev.* **2011**, *255*, 2933-2945.
197. N. J. Agard, J. A. Prescher, C. R. Bertozzi, *JACS* **2004**, *126*, 15046-15047.
198. R. K. Lim, Q. Lin, *Chem. Commun.* **2010**, *46*, 1589-1600.
199. P. V. Chang, J. A. Prescher, E. M. Sletten, J. M. Baskin, I. A. Miller, N. J. Agard, A. Lo, C. R. Bertozzi, *Proc. Natl. Acad. Sci. USA* **2010**, *107*, 1821-1826.
200. C. S. McKay, M. Chigrinova, J. A. Blake, J. P. Pezacki, *Org. Biomol. Chem.* **2012**, *10*, 3066-3070.
201. S. S. van Berkel, A. J. Dirks, M. F. Debets, F. L. van Delft, J. J. L. M. Cornelissen, R. J. M. Nolte, F. P. J. T. Rutjes, *ChemBioChem* **2007**, *8*, 1504-1508.
202. X. S. Wang, Y.-J. Lee, W. R. Liu, *Chem. Commun.* **2014**, *50*, 3176-3179.
203. R. Rossin, S. M. van den Bosch, W. ten Hoeve, M. Carvelli, R. M. Versteegen, J. Lub, M. S. Robillard, *Bioconjug. Chem.* **2013**, *24*, 1210-1217.
204. M. F. Debets, S. S. Van Berkel, J. Dommerholt, A. J. Dirks, F. P. Rutjes, F. L. Van Delft, *Acc. Chem. Res.* **2011**, *44*, 805-815.
205. H.-S. Han, N. K. Devaraj, J. Lee, S. A. Hilderbrand, R. Weissleder, M. G. Bawendi, *JACS* **2010**, *132*, 7838-7839.
206. N. K. Devaraj, R. Weissleder, S. A. Hilderbrand, *Bioconjug. Chem.* **2008**, *19*, 2297-2299.
207. K. Malzahn, F. Marsico, K. Koynov, K. Landfester, C. K. Weiss, F. R. Wurm, *ACS Macro Letters* **2013**, *3*, 40-43.
208. K. Kirshenbaum, P. S. Arora, *Nat. Chem. Biol.* **2008**, *4*, 527-528.
209. Y. A. Lin, J. M. Chalker, B. G. Davis, *JACS* **2010**, *132*, 16805-16811.
210. W. R. Algar, D. E. Prasuhn, M. H. Stewart, T. L. Jennings, J. B. Blanco-Canosa, P. E. Dawson, I. L. Medintz, *Bioconjug. Chem.* **2011**, *22*, 825-858.
211. Y.-X. Chen, G. Triola, H. Waldmann, *Acc. Chem. Res.* **2011**, *44*, 762-773.
212. H.-W. Shih, D. N. Kamber, J. A. Prescher, *Curr. Opin. Chem. Biol.* **2014**, *21*, 103-111.
213. K. Lang, J. W. Chin, *Chem. Rev.* **2014**, *114*, 4764-4806.
214. R. Huisgen, M. Seidel, G. Wallbillich, H. Knupfer, *Tetrahedron* **1962**, *17*, 3-29.
215. J. S. Clovis, A. Eckell, R. Huisgen, R. Sustmann, *Chem. Ber.* **1967**, *100*, 60-70.
216. Y. Wang, C. I. Rivera Vera, Q. Lin, *Org. Lett.* **2007**, *9*, 4155-4158.
217. W. Song, Y. Wang, J. Qu, Q. Lin, *JACS* **2008**, *130*, 9654-9655.
218. Y. Wang, W. Song, W. J. Hu, Q. Lin, *Angew. Chem.* **2009**, *121*, 5434-5437.
219. Y. Wang, W. J. Hu, W. Song, R. K. Lim, Q. Lin, *Org. Lett.* **2008**, *10*, 3725-3728.
220. P. An, Z. Yu, Q. Lin, *Chem. Commun.* **2013**, *49*, 9920-9922.
221. P. An, Z. Yu, Q. Lin, *Org. Lett.* **2013**, *15*, 5496-5499.
222. Z. Yu, T. Y. Ohulchanskyy, P. An, P. N. Prasad, Q. Lin, *JACS* **2013**, *135*, 16766-16769.
223. W. Song, Y. Wang, J. Qu, M. M. Madden, Q. Lin, *Angew. Chem.* **2008**, *120*, 2874-2877.
224. C. P. Ramil, Q. Lin, *Curr. Opin. Chem. Biol.* **2014**, *21*, 89-95.
225. G. Delaittre, A. S. Goldmann, J. O. Mueller, C. Barner-Kowollik, *Angew. Chem. Int. Ed.* **2015**, *54*, 11388-11403.
226. J. O. Mueller, D. Voll, F. G. Schmidt, G. Delaittre, C. Barner-Kowollik, *Chem. Commun.* **2014**, *50*, 15681-15684.
227. R. Roux, L. Sallet, P. Alcouffe, S. Chambert, N. Sintes-Zydowicz, E. Fleury, J. Bernard, *ACS Macro. Lett.* **2012**, *1*, 1074-1078.
228. B. Cao, Y. Zheng, T. Xi, C. Zhang, W. Song, K. Burugapalli, H. Yang, Y. Ma, *Biomed. Microdevices* **2012**, *14*, 709-720.
229. E. M. Alexandrino, P. Buchold, M. Wagner, A. Fuchs, A. Kreyes, C. K. Weiss, K. Landfester, F. R. Wurm, *Chem. Commun.* **2014**, *50*, 10495-10498.
230. U. Paiphansiri, G. Baier, A. Kreyes, D. Yiamsawas, K. Koynov, A. Musyanovych, K. Landfester, *Macromol. Chem. Phys.* **2014**, *215*, 2457-2462.
231. K. Malzahn, F. Marsico, K. Koynov, K. Landfester, C. K. Weiss, F. R. Wurm, *ACS Macro Letters* **2014**, *3*, 40-43.

232. K. Breitenkamp, T. Emrick, *JACS* **2003**, *125*, 12070-12071.
233. D. Samanta, K. Kratz, X. Zhang, T. Emrick, *Macromolecules* **2008**, *41*, 530-532.
234. K. Breitenkamp, T. Emrick, *J. Polym. Sci., Part A: Polym. Chem.* **2005**, *43*, 5715-5721.
235. A.-F. Mingotaud, M. Krämer, C. Mingotaud, *J. Mol. Catal. A: Chem.* **2007**, *263*, 39-47.
236. K. Piradashvili, M. Fichter, K. Mohr, S. Gehring, F. R. Wurm, K. Landfester, *Biomacromolecules* **2015**, *16*, 815-821.
237. J. M. Karp, R. Langer, *Curr. Opin. Biotechnol.* **2007**, *18*, 454-459.
238. K. Landfester, V. Mailänder, *Expert Opin. Drug Deliv.* **2013**, *10*, 593-609.
239. Y. Song, Y. Zhou, S. van Drunen Littel-van den Hurk, L. Chen, *Biomater. Sci.* **2014**, *2*, 1440-1449.
240. T. M. Allen, P. R. Cullis, *Science* **2004**, *303*, 1818-1822.
241. R. Singh, J. W. Lillard, Jr., *Exp. Mol. Pathol.* **2009**, *86*, 215-223.
242. W. Amass, A. Amass, B. Tighe, *Polym. Int.* **1998**, *47*, 89-144.
243. G. Luckachan, C. K. S. Pillai, *J. Polym. Environ.* **2011**, *19*, 637-676.
244. K. Knop, R. Hoogenboom, D. Fischer, U. S. Schubert, *Angew. Chem. Int. Ed.* **2010**, *49*, 6288-6308.
245. B. D. Ulery, L. S. Nair, C. T. Laurencin, *J. Polym. Sci., Part B: Polym. Phys.* **2011**, *49*, 832-864.
246. Z. Liu, Y. Jiao, Y. Wang, C. Zhou, Z. Zhang, *Adv. Drug Del. Rev.* **2008**, *60*, 1650-1662.
247. F. R. Wurm, C. K. Weiss, *Front Chem* **2014**, *2*, 49.
248. L. Schoonen, J. C. M. van Hest, *Nanoscale* **2014**, *6*, 7124-7141.
249. S. G. Gayakwad, N. K. Bejugam, N. Akhavein, N. A. Uddin, C. E. Oettinger, M. J. D'Souza, *J. Microencapsul.* **2009**, *26*, 692-700.
250. H. Wartlick, B. Spänkuch-Schmitt, K. Strebhardt, J. Kreuter, K. Langer, *J. Control. Release* **2004**, *96*, 483-495.
251. B. A. Rhodes, I. Zolle, J. W. Buchanan, H. N. Wagner Jr, *Radiology* **1969**, *92*, 1453-1460.
252. A. Arnedo, S. Espuelas, J. M. Irache, *Int. J. Pharm.* **2002**, *244*, 59-72.
253. W. J. Gradishar, *Expert Opin. Pharmacother.* **2006**, *7*, 1041-1053.
254. K. Landfester, *Annu. Rev. Mater. Res.* **2006**, *36*, 231-279.
255. K. Landfester, *Macromol. Rapid Commun.* **2001**, *22*, 896-936.
256. K. Landfester, A. Musyanovych, in *Chemical Design of Responsive Microgels, Vol. 234* (Eds.: A. Pich, W. Richtering), Springer Berlin Heidelberg, **2011**, pp. 39-63.
257. U. Paiphansiri, J. Dausend, A. Musyanovych, V. Mailänder, K. Landfester, *Macromol. Biosci.* **2009**, *9*, 575-584.
258. A. Badiee, N. Davies, K. McDonald, K. Radford, H. Michiue, D. Hart, M. Kato, *Vaccine* **2007**, *25*, 4757-4766.
259. A. Bandyopadhyay, R. L. Fine, S. Demento, L. K. Bockenstedt, T. M. Fahmy, *Biomaterials* **2011**, *32*, 3094-3105.
260. A. Pietrzak-Nguyen, M. Fichter, M. Dedters, L. Pretsch, S. H. Gregory, C. Meyer, A. Doganci, M. Diken, K. Landfester, G. Baier, *Biomacromolecules* **2014**, *15*, 2378-2388.
261. K. Landfester, A. Musyanovych, V. Mailänder, *J. Polym. Sci., Part A: Polym. Chem.* **2010**, *48*, 493-515.
262. C. Weber, C. Coester, J. Kreuter, K. Langer, *Int. J. Pharm.* **2000**, *194*, 91-102.
263. M. Merodio, A. Arnedo, M. J. Renedo, J. M. Irache, *Eur. J. Pharm. Sci.* **2001**, *12*, 251-259.
264. W. Lin, A. Coombes, M. Davies, S. Davis, L. Illum, *J. Drug Target.* **1993**, *1*, 237-243.
265. Y.-J. Hu, Y. Liu, T.-Q. Sun, A.-M. Bai, J.-Q. Lü, Z.-B. Pi, *Int. J. Biol. Macromol.* **2006**, *39*, 280-285.
266. K. Santhi, S. Dhanaraj, M. Koshy, S. Ponnusankar, B. Suresh, *Drug Dev. Ind. Pharm.* **2000**, *26*, 1293-1296.
267. S. Simões, V. Slepushkin, P. Pires, R. Gaspar, M. C. Pedroso de Lima, N. Düzgüneş, *Biochim. Biophys. Acta* **2000**, *1463*, 459-469.
268. M. Brzoska, K. Langer, C. Coester, S. Loitsch, T. O. F. Wagner, C. v. Mallinckrodt, *Biochem. Biophys. Res. Commun.* **2004**, *318*, 562-570.
269. T. A. D. Tetzner, N. Z. Saraiva, F. Perecin, S. C. M. Niciura, C. R. Ferreira, C. S. Oliveira, J. M. Garcia, *Revista Brasileira de Zootecnia* **2011**, *40*, 2135-2141.

270. F. Rusconi, É. Valton, R. Nguyen, E. Dufourc, *Anal. Biochem.* **2001**, *295*, 31-37.
271. S. Ishizaka, K. Nakatani, S. Habuchi, N. Kitamura, *Anal. Chem.* **1998**, *71*, 419-426.
272. K. Rausch, A. Reuter, K. Fischer, M. Schmidt, *Biomacromolecules* **2010**, *11*, 2836-2839.
273. M. Hemmelmann, K. Mohr, K. Fischer, R. Zentel, M. Schmidt, *Mol. Pharm.* **2013**, *10*, 3769-3775.
274. J. Banchereau, R. M. Steinman, *Nature* **1998**, *392*, 245-252.
275. L. Santambrogio, A. K. Sato, G. J. Carven, S. L. Belyanskaya, J. L. Strominger, L. J. Stern, *Proc Natl Acad Sci U S A* **1999**, *96*, 15056-15061.
276. G. W. Schwert, H. Neurath, et al., *J. Biol. Chem.* **1948**, *172*, 221-239.
277. H. Hemmi, T. Kaisho, O. Takeuchi, S. Sato, H. Sanjo, K. Hoshino, T. Horiuchi, H. Tomizawa, K. Takeda, S. Akira, *Nat. Immunol.* **2002**, *3*, 196-200.
278. C. Ogawa, Y.-J. Liu, K. S Kobayashi, *Current bioactive compounds* **2011**, *7*, 180-197.
279. H. Schwarz, G. Posselt, P. Wurm, M. Ulbing, A. Duschl, J. Horejs-Hoeck, *Immunobiology* **2013**, *218*, 533-542.
280. D. A. van Heel, S. Ghosh, M. Butler, K. A. Hunt, A. M. C. Lundberg, T. Ahmad, D. P. B. McGovern, C. Onnie, K. Negoro, S. Goldthorpe, B. M. J. Foxwell, C. G. Mathew, A. Forbes, D. P. Jewell, R. J. Playford, *The Lancet*, *365*, 1794-1796.
281. S. E. Girardin, I. G. Boneca, J. Viala, M. Chamaillard, A. Labigne, G. Thomas, D. J. Philpott, P. J. Sansonetti, *J. Biol. Chem.* **2003**, *278*, 8869-8872.
282. M. Fichter, K. Piradashvili, A. Pietrzak-Nguyen, L. Pretsch, G. Kuhn, S. Strand, M. Knuf, F. Zepp, F. R. Wurm, V. Mailänder, K. Landfester, S. Gehring, *Biomaterials* **2016**, *108*, 1-12.
283. J. P. Messina, I. Humphreys, A. Flaxman, A. Brown, G. S. Cooke, O. G. Pybus, E. Barnes, *Hepatology* **2015**, *61*, 77-87.
284. A. Macdonald, M. Harris, *J. Gen. Virol.* **2004**, *85*, 2485-2502.
285. K. Mohd Hanafiah, J. Groeger, A. D. Flaxman, S. T. Wiersma, *Hepatology* **2013**, *57*, 1333-1342.
286. R. A. Love, O. Brodsky, M. J. Hickey, P. A. Wells, C. N. Cronin, *J. Virol.* **2009**, *83*, 4395-4403.
287. J. Dunlop, A. Owsianka, V. Cowton, A. Patel, *Vaccine (Auckl)* **2015**, *2015*, 31-44.
288. C. M. Walker, A. Grakoui, *Curr. Opin. Immunol.* **2015**, *35*, 137-143.
289. B. Rehermann, A. Bertoletti, *Hepatology* **2015**, *61*, 712-721.
290. R. Thimme, M. Binder, R. Bartenschlager, *FEMS Microbiol. Rev.* **2012**, *36*, 663-683.
291. W. Li, D. K. Krishnadas, R. Kumar, D. L. J. Tyrrell, B. Agrawal, *Int. Immunol.* **2008**, *20*, 89-104.
292. O. V. Masalova, E. I. Lesnova, A. V. Pichugin, T. M. Melnikova, V. V. Grabovetsky, N. V. Petrakova, O. A. Smirnova, A. V. Ivanov, A. D. Zaberezhny, R. I. Ataullakhanov, *Vaccine* **2010**, *28*, 1987-1996.
293. H. Yu, L. A. Babiuk, S. Van Drunen Littel-van den Hurk, *J. Viral Hepat.* **2008**, *15*, 459-470.
294. M. L. Mbow, E. De Gregorio, N. M. Valiante, R. Rappuoli, *Curr. Opin. Immunol.* **2010**, *22*, 411-416.
295. J. K. Bohannon, A. Hernandez, P. Enkhbaatar, W. L. Adams, E. R. Sherwood, *Shock (Augusta, Ga.)* **2013**, *40*, 451.
296. F. Sarti, G. Perera, F. Hintzen, K. Kotti, V. Karageorgiou, O. Kammona, C. Kiparissides, A. Bernkop-Schnürch, *Biomaterials* **2011**, *32*, 4052-4057.
297. J. Beran, *Expert Opin. Biol. Ther.* **2008**, *8*, 235-247.
298. W. Kratky, C. R. e Sousa, A. Oxenius, R. Spörri, *Proc. Natl. Acad. Sci. USA* **2011**, *108*, 17414-17419.
299. P. J. Tacken, I. S. Zeelenberg, L. J. Cruz, M. A. van Hout-Kuijer, G. van de Glind, R. G. Fokkink, A. J. Lambeck, C. G. Figdor, *Blood* **2011**, *118*, 6836-6844.
300. J. M. Blander, R. Medzhitov, *Nature* **2006**, *440*, 808-812.
301. P. Elamanchili, M. Diwan, M. Cao, J. Samuel, *Vaccine* **2004**, *22*, 2406-2412.
302. X. Zhang, S. Bloch, W. Akers, S. Achilefu, *Current protocols in cytometry* **2012**, 12.27. 11-12.27. 20.

303. S. Ohnishi, S. J. Lomnes, R. G. Laurence, A. Gogbashian, G. Mariani, J. V. Frangioni, *Mol. Imaging* **2005**, *4*.
304. A. R. Stark, W. A. Carlo, J. E. Tyson, L.-A. Papile, L. L. Wright, S. Shankaran, E. F. Donovan, W. Oh, C. R. Bauer, S. Saha, *New Engl. J. Med.* **2001**, *344*, 95-101.
305. U. Bandyopadhyay, K. Biswas, D. Bandyopadhyay, C. Ganguly, R. Banerjee, *Mol. Cell. Biochem.* **1999**, *202*, 31-36.
306. J. Vardy, K. Chiew, J. Galica, G. Pond, I. Tannock, *Br. J. Cancer* **2006**, *94*, 1011-1015.
307. C. Gómez-Gaete, N. Tsapis, M. Besnard, A. Bochot, E. Fattal, *Int. J. Pharm.* **2007**, *331*, 153-159.
308. U. Bhardwaj, D. J. Burgess, *Int. J. Pharm.* **2010**, *388*, 181-189.
309. M. Fichter, G. Baier, M. Dedters, L. Pretsch, A. Pietrzak-Nguyen, K. Landfester, S. Gehring, *Nanomedicine* **2013**, *9*, 1223-1234.
310. P. Rohdewald, H. Möllmann, J. Barth, J. Rehder, H. Derendorf, *Biopharm. Drug Disposition* **1987**, *8*, 205-212.
311. J. Hemenway, V. J. Stella, in *Prodrugs*, Springer, **2007**, pp. 217-281.
312. N. Vargaftik, B. Volkov, L. Voljak, *J. Phys. Chem. Ref. Data* **1983**, *12*, 817-820.
313. D. Metcalf, *The thymus: its role in immune responses, leukaemia development and carcinogenesis, Vol. 5*, Springer Science & Business Media, **2012**.
314. R. H. Staff, K. Landfester, D. Crespy, in *Hierarchical Macromolecular Structures: 60 Years after the Staudinger Nobel Prize Ii, Vol. 262* (Ed.: V. Percec), **2013**, pp. 329-344.
315. A. S. Hoffman, *Adv. Drug Del. Rev.* **2013**, *65*, 10-16.
316. P. Couvreur, *Adv. Drug Del. Rev.* **2013**, *65*, 21-23.
317. J. Ge, E. Neofytou, J. Lei, R. E. Beygui, R. N. Zare, *Small* **2012**, *8*, 3573-3578.
318. J.-W. Yoo, D. J. Irvine, D. E. Discher, S. Mitragotri, *Nat. Rev. Drug Discov.* **2011**, *10*, 521-535.
319. Z. Y. Zhang, Y. D. Xu, Y. Y. Ma, L. L. Qiu, Y. Wang, J. L. Kong, H. M. Xiong, *Angew. Chem. Int. Ed.* **2013**, *52*, 4127-4131.
320. E. Fleige, M. A. Quadir, R. Haag, *Adv. Drug Del. Rev.* **2012**, *64*, 866-884.
321. Y.-J. Pan, Y.-Y. Chen, D.-R. Wang, C. Wei, J. Guo, D.-R. Lu, C.-C. Chu, C.-C. Wang, *Biomaterials* **2012**, *33*, 6570-6579.
322. S. Mura, J. Nicolas, P. Couvreur, *Nature materials* **2013**, *12*, 991-1003.
323. J. Nicolas, S. Mura, D. Brambilla, N. Mackiewicz, P. Couvreur, *Chem. Soc. Rev.* **2013**, *42*, 1147-1235.
324. Y. Jiang, J. Chen, C. Deng, E. J. Suuronen, Z. Zhong, *Biomaterials* **2014**, *35*, 4969-4985.
325. Y. Fan, C. Deng, R. Cheng, F. Meng, Z. Zhong, *Biomacromolecules* **2013**, *14*, 2814-2821.
326. Z. Yu, R. K. Lim, Q. Lin, *Chem. Eur. J.* **2010**, *16*, 13325-13329.
327. S. Ito, Y. Tanaka, A. Kakehi, K.-i. Kondo, *Bull. Chem. Soc. Jpn.* **1976**, *49*, 1920-1923.
328. A. Shawali, A. Fahmi, N. Eweiss, *J. Heterocycl. Chem.* **1979**, *16*, 123-128.
329. Y. Li, L.-X. Gao, F.-S. Han, *Chem. Commun.* **2012**, *48*, 2719-2721.
330. C. Y. Liu, Y. Li, J. Y. Ding, D. W. Dong, F. S. Han, *Chemistry–A European Journal* **2014**, *20*, 2373-2381.
331. Z. Li, L. Qian, L. Li, J. C. Bernhammer, H. V. Huynh, J. S. Lee, S. Q. Yao, *Angew. Chem. Int. Ed.* **2015**.
332. Y. Zhang, W. Liu, Z. K. Zhao, *Molecules* **2013**, *19*, 306-315.
333. W. Siti, A. K. Khan, H.-P. M. de Hoog, B. Liedberg, M. Nallani, *Org. Biomol. Chem.* **2015**, *13*, 3202-3206.
334. W. Feng, L. Li, C. Yang, A. Welle, O. Trapp, P. A. Levkin, *Angew. Chem. Int. Ed.* **2015**, *54*, 8732-8735.
335. M. Fichter, M. Dedters, A. Pietrzak-Nguyen, L. Pretsch, C. U. Meyer, S. Strand, F. Zepp, G. Baier, K. Landfester, S. Gehring, *Vaccine* **2015**, *33*, 838-846.
336. M. Jurk, F. Heil, J. Vollmer, C. Schetter, A. M. Krieg, H. Wagner, G. Lipford, S. Bauer, *Nat. Immunol.* **2002**, *3*, 499-499.
337. A. Iwasaki, R. Medzhitov, *Science* **2010**, *327*, 291-295.
338. S. Schöttler, G. Becker, S. Winzen, T. Steinbach, K. Mohr, K. Landfester, V. Mailänder, F. R. Wurm, *Nat. Nanotechnol.* **2016**, *11*, 372-377.

339. S. Ritz, S. Schöttler, N. Kotman, G. Baier, A. Musyanovych, J. r. Kuharev, K. Landfester, H. r. Schild, O. Jahn, S. Tenzer, *Biomacromolecules* **2015**, *16*, 1311-1321.
340. H. Greenfield, H. W. Sternberg, R. A. Friedel, J. H. Wotiz, R. Markby, I. Wender, *JACS* **1956**, *78*, 120-124.
341. K. A. Tallman, M. D. Armstrong, S. B. Milne, L. J. Marnett, H. A. Brown, N. A. Porter, *J. Lipid Res.* **2013**, *54*, 859-868.
342. M. Hesse, H. Meier, B. Zeeh, *Spektroskopische Methoden in der organischen Chemie. 7. Aufl., 2005*, Georg Thieme Verlag, Stuttgart.
343. N. Meinander, S. Forss, G. Bergström, *J. Raman Spectrosc.* **1981**, *11*, 155-167.
344. A. L. Jenkins, R. A. Larsen, T. B. Williams, *Spectrochim. Acta, Pt. A: Mol. Biomol. Spectrosc.* **2005**, *61*, 1585-1594.
345. G. Placzek, *Z. Phys.* **1931**, *70*, 84-103.
346. H. Schlaad, H. Kukula, J. Rudloff, I. Below, *Macromolecules* **2001**, *34*, 4302-4304.
347. G. Baier, A. Musyanovych, M. Dass, S. Theisinger, K. Landfester, *Biomacromolecules* **2010**, *11*, 960-968.
348. M. Fichter, M. Dedters, A. Pietrzak-Nguyen, L. Pretsch, C. U. Meyer, S. Strand, F. Zepp, G. Baier, K. Landfester, S. Gehring, *Vaccine* **2015**.
349. C. Scheicher, M. Mehlig, R. Zecher, K. Reske, *J. Immunol. Methods* **1992**, *154*, 253-264.
350. K. Gisch, N. Gehrke, M. Bros, C. Priesmeyer, J. Knop, A. B. Reske-Kunz, S. Sudowe, *Int. Arch. Allergy Immunol.* **2007**, *144*, 183-196.
351. T. Zal, A. Volkmann, B. Stockinger, *J. Exp. Med.* **1994**, *180*, 2089-2099.
352. S. Gehring, S. H. Gregory, P. Wintermeyer, M. San Martin, C. Aloman, J. R. Wands, *J. Immunol. Methods* **2008**, *332*, 18-30.
353. S. Gehring, S. H. Gregory, P. Wintermeyer, C. Aloman, J. R. Wands, *Clin. Vaccine Immunol.* **2009**, *16*, 163-171.
354. S. Gehring, E. M. Dickson, M. E. San Martin, N. van Rooijen, E. F. Papa, M. W. Harty, T. F. Tracy, Jr., S. H. Gregory, *Gastroenterology* **2006**, *130*, 810-822.
355. S. Tenzer, D. Docter, S. Rosfa, A. Wlodarski, J. Kuharev, A. Rekik, S. K. Knauer, C. Bantz, T. Nawroth, C. Bier, J. Sirirattanapan, W. Mann, L. Treuel, R. Zellner, M. Maskos, H. Schild, R. H. Stauber, *ACS Nano* **2011**, *5*, 7155-7167.
356. J. C. Silva, M. V. Gorenstein, G.-Z. Li, J. P. Vissers, S. J. Geromanos, *Mol. Cell. Proteomics* **2006**, *5*, 144-156.

Acknowledgements

Scientific Contributions